

**INFLUENCE OF Ni THIN FILM STRUCTURAL  
PROPERTIES OVER GRAPHENE GROWTH BY  
CVD**

A Thesis Submitted to  
the Graduate School of Engineering and Sciences of  
Izmir Institute of Technology  
in Partial Fulfillment of Requirement for Degree of  
  
**MASTER OF SCIENCE**  
  
**in Physics**

by  
**Elif ÖZÇERİ**

**July 2013**  
**İZMİR**

We approve the thesis of **Elif ÖZÇERİ**

**Examining Committee Members:**

---

**Assoc. Prof. Dr. Yusuf SELAMET**

Department of Physics, Izmir Institute of Technology

---

**Assit. Prof. Dr. Coşkun KOCABAŞ**

Department of Physics, Bilkent University

---

**Prof. Dr. R. Tuğrul SENGER**

Department of Physics, Izmir Institute of Technology

---

**11 July 2013**

---

**Assoc. Prof. Dr. Yusuf SELAMET**

Supervisor, Department of Physics  
Izmir Institute of Technology

---

**Prof. Dr. Nejat BULUT**

Head of the Department of Physics

---

**Prof. Dr. R. Tuğrul SENGER**

Dean of the Graduate School of  
Engineering and Sciences

## **ACKNOWLEDGEMENTS**

It is my pleasure to acknowledge and express my gratitude those who helped me along the way to completion of this thesis.

Firstly, I want to thank to Izmir Institute of Technology Department of Physics for giving me the chance to be a member of scientific study and supporting me as a research assistant during my postgraduate study.

Specially, I would like to express my endless respect and gratitude to my supervisor Assoc. Prof. Dr. Yusuf Selamet for his trust and accepting me as his student. Also, he has always made me feel that he has confidence in me. His patience, insightful guidance, encouragement, ingenious remarks and comments helped me finish this study and he never hesitated to spend his valuable time to help me. I learnt a lot from him. I will always remember and be inspired by his hard work and good heart for all the rest of my life.

I would also like to thank the other members of my thesis defense committee: Assist. Prof. Dr. Coşkun Kocabas and Prof. R. Tuğrul Senger for their helpful comments and suggestions.

Moreover, I would like to thank Assist. Prof. Dr. Süleyman Tari for establishing magnetism laboratory. I want to thank to Assist. Prof. Dr. Enver Tarhan for giving me the opportunity to use Raman Spectroscope whenever I needed. He has always answered to all my questions with patience. I am very thankful to Assoc. Prof. Dr. Bülent Aslan, Assoc. Prof. Dr. Uğur Serincan and Güven Korkmaz for giving me the chance to perform XRD measurements and for their warm friendship. Especially, thanks to Güven Korkmaz for spending his invaluable time for XRD measurements.

I am very thankful to my lab mates Atike İnce Yardımcı and Deniz Söylev for introducing me to the Carbon Nanostructure Laboratory for the first time. Also, I would like to thank Prof. Salih Okur, Hasan Aydin and Nesli Tekgüzel Yağmurcukardeş for giving me the opportunity of learning AFM. I will always be grateful to Ozan Arı for his helpful comments and giving his time whenever I need.

For SEM and EDX analysis, I send my thanks to IYTE Material Research Center staff. Thank to Prof. Dr. Orhan Öztürk for performing some XRD measurements.

Personally, my special thanks go to my home mate Corinna Wagner for her good heart and always being sympathetic. I am so happy to have her in my life. I also would like to give my special thanks to my friend Atila Orhon, and my dear uncle F. Mehmet Başol for their crucial support in the last days of deadline. I thank to my mother Emine Özçeri and my brother Erman Özçeri. I would not have accomplished anything without them by my side. I would like to thank all my precious family for ceaseless support, motivation and love in all my life and believing in me. I need them always by my side.

Last, but most importantly, I feel very lucky to have Fadıl İyikanat. He has been by my side in good days and bad days listening, advising, easing my troubles and cheering me up. I am grateful to him for his endless support, patience, generosity, love and faith in me.

I apologize to those whom I unwillingly forgot to mention. I wish all my loved ones to have a happy and successful life.

## **ABSTRACT**

### **INFLUENCE OF Ni THIN FILM STRUCTURAL PROPERTIES OVER GRAPHENE GROWTH BY CVD**

This thesis work focused on the effect of polycrystalline Nickel (Ni) TM thin film structure on the growth graphene by chemical vapor deposition (CVD). TM films were deposited by magnetron sputtering technique on Si/SiO<sub>2</sub> substrates. To grow 1-2 layer graphene on Ni thin film catalyst by methane decomposition thermal CVD method was carried out using various growth parameters.

To reduce the TM film surface roughness and grow larger size graphene layers on Ni film, Si/SiO<sub>2</sub> substrates were coated by a thin Al<sub>2</sub>O<sub>3</sub> buffer layers and Cr adhesive layers by magnetron sputtering. Ni film crystal structure and surface roughness, which affected the number of graphene layers, were examined by X-ray Diffraction (XRD) and Atomic Force Microscopy (AFM) techniques, respectively. The thickness and columnar structure of the films were measured from Surface Profiler and Scanning Electron Microscopy (SEM) images. Ni films were annealed at 800 °C, 900 °C and 950 °C in order to improve their crystal quality and to evaluate the effect of the crystallinity on graphene growth at atmospheric pressure. Samples were studied using XRD and AFM also to assess their crystal quality after the annealing process. It was observed that the calculated grain sizes depended on the film thickness and the annealing temperature. Surface roughness of the films was increased by increasing film thickness. A sole thin Al<sub>2</sub>O<sub>3</sub> buffer layer reduced the surface roughness significantly. However, sole Cr adhesive layer or Cr/Al<sub>2</sub>O<sub>3</sub> buffer layers did not reduce the surface roughness, but increased the crystallinity of Ni films in (111) direction.

Argon, Hydrogen or a mixture of these two gases was added to methane during graphene growth at ambient pressure by CVD. The Raman spectroscopy was utilized in order to determine the number of the layers and quality of graphene growth over the Ni catalyst film.

## ÖZET

### Nİ İNCE FİLM YAPISAL ÖZELLİKLERİİNİN CVD İLE GRAFEN BÜYÜTMESİ ÜZERİNE ETKİSİ

Bu tez, polikristal Nikel (Ni) geçiş metalinin yapışal özelliklerinin kimyasal buhar biriktirme (CVD) tekniği ile grafen büyütmesi üzerine etkisine odaklanmıştır. Filmler manyetik saçtırma yöntemiyle Si/SiO<sub>2</sub> alttaşlar üzerine büyütülmüştür. Ni ince film katalist üzerine 1-2 katman grafen büyütmek için metan dekompozisyonu termal kimyasal buhar biriktirme tekniği çeşitli parametrelerle çalışıldı.

Yüzey pürüzlülüğünü azaltmak ve Ni film üzerinde daha büyük boyutlarda grafen katmanları büyütmek için Al<sub>2</sub>O<sub>3</sub> ve Cr tampon katmanları manyetik saçtırma yöntemiyle kaplanmıştır. Büyütülen grafenin katman sayısını etkileyen Ni film kristal yapısı ve yüzey pürüzlülüğü X-ışını Kırınımı (XRD) ve Atomik kuvvet mikroskopu (AFM) teknikleri ile incelendi. Yüzey profili ve Taramalı Elektron Mikroskopu (SEM) görüntülerinden kolumnar yapıya sahip filmlerin kalınlığı gözlemlenmiştir. Ni filmler kristal kalitesini artırmak ve kristalinite etkisini değerlendirmek için 800 °C, 900 °C and 950 °C sıcaklıklarda atmosferik basınç altında tavlandı. Örnekler tavlandıktan sonraki kristal kalitelerini değerlendirmek için XRD ve AFM ile tekrar incelenmiştir. Hesaplanan tanecik boyutlarının film kalınlığına ve tavlama sıcaklığına bağlı olduğu gözlemlenmiştir. İnce bir Al<sub>2</sub>O<sub>3</sub> tampon katman tek başına yüzey pürüzlülüğünü önemli ölçüde azaltmıştır. Tek başına Cr tampon katman veya Cr/Al<sub>2</sub>O<sub>3</sub> tampon katmanı pürüzlülüğü azaltmamış, fakat (111) yönelimin kristalinitesini artırmıştır.

Argon, hidrojen ya da bu iki gazın karışımı ortam basıncındaki CVD ile büyütme süresince metana eklenmiştir. Ni kataliz film üzerinde büyütülen grafenin katman sayısı ve kalitesi Raman Spektroskopisi ile belirlenmiştir.

*Dedicated to;  
My Father*

## TABLE OF CONTENTS

TABLE OF CONTENTS .....	viii
LIST OF FIGURES.....	xi
LIST OF TABLES .....	xix
CHAPTER 1. INTRODUCTION .....	1
CHAPTER 2. BACKGROUND AND LITERATURE REVIEW .....	3
2.1 Carbon.....	3
2.1.1. Carbon Nanostructures.....	4
2.1.1.1. Three Dimensional Carbon Nanostructures .....	4
2.1.1.1.1. Graphite .....	4
2.1.1.1.2. Diamond .....	6
2.1.1.2. Two Dimensional Carbon Nanostructures .....	7
2.1.1.2.1. Graphene.....	7
2.1.1.2.2. Graphane.....	8
2.1.1.2.3. Graphyne.....	9
2.1.1.2.4. Carbon Nanowalls (CNWs) .....	9
2.1.1.3. One Dimensional Carbon Nanostructures .....	11
2.1.1.3.1. Carbon Nanofibers.....	11
2.1.1.3.2. Carbon Nanotubes .....	12
2.1.1.4. Zero Dimensional Carbon Nanostructures .....	14
2.1.1.4.1. Fullerene .....	14
2.1.1.4.2. Carbon-Encapsulated Metal Nanoparticles .....	15
2.1.1.4.3. Nanodiamond.....	15
2.1.1.4.4. Onion-Like Carbons .....	16
2.2. Graphene .....	16
2.2.1. Electronic Structure of Graphene: Tight Binding Approach .....	17
2.2.2. Vibrational Properties of Graphene .....	20

2.2.3. Other Properties of Graphene.....	22
2.2.4. Graphene Production Methods.....	24
2.2.4.1. Exfoliation and Cleavage .....	24
2.2.4.2. Thermal Decomposition of SiC.....	25
2.2.4.2. Chemical Vapor Deposition .....	26
2.2.4.3. Other Methods of Synthesis Graphene.....	27
 CHAPTER 3. EXPERIMENTAL TECHNIQUES.....	29
3.1. Thin Film Preparation .....	29
3.1.1. Substrate Cleaning .....	29
3.1.2. Thin Film Deposition: Magnetron Sputtering Technique .....	30
3.1.2.1. DC Magnetron Sputtering .....	31
3.1.2.2. RF Magnetron Sputtering .....	32
3.1.2.3. Film Deposition Process.....	32
3.2. Atomic Force Microscopy (AFM) .....	33
3.3. X-Ray Diffractometer (XRD) .....	35
3.4. Scanning Electron Microscopy (SEM) .....	37
3.5. Chemical Vapor Deposition (CVD).....	38
3.6. Raman Spectroscopy.....	43
 CHAPTER 4. Ni THIN FILM STRUCTURE.....	51
4.1. Nickel Crystal Structure.....	53
4.2. Thickness of Ni Films and Buffer Layers .....	55
4.3. Effect of Annealing on Ni Thin Films .....	64
4.4. XRD Results .....	70
4.4.1. Calculation of Ni (111) Grain Sizes.....	80
4.5. AFM and SEM Results .....	85
 CHAPTER 5. SYNTHESIS OF GRAPHENE BY CVD ON POLYCRYSTALLINE NICKEL AND CHARACTERIZATION BY RAMAN SPECTROSCOPY .....	105
5.1. Graphene Growth Process by CVD .....	105
5.2. Raman Spectroscopy Results .....	108

5.3. SEM Results.....	125
CHAPTER 6. CONCLUSIONS .....	129
REFERENCES .....	132

## LIST OF FIGURES

<u>Figure</u>	<u>Page</u>
Figure 2.1. The crystal structure of hexagonal single crystal graphite .....	4
Figure 2.2. The stacking patterns of AA, AB and ABC stacking between graphene layers .....	5
Figure 2.3. The crystal structure of diamond.....	6
Figure 2.4. Schematics of adding hydrogen converts graphene (a) into graphane (b) ....	8
Figure 2.5. The structure of a 2D graphyne layer .....	9
Figure 2.6. Scanning electron microscopy image ( $1.6 \times 1.6 \mu\text{m}$ ) of CNWs .....	10
Figure 2.7. Schematic representations for CNFs: (a) platelet-type CNF, (b) fishbone type CNF, (c) ribbon-type CNF, (d) cup stacked-type CNF.....	11
Figure 2.8. Schematic representations of singlewall nanotube (SWNT) and multiwall nanotube (MWNT).....	12
Figure 2.9. Schematic structures of SWNTs with different chirality. (a) A (10, 10) arm- chair nanotube, (b) A (12, 0) zigzag nanotube, (c) The (14, 0) zigzag tube, (d) A (7, 16) chiral tube. The cross-sections of the first two illustrations have been highlighted by the bold red lines showing the armchair and zigzag character, respectively .....	13
Figure 2.10. An illustration of Buckminsterfullerene and its fragment Corannulene ....	14
Figure 2.11. Hexagonal structure of graphene.....	16
Figure 2.12. (a) Schematic of $\text{sp}^2$ hybrid C-C bond structure containing in plane $\sigma$ -bond and perpendicular $\pi$ -bond, (b) unit cell and, (c) Brillouin zone of graphene are shown as the dotted rhombus and the shaded hexagon, and the red vectors show the nearest-neighbor vectors .....	18
Figure 2.13. A plot of the energy versus momentum dispersion relation for graphene shown throughout the BZ and the inset shows the energy dispersion relations along the high symmetry axes along the perimeter of the triangle shown in Figure 2.12 (c). .....	20
Figure 2.14. The dispersion relation of out-of-plane modes (a) and in-plane modes (b) of graphene are obtained using the second-nearest-neighbor model for graphene. The vertical axes are the phonon frequency, while the horizontal axes are the momentum space on the graphene lattice .....	21

Figure 2.15. Schematic representation of using Scotch tape. (a) pressing the tape on bulk graphite, (b) peeling a thin layer of graphite, (c-d-e) folding the tape over and pressing it against itself, the graphite was spread over two and more areas of the tape, (f) the thinned layer of graphite over the tape .....	24
Figure 2.16. Shematic representation of CVD set up for the synthesis of graphene .....	26
Figure 2.17. Illustration of various CNT unzipping methods.....	28
Figure 3.1. ATC AJA Orion 5 UHV Sputtering System in the Department of Physics at IZTECH. ....	30
Figure 3.2. The optical detection system from the software Nova of MNT-MDT.....	34
Figure 3.3. HA_NC etalon probe from NT-MDT .....	35
Figure 3.4. Representation of incoming and diffracting X-rays from different lattices .....	35
Figure 3.5. Ideal FWHM of a XRD peak .....	36
Figure 3.6. CVD growth system at Physics Department, CNL Lab, IZTECH.....	39
Figure 3.7. Schematic representations of the possible distribution of C isotopes on different metal substrates and their growth mechanisms. (a) Graphene with randomly mixed isotopes refers to surface segregation and/or precipitation. (b) Graphene with separated isotopes refers to surface adsorption. (c) Combined growth from surface adsorption and precipitation .....	40
Figure 3.8. Raman spectra from graphene composed of C <sup>13</sup> (blue), C <sup>12</sup> (green) and from the mixture of both (red) .....	41
Figure 3.9. Illustration of carbon segregation mechanism and effect of cooling rate on Ni substrate. ....	42
Figure 3.10. Theoretically calculated phonon dispersion of the six types of vibration modes as a function of E <sub>laser</sub> in the graphene where o=out-of-plane and i=in-plane modes.....	44
Figure 3.11. First order (a), and second order scattering processes (b,c,d) .....	45
Figure 3.12. Electronic structure of 2-LG near Dirac points .....	47
Figure 3.13. G' spectra for graphene as a function of as a function of the number of layers with 2.41 eV laser energy for (a) 1-LG, (b) 2-LG, (c) 3-LG, (d) 4-LG, (e) HOPG, (f) turbostratic .....	48
Figure 3.14. Raman spectra of 1 (red), 2 (blue), and ~3 (green) graphene layers from a CVD grown graphene films on SiO <sub>2</sub> /Si substrate (a). Raman spectra of the	

same layer numbered graphene films derived by the microcleaving of HOPG for comparison (b). The excitation wavelength is 532 nm .....	49
Figure 3.15. Raman spectra has the intensity ratio of $I_G/I_{G'}$ <1 (a) and both $I_G/I_{G'}<1$ and $I_G/I_{G'}>1$ (b).....	49
Figure 4.1. Representation of graphene growth (a) on Ni (111), and (b) on polycrystalline Ni. After growth by CVD optical image of (a) graphene/Ni (111) and (d) graphene/polycrystalline Ni.....	51
Figure 4.2. Cross sectional schematics of asgrown film structures with thickness less than $1\mu\text{m}$ and the different columnar structures which depend on deposition temperatures ( $T_d$ ). $T_d$ below about 0.2-0.3 $T_m$ (a), deposition temperature $T_d \geq 0.2-0.3 T_m$ (b) and $T_d \geq T_m$ (c). .....	52
Figure 4.3. Cross sectional SEM micrographs of asgrown polycrystalline Ni3 film (a) which has thickness of about 200 nm and asgrown Ni9 film (b) about 450 nm thick. ....	53
Figure 4.4. Three possible arrangements of the graphene layer on 1 <sup>st</sup> , 2 <sup>nd</sup> and 3 <sup>rd</sup> Ni layers with ball model on the top. The blue balls indicate the Ni atoms and the black ones carbon atoms. On the bottom line, cross sectional view of Ni layers and carbon atoms of graphene layer.....	54
Figure 4.5. Representation of the layer structure of deposited films with their thickness.....	56
Figure 4.6. Cross sectional SEM micrographs of Ni1, Ni2, Ni3, Ni4, Ni5 and Ni6 films .....	57
Figure 4.7. Relation between DC power and thickness of sputtered Ni films.....	58
Figure 4.8. Surface Profiler step height measurement of AlO-2 sample (~55 nm).....	59
Figure 4.9. Thickness versus time relation of Al <sub>2</sub> O <sub>3</sub> films .....	59
Figure 4.10. Cross sectional SEM micrograph of SiO <sub>2</sub> substrate that has 230 nm thick .....	60
Figure 4.11. Cross sectional SEM micrographs of asgrown Ni7 (a), and Ni9 (b) films.....	60
Figure 4.12. Surface Profiler step height measurement of Cr4 sample (~50 nm) .....	62
Figure 4.13. Thickness versus power relation of Cr films. All samples at this graph deposited during 10 minutes at room temperature.....	62
Figure 4.14. Thickness versus time relations of Cr films .....	63

Figure 4.15. Cross sectional SEM micrographs of asgrown Ni15 (a), and Ni16 (b) films.....	64
Figure 4.16. Cross sectional SEM micrographs of Ni3 film and thickness of films which are asgrown (a) and annealed at 800 °C (b) and 900 °C (c).....	65
Figure 4.17. The relation between annealing temperature and the (111) orientation intensity of Ni1 sample .....	66
Figure 4.18. Top view of a normal grain growth. Large grains tend to grow larger and small grains tend to shrink and disappear; (a) and (b). Asgrown Ni15 sample (c), and annealed Ni15 sample during 60 minutes at 900 °C (d) .....	67
Figure 4.19. Schematic representations of grains. (a) top view of finite curvatures, (b) cross sectional view of grain boundaries like arcs of circles and catenoid like shape of curvatures (c) cross sectional view of a groove.....	69
Figure 4.20. XRD $\theta$ - $2\theta$ measurements for 230 nm thick SiO <sub>2</sub> and 1μm thick SiO <sub>2</sub> ....	71
Figure 4.21. XRD $\theta$ - $2\theta$ measurement results for Ni1, Ni2 and Ni3 samples (a), and Ni4, Ni5, Ni6 samples (b) with both asgrown (light lines) and annealed at 900 °C (dark lines) cases .....	72
Figure 4.22. XRD $\theta$ - $2\theta$ measurement result of Al <sub>2</sub> O <sub>3</sub> film annealed at 900 °C .....	73
Figure 4.23. XRD $\theta$ - $2\theta$ measurement results for Ni7 and Ni8 samples with both asgrown and annealed at 900 °C cases .....	74
Figure 4.24. XRD $\theta$ - $2\theta$ measurement results for Ni9 and Ni11 (a), and Ni10 and Ni12 (b) samples with both asgrown and annealed at 900 °C cases .....	75
Figure 4.25. XRD $\theta$ - $2\theta$ measurement results for Ni13 and Ni14 films with both asgrown and annealed at 900 °C cases.....	76
Figure 4.26. XRD $\theta$ - $2\theta$ measurement results of 30 nm thick Cr film; asgrown (black line) and annealed at 900 °C (red line) cases .....	77
Figure 4.27. XRD $\theta$ - $2\theta$ measurement results for Ni15 (a) and Ni16 (b); asgrown and annealed at 900 °C during 30 minutes and 60 minutes .....	78
Figure 4.28. XRD $\theta$ - $2\theta$ measurement results for Ni17 (a) and Ni18 (b); asgrown and annealed at 900 °C during 30 minutes and 60 minutes .....	79
Figure 4.29. Fitted XRD peak of asgrown (a) and annealed at 900 °C (b) Ni1 films by Origin Data Analysis and Graphing software. Red lines refer to calculated profile and the background was subtracted.....	81
Figure 4.30. Fitted XRD $\theta$ - $2\theta$ measurement results of asgrown (a, b) and annealed Ni7 sample (c, d). Their potential NiO and Al <sub>2</sub> O <sub>3</sub> peaks calculated by X-Pert	

HighScore peak search software (a, c). Blue line refers to calculated profile and green line is background. Their potential NiO and Al <sub>2</sub> O <sub>3</sub> peaks calculated by origin data analysis and graphing software (a, c) .....	82
Figure 4.31. Fitted XRD $\theta$ - $2\theta$ measurements of Ni18 film. The dark blue line indicates asgrown Ni18 film, the light blue line indicates annealed at 900 °C during 60 minutes of Ni18 film.....	83
Figure 4.32. Fitted XRD $\theta$ - $2\theta$ measurements of Ni16 film. The dark blue line indicates asgrown Ni16 film, the light blue line indicates annealed at 900 °C during 60 minutes of Ni16 film.....	83
Figure 4.33. Calculated grain sizes of Ni (111) for all samples .....	84
Figure 4.34. SEM micrograph (a), AFM topographic image (b), and 1 dimensional grain analysis of the line on topographic image (c) of asgrown Ni1 film.....	85
Figure 4.35. SEM micrograph (a), AFM topographic image (b), 1 dimensional grain analysis of the line on topographic image (c), and cross sectional SEM micrograph (d) of annealed Ni1 film at 900 °C .....	86
Figure 4.36. SEM micrographs of annealed Ni1 film at 900 °C (a-b). Spectrums show the regions that EDX performed and the table shows the percentage distributions of the elements .....	87
Figure 4.37. SEM micrograph (a), AFM topographic image (b), and 1 dimensional grain analysis of the line on topographic image (c) of asgrown Ni4 film.....	88
Figure 4.38. SEM micrograph (a), AFM topographic image (b), and 1 dimensional grain analysis of the line on topographic image (c) of annealed Ni4 film at 900 °C.....	89
Figure 4.39. AFM topographic image (a), and 1 dimensional grain analysis of the line on topographic image (b) of asgrown Ni7 film. AFM topographic image (c), 1 dimensional grain analysis of the line on topographic image (d), and SEM micrograph (e) of annealed Ni7 film at 900 °C.....	91
Figure 4.40. Electron image of annealed Ni7 film at 900 °C. The bottom line shows weight percentages of Ni, Si, O and Al elements according to EDX results .....	92
Figure 4.41. Electron image of annealed Ni7 film at 900 °C. The bottom line weight percentages of Ni, Si, O and Al elements according to EDX results.....	93
Figure 4.42. SEM micrographs of annealed at 900 °C Ni1 film (a), and Ni7 film (b) ...	93

Figure 4.43. AFM topographic image (a), and 1 dimensional grain analysis of the line on topographic image (b) of asgrown Ni9 film. AFM topographic image (c), 1 dimensional grain analysis of the line on topographic image (d), and SEM micrograph (e) of annealed Ni9 film at 900°C.....	95
Figure 4.44. AFM topographic image (a), and 1 dimensional grain analysis of the line on topographic image (b) of asgrown Ni11 film. AFM topographic image (c), 1 dimensional grain analysis of the line on topographic image (d), and SEM micrograph (e) of annealed Ni11 film at 900°C .....	96
Figure 4.45. SEM micrographs of asgrown Ni13 (a), and Ni14 films (b). Ni13 (c), Ni14 (d) after annealed at 900 °C .....	97
Figure 4.46. AFM topographic image (a), and 1 dimensional grain analysis of the line on topographic image (b) of asgrown Ni15 film. AFM topographic image (c), 1 dimensional grain analysis of the line on topographic image (d), and SEM micrograph (e) of annealed Ni15 film at 900 °C .....	99
Figure 4.47. AFM topographic image (a), and 1 dimensional grain analysis of the line on topographic image (b) of asgrown Ni16 film. AFM topographic image (c), 1 dimensional grain analysis of the line on topographic image (d), and SEM micrograph (e) of annealed Ni16 film at 900 °C .....	100
Figure 4.48. AFM topographic image (a), and 1 dimensional grain analysis of the line on topographic image (b) of asgrown Ni17 film. AFM topographic image (c), 1 dimensional grain analysis of the line on topographic image (d), and SEM micrograph (e) of annealed Ni17 film at 900 °C .....	102
Figure 4.49. AFM topographic image (a), and 1 dimensional grain analysis of the line on topographic image (b) of asgrown Ni18 film. AFM topographic image (c), 1 dimensional grain analysis of the line on topographic image (d), and SEM micrograph (e) of annealed Ni18 film at 900 °C. ....	103
Figure 5.1. Heating, annealing, growth and cooling stages of graphene growth process by CVD .....	105
Figure 5.2. Comparison of the D band at 514.5 nm at the edge of bulk graphite and single layer graphene. The fit of the D <sub>1</sub> and D <sub>2</sub> components of the D band of bulk graphite is shown (left). Evolution of the spectra at 514 nm with the number of layers. They are scaled to have similar height of the 2D peaks (right) .....	109

Figure 5.3. G' band Raman spectrum of GRP1 sample which was grown on Ni1 film by Method1. The inset shows the same result fitted with a single Lorentzian peak. The green lines are the components of red line which is the fitted profile. At the bottom, the whole range of the respective spectrum is shown.....	110
Figure 5.4. G' band Raman spectrum of GRP20 sample which was grown on Ni1 film by Method3. The inset shows the same result fitted with a single Lorentzian peak. The green lines are components of red line which is fitted profile. At the bottom, the whole range of the respective spectrum is shown.....	111
Figure 5. 5. G' band Raman spectrum of GRP119 sample which grown on Ni1 film by Method10. The inset shows the same result fitted with two Lorentzians. The green lines are components of red line which is calculated profile. At the bottom, the whole range of the spectrum is shown.....	112
Figure 5.6. G' band Raman spectrum of GRP138 sample which grown on Ni1 film by Method12. The inset shows the same result fitted with two Lorentzians. The green lines are components of red line which is calculated profile. At the bottom, the whole range of the spectrum is shown.....	113
Figure 5.7. G' band Raman spectrum of GRP1 (a) and GRP20 (b) samples which grown on Ni1films by Method1 and Method3, respectively. The green lines refer to component of red line which is calculated profile. At the bottom, the whole ranges of the spectra are shown .....	114
Figure 5.8. G' band Raman spectrum of GRP21 sample which grown on Ni2 film by Method3. The red line is calculated profile. At the bottom, the whole range of the spectrum is shown.....	115
Figure 5.9. G' band Raman spectrum of GRP47 sample which grown on Ni2 film by Method4. The green lines are components of red line which is calculated profile. At the bottom, the whole range of the spectrum is shown. The inset shows the D' band of GRP47 .....	116
Figure 5.10. G' band Raman spectrum of GRP33 (a) and GRP75 (b) samples which grown on Ni2 sample by Method1 and Method6, respectively. The green lines refer to component of red line which is calculated profile. At the bottom, the whole ranges of the spectra are shown .....	117

Figure 5.11. G' band Raman spectrum of GRP22 sample which grown on Ni3 sample by Method3. The green lines refer to component of red line which is calculated profile. At the bottom, the whole ranges of the spectra are shown.....	118
Figure 5.12. Raman spectrum of GRP50 sample which grown on Ni5 substrate by Method4. The green lines refer to component of red line which is calculated profile.....	119
Figure 5.13. Two different Raman spectra of GRP81 sample which were grown on Ni8 film by Method6. The green lines refer to component of red line which is calculated profile in the insets. The inset (a) represent the G' band fit of black spectrum and (b) refer to the G' band fit of blue spectrum. ....	120
Figure 5.14. G' band Raman spectrum of GRP68 and GRP69 (a) and GRP55 (b) samples which grown on Ni9, Ni10 and Ni10 films; by Method5-5 and Method4, respectively. The green lines refer to component of red line which is calculated profile .....	121
Figure 5.15. G' band Raman spectrum of GRP44 (a) and GRP73 (b) samples which grown on Ni13 and Ni14 films; by Method1 and Method5, respectively. The red lines refer to calculated profile .....	122
Figure 5.16. Raman spectra of GRP24, GRP36, GRP40, GRP43, GRP51, GRP57, GRP78 and GRP93 samples and G' band line shape distortion.....	123
Figure 5.17. Two different Raman spectra of GRP166 and GRP167 samples which grown on Ni15 and Ni16 films by Method17. The green lines refer to component of red line which is calculated profile in the insets. The inset (a) represent the G' band fit of black spectrum and (b) refer to the G' band fit of blue spectrum .....	124
Figure 5.18. Raman spectra of GRP138, GRP139 and GRP134 samples which grown on Ni1, Ni12 and Ni12 films by Method12, 12 and 11, respectively. The green lines refer to component of red lines which are calculated profiles .....	125
Figure 5.19. SEM images of GRP23 sample with 2500x (a), 10000x (b), 50000x (c) and 10000x (d) magnifications .....	126
Figure 5.20. SEM image of GRP28 sample with 2500x (a), 10000x (b) and 10000x (c, d) magnifications .....	127
Figure 5.21. SEM image of SEM image of GRP30 sample (a, b) and GRP31 sample (c, d) with 10000x (a, c), 50000x (b, d) magnifications .....	128

## LIST OF TABLES

<u>Table</u>	<u>Page</u>
Table 2.1. The electron configuration of a ground state carbon atom. ....	3
Table 3.1. The calculated peak list of Ni using formula of a cubic crystal structure .....	37
Table 4.1. Calculated values for atomic structure of the three graphene/Ni (111) interface models and for the clean Ni (111) surface .....	55
Table 4.2. Deposition parameters of Ni1, Ni2, Ni3, Ni4, Ni5, Ni6 and NiW1 samples. ....	56
Table 4.3. The deposition parameters of Al <sub>2</sub> O <sub>3</sub> buffer layers and Ni films. (*) indicates the deposition temperature was 450 °C. ....	61
Table 4.4. The deposition parameters of Cr and Al <sub>2</sub> O <sub>3</sub> buffer layers and Ni films. (*) indicates the deposition temperature was 450 °C.....	64
Table 4.5. Average grain sizes and 2θ values of asgrown and annealed Ni1 samples. ..	66
Table 4.6. Surface roughness (RMS), average height of particles (mean Z) and thickness of Ni films of asgrown and annealed at 900 °C Ni1-6 films.....	90
Table 4.7. Surface roughness (RMS), average height of particles (mean Z) and Ni film thickness of asgrown and annealed at 900°C Ni7-14 films.....	98
Table 4.8. Surface roughness (RMS), average height of particles (mean Z) and Ni film thickness of asgrown and annealed at 900°C Ni15-18 films.....	104
Table 5.1. Growth parameters of graphene grown by CVD. RT indicates room temperature (23-24°C).....	106

# **CHAPTER 1**

## **INTRODUCTION**

Graphene is a wonder material of the early 21<sup>st</sup> century due to its unmatched excellent properties and a great number of potential applications. Graphene is a zero-gap semiconductor and shows metallic character. Some of graphene's attractive properties are that it has high charge mobility, ballistic transport, transparency in visible region, mechanical strength and flexibility. It also has high in-plane sound velocity which leads to very high thermal conductivities [1]. The optical phonon frequency of graphene is one of the highest property among all materials [2]. Also, the main property of single-atom-thick makes graphene very promising especially in nanoelectronics research area.

Graphene is seen by many to have a potential to replace Si in the field of electronics. Therefore, controllable production of graphene with known number of layers is of extreme importance. Large number of studies has been done on a wafer scale and high quality mono layer graphene production and characterization. One of the compelling production techniques is Chemical Vapor Deposition (CVD). It can be used to grow graphene over few hundred nm thick films grown on Si substrates or over thin foils of Ni, Cu and Au films. CVD is a vapor-phase process which relies on thermal cracking of carbon elements from a precursor hydrocarbon gas on transition metal substrate.

This study focused on the influence of crystallinity, surface roughness and the concentration of interface boundaries of Ni catalyst on the formation of graphene layers grown by CVD. A uniform thickness and grain boundary free surface of Ni (111) single crystal provides a smooth surface for uniform, high quality and single layer graphene formation. However, the rough surface of polycrystalline Ni, which rich in grain boundaries, causes the formation of multilayer graphene [3, 4]. So, the aim of the present study was to reduce surface roughness, grow grain sizes and increase the (111) crystal direction of Ni thin film. For that purpose, we deposited Al<sub>2</sub>O<sub>3</sub> as oxide/metal structure, Cr as metal/metal structure and Cr/Al<sub>2</sub>O<sub>3</sub> as metal/oxide/metal buffered

structures. Then, graphene growth was carried out using different growth parameters of CVD.

This thesis consists of six chapters. The first one provides general information about graphene and content of the thesis. The first part of Chapter 2 gives information about carbon and carbon nanostructures classified according to their dimensionality; their structure, discovery, types and growth methods with details. In the second part of Chapter 2, history and related literature about graphene, its properties and production methods are described in detail. In Chapter 3, thin film and graphene deposition and characterization techniques are presented. Chapter 4 includes Ni thin film crystal structure; annealing and its effects are described. Also, thickness calibration of films and their characterization results are given and discussed. In Chapter 5, the production of graphene and their identification results are discussed. The conclusions of this study are presented in Chapter 6.

# CHAPTER 2

## BACKGROUND AND LITERATURE REVIEW

### 2.1 Carbon

The element carbon found in every living organism is detected in abundance in the universe, in the sun, stars, comets, and in the atmosphere of the planets. It is the fourth most abundant element in the solar system, after hydrogen, helium, and oxygen. Carbon unites with hydrogen, nitrogen, oxygen and other elements to turn out more than ten million different compounds and isomers, but it can combine easier with itself to form polymorphs (or allotropes) [5]. Carbon has three naturally occurring isotopes, with  $^{12}\text{C}$  and  $^{13}\text{C}$  being stable, while  $^{14}\text{C}$  is radioactive. There are several allotropes of carbon with different physical properties, some known since ancient times (graphite, diamond) and some discovered ten to twenty years ago (nanotubes, graphene) [6]. Only two polymorphs of carbon are found on earth as minerals: natural graphite and diamond [5]. Carbon can also occur as an unordered binding of atoms; this is called amorphous carbon. The electron configuration of carbon element is shown in the Table 2.1, there are four electrons in the valance band of carbon and their electronic wave functions can easily mix with each other because the 2s and 2p energy levels have smaller energy difference compared with the binding energy of the chemical bonds [7]. The mixing results hybridization of carbon and variety of structural forms that has different atomic hybrid configurations:  $\text{sp}^3$  (tetragonal),  $\text{sp}^2$  (trigonal) or  $\text{sp}$  (digonal).

Table 2.1. The electron configuration of a ground state carbon atom.

Element		Shell					First Ionization Potential (eV)
		K	L				
Symbol	Z	1s	2s	2p <sub>x</sub>	2p <sub>y</sub>	2p <sub>z</sub>	
C	6	2	2	1	1		11.26

Depending on nanoscale range ( $<100$  nm) of carbon allotropes in different spatial directions low-dimensional carbon nanomaterials can be divided into four categories: zero-dimensional (0D), one-dimensional (1D), two dimensional (2D) and three-dimensional (3D) [8, 9].

In recent years, carbon nanostructures have been a focus of many theoretical and experimental study of nanotechnology. Recently, there has been a great deal of attention in graphene which is the two dimensional allotropic form of carbon since the famous discovery by isolating a single layer with the help of scotch tape in 2004 [10]. Before dealing with graphene, in this work the popular allotropes of carbon with categories of different dimensionality are examined.

## 2.1.1. Carbon Nanostructures

### 2.1.1.1. Three Dimensional Carbon Nanostructures

#### 2.1.1.1.1. Graphite

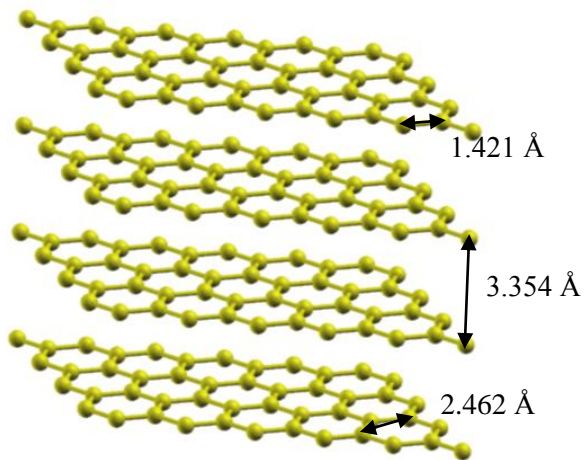


Figure 2.1. The crystal structure of hexagonal single crystal graphite

Graphite has been used for ages in a range of purposes from lubrication to use as a pencil, and is recognized as a carbon polymorph first in 1855 [5]. Each  $\text{sp}^2$ -hybridized carbon atoms combine with three other  $\text{sp}^2$ -hybridized atoms to form a series of

hexagonal structures containing two atoms per unit cell in each layer and all located in parallel planes are shown schematically in Figure 2.1. This structure has a very small in plane nearest neighbor distance of 1.421 Å, an in plane lattice constant of 2.462 Å, and an interplanar distance of  $c/2$  3.354 Å [11].

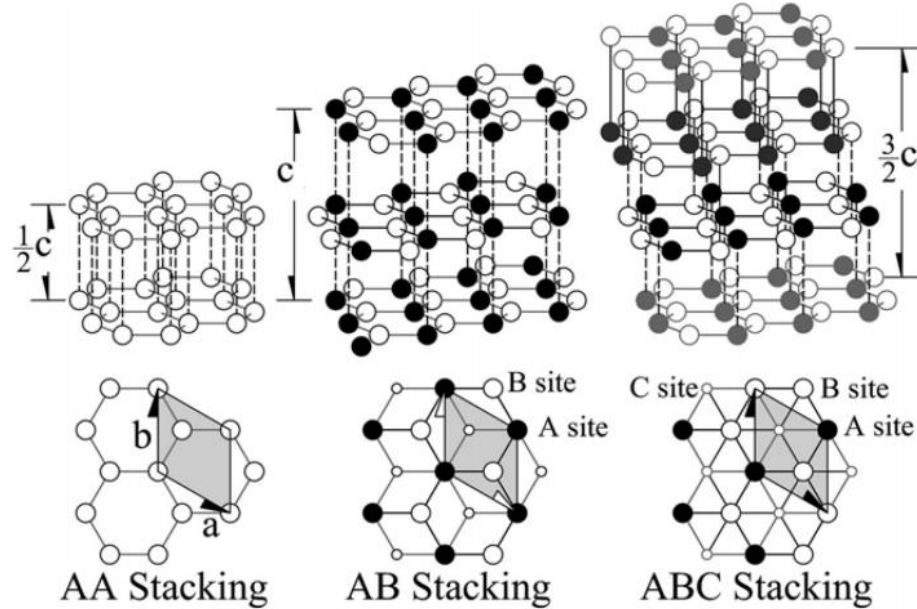


Figure 2.2. The stacking patterns of AA, AB and ABC stacking between graphene layers [12, 13]

A single layer of graphite is called graphene which has remarkable electrical, thermal, and physical properties. So, graphite is the 3D form of graphene. The carbon atoms in different graphene layers bond each other with weak Van der Waals forces [14]. The stacking of the graphene layers is arranged in many ways. Figure 2.2 shows that hexagonal AA stacking occurs when carbon atoms of the two layers have exactly identical lateral positions. On the other hand, the A and B atoms on consecutive layers are on top of one another and this structure is called Bernal AB stacking which is the most abundant type [12]. The most complex type is ABC stacking has a rhombohedral arrangement, which can be found in three or more layered graphene structures. The third C layer over the Bernal cell has the same orientation relative to the second layer but with a shift of  $2a/3 + b/2$  [12]. In addition, turbostratic graphite occurs when graphene layers stacked with  $\sim 30^\circ$  interlayer rotation and these layers have minimum interaction [15, 16].

Graphite is the most stable form of carbon at room temperature and atmospheric pressure [5, 17]. Graphite is opaque to the visible spectrum and electrical conductor with zero gap in contrast to diamond [5, 9, 17]. The delocalized electrons can move readily in-plane, but cannot easily move from one layer to another. As a result, graphite has anisotropic electronic conduction [5, 11].

There is a type of synthetic graphite or carbon product which is produced by using gaseous precursors. It is called pyrolytic graphite. Its production is based on the thermal decomposition (pyrolysis) of a hydrocarbon gas with Chemical Vapor Deposition process. The most common precursors to produce carbitic materials by using CVD are methane ( $\text{CH}_4$ ) and ethylene ( $\text{C}_2\text{H}_6$ ) [5]. Industrial production of pyrolytic graphite was first carried out in 1950's [5]. Its main use is in the different form of coatings, deposited on substrates such as molded graphite, carbon fibers. As such, it is part of a composite structure and is not as readily identifiable as other forms of carbon. It is similar, in this respect, to CVD diamond and diamond-like carbon (DLC) [5].

#### 2.1.1.1.2. Diamond

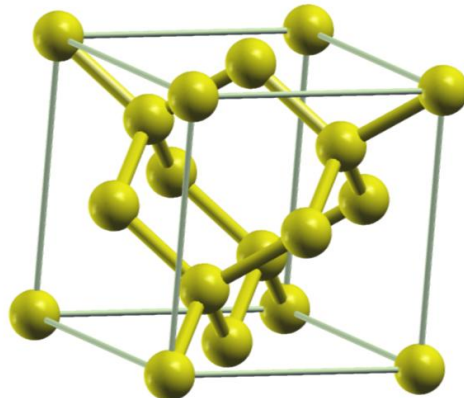


Figure 2.3. The crystal structure of diamond

Diamond which is an allotrope of carbon is sometimes found in combination with other type of carbon allotropes, such as some diamond-like carbon (DLC) materials produced by low-pressure synthesis, which are actually the mixtures of microcrystalline diamond and graphite. The studies in the related area have also revealed the existence of both cubic and hexagonal diamond (Lonsdaleite) which is a

polymorph of diamond first identified in 1967 [18]. There are series of polytype of diamond (4H, 6H, 8H, 10H) and these have structure between cubic and hexagonal.

Discovery of the carbon composition of diamond was in 1797 [5]. Diamond is the hardest known natural mineral due to its strong covalent bond that consists of  $sp^3$  hybridization between its atoms. It has a FCC crystal structure and occurs from tetrahedrally bonded carbon atoms, which also known as diamond structure. Hence, it is electrically insulator. Also, it is thermally highly conductive, transparent to the visible spectrum and has high optical dispersion, unusually high index of refraction [5]. Because of its excellent physical properties diamond has many uses in industry. Industrial production of diamond by CVD was carried out in 1992 [5]. The known forms of diamond are natural diamond, high-pressure synthetic diamond, CVD (vapor-phase) grown diamond.

### **2.1.1.2. Two Dimensional Carbon Nanostructures**

#### **2.1.1.2.1. Graphene**

Graphene, a single sheet of graphite with a honeycomb (hexagonal) lattice structure of  $sp^2$  bond carbon atoms, is a rising star early of the 21<sup>st</sup> century, because of it is truly two-dimensional crystalline material and has unmatched excellent properties. It was the only missing member of carbon nanostructure family until experimental isolation in 2004 [10]. In recent years, the scientific interest generated by graphene due to its exceptional electronic and mechanical properties shows that it can be the next generation of electronic material. The subject of this work is to control the production of graphene with a known number of sheets, so in the next section the detailed discussion of properties of graphene will be given, in order that its structure is well understood.

Besides graphene, researchers are also paying attention to graphene derived materials. Among those, the most attractive two-dimensional ones are graphane ( $CH$ ) and graphyne ( $C-C\equiv C-C$ ) that have similar structures as graphene.

### 2.1.1.2.2. Graphane

Graphane, a wide gap semiconductor, is a two-dimensional hydrocarbon and has the same honeycomb lattice structure as graphene with formula CH. It was theoretically calculated that it would form in 2003 [19].

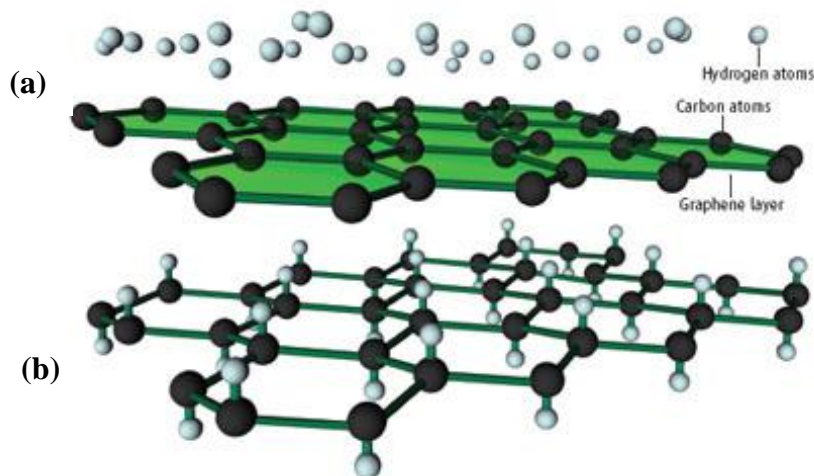


Figure 2.4. Schematics of adding hydrogen converts graphene (a) into graphane (b) [20]

In contrast to graphene, graphane has  $sp^3$  hybridized orbital with the calculated C-C bond length of 1.52 Å is similar to the diamond and is much greater than 1.42 Å characteristic of  $sp^2$  carbon in graphene [21]. As seen from Figure 2.4 (b), all carbon atoms of A-sublattice can bond to hydrogen atoms at the same side of the plane and B-sublattice atoms bond at the other side of the plane. This type of conformation is called chair-like, and hydrogen atoms also can alternate in pairs, so called boat-like conformation. 3D graphane can exist in different stackings of 2D graphane layers at pressures up to 300 GPa [22]. It is possible to transform graphene sheet that is highly conductive semimetal into an insulator by exposing graphene to atomic hydrogen (Figure 2.4) [23]. This is a distinction between graphene and graphane can be used in application areas such as graphene based nanoelectronics and hydrogen-fuel technologies [24]. Graphane provides means to rich science and number of technological applications [21].

### **2.1.1.2.3. Graphyne**

Graphene contains  $sp$  and  $sp^2$  bonded carbon atoms and unlike graphene, it does not have hexagonal structure (Figure 2.5). It has acetylene bonds which connect benzene rings ( $C-C\equiv C-C$ ) [25].

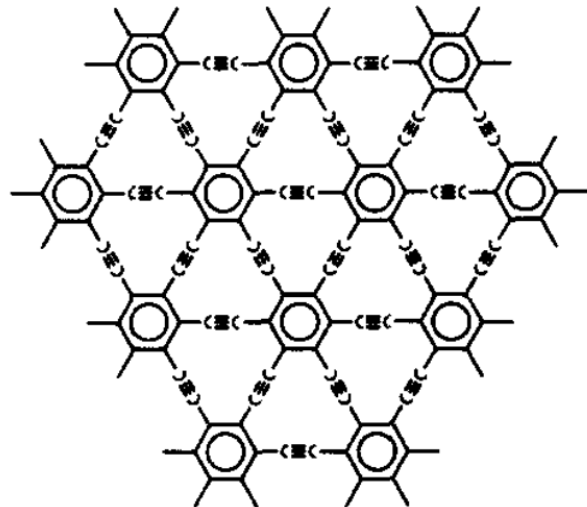


Figure 2.5. The structure of a 2D graphyne layer [25]

The theoretical studies showed that graphyne has Dirac cone-like band structure around the Fermi level like graphene [26]. Electronic, optical properties and transport behaviors of graphyne are theoretically studied [25, 27]. The theoretically reported properties of graphyne, makes it is a viable studied competitor of graphene and promising materials for nanoelectronics and energy storage applications. However, bulk graphyne has not been experimentally obtained yet, so far only nanoscaled-graphyne structures were demonstrated experimentally [26, 28].

### **2.1.1.2.4. Carbon Nanowalls (CNWs)**

Carbon nanowalls (CNWs) are vertically aligned graphene sheets standing on a base, have 2D wall structure with large surface areas, sharp edges and similar properties as graphene [29]. They were accidentally discovered during the growth of carbon nanotubes in 2002 using microwave plasma enhanced chemical vapor deposition

(MPECVD) [30]. CNWs can exist either in pure forms or in a composite form of other carbons [31]. CNWs have typical lateral dimensions of several micrometers [32] and its thickness ranges from a few nm to a few tens of nm [33].

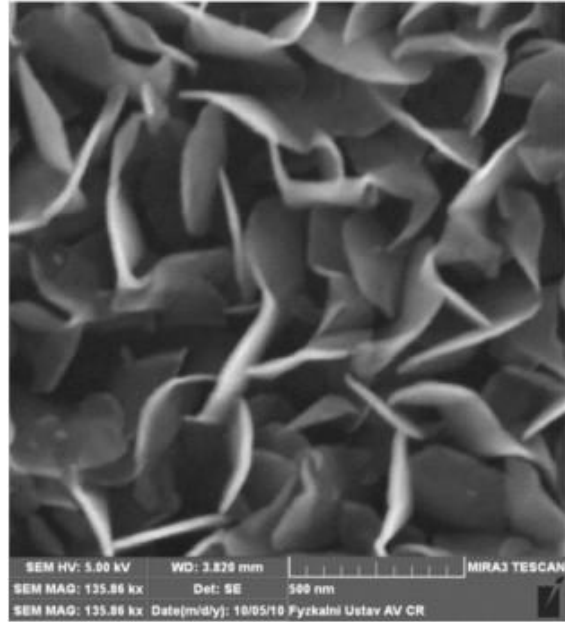


Figure 2.6. Scanning electron microscopy image ( $1.6 \times 1.6 \mu\text{m}$ ) of CNWs [34]

Their growth mechanism is similar to that of carbon nanotubes when they are grown using chemical vapor deposition (CVD) technique. Similarly, their synthesis methods can be based on different CVD techniques such as, microwave plasma enhanced chemical vapor deposition (MWPECVD) [31], radio frequency plasma enhanced chemical vapor deposition (RFPECVD) [35, 36] (RF inductively coupled plasma (ICP) and RF capacitively coupled plasma (CCP)), Hot-wire chemical vapor deposition (HWCVD) [37], Electron beam excited plasma-enhanced chemical vapor deposition (EBEPECVD) [38]. HWCVD enables to grow at large scales easier than the MWPECVD and RFPECVD methods. CNWs have many application areas such as, field emission material due to vertical alignment [39, 40], catalyst support due to high surface area [29], batteries [41], capacitors [42].

### 2.1.1.3. One Dimensional Carbon Nanostructures

#### 2.1.1.3.1. Carbon Nanofibers

Carbon can also form a tubular microstructure called carbon fiber. Thomas Edison made the first carbon fibers on record in 1879 while he carbonized cotton thread to produce a filament for a light bulb. His effort was not entirely successful and Edison eventually replaced the fiber by a tungsten wire [5, 43]. This kind of carbon material consisting of fibers of about 5–10  $\mu\text{m}$  in diameter was reported first by Hughes and Chambers in 1889 [44]. Carbon nanofibers (CNFs), which are also known as carbon filaments or filamentous carbon, have diameters vary from a few to hundreds of nanometers, while their lengths range from less than a micrometer to several millimeters. CNFs did not actually attract much attention of the academic community until the 1980s when their extraordinary physical and chemical properties were found. Their potential applications, such as catalysts, catalyst supports, gas storage materials, electrodes for fuel cell, probe tips, and polymer additives have been searched since then [45, 46].

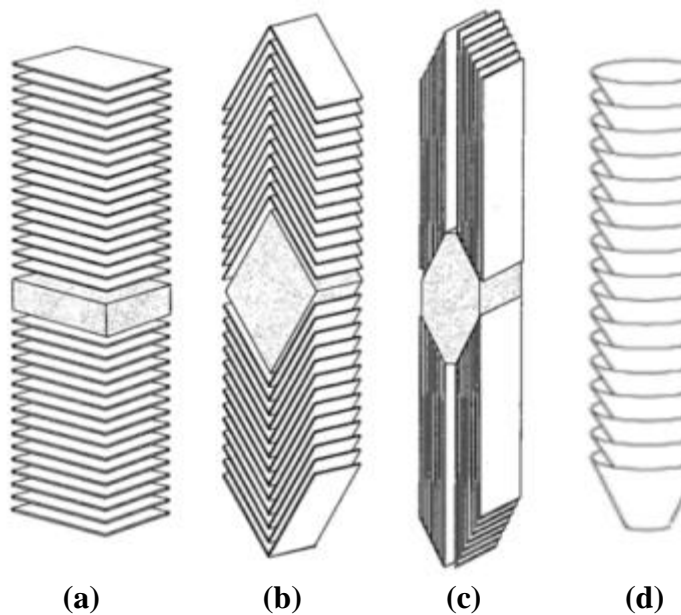


Figure 2.7. Schematic representations for CNFs: (a) platelet-type CNF, (b) fishbone type CNF, (c) ribbon-type CNF, (d) cup stacked-type CNF [47]

CNFs are composed of stacked and curved graphene layers to form a quasi-one-dimensional filament. CNFs are cylindrical or conical nanostructures. As shown in Figure 2.7, there are mainly four types of CNFs. The first one is fishbone or herringbone CNFs (f-CNFs or GNF-H), their graphene layers stacking obliquely with respect to the fiber axis. The second one is platelet CNFs (GNF-P), their graphene layers being perpendicular to the axis. The third one is ribbon CNFs (GNF-R), and their graphene layers are parallel to the growth axis [45, 48, 49]. The last one is cup stacked CNFs, their sidewalls composed of angled graphene sheets. These morphological structures only provide stacking modes of the graphene sheets, which help to account for the growth mechanism of CNFs. CNFs are grown mainly by CVD from the catalytic decomposition of certain hydrocarbons over small metal particles such as iron, cobalt, nickel, and some of their alloys [5, 43, 45].

### 2.1.1.3.2. Carbon Nanotubes

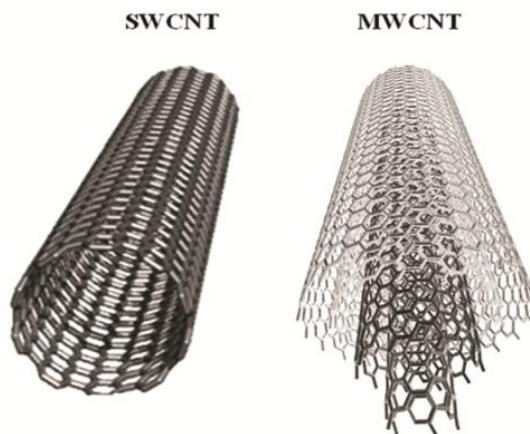


Figure 2.8. Schematic representations of singlewall nanotube (SWNT) and multiwall nanotube (MWNT) [50]

Carbon nanotubes were discovered in 1991 [51], they are rolled up into tubular structures by  $sp^2$ -bonded graphite sheets and capped at both ends of the tube with a half of fulllrene molecule with diameters as small as 0.4 nanometer and very large aspect ratio. There are two different types of carbon nanotubes. Namely, multiwall nanotubes (MWNTs), discovered by Iijima [51], made of 4–24 concentric cylinders of graphene layers with interlayer spacing close to that of the interlayer distance in graphite (0.34

nm) [50] and a diameter typically of the order 10–20 nm and the successive production of single-wall nanotubes (SWNT) [50, 52] made of single layers of graphene cylinders with typical diameter of the order of 1 nm [8].

There are also three types of SWNT with respect to the orientation of the hexagon relative to the axis of the nanotube. These are chiral, armchair and zigzag nanotubes [53, 54]. Chirality and diameter of tube defines its electronic band structure. Hence, CNTs can be semiconductors or metals with different size energy gaps, although graphene is a zero-gap semiconductor [54].

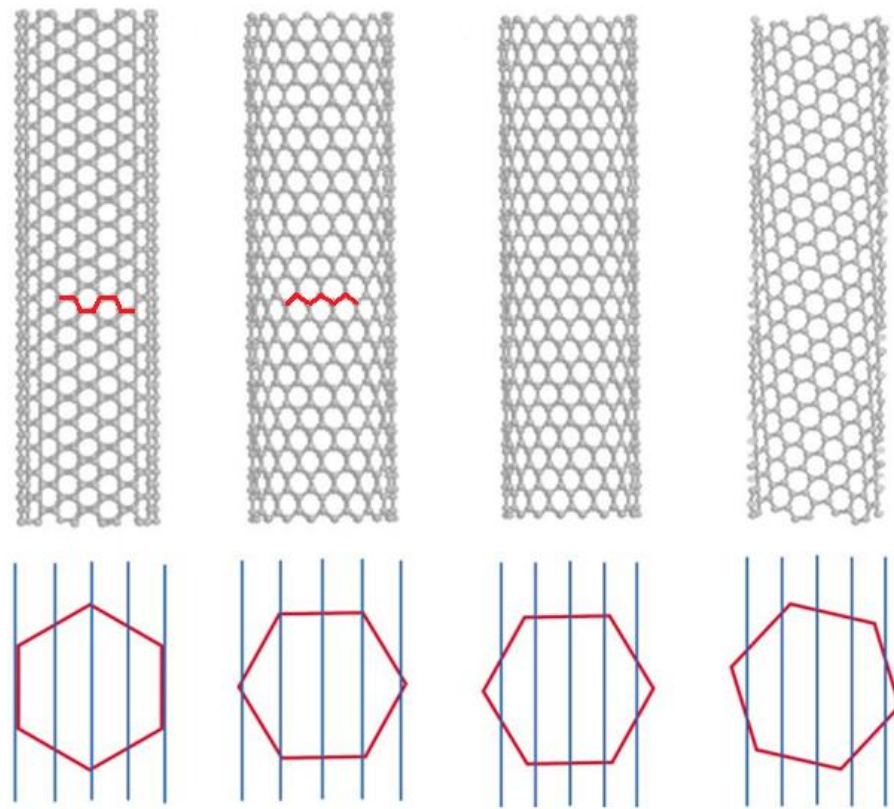


Figure 2.9. Schematic structures of SWNTs with different chirality. (a) A (10, 10) armchair nanotube, (b) A (12, 0) zigzag nanotube, (c) The (14, 0) zigzag tube, (d) A (7, 16) chiral tube. The cross-sections of the first two illustrations have been highlighted by the bold red lines showing the armchair and zigzag character, respectively [55]

There are four types of CNTs. The hexagons under each structure represent the first Brillouin zone of the graphene sheet in reciprocal space and the vertical lines represent the electronic states of the nanotube. For the arm-chair nanotube (Figure 2.9 (a)), the center line crosses two corners of the hexagon, resulting in a metallic nanotube.

For the zigzag nanotube (Figure 2.9 (b)), the electronic states cross the hexagon corners, but a small band gap can develop due to the curvature of the nanotube. In Figure 2.9 (c), a semiconducting zigzag tube is illustrated. The hexagon under that represents the states on the vertical lines; miss the corner points of the hexagon so that there is a gap at K point in reciprocal space. As shown in Figure 2.9 (d), semiconducting chiral tube illustrates the extreme sensitivity of nanotube electronic structures to the diameter and chirality of nanotubes [55].

One of the most significant property of CNTs is that they are ballistic conductors along their tube axis and very good insulators perpendicular to the tube axis [56]. The other main physical properties of CNTs are high tensile strength, high aspect ratio, high thermal conductivity, and high surface area [53]. Excellent mechanical, electronics and well defined atomic structural properties of CNTs makes them desired in many technological applications such as reinforcing agents in composite materials, sensors, field emission devices, flat panel displays, energy storage, electrochemical devices and electronic devices [57].

#### 2.1.1.4. Zero Dimensional Carbon Nanostructures

##### 2.1.1.4.1. Fullerene

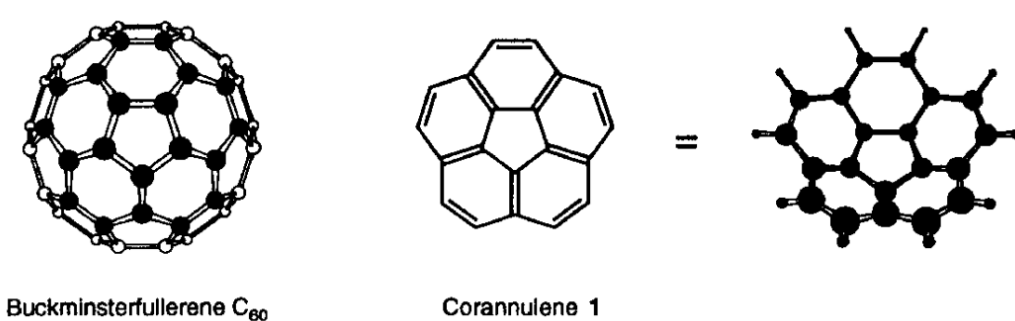


Figure 2.10. An illustration of Buckminsterfullerene and its fragment Corannulene [58]

The new era in carbon nanomaterials has begun with the structure of a  $C_{60}$  molecule is called Buckminsterfullerene and it was discovered in 1985 by laser vaporization of graphite target [59], and led to the Nobel Prize in chemistry in 1997

[55]. Family of fullerene, cage-like molecules, which are considered to be one of the major allotropic forms of carbon contain 60, 70 or 82 carbon atoms and these combine both  $sp^2$  and  $sp^3$  bonds [5]. They are closed spheres composed of pentagons and hexagons. These pentagons and hexagons are the reason of its curvature shape so resembles a soccer ball. A bowl-shaped fragment of buckminsterfullerene is called as corannulene (COR) [58, 60]. This novel aromatic hydrocarbon  $C_{20}H_{10}$  was first synthesized in 1966 by Bart and Lawton [61]. Fullerenes are very strong and elastic. Pure fullerenes are not conductor but when they are doped with alkali metals their conductivity becomes as high as metals.

Other than C60, some of the isomers of fullerene are C70, C76, C78, C80, C84 [62], C90, C100 [63], C122-C130, C162-C180 [64].

#### **2.1.1.4.2. Carbon-Encapsulated Metal Nanoparticles**

Carbon-Encapsulated Metal Nanoparticles (CEMNPs) are zero-dimensional carbon-metal composite nanomaterials firstly reported in 1993 [65]. The polyhedral metallic core is entirely encapsulated by the multilayer-graphitized carbon shells that isolate the particles magnetically from external environment and protect them against corrosion and magnetic coupling between individual particles [8].

#### **2.1.1.4.3. Nanodiamond**

Cubic structure of diamond, “nanodiamond” contains a variety of diamond-based materials including pure-phase diamond films, diamond particles, and their structural assemblies [8]. In 1987 nanodiamond (ND) particles found in meteorites with size of interstellar diamond particles ~5 nm [66] and the length scale at nanoscale of approximately 1–100 nm [8].

#### 2.1.1.4.4. Onion-Like Carbons

A very interesting transformation between carbon forms at the nanoscale is carbon onions. When they are observed first time after annealing nanodiamond particles at around 1300 to 1800 K, they transform to carbon onions in 1992 [33, 67]. Carbon onions or onion-like carbons (OLCs) consist of concentric quasi-spherical graphitic sheets. Generally outer diameters are vary between 10 nm and 1 $\mu$ m, also inner diameters vary between 0.7-1 nm ( $\sim C_{60}$ ) [33]. Carbon Onion is an important member of fullerene family and has many applications in areas of conductivity catalyst and nano-compound materials.

Yet all this structures have the same carbon atoms, but have different arrangements of atomic structures and the only missing member of this family was 2D graphene which is the mother of all graphitic forms.

## 2.2. Graphene

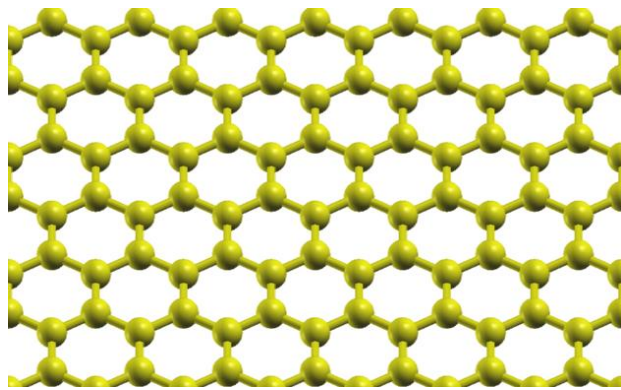


Figure 2.11. Hexagonal structure of graphene

The concept of two-dimensional graphene, dates back to 1947 was clarified by P.R. Wallace theoretically [68]. B. Lang carried out of the earliest experimentally trial of synthesizing single or few layer graphene through thermal decomposition of ethylene on Pt surface at 1975 [69]. However, the researchers could not realize the importance of that type of structure at that time. Also, in 1999, another trial of synthesizing graphene on faceted Ni (755) surface were reported [70]. Single layer graphene was isolated first

from Highly Oriented Pyrolytic Graphite (HOPG) by mechanical exfoliation method using ‘Scotch tape’ in 2004 [10], whereas 2D Graphene was regarded to be thermally unstable and the atomic single layer tended to role or fold in order to reach the lowest potential energy state, therefore could not freely exist [71, 72]. Discovery of intrinsic ripples in third directions [73] explained the reason why the atomic layer graphene could be observed [6]. The intrinsic ripples are believed to prevent graphene from rolling and to help suppress the thermal fluctuation. After isolation of graphene Novoselov et. al. explored its physical [10, 74-76] and chemical properties [77]. After experimentally realized by Konstantin Novoselov and Andre Geim it went on to win the Nobel Prize in 2010 [78], as it is the first truly two-dimensional crystalline material. Graphene has extraordinary properties, such as; high charge mobility, transparency, mechanical strength and flexibility etc., and, there is also an extra quantum confinement of the electrons due to the lack of a third dimension. A 2D material, graphene attracts great interest for research in material science due to its unique electronic properties.

### **2.2.1. Electronic Structure of Graphene: Tight Binding Approach**

Carbon has four electrons in its valence level with a configuration of  $2s^2 2p^2$  and the energy of these sublevels is so close that their orbitals hybridize. Graphene is composed of single-atomic layer of  $sp^2$  bond carbon atoms with closely and strongly packed in a hexagonal lattice structure (Figure 2.12 (b)).

Figure 2.12Figure 2.12 (a) shows the electron orbitals in graphene, the number of sigma ( $\sigma$ ) bonds in carbon atoms with  $sp^n$  hybridization given by  $(n+1)$ , so in graphene, each carbon atom has three  $\sigma$ -bonds with other neighbor carbon atoms. The remaining  $p_z$  orbital has only one electron and, this  $p_z$  orbital overlaps with the  $p_z$  orbital of a neighbor carbon atom to form a  $\pi$ -bond. In a finite graphene sheet  $p_z$  electrons are contribute to one conducting electron per carbon atom, which result in the weak Van der Waals force between graphene layers in graphite. Then,  $\pi$ -bonds are hybridized together to form the  $\pi$ -band and  $\pi^*$ -bands. These bands are responsible for most of the unique electronic properties of graphene.

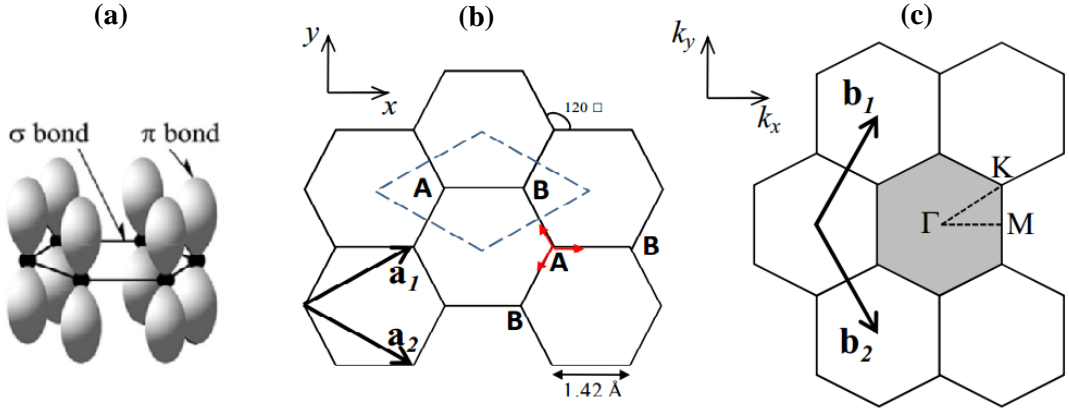


Figure 2.12. (a) Schematic of  $sp^2$  hybrid C-C bond structure containing in plane  $\sigma$ -bond and perpendicular  $\pi$ -bond [13], (b) unit cell and, (c) Brillouin zone of graphene are shown as the dotted rhombus and the shaded hexagon, and the red vectors show the nearest-neighbor vectors [3].

In 1946, Wallace theoretically calculated the band structure for a single graphite layer using a tight binding approximation [68]. With reference to this approximation, the graphene honeycomb lattice is composed of two equivalent sublattices of carbon atoms. In Figure 2.12 (b), each atom in one sublattice is shown as **A** and the other atoms in the other sublattice **B**. The unit cell which includes two atoms is displayed as a dotted rhombus in Figure 2.12 (b), and the first hexagon Brillouin zone (BZ) of graphene as a shaded hexagon in Figure 2.12 (c), can be constructed by using a Wigner-Seitz cell method. Shown  $a=1.42 \text{ \AA}$  is the carbon-carbon bond length accordingly; the unit vectors in real space can be expressed as following:

$$a_1 = a \left( \frac{3}{2}, \frac{\sqrt{3}}{2} \right), \quad a_2 = a \left( \frac{3}{2}, -\frac{\sqrt{3}}{2} \right)$$

The reciprocal lattice vectors can be calculated as following:

$$b_1 = \frac{2\pi}{a} \left( \frac{1}{3}, \frac{\sqrt{3}}{3} \right), \quad b_2 = \frac{2\pi}{a} \left( \frac{1}{3}, -\frac{\sqrt{3}}{3} \right)$$

Using the tight binding approximation energy dispersion relations can be calculated along the perimeter of the dotted triangle connecting the high symmetry points  $\Gamma$ , **K**, and **M** (the center, the corner, and the center of the edge of the hexagonal Brillouin zone, respectively, Figure 2.12 (c)). Corners of first BZ are **K** and **K'** and their positions in momentum space are given by

$$\mathbf{K} = \left( \frac{2\pi}{3a}, \frac{2\pi}{3\sqrt{3}a} \right), \quad \mathbf{K}' = \left( \frac{2\pi}{3a}, -\frac{2\pi}{3\sqrt{3}a} \right)$$

To approximate the low energy electronic property just one may consider the  $p_z$  electrons only hop to the nearest neighbor atoms and constructing Bloch wave functions

for two inequivalent carbon atoms **A** and **B** in the unit cell, Hamiltonian including only  $p_z$  states can be calculated. Resulting electronic structure of graphene can be approximated with the following eigenvalues expression as a function of  $\mathbf{k}_x$  and  $\mathbf{k}_y$ :

$$E(k_x, k_y) = \pm \gamma \sqrt{1 + 4 \cos\left(\frac{\sqrt{3}k_x a}{2}\right) \cos\left(\frac{k_y a}{2}\right) + 4 \cos^2\left(\frac{k_y a}{2}\right)}$$

where  $\gamma$  ( $\approx 2.7$  eV) is the nearest neighbor hopping (overlap) energy and  $E_+$  and  $E_-$  refer to the conduction and valence  $\pi$ -bands of the electrons. Wallace calculated linear energy dispersion relation near Fermi level when the band structure close to one of the **K** or **K'** corner points as  $\mathbf{k}=\mathbf{K}+\mathbf{q}$ , with  $|\mathbf{q}| \ll |\mathbf{K}|$  [68].

$$E_{\pm}(q) \approx \pm v_F |q| + O[(q/K)^2]$$

where  $\mathbf{q}$  is the momentum measured relatively to the **K** points and Fermi velocities of charge carrier  $v_F$  reach the value 1/300 of the speed of light  $c$ . As seen Figure 2.13, this dispersion leads to linear energy versus wave vector relation at all the six corners of the BZ. As a result of that near the Fermi level, the low energy quasiparticles can be described by the Dirac-like Hamiltonian:

$$\hat{H} = \begin{pmatrix} 0 & k_x - ik_y \\ k_x + ik_y & 0 \end{pmatrix} = \hbar v_F \sigma \cdot \boldsymbol{\kappa}$$

It gives us the following relation:

$$\left( \frac{d^2 E}{d \kappa^2} \right) = \infty$$

Therefore, the electron effective mass expressed in

$$m^* = \hbar^2 \left( \frac{d^2 E}{d \kappa^2} \right)^{-1}$$

will be zero. It indicates that near these six points at the Fermi level, the electrons and holes behave as zero-effective-mass Dirac fermions and they cannot be described by independent Schrödinger equations. Instead, the electrons and holes are described by Dirac's equation for spin half particles [13]. Therefore, the six corners of the Brillouin zone, **K** and **K'** are called Dirac points, and the electrons and holes at these points are named fermions [12].

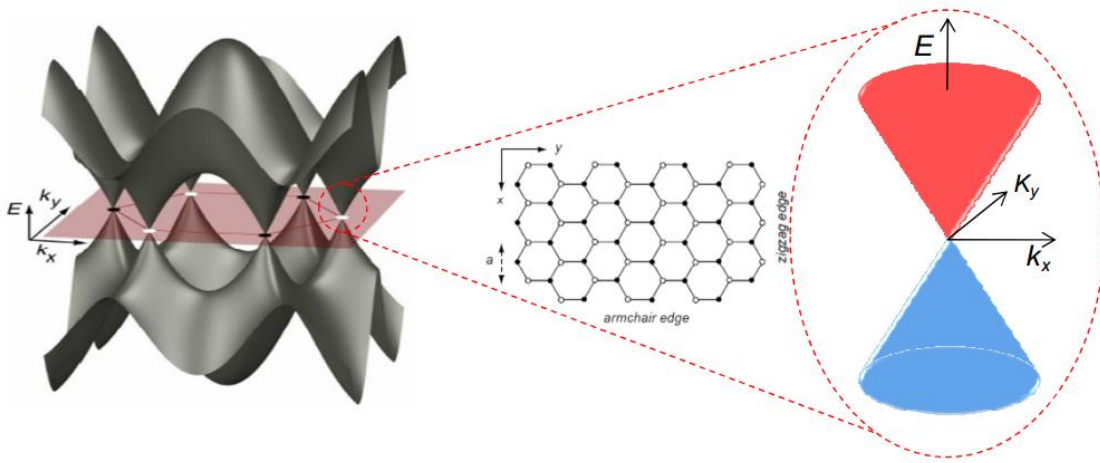


Figure 2.13. A plot of the energy versus momentum dispersion relation for graphene shown throughout the BZ and the inset shows the energy dispersion relations along the high symmetry axes along the perimeter of the triangle shown in Figure 2.12 (c) [3].

Sublattice atoms **A** and **B** have one each  $\pi$  electron, so there are two  $\pi$  electrons which fully occupy the lower  $\pi$ -bonding energy band in a unit cell. Hence, the density of states at the Fermi energy is zero, and graphene is a zero-gap semiconductor [3]. Zero-gap property gives most of the unique and attracted aspects to graphene.

### 2.2.2. Vibrational Properties of Graphene

By considering the vibration modes of the crystal in thermal equilibrium, phonon dispersion of graphene is obtained. The phonon dispersion is very similar to its electronic band structure which discussed in the previous section (Figure 2.13). Despite, graphene is a 2D material, the two sublattices **A** and **B** atoms can vibrate in all three dimensions. There are two out-of-plane modes (atomic vibrations are perpendicular to the graphene plane) and four in-plane phonon vibration modes. Out-of-plane modes are acoustic (ZA) and optical (ZO). Traditionally, the directions of the vibrations are considered with respect to the direction of the nearest carbon-carbon atoms and, therefore, the phonon modes are classified as longitudinal (L) or transverse (T) according to vibrations parallel with or perpendicular to, respectively, the A-B carbon-carbon directions. So, in-plane modes are classified transverse acoustic (TA), transverse optical (TO), longitudinal acoustic (LA) and longitudinal optical (LO) [79].

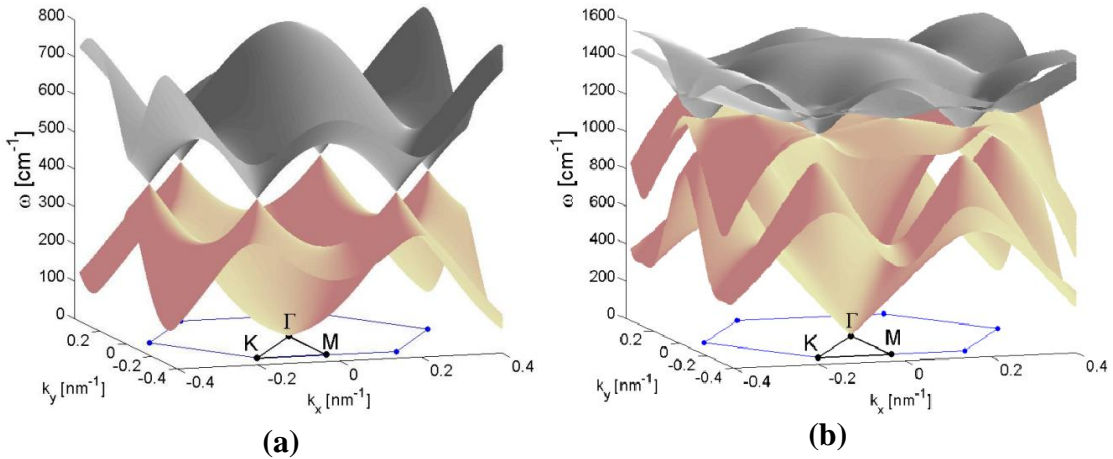


Figure 2.14. The dispersion relation of out-of-plane modes (a) and in-plane modes (b) of graphene are obtained using the second-nearest-neighbor model for graphene. The vertical axes are the phonon frequency, while the horizontal axes are the momentum space on the graphene lattice [80]

The dispersion relation of the vibration modes of graphene as a function of the in-plane reciprocal vector  $\vec{k}$  and the corresponding  $\mathbf{K}$ ,  $\Gamma$ , and  $\mathbf{M}$  points of the Brillouin zone are shown in Figure 2.14. In the Figure 2.14 (a), one represents the out-of-plane modes; gray surface corresponds to the ZO (optical) mode, whereas the pink surface shows the ZA (acoustic) mode. The dispersion is quadratic at the  $\Gamma$  point. This is congruent with the experimental data, but it is unusual for acoustic modes [80]. The in-plane modes are shown in the Figure 2.14 (b). The dispersion have cone shape at the  $\mathbf{K}$  and  $\mathbf{K}'$  points. At these points, because of the presence of the in-plane modes the phonon density of states does not vanish. The gray surface corresponds to the optical modes; TO and LO, whereas the pink surface shows the acoustic modes; TA and LA. The transverse modes have slightly lower frequency than the longitudinal modes. The dispersion is linear at the  $\Gamma$  point. The optical phonon frequencies of graphene,  $\omega_0$  ( $\sim 0.2 \text{ eV} - 1600 \text{ cm}^{-1}$ ), are one of the highest among all materials [2]. Vibrational properties of graphene provide to understand some other graphene features. These features are optical properties include phonon-photon scattering (e.g. in Raman scattering which will be discussed in next chapter), electronic properties include electron-phonon scattering and high in-plane sound velocity, close to  $c_{\text{ph}} \approx 20 \text{ km/s}$  [1], which leads to very high thermal conductivities.

### 2.2.3. Other Properties of Graphene

Graphene has linear dispersion, and this significant feature leads to other subfeatures. The first one is electrons and holes belonging to the same branch of the dispersion curve are described by a pseudospin quantum number ( $\sigma$ ) that is parallel to the electron momentum, but opposite to the hole momentum. This independence ‘chirality’ means that because of the inability to transform one type of dispersion into another an electron hopping from  $\mathbf{K}$  to  $\mathbf{K}'$  is not allowed since the pseudospin is not conserved. This conservation rule gives rise to the ballistic transport observed in graphene and CNTs as well [13].

The second subfeature is ‘tunability’ or ambipolar electric field effect. The gate voltage induces a surface charge density,

$$n = \epsilon \epsilon_0 \frac{V_g}{te}$$

with a shift of the position of Fermi energy level. Here,  $\epsilon_0$  and  $\epsilon$  are permittivities of free space and  $\text{SiO}_2$ , respectively,  $e$  is the electron charge,  $t$  the thickness of  $\text{SiO}_2$ , layer ( $\leq 300$  nm thick on which graphene is visible under optical microscope [81], since, in this case, even a single layer adds to the optical path of reflected light to change the interference color with respect to the empty substrate [82]). As a zero band gap semiconductor, graphene has no charge carrier at  $E_F=0$ , between two branches. However, without the necessity of doping, the Fermi level can be moved into the conduction or valence bands by applying an external electric field. This allows conduction by changing the concentrations of either holes or electrons as high as  $10^{13} \text{ cm}^{-2}$ , with room temperature mobilities of up to  $20000 \text{ cm}^2 \text{V}^{-1} \text{s}^{-1}$  [83-85] which exceeds the intrinsic mobility of any other known semiconductors. Minimizing impurity scattering is make less loss of energy, so carrier mobilities higher than  $200000 \text{ cm}^2 \text{V}^{-1} \text{s}^{-1}$  were achieved in suspended graphene at electron densities of  $2 \times 10^{11} \text{ cm}^{-2}$  at room temperature [85-88]. The band gap of graphene also depends on its shape, size [89] or layer number [90]. The zigzag GNRs are always metallic while armchairs can be either metallic or semiconducting. The energy gap of armchair GNRs can be tuned and scales inversely with the width [91, 92]. The band gap of graphene bi-layer FET can be tuned by application of a potential difference and its optical response can be changed with a magnetic field [93].

Moreover, observations show the electron-phonon scattering and temperature also limited the mobility, but below 300 K the dominant scatterings belong to phonons [85]. Another effect of limiting the mobility is the dominant electron-phonon scattering of the substrate for graphene on SiO<sub>2</sub> substrates [87].

Another subfeature of graphene's unique electronic structure is it exhibits very high transparency. One or two layer of suspended graphene film show white light absorption of 2.3 and 4.6%, respectively with a negligible reflectance (R), less than 0.1% [74]. The transparency of the graphene layer decreases with the increase of thickness. Each graphene layer adds light absorption of 2.3%. Just as graphene has high transparency, it has also high flexibility. It can be intact [94] under bending conditions. Especially, its high flexibility and transparency enables it to be used instead of ITO for photovoltaic device technology [94]. Low cost, high conductivity, transparency, chemical and mechanical stability of graphene make it suitable for transparent and flexible electrode [12].

Graphene has many other features. One of them is that it regards as mechanically the strongest material due to the in-plane  $\sigma$ -bonds [95] and it shows a breaking strength of 42 N/m and Young's modulus of  $E=1.0 \pm 0.1$  TPa [12, 96]. Graphene morphologically has high specific surface area that theoretically was predicted ( $>2500$  m<sup>2</sup>g<sup>-1</sup>) in 2004 [97], but experimentally this value is not reached yet. This high surface areas lead to using as gas and energy storage applications.

Some experiments were shown that in contrast to traditional semiconductors, the particles that are governed by the Dirac equation obey the Klein tunneling [98]. So, the transmission probability increases with increasing barrier height. In the case of graphene, the chirality discussed earlier also leads to a varying transmission probability depending on the angle of incidence to the barrier [99].

Graphene exhibits a very high sound velocity due to very strong in-plane bonding. This large sound velocity is responsible for the extraordinary high room temperature thermal conductivity up to 5300 W/m K [100], that is useful in many applications such as, better thermal contact with SiO<sub>2</sub> than other carbon nanomaterials [101]. Also, high thermal conductivity facilitates the diffusion of heat to the contacts and allows for more compact circuits.

In addition discovery of Quantum Hall Effect, enhanced Coulomb interaction [102] of graphene and other unmatched scientific and industrially applicable properties make it a promising material for electronic circuits [80, 100, 103] such as, high-

frequency oscillators, transparent flexible touch screens, solar energy processing panels [94, 104], and yet light-weight material applications including hydrogen visualization templates for TEM, components of satellites and aircraft technology [105], high electron mobility transistors [106], intersubband infrared detectors, quantum cascade lasers [107], giant magnetoresistance (GMR) [108], light-emitting diodes [109], and spin-valves [110] and so on.

## 2.2.4. Graphene Production Methods

### 2.2.4.1. Exfoliation and Cleavage

Graphite is formed by overlapping graphene layers. It is possible to extract graphene flakes from a graphite sheet, if weak Van der Waals bonds can be broken by using mechanical or chemical energy [111]. By exfoliation and cleavage techniques single or few layer graphene flakes can be obtained.

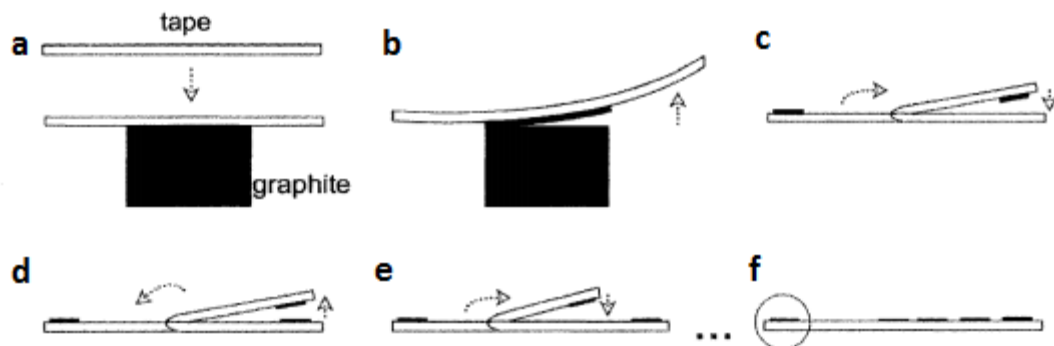


Figure 2.15. Schematic representation of using Scotch tape. (a) pressing the tape on bulk graphite, (b) peeling a thin layer of graphite, (c-d-e) folding the tape over and pressing it against itself, the graphite was spread over two and more areas of the tape, (f) the thinned layer of graphite over the tape [112]

A research group at the University of Manchester succeeded in separated few and single layer graphene flakes with dimensions of up to  $10\text{ }\mu\text{m}$  from HOPG sheet of 1 mm thickness by mechanical exfoliation (repeated peeling) method using ‘Scotch tape’ in 2004 [10]. To obtain  $5\text{ }\mu\text{m}$  deep mesas (of area  $0.4$  to  $4\text{ mm}^2$ ) the HOPG sheets was subjected to a dry etching in oxygen plasma and then these mesas were pressed into

photoresist and baked. The HOPG was cleaved from the resist. As seen from Figure 2.15, Scotch tape was used to repeatedly peel flakes of the graphite mesas. The obtained thin flakes were then released in acetone and captured on the surface of a Si/SiO<sub>2</sub> wafer [10]. These single and few layer graphene (FLG) flakes could be identified from the contrast difference in an optical microscope [10].

Many studies focus on also producing graphene either from graphite or graphite oxide powder and using different solvents [113-116], from potassium-graphite intercalation compound (GIC) by sonication [117] and from partially reduced graphene oxide (GO) nanosheets by ultra-sonication [118, 119]. These methods have some drawbacks such as oxygen, therefore, some researchers use another liquid exfoliation processes without oxidization to produce larger scale of graphene layers with higher quality [120, 121].

Exfoliation and cleavage are very reliable and easy techniques. However, graphene flakes obtained by these methods have just as a lot of defects, also are limited in small sizes and randomly placed. For applications of graphene in electronics large-area and high quality synthesis of graphene are needed.

#### **2.2.4.2. Thermal Decomposition of SiC**

Thermal Decomposition of SiC technique relies on heating SiC and sublimating Si in ultrahigh vacuum (UHV), generally to temperatures between 1000 °C and 1500 °C for a short time (1 to 20 minutes) [111]. The remaining carbon rich surface is graphitic in nature and shows similar electronic properties with the isolated graphene sheet [13, 122]. There are two polar faces of SiC perpendicular to c-axis. Graphene, grown on these two polar planes, shows different growth behaviors and electronic properties [13, 123].

A recent study has revealed that the epitaxial graphene can be synthesized on SiC at low temperature (750 °C) [124] and ambient pressure [125]. This technique is cost effective to the industry and attracts much interest as this process may be a viable technique in post-CMOS age [13]. On the other hand, there are some issues to be solved such as controllable thickness uniformity, repeated production of wafer-scale graphene and interface effects with the SiC substrate [111, 126]. In addition, it can also be used other substrates to thermal decomposition such as a single crystal Ru (0001) [127, 128]

and single crystal transition metal surfaces; including Ir, Ni, Co, Pt, etc. [111, 129]. However, Sutter et. al. concluded that the first graphene layer grown on Ru (0001) has very low electrical conductivity because, strongly bond to the Ru (0001) surface. Because of the out-of-plane  $\pi$  orbitals of graphene, interactions between graphene and a substrate or between graphene layers should influence the electronic structure of graphene [13]. Hence, the choice of production technique is important to obtain large area, single layer and high quality graphene layer.

#### **2.2.4.2. Chemical Vapor Deposition**

Chemical vapor deposition (CVD) is a vapor-phase process which relies on the chemical reaction of a vapor near or on a heated surface. The process patented first in 1880 and is very suitable to the deposition of carbon on metal surfaces [5]. As seen from Figure 2.16, to synthesis single layer graphene, this technique is performed by placing transition metal substrates like Ni [130-132], Cu, Ir [133], Pt [134, 135], Ru [127, 136] or Co [137] in a gas phase carbon source precursor ( $\text{CH}_4$ ,  $\text{C}_2\text{H}_2$  etc.) in the CVD furnace to temperatures between 800 °C and 1100 °C. Then, by thermally cracking of Carbon elements on transition metal substrate desired graphene layers are obtained.

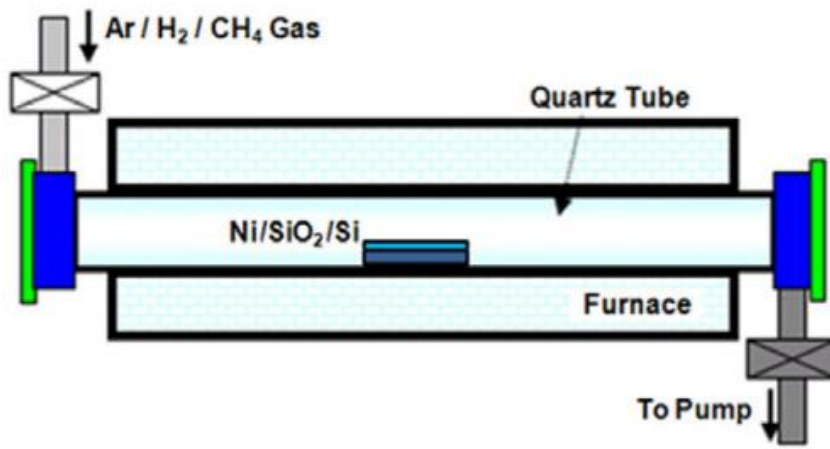


Figure 2.16. Shematic representation of CVD set up for the synthesis of graphene [103]

CVD technique in synthesis of graphene has drawn much attention because it can produce wafer scale graphene in economical way compared with the previous two

methods. In this work CVD technique utilizes to growth single and few layer graphene on sputtered polycrystalline Nickel (catalyst) thin film substrate. Hence, this method will be examined in detail in next chapter.

#### **2.2.4.3. Other Methods of Synthesis Graphene**

There are other methods to synthesis single or few layer graphene. One of them is radio frequency plasma enhanced chemical vapor deposition (PECVD) technique which succeeded in synthesis graphene first in 2004 [138]. The process used Si, W, Mo, Zr, Ti, Hf, Nb, Ta, Cr, 304 stainless steel,  $\text{SiO}_2$ , and  $\text{Al}_2\text{O}_3$  as substrates and a carbon source gas  $\text{CH}_4$  in a  $\text{H}_2$  environment [139]. There is no need to use catalyst on substrates in this procedure. It is proposed that the thickness of graphene sheet depends on a balance between C diffused species and etching caused by atomic hydrogen, in PECVD process. Also, the interaction between the plasma electric field with their anisotropic polarizability causes vertical orientation of grown sheets [140].

To synthesis large area, high quality single layer graphene, molecular beam deposition technique is maybe the most appropriate one due to the layer-by-layer growth mechanism. In this technique, a carbon gas source such as ethylene is broken down at 1200 °C using a thermal cracker and deposited on a nickel substrate and graphene layers were produced at 800 C. The most important differences between MBE and CVD are the number of graphene layers produced are independent of cooling rate and carbon does not absorbed into the bulk of the Ni [141].

Moreover, wet chemical synthesis methods also attract attention. Among them the most common one is Hummers method [142]. However, oxidation affects the electrical and thermal conductivity of graphene obtained by these kinds of methods. The other, recent highly attractive method is unzipping CNTs. Unzipping methods varies widely and one of them is that suspending CNTs in  $\text{H}_2\text{SO}_4$  and then treating them with  $\text{KMnO}_4$  to peel off graphene sheets and reducing chemically from oxygen, electrically offgrade graphene nanoribbons (GNRs) are obtained [143] (Figure 2.17 (a)). In Figure 2.17 (b), there is another unzipping method is that the MWCNTs are partially embedded in a polymer film and using KOH solution the polymer is peeled off from substrate then exposing to Ar plasma the outer part of MWCNT is etched [92]. The last process is calcination to remove polymer. Used MWCNT verify the diameter and layer

number of resulting GNRs. Also, exposure time to Ar plasma identify the layer number of graphene nanoribbon [92].

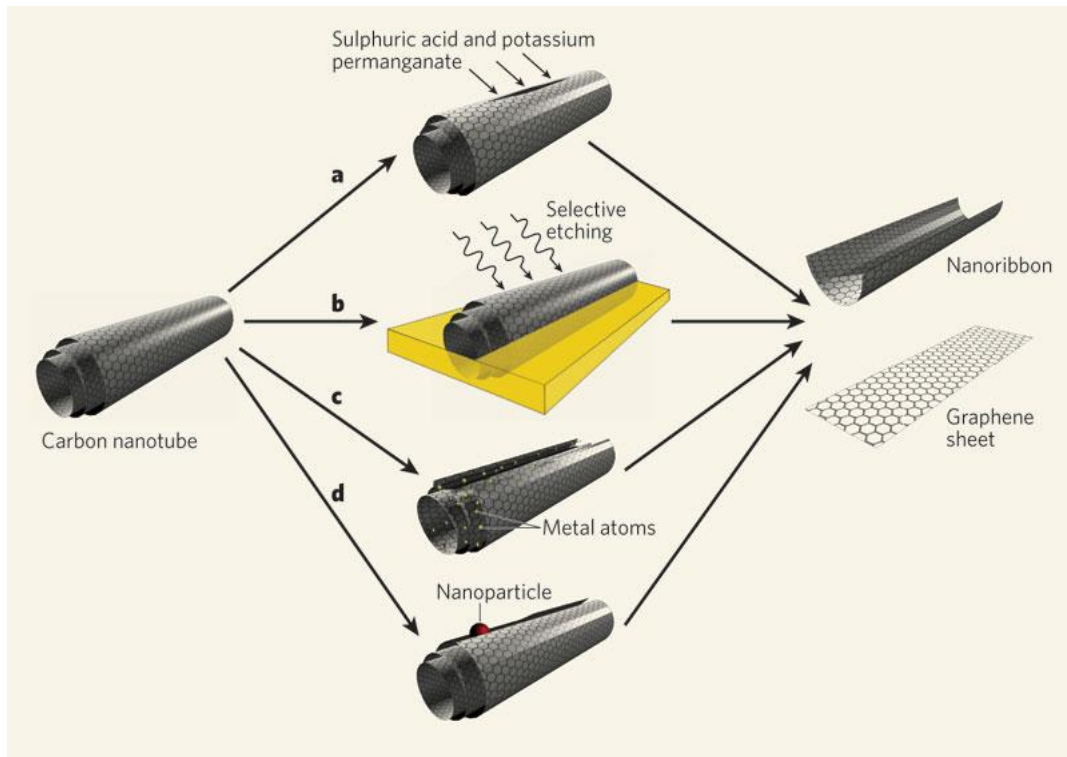


Figure 2.17. Illustration of various CNT unzipping methods [144]. (a) [143], (b) [92], (c) [145] (d) [146]

An alternative unzipping method is that alkali metal atoms are intercalated between open ended MWCNT layers and  $\text{Li}_2\text{C}$  intercalation compounds, or lithium carbide are produced [145]. Then exfoliation with acid treatment open along their axis and completely unwrapped nanotubes (ex-MWNTs) are obtained [145]. Moreover, using metal nanoparticles as nanoscalpers such as iron and nickel, MWCNTs can be cut to obtain GNRs [146] (Figure 16 (d)).

# **CHAPTER 3**

## **EXPERIMENTAL TECHNIQUES**

This study aimed controllable production of graphene with known number of layers by investigating the effect of thickness and surface structure of sputtered Ni thin films on layer numbers of graphene. Direct Current Magnetron Sputtering (DCMS) and Radio Frequency Magnetron Sputtering (RFMS) are employed for the deposition of the several samples of various thick of polycrystalline Ni catalyst films, thin Al<sub>2</sub>O<sub>3</sub> buffer films and Cr adhesive layers under the Ni catalyst film on Si/SiO<sub>2</sub> substrates.

Surface roughness properties, crystal structures, and thickness of the films were investigated by Atomic Force Microscope (AFM), X-Ray Diffractometer (XRD), Surface Profiler and Scanning Electron Microscope (SEM), respectively. These films were annealed at 800 °C, 900 °C and 950 °C in CVD furnace. And a set of samples were studied again using these techniques to assess their crystal quality after annealing process. Then the CVD growth of graphene was carried out using Ar, H<sub>2</sub> and CH<sub>4</sub> gases exactly at annealing temperature. The Raman spectroscopy technique was utilized in order to determine the number of the layers, the size and quality of graphene growth over Ni catalyst films.

This chapter involves experimental techniques about the study. Firstly, preparation of samples including sample cleaning and thin film deposition was explained. Then characterization techniques were employed. Lastly, the growth technique of graphene films and their characterization techniques were explained.

### **3.1. Thin Film Preparation**

#### **3.1.1. Substrate Cleaning**

SiO<sub>2</sub> substrates were subjected to a cleaning process prior to films growth to prevent samples from contaminations. First, they were rinsed in acetone, cleaned in an ultrasonic bath in the order of acetone during 15 minutes. Then the substrates were

rinsed with acetone, ethanol and de-ionized water respectively, 30 second in each. Nitrogen flow was used for dry up during 30 seconds. Also, spin coater was used for dry up during 4 minutes with 5000 rpm prior to introducing them into the growth chamber of sputter or CVD. Before the deposition of certain thick Ni, Al<sub>2</sub>O<sub>3</sub> and Cr films their thickness, power and time relations were calibrated by depositing several films. After the substrate cleaning process and before thin film growth a little drop of photoresist was placed on a corner of Si/SiO<sub>2</sub> substrates for thickness measurement after film growth. After the deposition, the photoresist was removed in an ultrasonic bath in acetone for a few minutes. Then, the cleaning proceeded under the flow of acetone, ethanol and de-ionized water respectively, for 30 seconds in each. To dry the sample a spin coater was used for 4 minutes with 5000 rpm again. The deposited films were kept under nitrogen in desiccators.

### **3.1.2. Thin Film Deposition: Magnetron Sputtering Technique**



Figure 3.1. ATC AJA Orion 5 UHV Sputtering System in the Department of Physics at IZTECH.

Magnetron sputtering (MS) is a physical vapor deposition (PVD) technique which deposits physically removed target atoms onto a substrate. The growth system (Figure 3.1 ATC AJA Orion 5) is controlled by a computer and was evacuated down to the base pressure of about  $1.9\text{-}2 \times 10^{-7}$  Torr using mechanical and turbo pumps. There are

some magnets located under target and these magnets increase the ionizing probability by holding the electrons close to the target area.

A potential difference is created between the target and the substrate. The target was held at the negative voltage (as a cathode). In the deposition process firstly, Ar atoms are ionized by colliding with electrons and these ions are accelerated away from the negatively charged electrode. Ar plasma starts to form at a Ar background pressure of  $10^{-3}$  Torr. Positively charged, energetic  $\text{Ar}^+$  ions are accelerated towards the negatively charged cathode target material by electric field. These  $\text{Ar}^+$  ions strike and erode the target material via momentum transfer. The ejected target material is in the form of neutral particles and they are either individual atoms or clusters of atoms and molecules. These neutral particles are not affected by electric or magnetic field and they travel in a line of sight strike the substrate surface, if they don't encounter with other particles on their way. Existing  $\text{Ar}^+$  ions can recombine with removed electrons and return to their ground states by releasing photons within the visible range of EM spectrum which give the glowing appearance of the plasma. Around the target, there are additional free electrons confined by the magnetic field the neutral Ar atoms collide with an electron and turns to an  $\text{Ar}^+$  ion. These electrons sustain the formation of ions and the continuation of the plasma following a closed-path  $\mathbf{E} \times \mathbf{B}$  cycloidal drift loop [147].

In this study, the deposition of Ni and Cr thin films was carried out by DC magnetron sputtering (DCMS), whereas deposition of  $\text{Al}_2\text{O}_3$  was carried out by RF magnetron sputtering (RFMS) technique.

### 3.1.2.1. DC Magnetron Sputtering

DCMS technique owes its name to the DC power supply that was used for plasma discharge. During DCMS process, ion-induced secondary electrons are generated on the target material. Electron emission increases almost linearly with the ion velocity. Hence the cathode discharge voltage is high for DCMS to sustain the plasma. Secondary electrons can be also removed from insulator target material and some positive charges may build up on the insulating target where they cannot be discharged when  $\text{Ar}^+$  ions strike it. The positive charging prevents positive  $\text{Ar}^+$  ions to

hit the target due to repulsive coulombic force. Therefore, DCMS is used for conducting target materials.

### **3.1.2.2. RF Magnetron Sputtering**

Charge built-up problem which is observed in insulator targets can be solved by RFMS. DC sputtering occurs when electrons and ions follow the alternative switching of the anode and cathode at frequencies less than 50 kHz. The relatively heavy ions cannot follow these rapid polarity switches; while the electrons can follow the switching and neutralize positive charge build up at these frequencies. Hence, the oscillation of secondary electrons in a RF plasma increases their chance of colliding with Ar atoms. RFMS requires a large DC voltages around  $10^{12}$  V and high switching frequencies. The low discharge voltages lead to significantly lower deposition rates for an RF magnetron discharge compared to a dc sputtering process under the condition of constant discharge power [148].

### **3.1.2.3. Film Deposition Process**

After the substrate cleaning, mentioned above, was done, substrates placed firstly preparation chamber when two chambers has the same pressure on the order of  $10^{-7}$  Torr, substrate was installed in the growth chamber. Then system was evacuated down to the base pressure of about  $1.9\text{-}2 \times 10^{-7}$  Torr. The substrates were cleaned by RF bias for 10 minutes ( $\sim 10$  Å/min) at 15 watts and the targets were always pre-sputtered in order to remove any contamination and oxidation of the surface. In our system, 9,95 sccm Ar gas flow corresponding to  $\sim 7$  mTorr of deposition pressure was used for both DC and RF sputtering. DC and RF sputtering can be done with the maximum powers of 500 W and 300 W, respectively. Our system also has a halogen lamp based heater to heat the substrates during deposition up to 850 °C. Some of Ni films were deposited at a substrate temperature of 450 °C. In the next chapter, the deposition conditions studied on this work will be given in detail.

### 3.2. Atomic Force Microscopy (AFM)

Atomic Force Microscopy (AFM) is one of the most common and useful surface analysis technique on an atomic scale, which was developed in 1986 [149]. Its principles are based on a combination of Scanning Tunneling Microscopy (STM) and stylus profilometer (SP). AFM basically, consists of a sharp tip, a cantilever, piezoelectric scanner, photodiode, detector and feedback electronics.

AFM images are obtained by a measurement of the force on a sharp tip which moves over the surface interacting with the sample by means of long range Van der Waals forces and repulsive forces. The trace of the movement of tip is obtained by determining the deflection and torsion of the tip. Considering two identical inert gas atoms and their behavior with the distance between them, interactive forces between tip and surface atoms are explained. Induced moments cause an attractive interaction between atoms when they closer to each other and Van der Walls interaction or London interaction is observed [150]. Then, the total energy of the system would be

$$\Delta U = -\frac{A}{R^6}$$

where  $R$  is the distance between two atoms and  $A$  is an empirical constant. Electrostatic energy of the system changes if the atoms continue to get closer and charge distributions overlap. Pauli Exclusion Principle causes this overlap energy gives repulsive contribution to the interaction when the atoms get a certain distance. To fit experimentally an empirical repulsive potential of the form of  $B/R^{12}$  is added to the total energy expression of the system.  $A = 4\epsilon\sigma^6$  and  $B = 4\epsilon\sigma^{12}$  where the  $\epsilon$  and  $\sigma$  are also experimentally measured parameters. This energy is called Lennard-Jones potential. By differentiating this energy with respect to the distance, the force between two atoms can be written as follows

$$\vec{F}(r) = 24 \frac{U_0}{\sigma} \left[ 2 \left( \frac{\sigma}{r} \right)^{13} - \left( \frac{\sigma}{r} \right)^7 \right] \hat{r}$$

Using the forces between tip and surface atoms, the sample surface is analyzed with two modes of AFM which are Contact mode and Tapping mode. In contact mode the tip and sample surface atoms contact each other, whereas, in tapping mode tip oscillates at a fixed frequency and during scan of the surface amplitude is changed by oscillation frequency which detected by amplifiers. To not damage the sample surface

and obtain better resolution in small areas ( $< 40\mu\text{m}$ ) we used tapping mode and optical detection method.

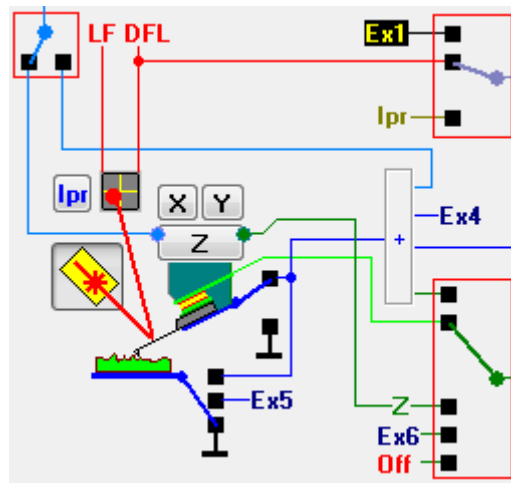


Figure 3.2. The optical detection system from the software Nova of MNT-MDT

In this work, AFM surface characterization was performed in semicontact (tapping) mode using commercial Scanning Probe Microscopy instrument (Solver Pro 7 from MNT-MDT, Russia). And as seen in Figure 3.2, a laser source and a four-quadrant photodiode are used. DFL refers the difference signal between top and bottom halves of the photodiode and LF refers left and right. The laser beam is struck on the center of the cantilever and the reflected signal that has the intensity proportional with the signal comes from all four segments of the photodiode. The deflection or torsion of the reflected beam is detected by photocurrents that are created by all quadrant of the photodiode when the laser beam hit to the photodiode. Each quadrant of the photodiode creates the individual photocurrents and deflection and torsion of cantilever can be characterized with  $\Delta I_Z = [(I_1+I_2)-(I_3+I_4)]$  and  $\Delta I_Z = [(I_1+I_4)-(I_2+I_3)]$ , respectively.

This current difference is input signal of feedback which keeps tip and surface distance is constant. Firstly, operator determine the surface relief height using Mag(Height) curve that obtain by applied voltage to the z-electrode of the piezoelectric scanner. Then, the scanner generates a mechanical stress and tip-surface separation changes proportionally to the applied voltage. Topographical image of the surface is obtained by the trace of the tip movement about the changing tip-surface separation. During all the measurements, HA\_NC silicon tips with a curvature radius of 10 nm and force constant of 12 N/m were used.

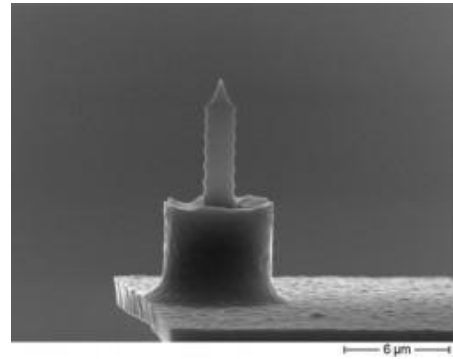


Figure 3.3. HA\_NC etalon probe from NT-MDT [151]

### 3.3. X-Ray Diffractometer (XRD)

The diffraction of X-rays occurs by interference between the waves scattered by the individual atoms and the incident waves. This is the most common crystalline structure determination technique. An incident X-ray beam hits an atom and oscillates its electrons with the same frequency. As seen in Figure 3.4 atoms in a crystal are arranged in a regular pattern, and in a very few directions we will have constructive interference, if so combining waves are in phase and well defined x-ray beams leave the crystalline at certain directions.

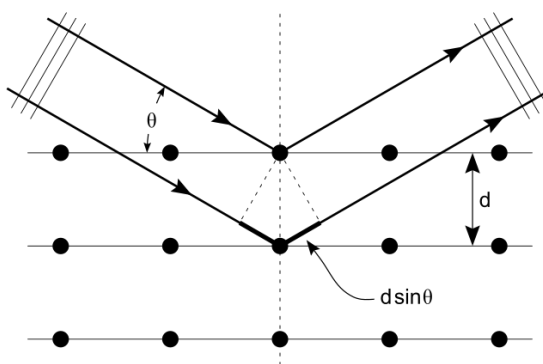


Figure 3.4. Representation of incoming and diffracting X-rays from different lattices

The crystalline properties of sample are obtained by using Bragg's law:

$$2d \sin \theta = n\lambda$$

where  $d$  is interplanar lattice spacing,  $\theta$  is the angle of incidence relative to the planes,  $n$  is an integer and  $\lambda$  is the wavelength of the x-ray radiation (Figure 3.4). The interplanar distance between planes of atoms is a function of the Miller indices ( $h$ ,  $k$ ,  $l$ ). The lattice parameter and the interplanar spacing  $d_{hkl}$  for cubic, hexagonal and tetragonal structures are calculated by the following equations:

$$\text{Cubic} \quad \frac{1}{d_{hkl}^2} = \frac{h^2+k^2+l^2}{a^2}$$

$$\text{Hexagonal} \quad \frac{1}{d_{hkl}^2} = \frac{4}{3} \left( \frac{h^2+k^2+l^2}{a^2} \right) + \frac{l^2}{c^2}$$

$$\text{Tetragonal} \quad \frac{1}{d_{hkl}^2} = \frac{h^2+k^2}{a^2} + \frac{l^2}{c^2}$$

Furthermore, by means of Scherrer's equation;

$$\tau = \frac{K\lambda}{B \cos \theta}$$

grain sizes of the crystals in deposited films can be estimated  $\tau$  is the mean grain size of the crystalline domains and  $K$  is a dimensionless shape factor typically about 0.9.  $B$  is the FWHM of the diffraction peak (in radians) and  $\theta$  is the diffraction angle corresponding to the XRD peak (Figure 3.4). The intensity, position and FWHM of the diffraction peaks are used to determine crystalline structure and quality of the sample.

The FWHM is calculated by the following formula and is shown in Figure 3.5.

$$B = \frac{1}{2}(2\theta_1 - 2\theta_2)$$

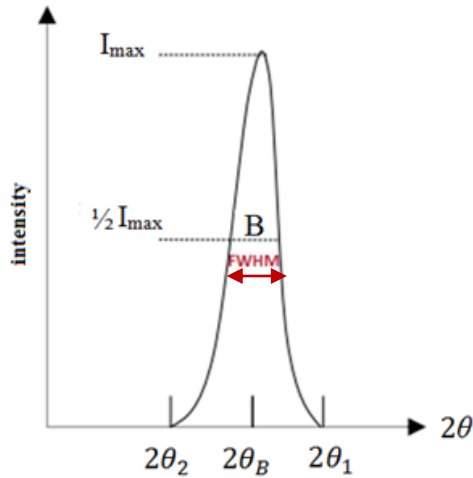


Figure 3.5. Ideal FWHM of a XRD peak

As seen Figure 3.5, FWHM represents how sharp that peak is, hence smaller FWHM means better crystallinity and bigger grain sizes. The peak position and FWHM both give us information about the strain in a crystal structure. A diffraction peak shifted towards left or right refers a uniform strain in the thin film. If the diffraction peak was both shifted and broadened, then the non-uniform strain is present within the grown film.

Table 3.1. The calculated peak list of Ni using formula of a cubic crystal structure

	$d (\text{\AA})$	$2\theta (\text{degree})$
<b>Ni(111)</b>	2.0346	44.49
<b>Ni(200)</b>	1.7620	51.85
<b>Ni(220)</b>	1.2459	76.38
<b>Ni(311)</b>	1.0625	92.94
<b>Ni(222)</b>	1.0173	98.44

In this study, most of the XRD  $\theta - 2\theta$  scans were performed by a PANalytical X-Pert Pro MRD (multi-purpose X-ray diffraction) X-ray diffractometer, operating with a Cu-K $\alpha$  X-ray source ( $\lambda=0.15406 \text{ nm}$ ) and adjusted to 45 kV and 40 mA Ni filter at Nanoboyut Research Laboratory at Anadolu University. Some of the XRD measurements were performed the old version of the same system assisted with X'Pert HighScore Software at IZTECH. All the XRD  $\theta - 2\theta$  scans were performed in the 30-100° and 30-90°  $2\theta$  ranges.

### 3.4. Scanning Electron Microscopy (SEM)

Scanning Electron Microscopy (SEM) gives the magnified image by scanning the surface with a high energy beam of electrons. The first such microscope is constructed by Dennis McMullan in 1951 [152]. An electron gun produces the electron beam and the beam is directed to the sample by electromagnetic fields and lenses. When the beam strikes the sample and interacts with the electrons of the sample, secondary electrons (SE), backscattered electrons (BSE), characteristic X-rays, specimen current and transmitted electrons are ejected from the sample. Different types of detectors collect and convert these signals into a 2-dimensional image on the screen. This image

includes information about sample such as, secondary electrons that are the most valuable for showing morphology and topography, backscattered electrons illustrate contrasts in composition in multiphase samples, diffracted backscattered electrons that are used to determine crystal structures and orientations of minerals, energy dispersive X-ray spectroscopy (EDX) characteristic X-rays that are used for elemental analysis and continuum X-rays, produced by inelastic collisions of the incident electrons with electrons in discrete orbitals of atoms in the sample, visible light (cathodoluminescence-CL), and heat.

As a non-destructive analysis technique of SEM was taken with Quanta FEG 250, at IYTE for this thesis work. By placing our Nickel samples cross-sectional on holders by means of a conductive band, we observed the thickness and the difference of their structure after annealing carried out to the films. In addition, energy dispersive X-ray (EDX) analysis was also used to analyze near surface (about 2 microns in depth) elements and estimate their proportion at different position by Oxford Aztec X-Act detector.

### **3.5. Chemical Vapor Deposition (CVD)**

As mentioned in the previous chapter, CVD is a vapor-phase process which relies on thermal cracking of carbon elements from a precursor hydrocarbon gas on transition metal substrate, and desired carbon source is obtained. The formation of graphene takes place in two different mechanisms; direct deposition or dissolution-segregation.

Direct deposition occurs by adsorption of thermally decomposed hydrocarbon on metal surface (on Cu [153, 154]). On the other hand, if temperature dependently dissolved carbon atoms, which turn out a solid solution with metal substrate, are supersaturated during cooling or increasing the carbon concentration (on Ni [3, 154-156]) induces segregation of carbon atoms [154, 155]. Then the carbon atoms precipitate as single layer graphene or multilayer graphite on the surface of the substrate. Segregation refers to one or more components of solid solution congregate on free surface without phase transformation, whereas precipitation refers to a perturbation such as fluctuations with phase transformation. Generally, precipitation occurs in advance of segregation process [155].



Figure 3.6. CVD growth system at Physics Department, CNL Lab, IZTECH

In 1974, Blakely et. al. [130] studied on segregation mechanism of carbon to a Ni (111) surface and realized from their Auger spectroscopy measurements single layer graphene could be grown on a Ni (111) surface. During graphite growth researches, decomposition mechanism of carbon containing gases began to be used in 1960s [157, 158]. Transition metals catalyze the dehydrogenation of aliphatic hydrocarbons such as CH<sub>4</sub> and C<sub>2</sub>H<sub>2</sub>. Nickel has higher dehydrogenation ability and carbon solubility [159]. Also, Banerjee et. al. concluded that the graphite films grown on Ni substrate have higher degree of crystallinity compared to porcelain, copper and platinum [155, 157, 158].

In this work, all these properties are the reasons to choice Ni as substrate to grow on graphene layers. Figure 3.7 shows the difference between direct deposition and dissolution-segregation process using two different metal substrates, Cu has negligible carbon solubility as compared with Ni at the same temperature [154].

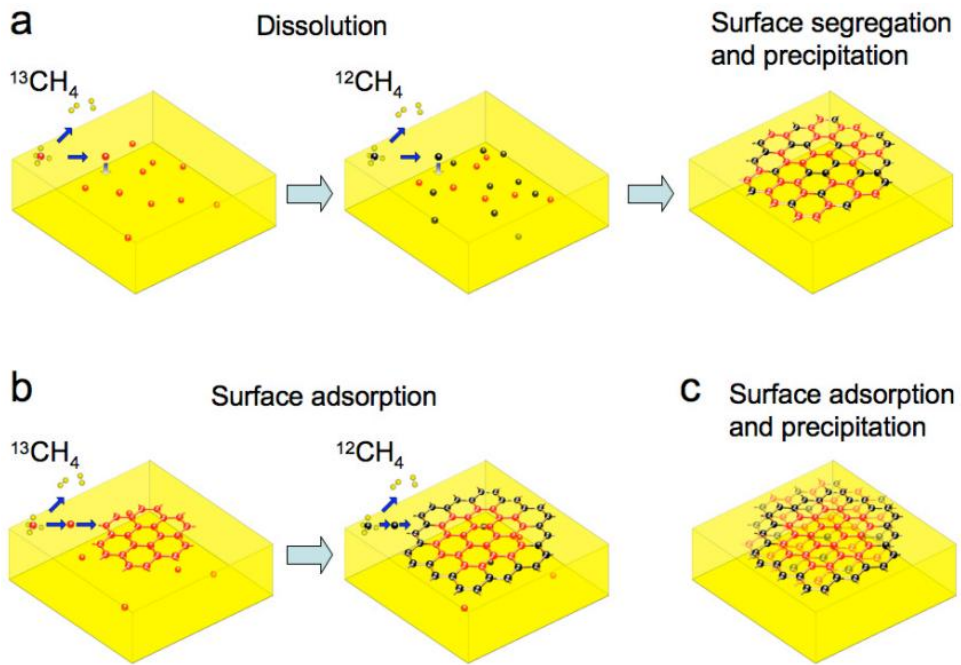


Figure 3.7. Schematic representations of the possible distribution of C isotopes on different metal substrates and their growth mechanisms. (a) Graphene with randomly mixed isotopes refers to surface segregation and/or precipitation. (b) Graphene with separated isotopes refers to surface adsorption. (c) Combined growth from surface adsorption and precipitation [154]

Using the fact that C<sup>12</sup> and C<sup>13</sup> isotopes have different Raman spectroscopy G-band frequency due to the mass differences (Figure 3.8), Li et. al. [154] switched the labeled methane gases with these isotopes and realized that the graphene growth on Ni has randomly distributed carbon isotopes due to the dissolution-segregation-precipitation mechanism (Figure 3.7 (a)), but the graphene growth on Cu has spatial distributions of carbon isotopes (Figure 3.7 (b)), due to the direct adsorption mechanism. Also, the composition of these two process shows in Figure 3.7 (c).

Ni or Cu surface once covered by single layer graphene (1-LG) the catalytic activity and carbon species reduces due to reduced hydrocarbon decomposition and could not carry on graphite growth so, the growth of 1-LG is self limiting [153-155].

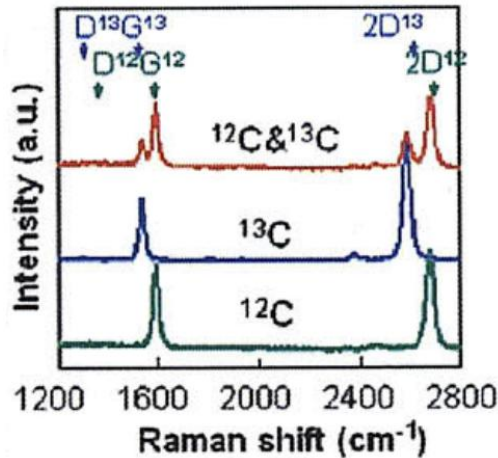
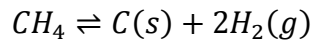


Figure 3.8. Raman spectra from graphene composed of C<sup>13</sup> (blue), C<sup>12</sup> (green) and from the mixture of both (red) [154].

CVD process involves basically three stages except heating the system from room temperature to desired annealing and growth temperature. Annealing stage is done to increase crystallinity and grain sizes of the Ni films under Ar and H<sub>2</sub> gas flow, then exposure to CH<sub>4</sub> as carbon source under Ar and H<sub>2</sub> flow is done. Methane decomposed and its carbon atoms dissolve in Ni substrate by the following reaction [160]:



The atoms in face centered cubic Ni crystal can move via vacancy motion. We can describe the diffusion mechanism in solutions, if there is no interaction between solute and solvent atoms, by Adolf Fick's first law of diffusion [161]:

$$\vec{J} = -D \frac{\partial c(x)}{\partial x}$$

**J** is the flux or quantity per second, of diffusing matter passing normally through a unit area under the action of a concentration gradient and **D** is called diffusivity. This coefficient must be constant at fixed temperatures if there is no composition of two or more gases [161]. The time dependent concentration of carbon atoms in Ni can be obtained from this law as following:

$$\frac{\partial c(x, t)}{\partial t} = \frac{\partial \vec{J}(x)}{\partial x} = -D \frac{\partial^2 c(x)}{\partial^2 x}$$

Assuming there is no initial carbon and changing concentration of carbon atoms inside the Ni film the boundary conditions can be identify as  $c(t, 0) = C_s$  and  $c(0, x) = 0$  where C<sub>s</sub> is the surface concentration. At the Ni-SiO<sub>2</sub> interface (x=l) there is no flux,

$$\frac{\partial c(x, t)}{\partial x} = 0$$

The solution for the concentration distribution of carbon atoms inside the Ni film is described by [155]:

$$\frac{c(x, t)}{C_s} = 1 - \frac{4}{\pi} \sum_{n=0}^{\infty} \frac{(-1)^n}{2n+1} \exp\left(\frac{-D(2n+1)\pi^2 t}{4l^2}\right) \cos\left(\frac{(2n+1)\pi(x-l)}{2l}\right)$$

As can be seen from the result, carbon concentration in film increases with its thickness and also the temperature and when the temperature reaches 550 °C then the concentration will be same for the same thick substrate [155]. So, to diffuse always carbon atoms in bulk Ni, the suggested temperature is at least 900 °C. Temperature dependence of 1or 2-LG growth is relied on used substrate and which mechanism expects. Some researchers use low temperatures (500-700 °C) to avoid diffusion to the substrate [162], whereas, some use high temperatures (850-1150 °C) to raise carbon dissolution and segregation [128] to growth of 1or 2-LG

The last stage is cooling and formation of graphene layers on Ni via segregation process.

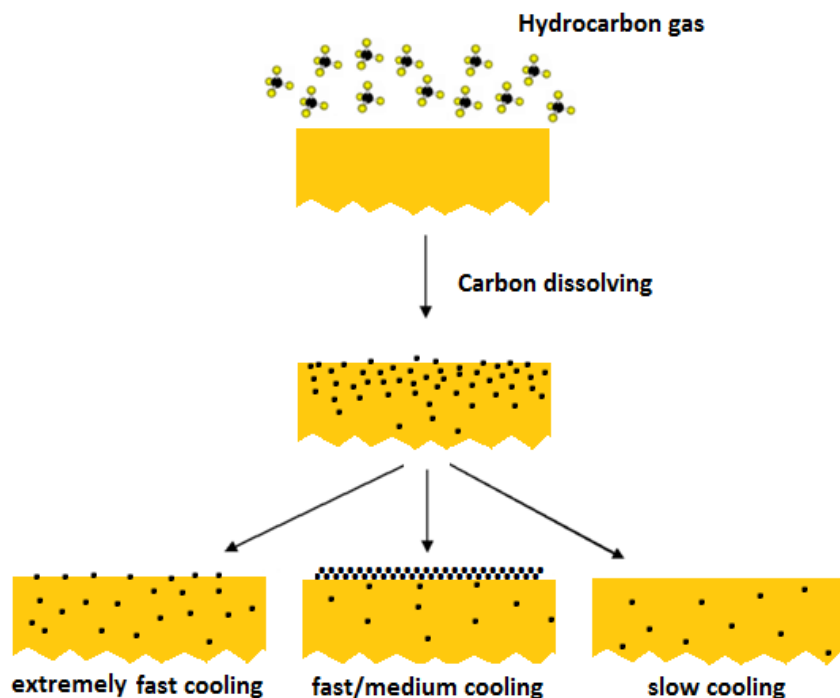


Figure 3.9. Illustration of carbon segregation mechanism and effect of cooling rate on Ni substrate

Raman spectra of Ni surface, which deposited with different cooling rates, verify that, the cooling rate specify the layer number of grown graphene as shown in Figure 3.9 [159]. Cooling carries out either under Ar or Ar and H<sub>2</sub> flow in this work. Then, most of the studies carry out with Ar and H<sub>2</sub> the annealing, to clean and crystallization of the Ni, and cooling stages, to avoid of remethanization [103, 155, 160, 163].

In this work, an oven (Lindberg/Blue TF55035C Split Mini tube Furnace), which is pictured in Figure 3.6, composed of a horizontally mounted quartz tube with outer diameter of 2.54 cm and length of 60 cm and quartz boat, equipped with various gas lines and mass flow controllers was used to carry out graphene growth.

### 3.6. Raman Spectroscopy

Raman spectroscopy is the most useful method to identify information about sample and can be used to study solid, liquid and gaseous samples. Sir Chandrasekhara Venkata Raman has got the Nobel Prize in Physics in 1930 for his work on the scattering of light and for the discovery of the effect named after him as Raman Effect. Incoming monochromatic light is scattered from an atom or molecule by interacting vibration modes of the crystal atoms. Most photons are elastically scattered and called Rayleigh scattering, so scattered and incoming photons have the same kinetic energy. Just inelastic scattered photons contribute to Raman Effect. In such that way, energy of the scattered photons is shifted up or down in comparison with the energy of incoming photons. This shift provides information about vibrational, rotational and other low frequency transitions in molecules. The interaction between the light and the material includes both incoming photon-electron and electron-phonon interactions.

Monochromatic laser light with frequency  $v_0$  excites molecules and transforms them into oscillating dipoles. Induced electrical dipole moment of the crystal can be determined by the laser beam which creates an oscillating electromagnetic wave with electrical vector  $\vec{E}$  and molecular polarizability tensor of the atom  $\alpha$ , following:

$$\vec{P} = \alpha \vec{E}$$

Polarization vector represents the displacement between positive and negative charges. Assuming the polarizability of the material modulates by the vibration of the lattice, the polarization description can be expanded as

$$\vec{P} = \vec{E}_0 (\alpha_0 + \alpha_1 \sin \omega_q t) \sin \omega_0 t$$

$$\vec{P} = \vec{E}_0 (\alpha_0 \sin \omega_0 t + 1/2 \alpha_1 \cos(\omega_0 - \omega_q)t - 1/2 \alpha_1 \cos(\omega_0 + \omega_q)t)$$

where  $\omega_q$  is the frequency of the atomic vibration coupled to the incoming light. Due to the interaction molecules start to vibrate with a characteristic frequency and a phonon can be emitted or absorbed or about 99.99% of all incident photons can be scattered elastically. The last description of polarization involves these three different ways for scattering. The first term belongs elastic scattering with no shift of light frequency. The second term refers inelastic scattering by a down-shift, this Raman frequency is called Stokes and the third term refers an up-shift which is called Anti-Stokes.

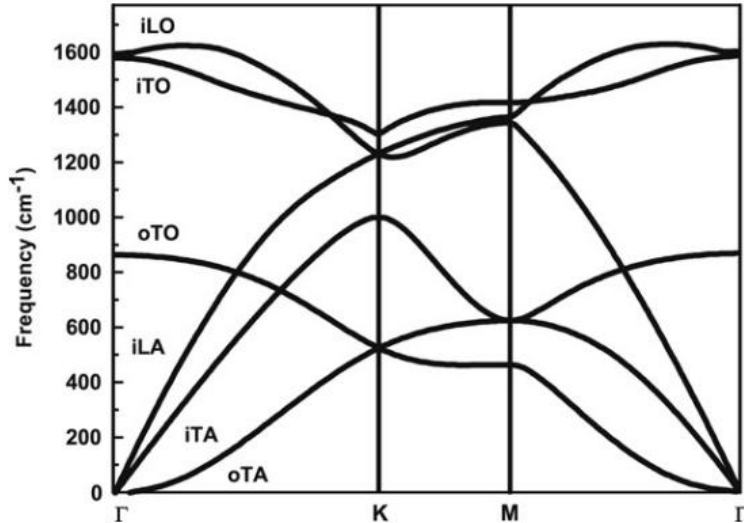


Figure 3.10. Theoretically calculated phonon dispersion of the six types of vibration modes as a function of  $E_{\text{laser}}$  in the graphene [164] where o=out-of-plane and i=in-plane modes

To figure out the Raman Effect on graphene it is essential that understanding electron–phonon coupling and phonon dispersion of graphene meaning the frequency as a function of wavelength. As mentioned in previous chapter, phonon dispersion is quadratic at  $\Gamma$  point for out-of-plane modes of graphene (Figure 2.14 (a)), but it is linear for in-plane modes (Figure 2.14 (b)). Figure 3.10 shows the dispersion relation of graphene with following surface cuts along the lines  $\Gamma$ -K-M- $\Gamma$  in the Brillouin zone. The excitation of only one phonon process is known first order Figure 3.11 (a)), whereas, two phonons which have equal wave vector magnitude but opposite signs

(Figure 3.11 (d)), or one phonon and one defect (Figure 3.11 (b) can be excited and this process is known as second order scattering. There are three most prominent peaks in the Raman spectra of 1-LG. One of them is G band that is the only first order Raman scattering appearing at  $\sim 1582 \text{ cm}^{-1}$ , using laser excitation at 2.41 eV (514 nm wavelength). As seen from Figure 3.10, iTO and iLO modes are doubly degenerate at  $\Gamma$  point where phonon wave vector is about zero  $\mathbf{q} \approx 0$ , and according to Group Theory, the degenerate phonon modes are Raman active modes [164]. In Figure 3.11 (a), the first order Raman process is shown at  $\Gamma$  point, an electron around  $\mathbf{K}$  absorbs the photon energy and inelastically scattered by a phonon. This process is responsible for Raman G band of graphene. The other prominent peaks are D appearing at  $\sim 1350 \text{ cm}^{-1}$  which is induced by disorder and  $G'$  at about  $2700 \text{ cm}^{-1}$ , using laser excitation at 2.41 eV (514 nm wavelength). As seen from the phonon dispersion (Figure 3.10) iTO branch is non-degenerate at  $\mathbf{K}$  point, but iLO and iLA phonon branches coincide at  $\mathbf{K}$  point by doubly degenerating. 2<sup>nd</sup> order-one phonon process, one elastic scattering of defect scattering and one inelastic scattering event by emitting or absorbing an iTO phonon, comprise D band (Figure 3.11 (b)), thus this band gives information about defects. 2<sup>nd</sup> order two iTO phonon process (intervalley process) comprises  $G'$  band (Figure 3.11 (d)) by scattering iTO phonons to opposite directions ( $\omega_{G'} \approx 2\omega_D$ ). In Figure 3.11 (c), also there is D' band process with one iLO phonon and one defect scattering (intravalley process) appearing at  $\sim 1620 \text{ cm}^{-1}$ . The  $G^*$  Raman band is also shown near  $\sim 2450 \text{ cm}^{-1}$  which can also be explained by the DR Raman model with an intervalley process but involving one iTO and one LA phonon.

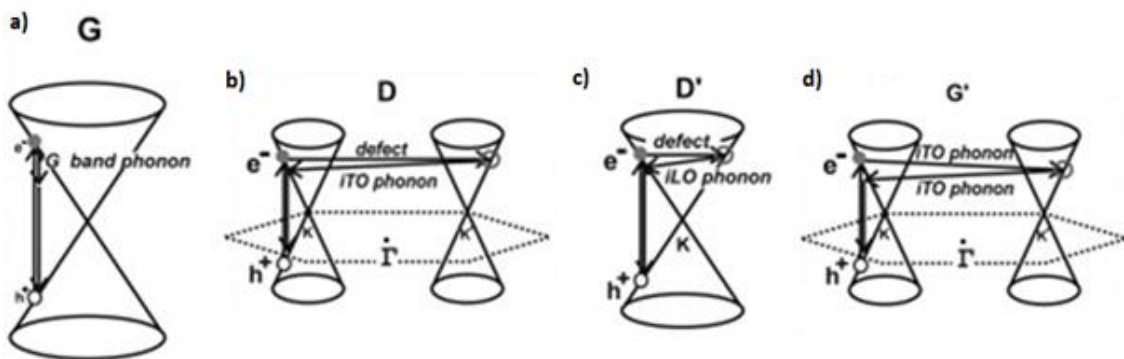


Figure 3.11. First order (a), and second order scattering processes (b,c,d) [164]

There is a discontinuity in the derivative of the dispersion relation, which known as Kohn anomaly. Only optical phonons at  $\mathbf{K}$  and  $\Gamma$  points can be coupled to the Fermi level electrons. The phonon branches exhibiting the Kohn anomaly at the  $\mathbf{K}$  and  $\Gamma$  points are those associated with the Raman G' band and G band, respectively. In real part of dielectric function expression there is a singularity on Fermi surface for  $\mathbf{q} \approx 2\mathbf{k}_F$ . However, this singularity is so small in reciprocal space and taking the Fourier transform the Gibbs phenomena causes an oscillation of the expression. These oscillations are called Kohn anomalies and appear as vertical tangent in the plot of the  $\omega^2(\mathbf{q})$  [165]. So, the slope of the branches at  $\mathbf{K}$  and  $\Gamma$  points also describes the electron-phonon coupling [166]. There is such a cusp at K point, seen Figure 3.10. Wirtz et. al. say that for graphene grown on a Ni (111) surface, a total suppression of the Kohn anomaly occurs: the highest optical branch around K becomes completely flat. This is due to the strong hybridization of the graphene  $\pi$ -bands with the Nickel d-bands which lifts the linear crossing of the  $\pi$ -bands at  $\mathbf{K}$  [167].

Double Resonance (DR) Raman process can be appeared when phonon wave vector of D and G' band is not zero at  $\mathbf{K}$  point, because they could couple to the electronic states, such that  $\mathbf{q} \approx 2\mathbf{k}$ . Thus, the wave vector of phonons depends on the wave vector of excited electrons. This dependence cause the dispersive behavior of D and G' bands (shifting of Raman peak positions due to laser frequency).

The Fermi level movement from the Dirac point induces rise in the frequency and decrease in the width of the G band of 1-LG, appearing in Raman spectra around  $1580 \text{ cm}^{-1}$ , and these changes are ascribed to the dependence of the electron-phonon process.

DR Raman process (Figure 3.11 (b, c, d)) is also used to get information about stacking and layer number of graphene. The G' band has only one main DR process for 1-LG at room temperature, thus 1-LG exhibits a single Lorentzian peak with a FWHM of  $\sim 24 \text{ cm}^{-1}$  which depends on the production method (Figure 3.13 (a)) [164]. In the case of 2-LG with AB-Bernal stacking, there are two conduction and two valance bands of  $\pi$  electrons of each layer. The bands are parabolic near  $\mathbf{K}$  point. There are eight possible DR Raman processes (Figure 3.12) [168].

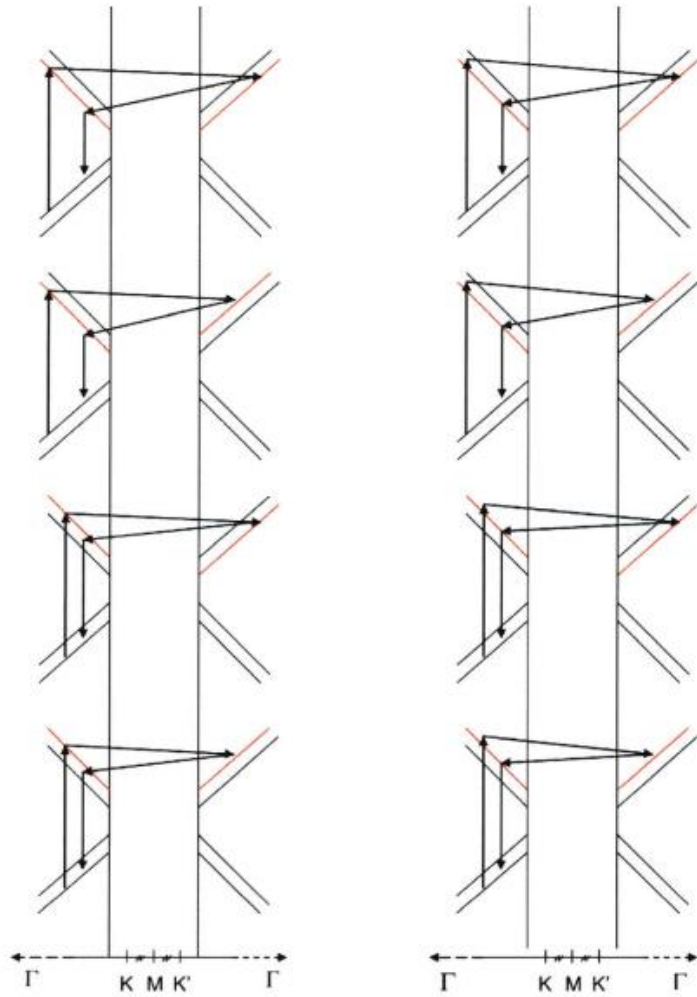


Figure 3.12. Electronic structure of 2-LG near Dirac points [155]

According to Group Theory and density-functional theory calculations, just four of these eight possible scattering processes on the left of the Figure 3.12 are degenerate and Raman active [164, 168]. These four different degenerate processes lead up to four different Raman peaks in the G' band spectrum [169]. The Raman spectra of a 2-LG is fitted with four Lorentzians  $2D_{1B}$ ,  $2D_{1A}$ ,  $2D_{2A}$  and  $2D_{2B}$  each with a FWHM of  $\sim 24 \text{ cm}^{-1}$  (Figure 3.13 (b)) and  $2D_{1A}$ ,  $2D_{2A}$  are more intense ones [82, 164]. In the case of 3-LG, using the same Group Theory the number of allowed Raman peaks in the G' band is found fifteen. Experimentally, it is shown that minimum six Lorentzians each with a FWHM of  $\sim 24 \text{ cm}^{-1}$  (Figure 3.13 (c)) is used to fit the G' band spectrum.

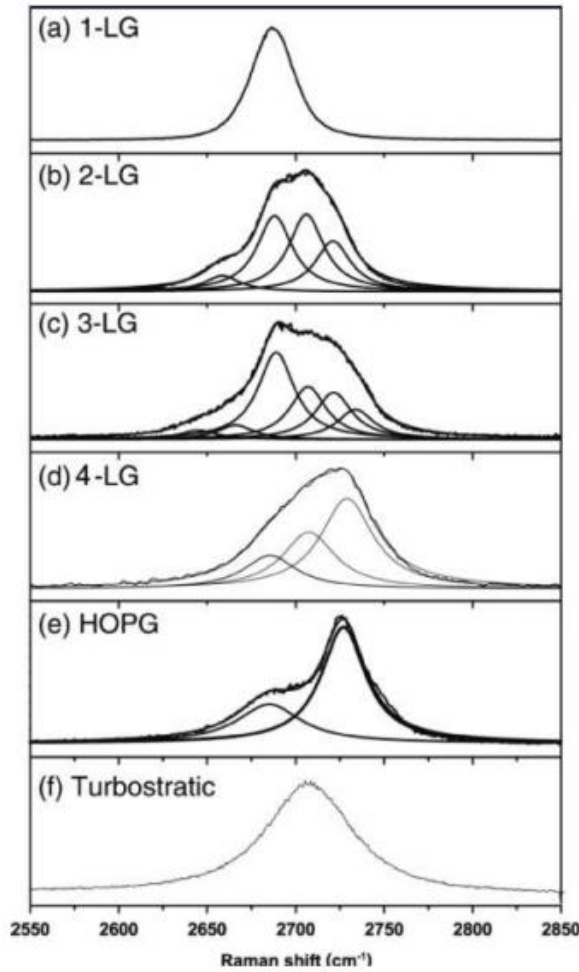


Figure 3.13. G' spectra for graphene as a function of as a function of the number of layers with 2.41 eV laser energy for (a) 1-LG, (b) 2-LG, (c) 3-LG, (d) 4-LG, (e) HOPG, (f) turbostratic [164, 170]

The numbers of allowed Raman peaks in G' band for AB-stacked 4-LG is shown three (Figure 3.13 (d)). For HOPG, the G' band describes with two peaks,  $2D_1$  and  $2D_2$ ,  $\frac{1}{4}$  and  $\frac{1}{2}$  of G peak (Figure 3.13 (e)) [82]. Looking Figure 3.13, we can see that the splitting of peaks opens up from 1-LG to 3-LG, but then the intensity of high frequency side of the G' band reduces with adding up more layers. It should be remembered that this layer number and G' band splitting relations just valid for the case of AB-Bernal stacking. For example, turbostratic graphene where graphene layers are stacked uncoupled has single Lorentzian due to the absence of an interlayer interaction between the graphene layers but has a larger linewidth (FWHM of  $\sim 45\text{-}60\text{ cm}^{-1}$ ) than 1-LG has. So, the electronic structure of turbostratic graphite is described in the same way as 1-LG. Also, the intensity ratio of G' and G band ( $I_{G'}/I_G$ ) of turbostratic graphite is lower and the frequency of G' band is shifted to upper than 1-LG [164]. The difference

between the single layer and the misoriented bilayer G' Raman spectra is the frequency of the peak, which for the misoriented bilayer is up-shifted and broadened in line width.

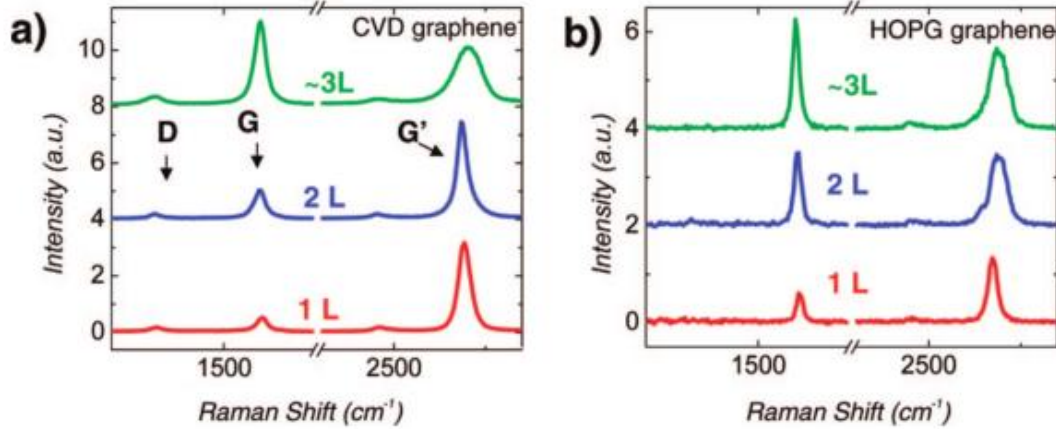


Figure 3.14. Raman spectra of 1 (red), 2 (blue), and  $\sim 3$  (green) graphene layers from a CVD grown graphene films on  $\text{SiO}_2/\text{Si}$  substrate (a). Raman spectra of the same layer numbered graphene films derived by the microcleaving of HOPG for comparison (b). The excitation wavelength is 532 nm [131]

Type of stacking and FWHM of G' peak are related to production method. There are lots of reports about the relation among line shape and FWHM of G' band, and stacking order which are confirmed with AFM and electron diffraction measurements [131, 155, 164]. First off all line shape of CVD grown graphene G' band is not distorted like AB stacked graphene or HOPG graphene. The difference of line shapes between CVD grown and HOPG are shown in Figure 3.14.

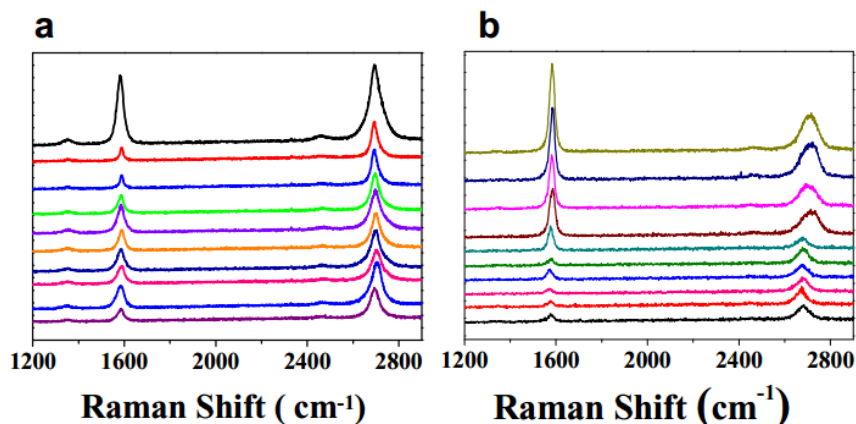


Figure 3.15. Raman spectra has the intensity ratio of  $I_G/I_{G'} < 1$  (a) and both  $I_G/I_{G'} < 1$  and  $I_G/I_{G'} > 1$  (b) [3]

According to J. Kong et. al. for CVD growth graphene, both 1-LG and 2-LG has maximum G' band FWHM of  $\sim 43$  cm $^{-1}$  [155]. The lineshape change and broadening is not observed for CVD growth graphene due to the misorientation between layers. However, according to A. Reina et. al. a single Lorentzian profile of the G' band ( $\sim 2700$  cm $^{-1}$ ) show a sharp line width on the order of  $\sim 30$  cm $^{-1}$  [131]. A. Reina et. al. also conclude that 2-L and 3-L graphene can show maximum FWHM of  $\sim 30$  cm $^{-1}$  with undistorted G' band line shape. Gomez De Arco performed Raman measurements of graphene on Ni (111) substrate, and with a single Lorentzian shape G' band spectra from ten different sample are shown in Figure 3.15 (a) [3]. All spectra of G' band have FWHM of  $25 - 55$  cm $^{-1}$  and  $I_G/I_{G'}$  ratio is less than one, which are considered for 1-L and 2-L graphene. Figure 3.15 (b) shows that G' band intensity which increases from bottom to top by up-shifting. When the  $I_G/I_{G'} > 1$  the layer number of graphene is more than 2-L with FWHM  $> 50$  cm $^{-1}$ . According to Gomez De Arco, if graphene films are transferred to SiO<sub>2</sub> substrate the single Lorentzian G' band line shape can has  $\sim 30$  cm $^{-1}$  width and  $I_G/I_{G'} < 1$  which is in accordance with A. Reina et. al. and J. Kong et. al. also [3].

Considering all these reports, all Raman spectra of various numbered layer graphenes were fitted by the least squares method to the minimum number of peak components to obtain a coefficient of determination above 0.99 [155]. Only one Lorentzian peak is enough for 1 or 2-LG, but more than 2-L four or more peaks are necessary to fit the G' band spectrum of graphene which is on Ni substrate [3]. As regards to line shape of G' band is analyzed with the change of layer number.

To sum up, for CVD growth 1-L graphene, peak intensity ratios are  $I_D/I_G$  in the range  $0.05 < I_D/I_G < 0.3$  [131]. The  $I_D$  largely comes from graphene edges which are mostly on Ni grain boundaries. Sharp line width ( $\sim 30-83$  cm $^{-1}$ ), line shape and fitting the G' band with one single Lorentzian peak refers 1-L or 2LG [164]. However, turbostratic graphite shows the same signs and it is difficult to differentiate turbostratic from 1-L or 2LG when Raman measurements performed on Ni substrate. So, to conclude layer number we will use the intensity ratio of  $I_{G'}/I_G < 1$ . Reported  $I_{G'}/I_G$  values varied over a wide range of FLG [16]. Also,  $I_{G'}/I_G$  values of FL-CVD-graphene were reported to split into two regions (the high and low  $I_{G'}/I_G$  values refer to turbostratic stacking and AB stacking, respectively). For 2-LG and multilayer graphene, there are frequency up-shifts of G and G' bands and FWHM of G' band increases [3, 131].

## CHAPTER 4

### Ni THIN FILM STRUCTURE

In previous chapter the formation of single and few-layer graphene by CVD was explained in detail. The effect of Ni film structure with the help of high temperatures investigated in this work is reported in this chapter. Ni has a high carbon solubility and it causes dehydrogenation of carbon atoms from  $\text{CH}_4$  precursor diffuse into the Ni film. After dissolution of carbon in the film, Graphene grows on Ni by precipitation at the cooling stage. Therefore, Ni film surface has the role of both a catalyst and support. Uniform segregation of diffused carbon atoms onto Ni catalyst surface creates honeycomb lattice structure of graphene sheets.

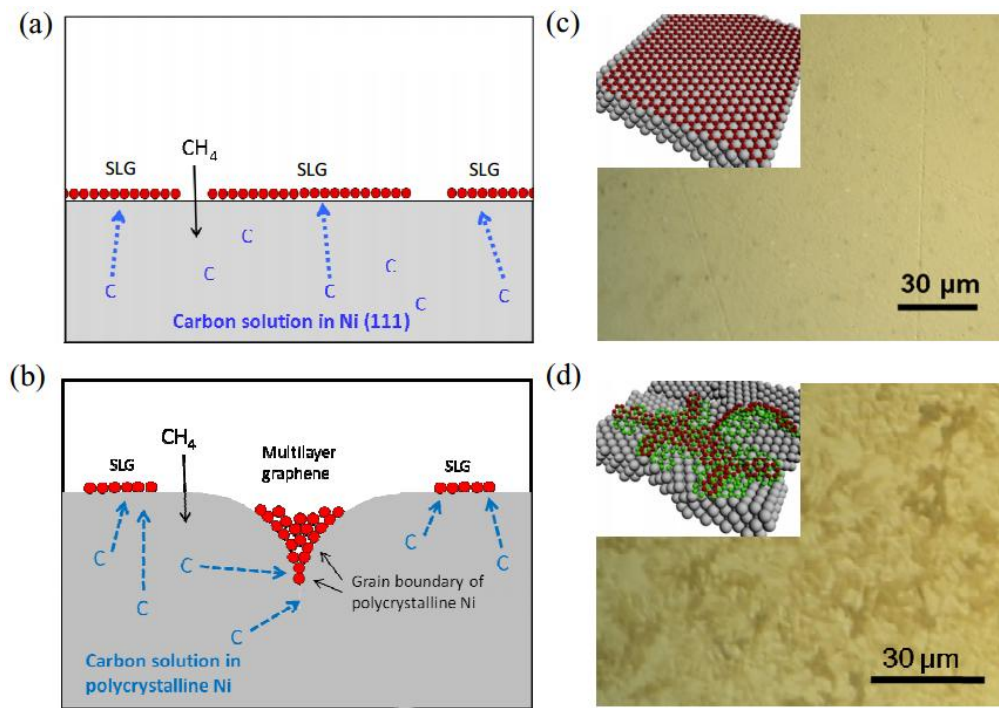


Figure 4.1. Representation of graphene growth (a) on Ni (111), and (b) on polycrystalline Ni. After growth by CVD optical image of (a) graphene/Ni (111) and (d) graphene/polycrystalline Ni [3]

Concentration of carbon atoms in Ni film affects the precipitation and segregation processes on the surface. Figure 4.1 (a-b) show the single layer graphene on

Ni (111) film which has smooth surface with almost no grain boundaries. Figure 4.1 (c-d) show a single layer graphene formation on smooth parts of a polycrystalline Ni surface and multilayer graphene formation in grooves where grain boundaries intersect. There are 3D insets in Figure 4.1 (c) and (d) that show graphene layer formation on (111) crystalline and polycrystalline Ni surfaces, schematically [3]. At grain boundary regions of transition metals the existence of impurities and vacancies activates these regions for interaction and gathering impurities. Hence, as seen from the Figure 4.1 (b) and the inset of Figure 4.1 (d), the grain boundaries have higher concentration of carbon atoms and form multilayer graphene by breaking segregation uniformity.

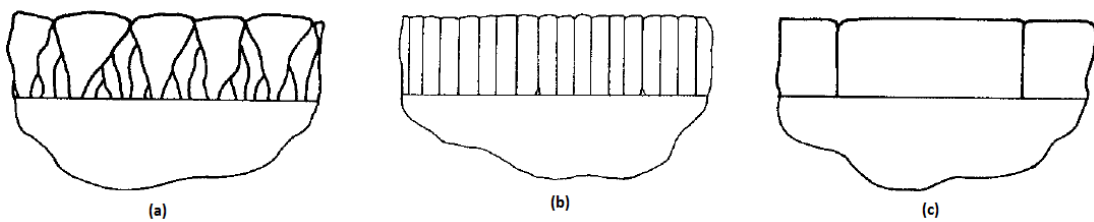


Figure 4.2. Cross sectional schematics of as-grown film structures with thickness less than  $1\mu\text{m}$  and the different columnar structures which depend on deposition temperatures ( $T_d$ ).  $T_d$  below about  $0.2-0.3T_m$  (a), deposition temperature  $T_d \geq 0.2-0.3 T_m$  (b) and  $T_d \geq T_m$  (c) [173].

Refractory metals tend to have different structures depend on the deposition temperature ( $T_d$ ) about melting point ( $T_m$ ) in K. Figure 4.2 (a) occurs at deposition temperatures below about  $0.2-0.3 T_m$  [173]. In this study Ni which has melting point of 1728 K, was deposited at room temperature (300 K) and it is below  $0.2 T_m$ . This temperature corresponds to cross sectional SEM micrographs of Ni films, which is also seen from Figure 4.3. Semiconductors tend to be amorphous when  $T_d \leq 0.5T_m$ , and have type Figure 4.2 (a) structure when  $0.5T_m \leq T_d \leq 0.9T_m$ . Face centered cubic materials such as Ni tend to have Figure 4.2 (c) structure when  $T_d \geq 0.2-0.3 T_m$ . Figure 4.2 (c) occurs when  $T_d \geq T_m$ . During or after deposition, heating of these metals with structures (a) and (b) evolve toward structure (c) (Figure 4.2). During segregation process carbon atoms accumulate on both inter-plane and planar boundaries.

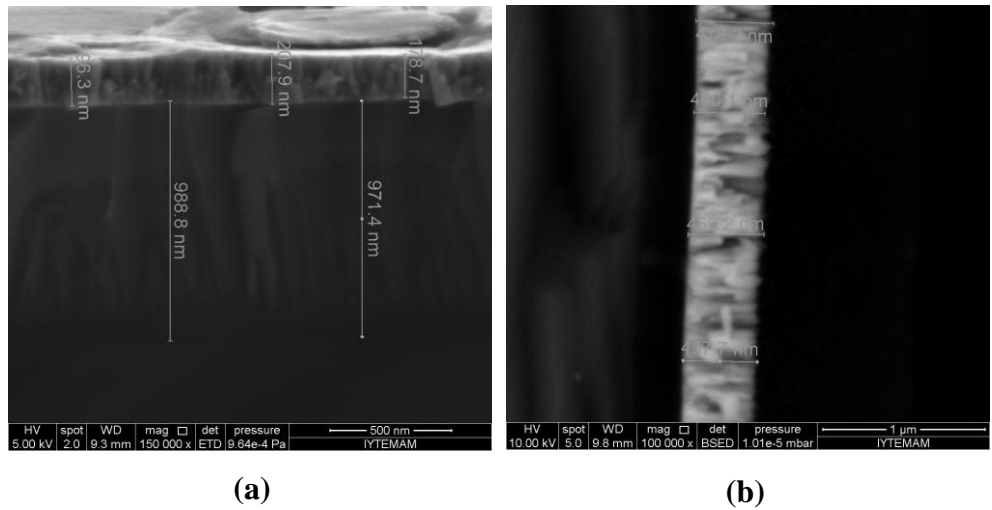


Figure 4.3. Cross sectional SEM micrographs of asgrown polycrystalline Ni<sub>3</sub> film (a) which has thickness of about 200 nm and asgrown Ni<sub>9</sub> film (b) about 450 nm thick.

In this study, to grow large size graphene layers on Ni film the aim must be reduce grain boundaries and depth of the grooves, and also increase the average grain sizes of Ni films to increase the intensity of smooth parts on the surface without boundaries. Hence, films were annealed after the deposition and before graphene growth by CVD. Initial grain sizes of Ni catalyst film specify the nucleation distribution of layers and the number of layers. Thus, to control the resulting graphene layers morphology, it is essential to control polycrystalline Ni grain morphology. However, the main problem is dewetting of Ni film. To reduce dewetting effect the thickness of Ni films were increased, and Alumina (Al<sub>2</sub>O<sub>3</sub>) buffer and Cr adhesive layers were deposited by magnetron sputter.

#### 4.1. Nickel Crystal Structure

To figure out the interaction between graphene and Ni substrate surface and the effects of substrate on growing graphene layer, it is essential to investigate the crystal structures. Ni has close-packed fcc lattice structure similar to the hcp structure. The nearest neighbor distance is 1.421 Å, which is very close to the characteristic distance of Ni (111) surface  $a_{Ni}/\sqrt{6} = 1.44$  Å where measured lattice parameter for fcc nickel  $a_{Ni} = 3.52$  Å [174]. The in plane lattice constant of graphene is 2.462 Å, which is also

very close to distance between Ni atoms in different layers measured on top view of Ni (111)  $a = 2.49 \text{ \AA}$  [175]. This lattice match is sufficient to allow continuous growth of graphene films on the surface of the Ni (111) films [164].

There are three possible arrangements of the graphene layer matching threefold symmetry on top of the close-packed Ni (111) surface (Figure 4.4) [132, 174, 175].

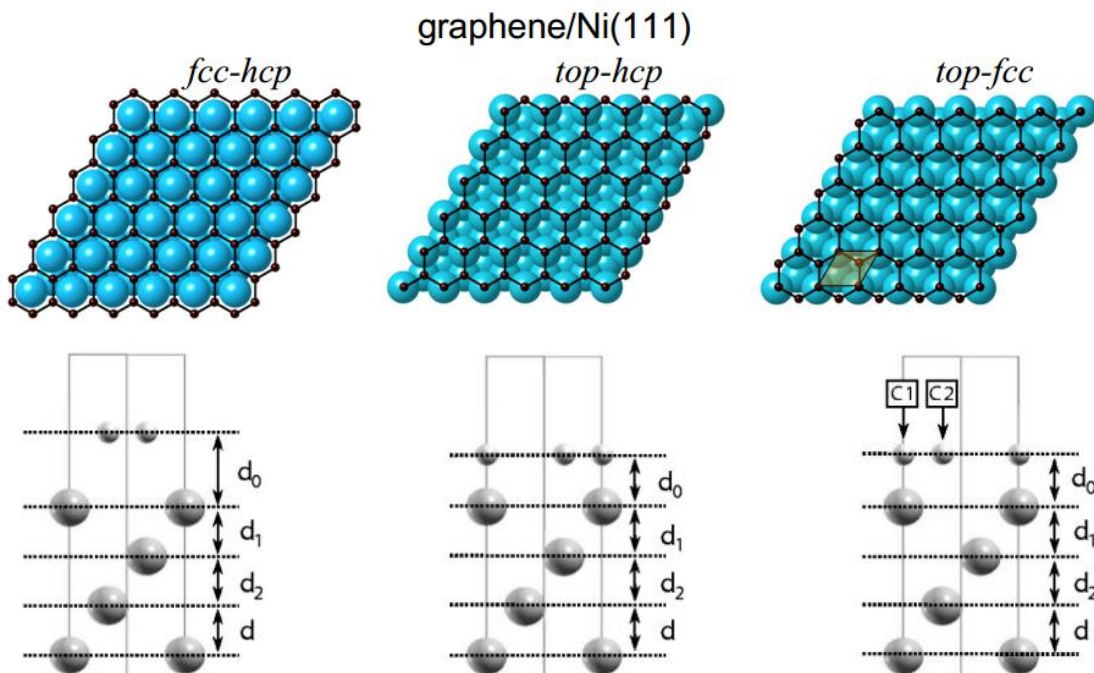


Figure 4.4. Three possible arrangements of the graphene layer on 1<sup>st</sup>, 2<sup>nd</sup> and 3<sup>rd</sup> Ni layers with ball model on the top. The blue balls indicate the Ni atoms and the black ones carbon atoms [175]. On the bottom line, cross sectional view of Ni layers and carbon atoms of graphene layer [174]

Table 4.1 shows the calculated the interface/surface nickel spin magnetic moment ( $m$ ), energy for three possible arrangements of the graphene layer on Ni (111) surface ( $\Delta E$ ) and equilibrium distances.  $d_0$  is the distance between the graphene layer and the Ni (111) surface, and the  $d_1$  and  $d_2$  distances are between the first three layers of the nickel substrate. Figure 4.4 (a) shows fcc-hcp model that carbon atoms are located hollow sites of Ni atoms above the 2<sup>nd</sup> and 3<sup>rd</sup> Ni layer fcc-hcp structure overlapping of the graphene  $\pi$ -orbitals and Ni d-bands [176]. As seen from the Table 4.1 the carbon layer in this model floats at 3.050 Å over the 1<sup>st</sup> Ni layer. The graphene  $\pi$ -bands change significantly due to the overlapping [174]. There is top-hcp model in Figure 4.4 (b), in which carbon atoms of A-sublattice are located just above the interface Ni atoms of the

1<sup>st</sup> layer, while the B-sublattice atoms are located either in the hcp hollow sites of Ni atoms of the 2<sup>nd</sup> layer. Figure 4.4 (c) represents top-fcc model, in which carbon atoms of A-sublattice are located just above the interface Ni atoms of the 1<sup>st</sup> layer, while the B-sublattice are located in the fcc hollow sites of Ni atoms of the 3<sup>rd</sup> layer. Also, in Figure 4.4 (c), the two nonequivalent carbon atoms are indicated as C1 and C2. The distances between top Ni layer and these two carbon atoms are shown in the Table 4.1 as  $d_0$ . The most possible model is top-fcc which has no energy difference, whereas fcc-hcp and top-hcp models have 62 meV and 66 meV energy differences, respectively. The electronic structure of graphene will not be strongly modified by the nickel surface in fcc-hcp configuration due to the high distance between graphene and top Ni layer (is 3.050 Å).

Table 4.1. Calculated values for atomic structure of the three graphene/Ni (111) interface models and for the clean Ni (111) surface [174]

	Ni (111)	fcc-hcp	top-hcp	top-fcc
$d_0$ (Å)		3.050 / 3.050	2.113 / 2.120	2.122 / 2.130
$d_1$ (Å)	2.006	1.975	2.034	2.011
$d_2$ (Å)	2.029	1.999	2.015	2.014
$\Delta E$ (eV)		+0.062	+0.066	0.000
$m$ ( $\mu_B$ )	0.716	0.673	0.514	0.553

## 4.2. Thickness of Ni Films and Buffer Layers

Before carrying out Ni film growth, Ni thickness was calibrated for various DC powers and given time of growth. SEM was used to measure the thickness of Ni films (Figure 4.6).

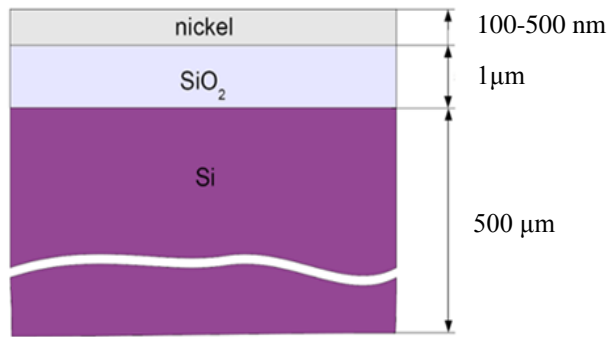


Figure 4.5. Representation of the layer structure of deposited films with their thickness

Seven different Ni thin films were deposited onto Si(500-550 $\mu$ m)/SiO<sub>2</sub>(1 $\mu$ m) (100) substrates by DC sputtering. The substrate cleaning and film deposition were carried out as given in detail in Chapter 3. These seven Ni films were deposited under 9.95 sccm Ar gas with a substrate rotation of 40 rpm at room temperature. To monitorize the thickness of first six Ni films, the films were placed cross sectional on the stubs by means of Al grounds, whereas thickness of NiW1 film was measured by Surface Profiler. The parameters of film deposition process are given in Table 4.2.

Table 4.2. Deposition parameters of Ni1, Ni2, Ni3, Ni4, Ni5, Ni6 and NiW1 films

Sample ID	Pressure (mTorr)	Power (Watt)	Time (min)	Thickness (nm)
Ni1	3.0	20	120	~100
Ni2	3.0	30	120	~160
Ni3	3.1	35	128	~200
Ni4	3.0	40	120	~230
Ni5	3.0	40	110	~200
Ni6	3.1	25	120	~130
NiW1	7.0	100	120	~500

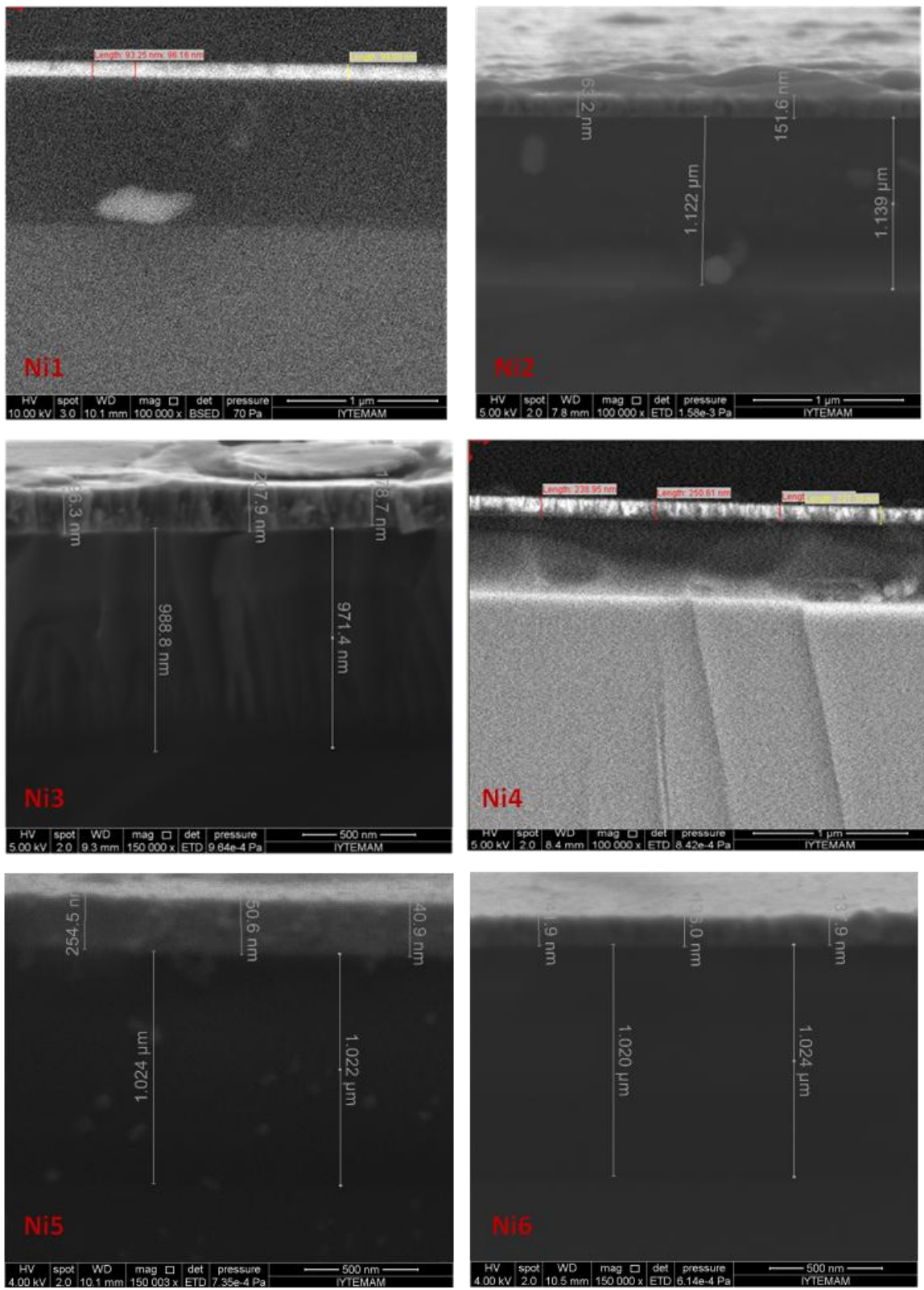


Figure 4.6. Cross sectional SEM micrographs of Ni1, Ni2, Ni3, Ni4, Ni5 and Ni6 films

The thicknesses of Ni films were ranging from 100 nm to 230 nm. Under the Ni films there were Si/SiO<sub>2</sub> substrates which have 500  $\mu\text{m}$  and 1  $\mu\text{m}$  thick, respectively. The relation of power and thickness was set up by fixing all time parameters at 120 min (Figure 4.7). Then, almost linear relation was observed from Figure 4.7 at lower powers. However, increasing power led thinner films than expected.

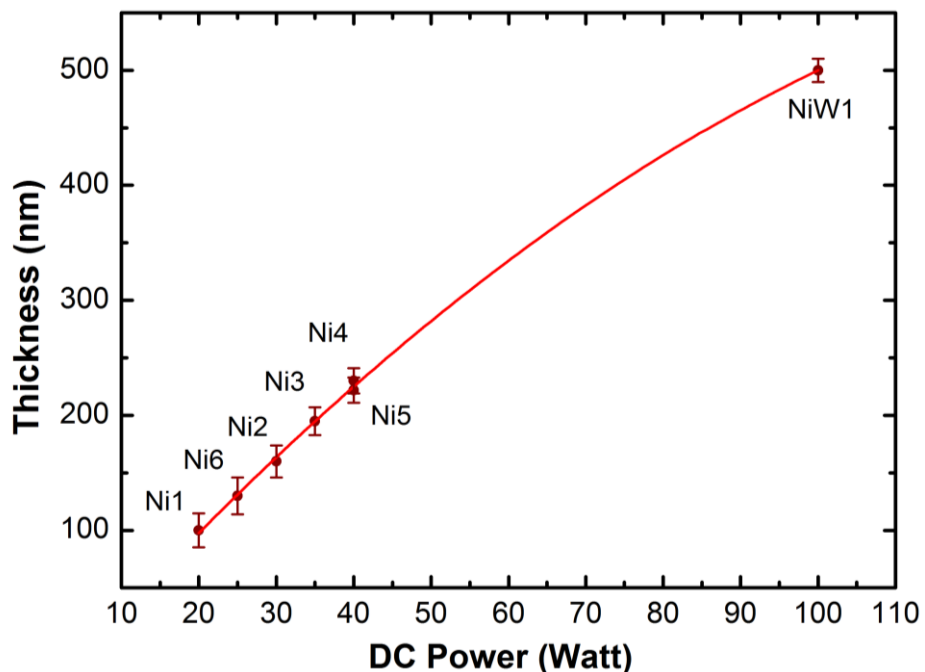


Figure 4.7. Relation between DC power and thickness of sputtered Ni films

Then, eight different Ni films were deposited with different parameters which are shown in Table 4.3. Ni12 and Ni14 samples were deposited onto Si/SiO<sub>2</sub>(100) substrates by DC sputtering. For Ni10 sample Al<sub>2</sub>O<sub>3</sub> buffer layer was deposited firstly and then Ni film was deposited on the top. To estimate the thickness of Al<sub>2</sub>O<sub>3</sub>, four samples were deposited during different time intervals at 150 watt and two samples at 120 watt RF power at room temperature. Surface Profiler was used to measure their thickness from the step between Al<sub>2</sub>O<sub>3</sub> and substrate film (Figure 4.8). Figure 4.9 shows the thickness versus time relation of six different samples which are AlO-1, AlO-2, AlO-3, AlO-4, AlO-5 and AlO-6. Using that relation Al<sub>2</sub>O<sub>3</sub> buffer layers were grown with known thickness.

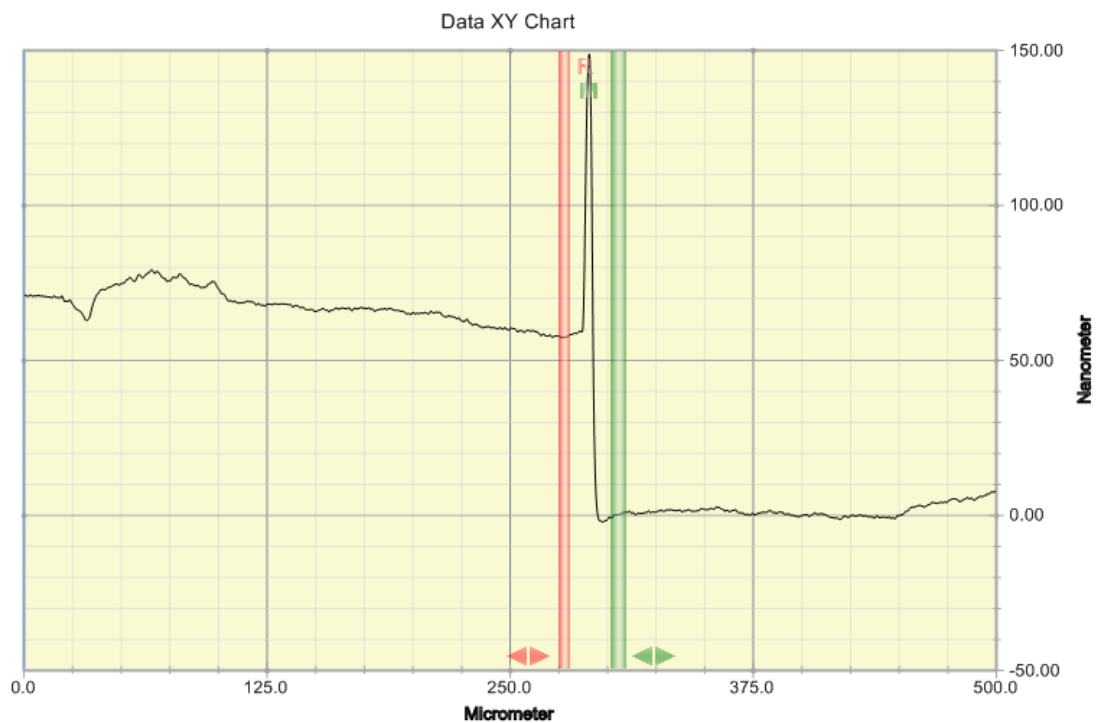


Figure 4.8. Surface Profiler step height measurement of AlO-2 sample (~55 nm)

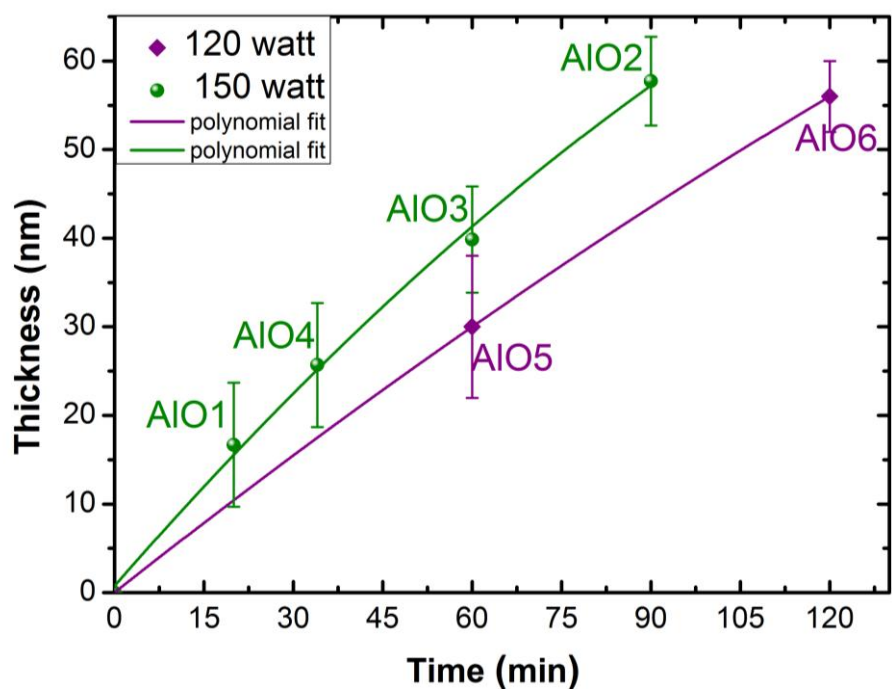


Figure 4.9. Thickness versus time relation of Al<sub>2</sub>O<sub>3</sub> films

Also, SiO<sub>2</sub> substrates which were thinner than 1 μm were obtained on Si by wet oxidation. The thickness of oxidized SiO<sub>2</sub> is shown in Figure 4.10 by cross sectional SEM image. Ni7, Ni8, Ni9, Ni11 and Ni13 samples were deposited onto these 230 nm thick SiO<sub>2</sub> substrates. Ni7, Ni8 and Ni9 films had Al<sub>2</sub>O<sub>3</sub> buffer layer. Ni13 and Ni14 films were deposited by heating the substrate to 450 °C, whereas other films were deposited at 26-27 °C. The deposition parameters and thicknesses are shown in Table 4.3.

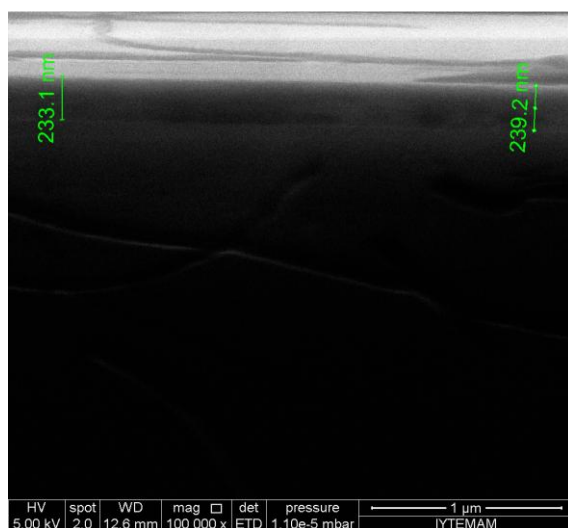


Figure 4.10. Cross sectional SEM micrograph of SiO<sub>2</sub> substrate that has 230 nm thick

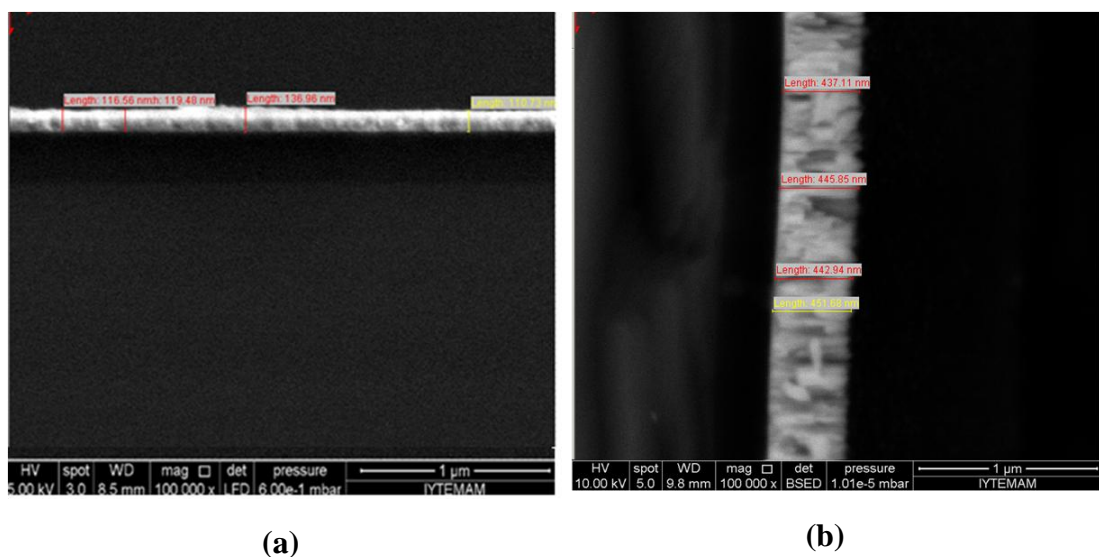


Figure 4.11. Cross sectional SEM micrographs of asgrown Ni7 (a), and Ni9 (b) films

Table 4.3. The deposition parameters of Al<sub>2</sub>O<sub>3</sub> buffer layers and Ni films. (\*) indicates the deposition temperature was 450 °C.

Sample ID	Pressure (mTorr)	Al <sub>2</sub> O <sub>3</sub> Buffer Layer Power (Watt)	Time (min)	Thickness (nm)	Ni Power (Watt)	Time (min)	Thickness (nm)
<b>Ni7</b>	7.7	120	60	~30	20	120	~100
<b>Ni8</b>	7.7	120	120	~56	20	120	~100
<b>Ni9</b>	7.7	120	120	~56	40	260	~400
<b>Ni10</b>	7.7	120	120	~56	40	260	~400
<b>Ni11</b>	7.3	-	-	-	40	260	~400
<b>Ni12</b>	7.3	-	-	-	40	260	~400
<b>Ni13*</b>	7.7	-	-	-	20	120	~100
<b>Ni14*</b>	7.7	-	-	-	20	120	~100

Then, four different Ni films were deposited with different parameters which are shown in Table 4.4. For Ni17 and Ni18 samples Cr adhesive layers deposited firstly. However, for Ni15 and Ni16 films both Al<sub>2</sub>O<sub>3</sub> buffer layers and Cr adhesive layers were deposited, respectively. Then Ni films were deposited onto top of all films. To estimate the thickness of Cr, four Cr films deposited with different DC powers during 10 minutes at room temperature. Then, Surface Profiler was used to measure their thickness from the step between Cr and the substrate film (Figure 4.12). Figure 4.13 shows the thickness versus time relations of five different films which are Cr1, Cr2, Cr3, Cr11 and Cr13.

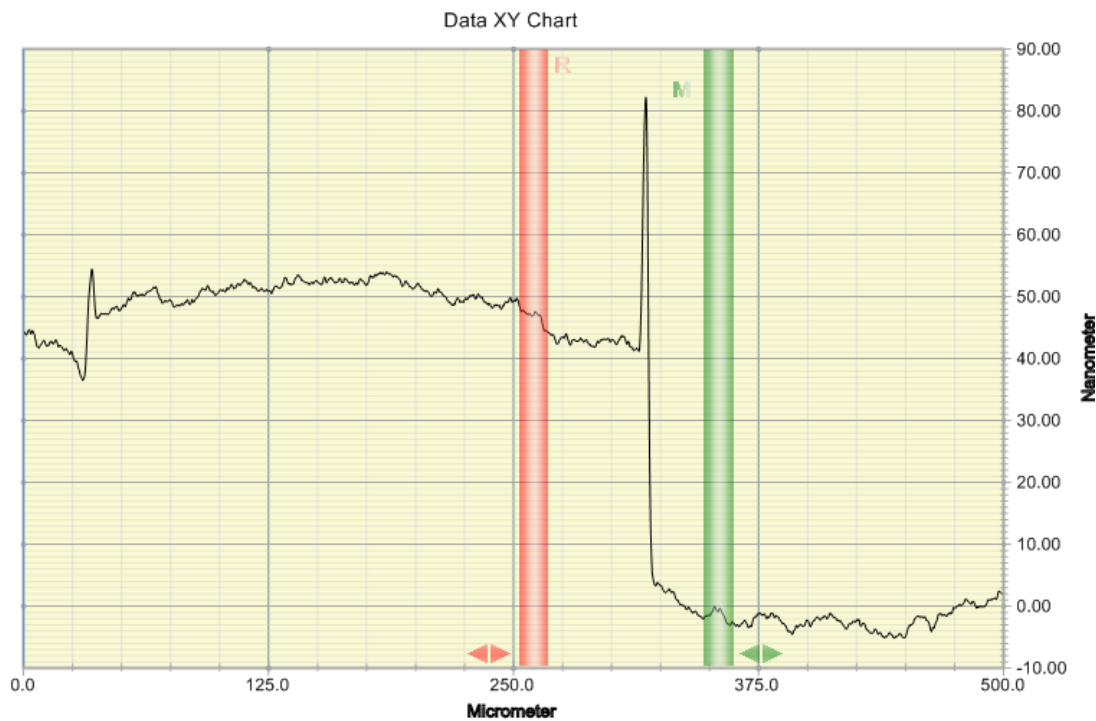


Figure 4.12. Surface Profiler step height measurement of Cr4 sample (~50 nm)

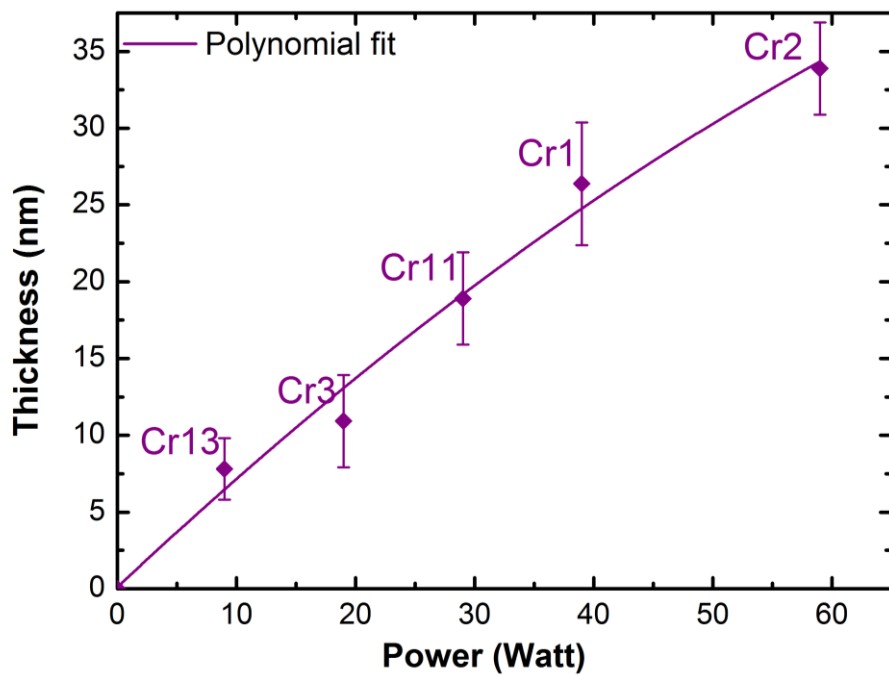


Figure 4.13. Thickness versus power relation of Cr films. All samples at this graph deposited during 10 minutes at room temperature.

For power of 40 watt and 20 watt, seven films which are Cr1, Cr4, Cr5, Cr6, Cr7, Cr8, Cr14, and three samples which are Cr3, Cr10 and Cr12 were deposited, respectively, during different time intervals. The thickness versus time relations of these films are shown in Figure 4.14.

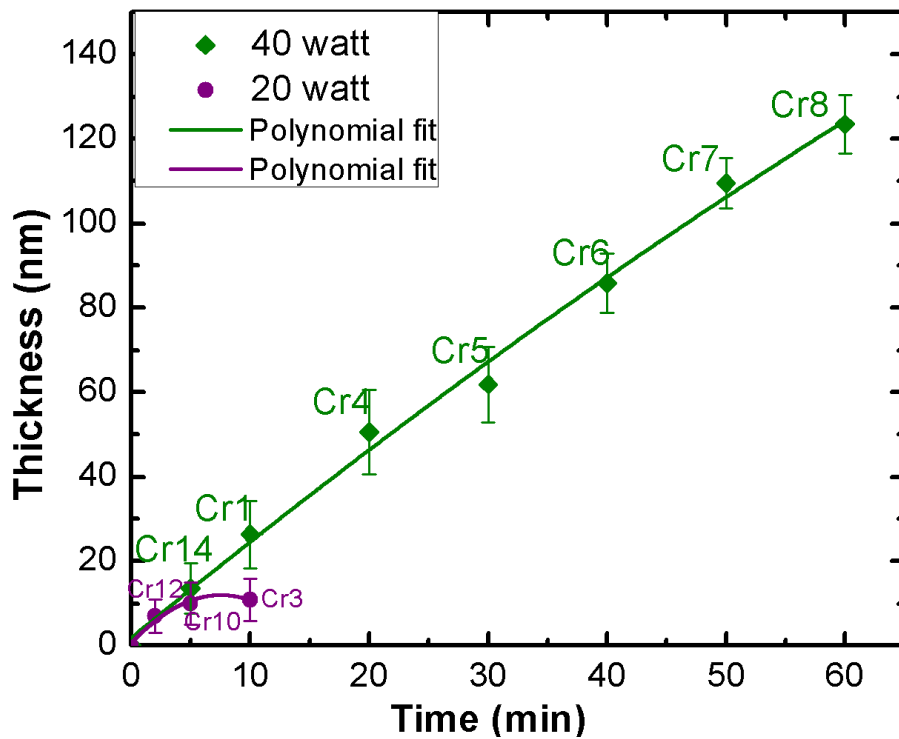


Figure 4.14. Thickness versus time relations of Cr films

Ni18 and Ni16 films were deposited by heating the substrate to 450 °C, whereas Ni17 and Ni15 films were deposited at 26-27 °C. Also, all samples deposited under 9.95 sccm Ar gas with 40 rpm. The deposition parameters and thickness of the films are shown in Table 4.4.

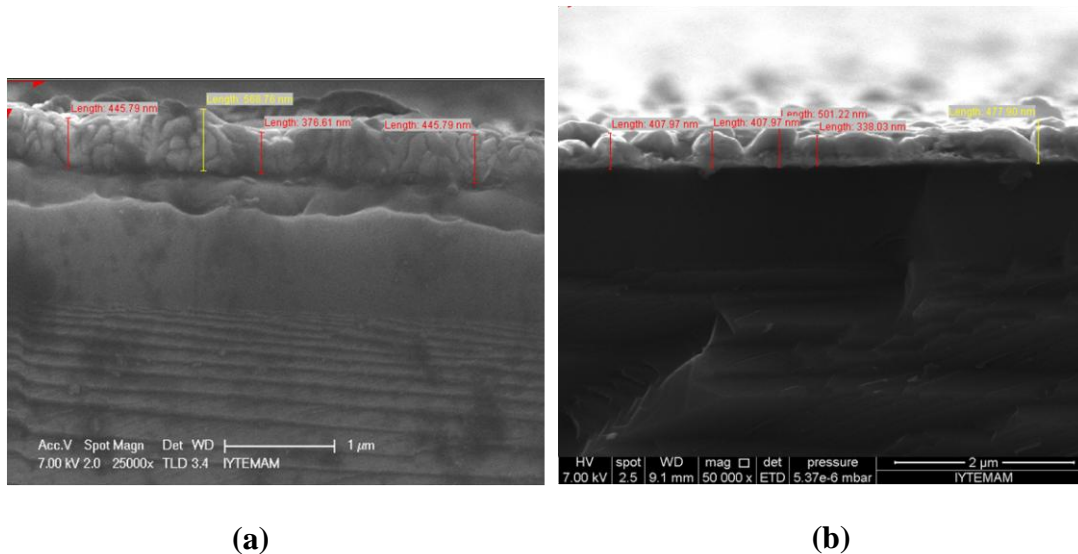


Figure 4.15. Cross sectional SEM micrographs of asgrown Ni15 (a), and Ni16 (b) films

Table 4.4. The deposition parameters of Cr adhesive layers, Al<sub>2</sub>O<sub>3</sub> buffer layers and Ni films. (\*) indicates the deposition temperature was 450 °C.

Sample ID	Pressure (mTorr)	Cr Buffer Layer Power (Watt)	Time (min)	Thickness (nm)	Al <sub>2</sub> O <sub>3</sub> Buffer Layer Power (Watt)	Time (min)	Thickness (nm)	Ni Power (Watt)	Time (min)	Thickness (nm)
Ni15	6.9	40	4	~10	150	60	~40	100	80	~400
Ni16*	6.9	40	4	~10	150	60	~40	100	80	~400
Ni17	6.9	40	4	~10	-	-	-	100	80	~400
Ni18*	6.9	40	4	~10	-	-	-	100	80	~400

### 4.3. Effect of Annealing on Ni Thin Films

The formation of single or multilayer graphene correlates to different factors including the abundance of defects and grain boundaries on the polycrystalline Ni substrate. The percentage of layer number or size of CVD grown graphene are limited by the grain size of crystalline Ni obtained after thermal annealing of Ni thin film. Annealing of Ni films at sufficient temperatures causes grain boundary motion and change of average grain size. As mentioned above, grain growth leads to evolution from

the grain structures represented in Figure 4.2 (a) and (b) to that of Figure 4.2 (c). The change of average grain size with time in bulk materials is described by following

$$d^2 - d_0^2 = c_0 t \exp\left(-\frac{Q}{kT}\right)$$

where  $d_0$  is average grain radius at  $t = 0$ ,  $d$  is average grain radius during time  $t$ ,  $Q$  is activation energy for grain boundary motion,  $k$  is Boltzmann constant at the temperature  $T$  [173, 177]. Grain growth processes are examined by grain boundary engineering (GBE). The relation of temperature and activation energy depends on material.

Figure 4.16 shows the cross sectional SEM micrographs of Ni3 sample and thickness of films which are asgrown and annealed at 800°C and 900°C.

To decrease the excess energy, system tends to minimize interfacial area between itself and the substrate. This diffusion driven process is called dewetting [178].

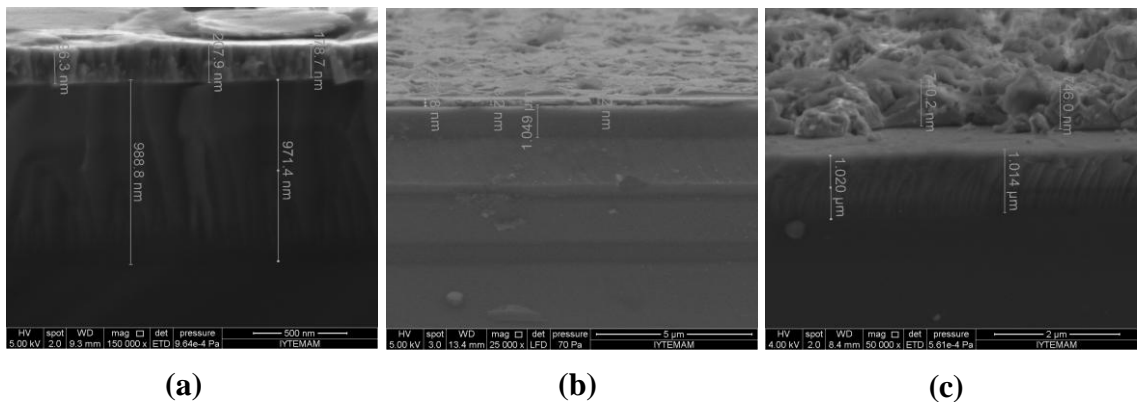


Figure 4.16. Cross sectional SEM micrographs of Ni3 film and thickness of films which are asgrown (a) and annealed at 800 °C (b) and 900 °C (c).

Ni films were annealed at 800 and 900 °C under 150 sccm Ar environment during one hour. Asgrown Ni3 film was about 200 nm thick (Figure 4.16). Annealing at 900 °C caused the film cluster by the effect of dewetting and their average thickness reached about 750 nm, but annealing at 800 °C caused the average thickness of particles just reached about 210 nm. Increasing temperature increased the dewetting effect. Ni1 film was about 100 nm thick. As seen from XRD  $\theta$  -  $2\theta$  scan of asgrown and annealed at 800 and 900 °C Ni1 films (Figure 4.17), increasing annealing temperature led to polycrystalline Ni has mostly (111) orientation by correlating the change of average grain size with time and temperature expression which mentioned above.

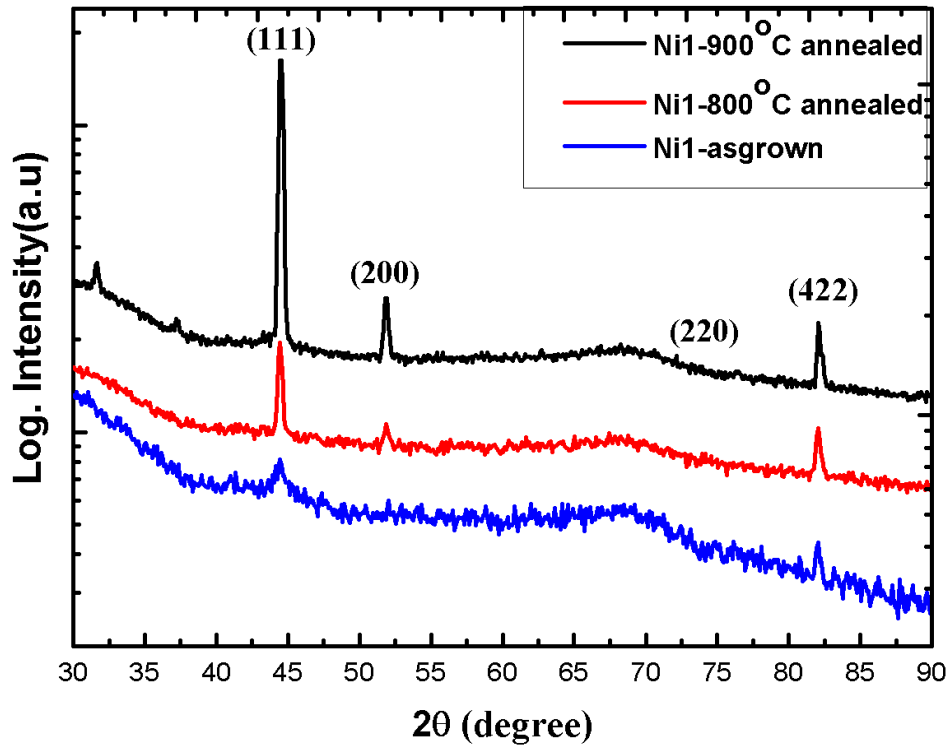


Figure 4.17. The relation between annealing temperature and the (111) orientation intensity of Ni1 film

Figure 4.17 shows that  $2\theta$  peak of Ni (111) is at  $44.49^\circ$ , and calculated average grain sizes increasing with annealing temperature (Table 4.5). However, graphene growth could not perform at  $800^\circ\text{C}$ . Thus, graphene growth temperature was chosen as at least  $900^\circ\text{C}$ .

Table 4.5. Average grain sizes and  $2\theta$  values of asgrown and annealed Ni1 films

	$2\theta$ (degree)	B (θ)	τ (nm)
Ni1 annealed at 900 °C	44.49	0.003036	60
Ni1 annealed at 800 °C	44.46	0.002959	51
Ni1 asgrown	44.45	0.004567	22

However, increasing annealing temperature increased excess energy of the system and as mentioned increased the effect of dewetting. During annealing larger grains grow and smaller grains shrink (Figure 4.18). So, total grain boundary area

decreases if thickness of the film ( $d$ ) is increases. This causes reduction of the excess free energy of grain boundaries by decreasing energy of the system.

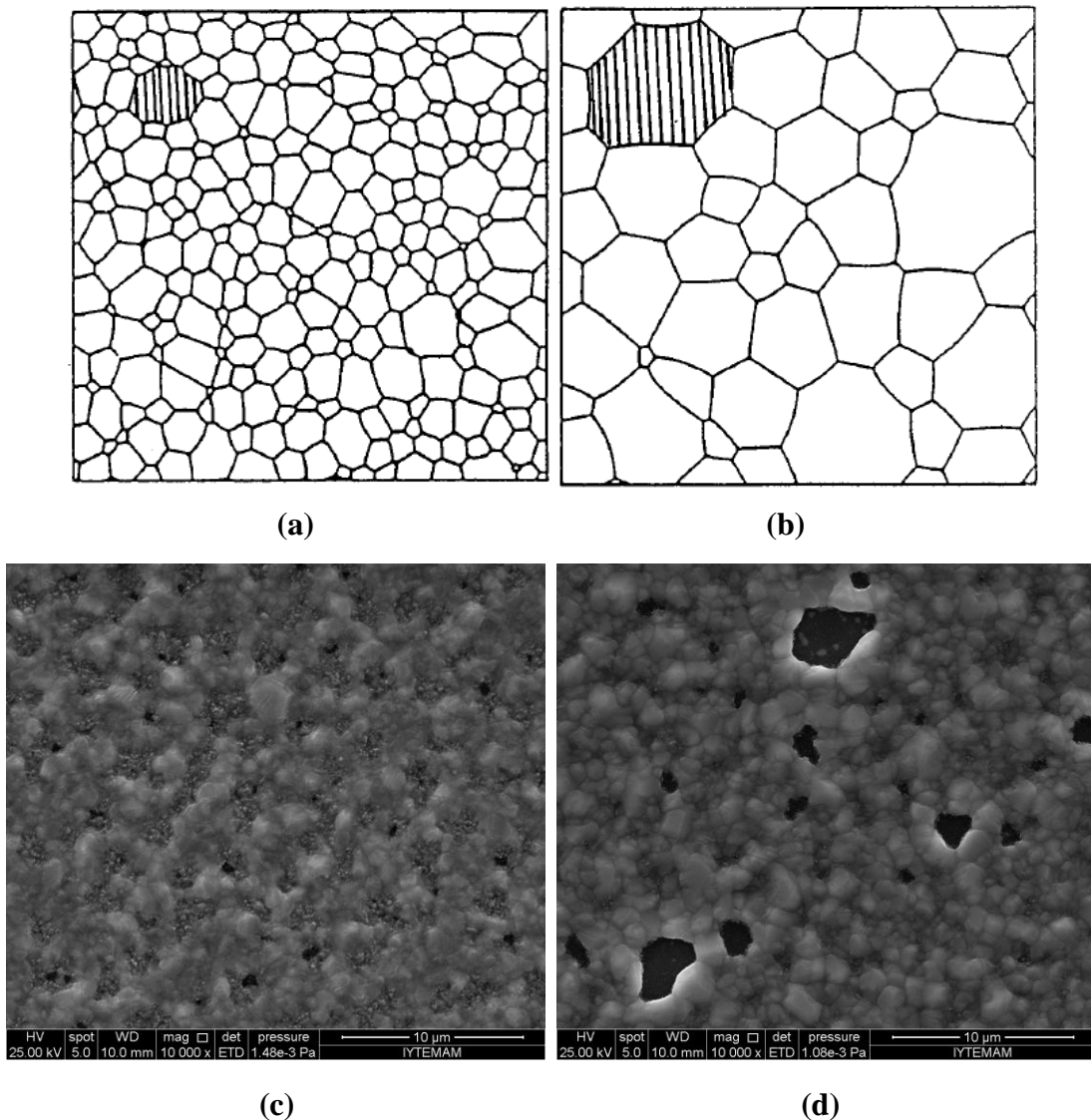


Figure 4.18. Top view of a normal grain growth. Large grains tend to grow larger and small grains tend to shrink and disappear; (a) and (b) [173]. Asgrown Ni15 sample (c), and annealed Ni15 sample during 60 minutes at 900 °C (d)

This procedure is known as Normal Grain Growth and valid for the case of  $2d < h$  where  $h$  is the film thickness. To relax the internal stress and to prevent the accumulation of crystallographic flaw, hillocks and holes are built during deposition and also bulk diffusion occurs [179]. It was seen that dewetting caused some holes on the deposited film (Figure 4.18). The grain boundaries on the side of the holes appear brighter; this means  $\gamma_{gb}$  excess energy per unit area of grain boundary is much more on

these sides (Figure 4.18). In ideal case, considering all boundaries have the same  $\gamma_{gb}$ , energy change with in-plane grain boundary motion and change in grain size by surface and boundary energy minimization is described by following [173]

$$\Delta F_{gb} = \gamma_{gb} \left( \frac{2}{d_0} - \frac{2}{d} \right)$$

The growth rate is  $d(d)/dt$  proportional to the average boundary energy per unit volume  $E = \beta\gamma_{gb}/d$ , where  $\beta$  is the geometric constant, and the portion is mobility of grain boundary motion  $M = M_0 \exp(-Q/kT)$  [155]. Considering slower thermal annealing favors the formation of crystalline Ni (111) grains with less grain boundaries for polycrystalline Ni samples [3], in this work slow annealing rate of 28 °C/min performed for all experiments.

Grain sizes increases with annealing time. After a certain time, grain growth saturates. In this work all annealing processes were performed during 60 minutes. However, for some samples annealing was carried out also in 30 minutes, but XRD measurements showed us 60 minutes annealing makes better crystallinity of Ni (111). Besides the annealing time, as mentioned film thickness affects the grain sizes during annealing, when growing grain sizes reach the value about  $h$ , growth slows and finally stop. There are some slowdown mechanisms. One of them is thermal grooves which causes the pinning of grain boundaries (Figure 4.19 (c)) [155]. Grain sides composed from finite curvatures which can be considered arcs of circles (Figure 4.19 (b)). These arcs can be considered as equator sides of a catenoid. There is relation between film thickness  $h$  and the curvature radius  $r$ , so the grain sizes, as following [155]

$$\theta = \frac{h}{2r}$$

where the angle  $\theta$  at grooves with respect to the surface normal. Formation of grooves depends on grain boundary surface tension. Under the critical angle  $\theta_0$ , boundaries move by increasing their length and area, contrarily, above the critical angle  $\theta_0$ , boundaries move without pinning from the groove. Thus, growth stops when grain curvature radius exceeds the value of  $h/2\theta_c$ . Grain size and thickness relation of the samples will give in next section.

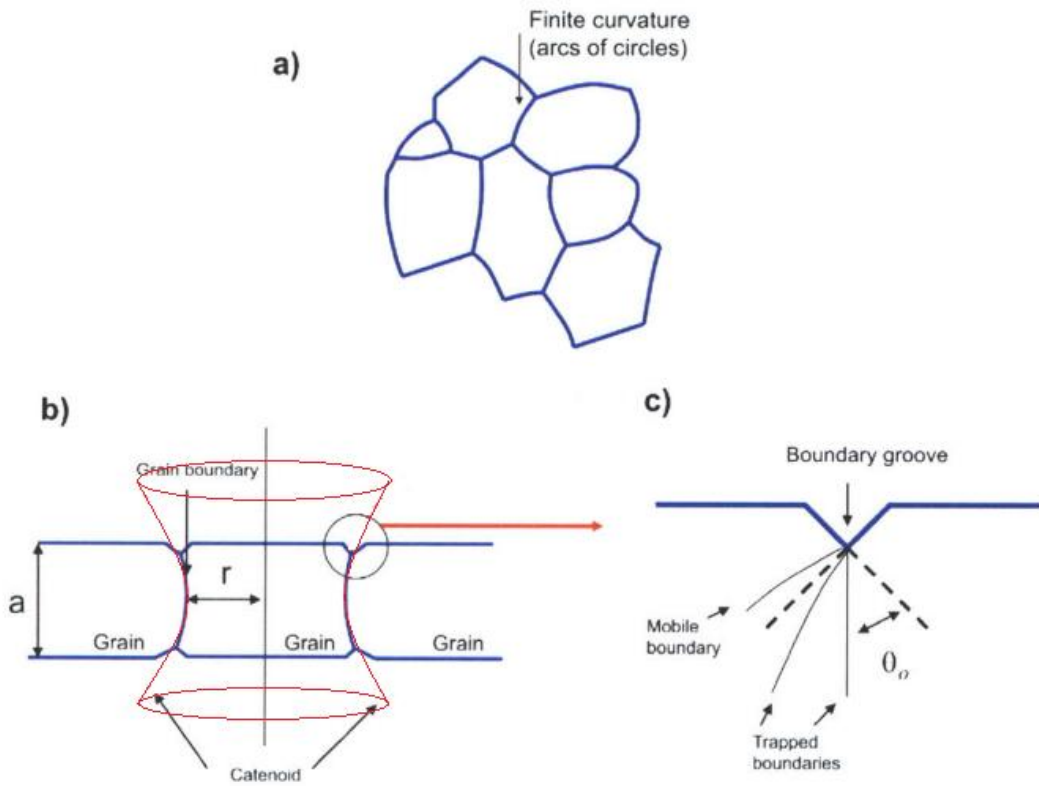


Figure 4.19. Schematic representations of grains. (a) top view of finite curvatures, (b) cross sectional view of grain boundaries like arcs of circles and catenoid like shape of curvatures (c) cross sectional view of a groove [155]

To reduce the boundary area and dewetting of Ni film we inspired from previous study on CNT growth by CVD [180] and we deposited Nickel catalyst thin films on to Si/SiO<sub>2</sub>/Al<sub>2</sub>O<sub>3</sub> substrates by magnetron sputtering. Alumina (Al<sub>2</sub>O<sub>3</sub>) is an electrical insulator, porous material, it has high thermal conductivity and generally better than SiO<sub>2</sub> as a support layer for hydrocarbon CVD process [181]. It prevents the interaction between substrate by forming metal silicide between substrate and the catalyst metal particles [182]. Metal on buffer layer has much less mobility [180]. Al<sub>2</sub>O<sub>3</sub> buffer gave better results for density of CNTs on the surface of samples. Porous feature is important to grow vertical carbon nanotubes. However, in this study, to improve the crystal quality of Ni (111), prevent dewetting by decreasing mobility of Ni and obtain smoother surfaces thin Al<sub>2</sub>O<sub>3</sub> layer should be deposited because of its porous structure. The interfacial stoichiometry and the interfacial energy on the interface between Al<sub>2</sub>O<sub>3</sub> and Ni have important role on dewetting [183]. In this study, the effect on Ni film structure of buffer layer, and its indirect effect on grown graphene were observed. Besides metal/oxide structure, we used Chromium buffer layer as metal/metal structure. Cr is

also a transition metal with electron configuration of  $1s^2, 2s^2, 2p^6, 3s^2, 3p^6, 3d^5, 4s^1$ . The 3d orbital is actually half filled and stable. However, the electron configuration of Ni ends with  $3d^8 4s^2$ , so 4s sub shell is filled first rather than the 3d sub shell. 4s is lower energy level than 3d. Ni is un-filled and un-stable, more effective to form cluster due to internal forces when excess energy increased. Thus, in this study, Cr was used as adhesive layer to decrease the effect of dewetting.

#### 4.4. XRD Results

During annealing the system tends to minimize its energy to become equilibrium and grain growth. In fcc lattice of Ni, (111) orientation has the lowest surface energy, because it is the closest packed face. However, related to excess energy, which depends on deposition conditions system can be textured in different directions. XRD  $\theta - 2\theta$  measurement results were analyzed by regarding calculated characteristic Ni  $2\theta$  peak positions, which were given in Table 3.1, and FWHM values of the peaks. Also, X-Pert HighScore Peak Search software was used to analyze the results of XRD measurements by comparing the Powder Diffraction File (PDF) is a database of X-ray powder diffraction patterns maintained by the International Center for Diffraction Data (ICDD).

Before examining the crystal structure of Ni films, to consider as background, XRD  $\theta - 2\theta$  measurement results of two different  $\text{SiO}_2$  substrates are shown in Figure 4.20. Some XRD  $\theta - 2\theta$  measurement results of Ni films had the characteristic peaks of  $\text{SiO}_2$ , due to their thickness and dewetting of Ni by annealing process. Thinner films or some samples, which were under the effect of dewetting, had more intense  $\text{SiO}_2$  peaks than the thicker films, because the incident angle of X-ray is about  $15^\circ$ .

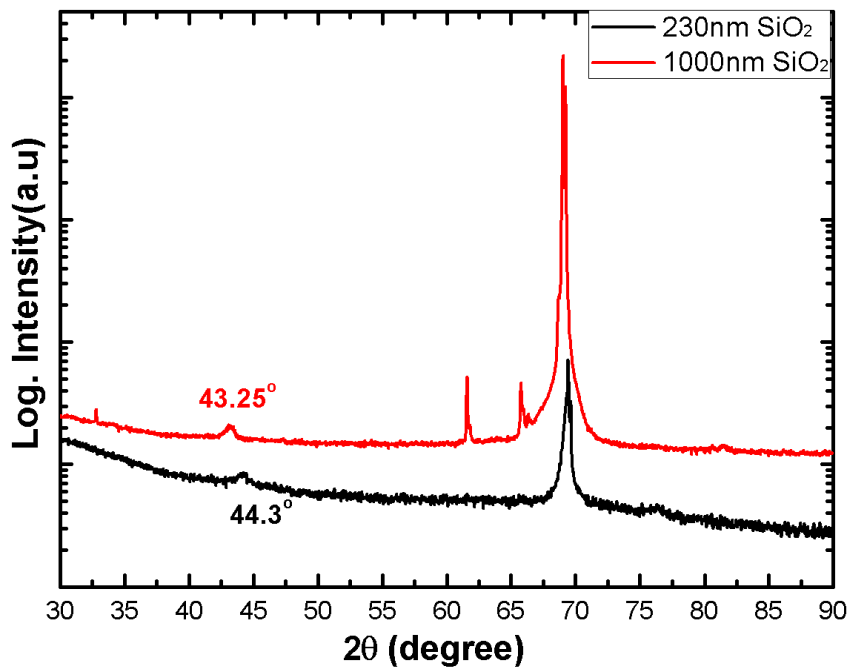


Figure 4.20. XRD  $\theta$  -  $2\theta$  measurements for 230 nm thick SiO<sub>2</sub> and 1μm thick SiO<sub>2</sub>

According to XRD  $\theta$  -  $2\theta$  measurement of two substrate (Figure 4.20), for 1μm thick substrate there are lots of peaks, for 230 nm thick substrate there are three peaks which are correspond to K<sub>β</sub> (0.139 nm), K<sub>α1</sub> (0.1540 nm), K<sub>α2</sub> (0.1544 nm), L<sub>α</sub> (1.333 nm), L<sub>β</sub> (1.304 nm). The most important peaks are at  $2\theta=43.25^\circ$  for red line, and  $2\theta=44.3^\circ$  for black line, because these two peaks are very close to characteristic Ni (111) peak position at  $2\theta=44.5^\circ$  and NiO peak is at  $2\theta=43.3^\circ$ . Their contributions were regarded when analyzing XRD  $\theta$  -  $2\theta$  measurement results of all Ni films.

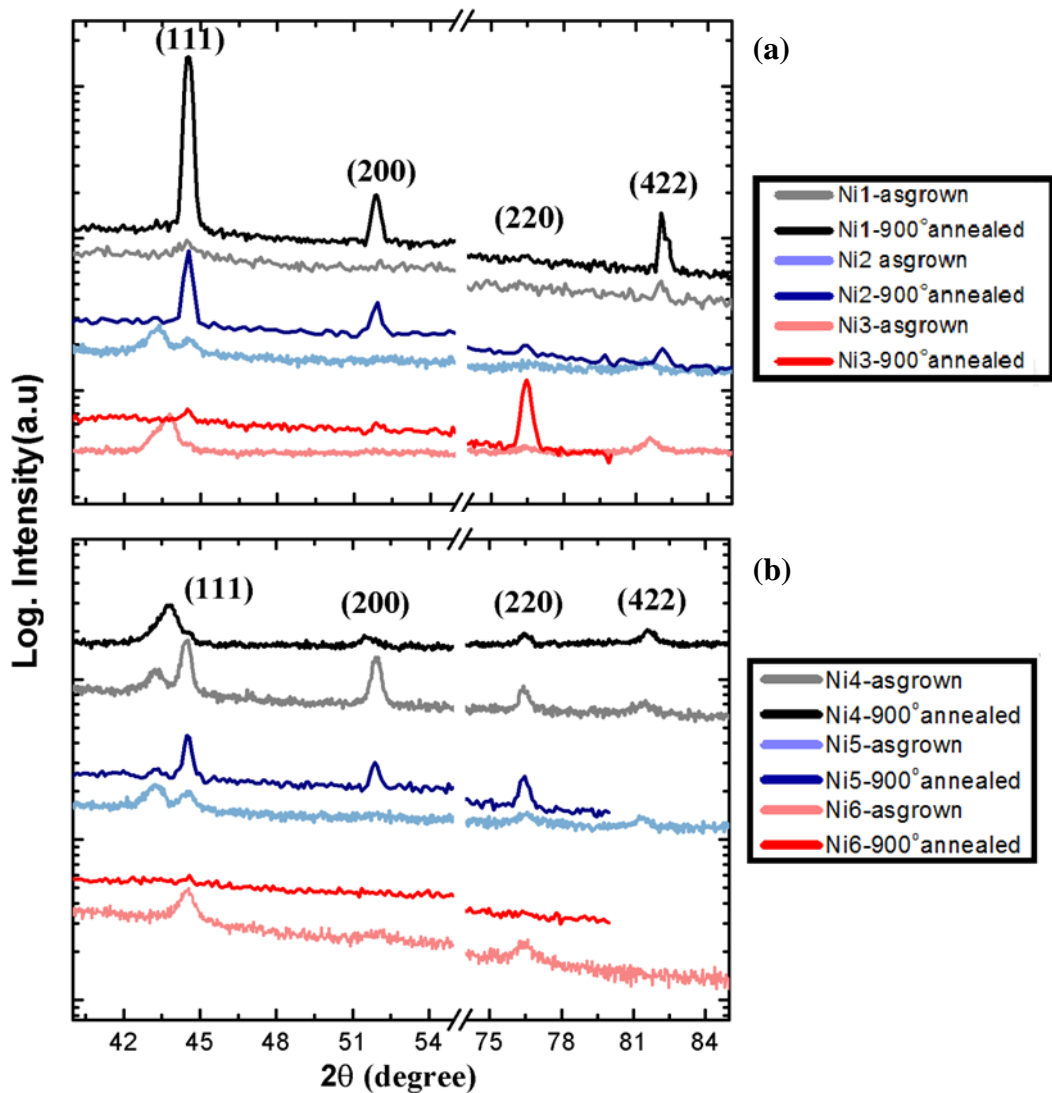


Figure 4.21. XRD  $\theta$  -  $2\theta$  measurement results for Ni1, Ni2 and Ni3 samples (a), and Ni4, Ni5, Ni6 samples (b) with both asgrown (light lines) and annealed at 900 °C (dark lines) cases

For all Ni1-6 films, 1 $\mu$ m thick SiO<sub>2</sub> substrates were used. Thus, there was a little contribution from substrate at  $2\theta=43.25^\circ$  for all XRD results (Figure 4.21). However, considering the shifting of the peak positions and arising intensity it can be concluded that there was also contribution from NiO which has the peak at  $2\theta=43.3^\circ$ . As seen from Figure 4.21, all of the asgrown samples are grown along the [111] direction and nearly well-defined (111) peak appears at  $2\theta=44.5^\circ$ . When these samples were annealed at 900 °C, intensity of (111) peak of Ni1-2-5 samples increased, significantly. The other films preserved their polycrystalline structures. To texture in (111) direction of the film, power and thickness should be low as soon as possible.

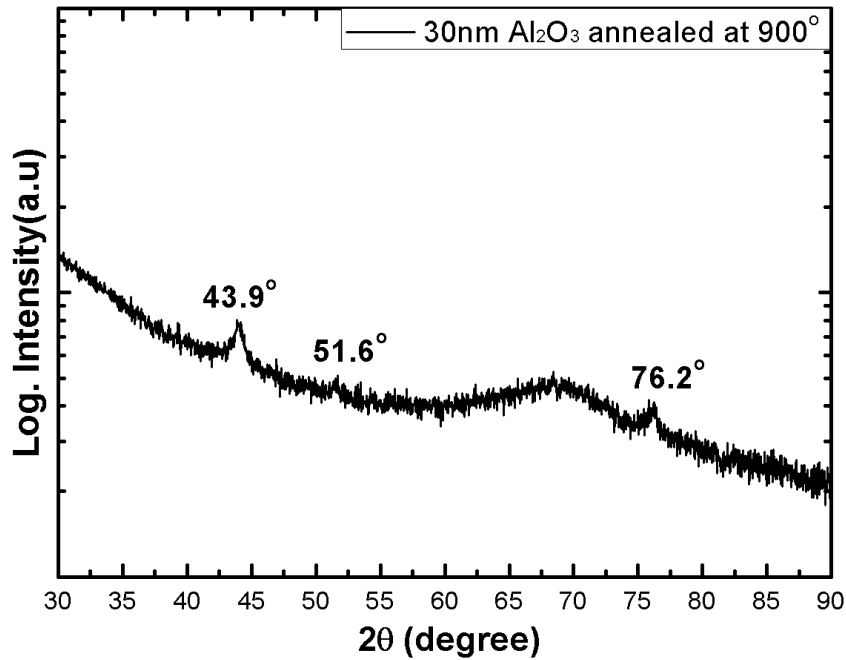


Figure 4.22. XRD  $\theta$  -  $2\theta$  measurement result of  $\text{Al}_2\text{O}_3$  film annealed at  $900^\circ \text{C}$

Ni7, Ni8, Ni9 and Ni10 samples were deposited with  $\text{Al}_2\text{O}_3$  buffer layer. Annealing of the films caused dewetting of the Ni particles, so XRD results of these annealed films involved more  $\text{Al}_2\text{O}_3$  peaks than asgrown films. To consider as background for analyzing XRD  $\theta$  -  $2\theta$  measurement results of buffered films, Figure 4.22 shows the XRD  $\theta$  -  $2\theta$  result of  $\text{Al}_2\text{O}_3$  film annealed at  $900^\circ \text{C}$ . There are three main peaks and all of them are close to characteristic Ni film peaks (Figure 4.22).

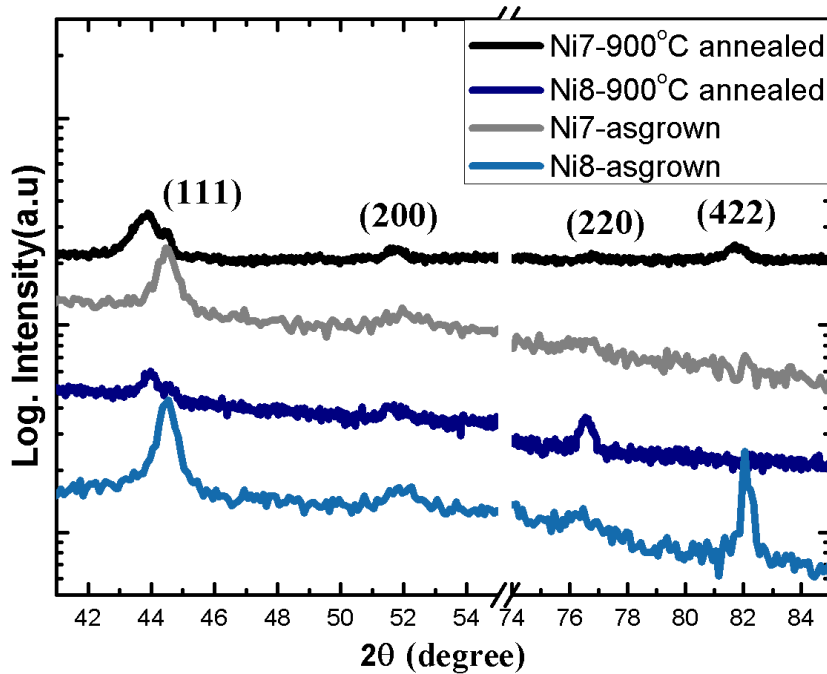


Figure 4.23. XRD  $\theta$  -  $2\theta$  measurement results for Ni7 and Ni8 samples with both asgrown and annealed at 900 °C cases

In Figure 4.23, the light lines refer to asgrown and the dark ones annealed at 900 °C cases of Ni7 and Ni8 films. Ni (111) peak is at  $44.5^\circ$  and the second peaks of annealed samples are at  $43.9^\circ$  refer to  $\text{Al}_2\text{O}_3$  (Figure 4.23). Also, around Ni (200) peak and (220) peak there are  $\text{Al}_2\text{O}_3$  peaks. It was difficult to decide which crystal system these  $\text{Al}_2\text{O}_3$  peaks belong, because there are lots of peaks which already close to cubic Nickel peaks. The interference of two or three characteristic peaks made so broaden XRD peaks. To calculate the grain sizes these peaks were fitted by considering the contributions of substrates and  $\text{NiO}$  as well. In Figure 4.30, calculation of peak position is shown for Ni7 sample. And for all samples this calculation was performed in detail. Ni (111) peak was more intense in XRD result of annealed Ni7 film. This means the thinner buffer was more effective to increase (111) orientation of Ni film.

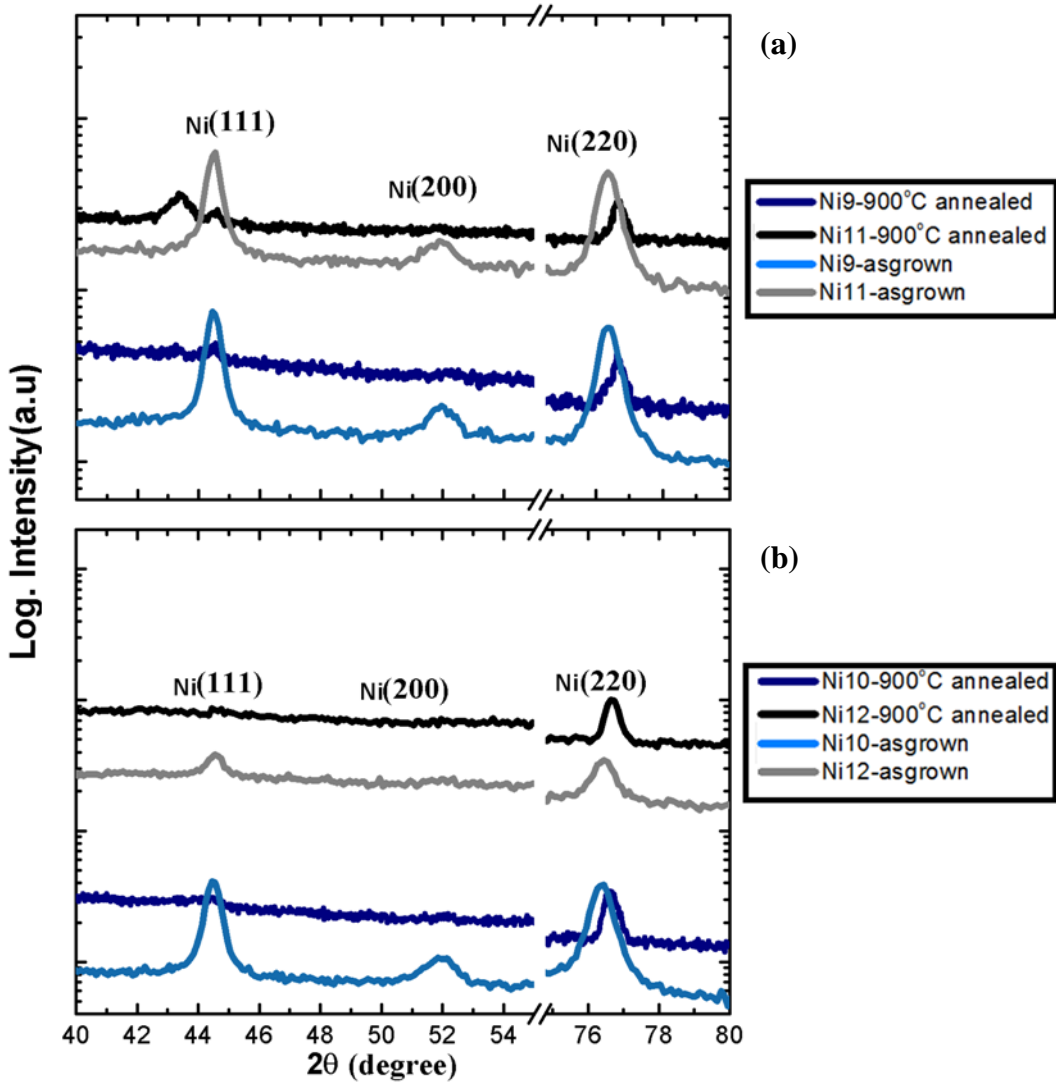


Figure 4.24. XRD  $\theta$  -  $2\theta$  measurement results for Ni9 and Ni11 (a), and Ni10 and Ni12 (b) samples with both asgrown and annealed at 900 °C cases

230 nm  $\text{SiO}_2$  film was used as substrate for Ni9 and Ni11 films, whereas for Ni10 and Ni12 1 $\mu\text{m}$  thick  $\text{SiO}_2$  was used (Figure 4.24 and Table 4.3). The thicker  $\text{SiO}_2$  substrate made the crystal go toward more crystallinity. Ni9 and Ni10 samples had  $\text{Al}_2\text{O}_3$  buffer layer shown in blue lines, but Ni11 and Ni12 films were non-buffered films shown in black lines (Figure 4.24). Annealed Ni11 was a good example to see NiO peak, because it had no buffer layer, and congruently the second peak at 43.3° refers to just NiO. Asgrown films had polycrystalline structure, and annealing increased texturing in the (220) direction mostly for all four samples, so crystal structure changed. There was also up shifting of the peak positions due to annealing. The reason of this situation was not NiO, because NiO peak at  $2\theta = 75.6^\circ$ . Ni9, Ni10, Ni11 and Ni12

samples were ~400 nm thick. The amount of shift and broadening of the peaks show the degree of the strain. The strain was calculated by the formula

$$\varepsilon = \frac{\beta}{4 \tan \theta}$$

where  $\beta$  is the full width of diffraction peak at half of the maximum intensity and  $\theta$  is Bragg's angle. According to the formula shifting can be observe more obvious to the higher Bragg's angle values.

Strain caused by energy accumulations due to mismatch between film and substrate. Increasing thickness means extra energy released by the formation of lattice defects. Annealing also gives extra energy to the system and this energy was assumed to release by stretching of the cubic lattice parameter of the FCC structure. This case corresponds to orthorhombic crystal structure. So, strain was reduced by releasing extra energy. The same effect was also assumed to be the increase in grain size. It was seen that increasing thickness caused decreasing of strain in the films by decreasing lattice constant. This strain reducing by annealing was 52% and 38% for Ni9 and Ni10; 44% and 31% for Ni11 and Ni12, respectively. As result,  $\text{Al}_2\text{O}_3$  buffer was more effective to reduce strain.

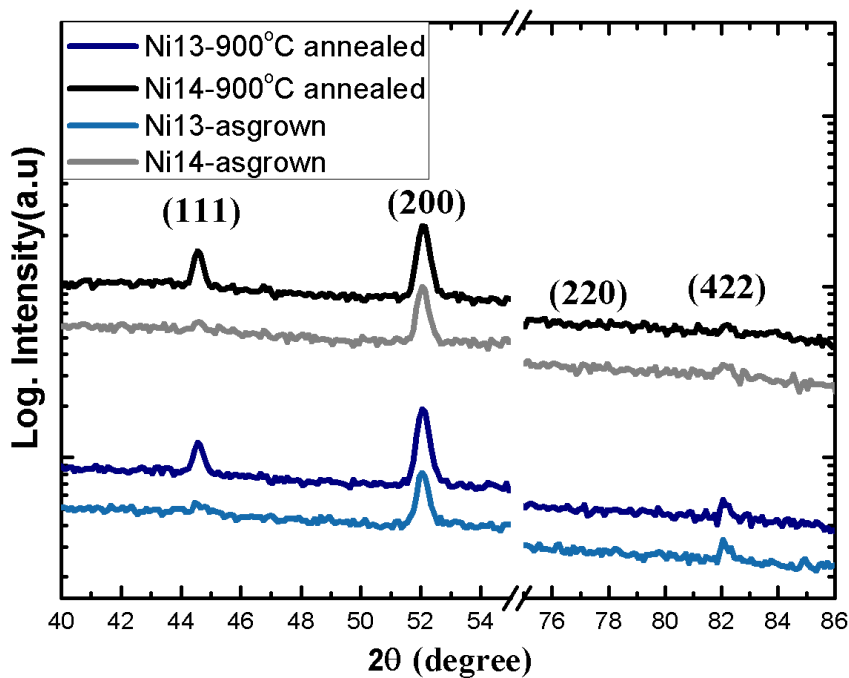


Figure 4.25. XRD  $\theta$  -  $2\theta$  measurement results for Ni13 and Ni14 films with both asgrown and annealed at 900 °C cases

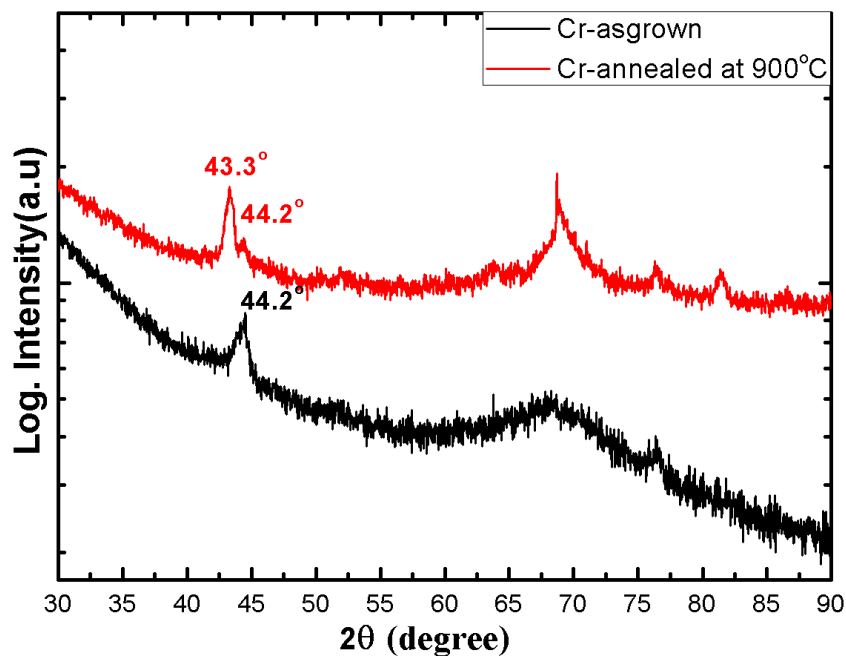


Figure 4.26. XRD  $\theta$  -  $2\theta$  measurement results of 30 nm thick Cr film; asgrown (black line) and annealed at 900 °C (red line) cases

Ni13 and Ni14 deposition were performed by heating the substrate to 450 °C, and this caused mostly texturing in (200) direction of the film, which was completely separate from non-heated deposited films. Also, there was no considerable effect of thin or thick SiO<sub>2</sub> substrate on crystallinity of deposited Ni films.

Characteristic Cr peak is at  $2\theta=44.2^\circ$  (Figure 4.26). When the film annealed at 900 °C, the contribution of Cr substrate was observed on XRD spectrum.

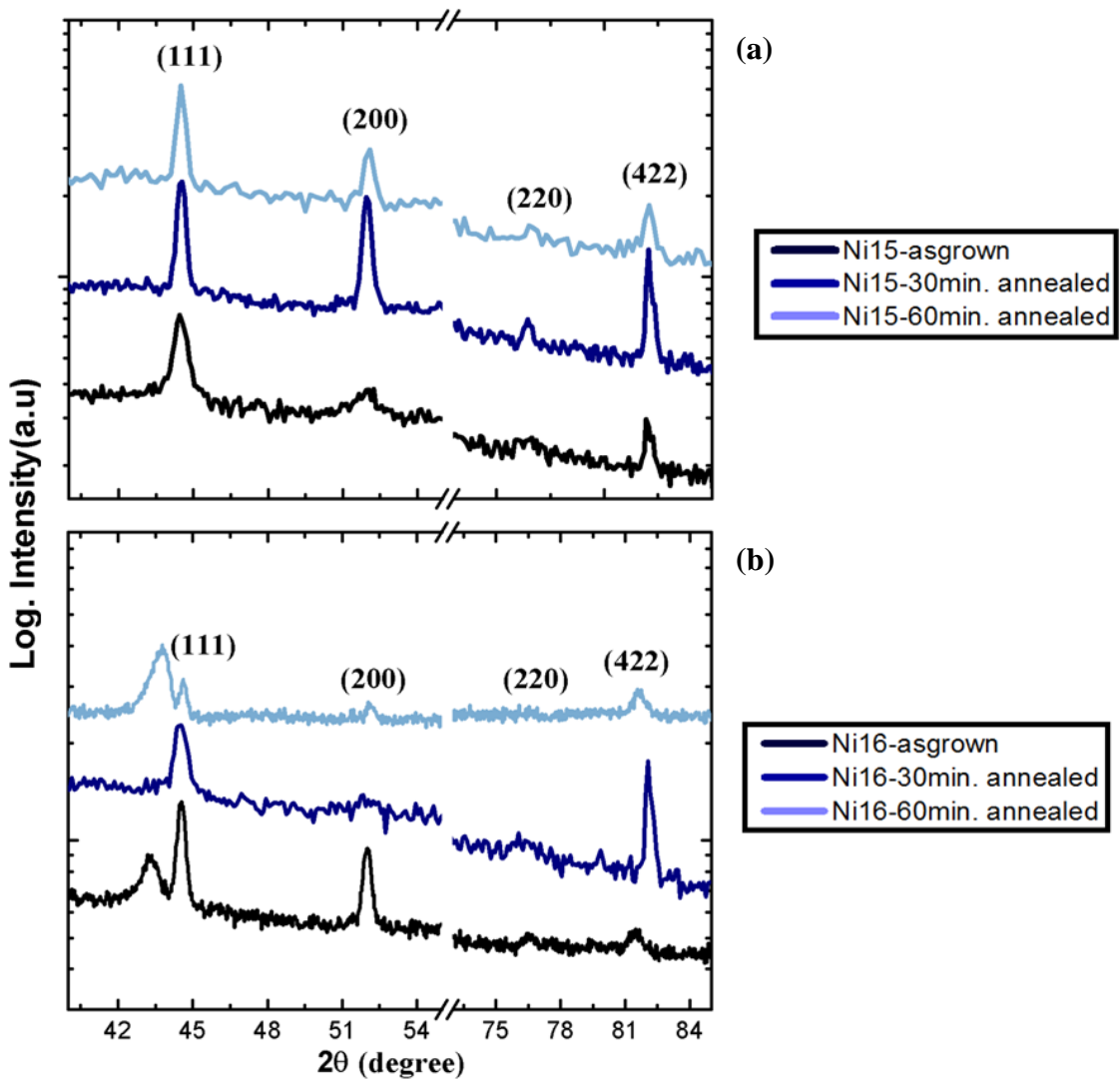


Figure 4.27. XRD  $\theta$  -  $2\theta$  measurement results for Ni15 (a) and Ni16 (b); asgrown and annealed at 900 °C during 30 minutes and 60 minutes

Asgrown Ni15-16-17-18 samples, which were deposited at higher pressure than Ni1-6 samples, had more intense formation of crystalline Ni (111) grains (Figure 4.27 and Figure 4.28). The structure of Ni15 was Si(500μm)/ SiO<sub>2</sub>(1μm)/ Cr(10nm)/ Al<sub>2</sub>O<sub>3</sub>(40nm)/ Ni(400nm) and it was un-heated deposited case of Ni16 film (Table 4.4). The structure of Ni17 was Si(500μm)/ SiO<sub>2</sub>(1μm)/ Cr(10nm)/ Ni(400nm) and it was un-heated deposited case of Ni18 film (Table 4.4). Ni16 (Figure 4.27 (b)) and Ni18 (Figure 4.28 (b)) were deposited by heating the substrate to 450 °C, so also (200) direction textured in asgrown films more than un-heated deposited films. This observation was compatible with Ni13 and Ni14 films which were also deposited by heating the substrate. But, non-buffered Ni13 and Ni14 films had no more intense (111)

peaks by contrast with Ni16 and Ni18 films. So, only Cr buffer could not prevent the effect of heating on texturing in (200) direction (Figure 4.28 (b)).

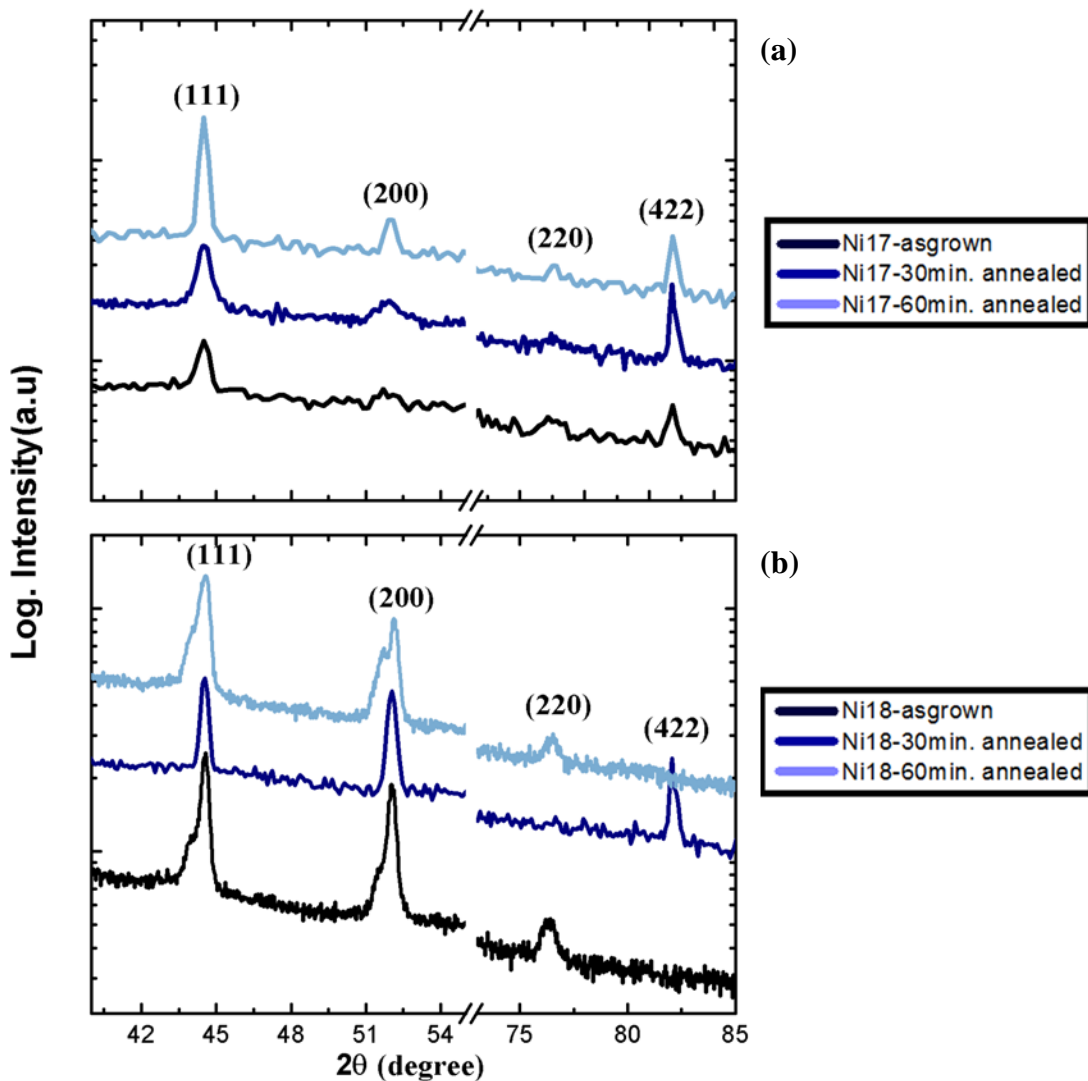


Figure 4.28. XRD  $\theta$  -  $2\theta$  measurement results for Ni17 (a) and Ni18 (b); asgrown and annealed at 900 °C during 30 minutes and 60 minutes

However, when annealing was performed during 60 minutes, Cr buffer prevented texturing in (200) direction, and the XRD peak intensity of (111) direction was more than (200) by contrast with Ni13 and Ni14 films (Figure 4.27 (b) and Figure 4.28 (b)). When Ni7-10 films with Ni15-18 films were compared the effect of Cr adhesive layer was more than Al<sub>2</sub>O<sub>3</sub> buffer layer on direction of the crystal.

Buffer and adhesive layers affected the formation of (111) direction comparing with Ni9 and Ni10 films which had just Al<sub>2</sub>O<sub>3</sub> buffer, and with Ni11 and Ni12 films

which were non-buffered samples. Annealed Ni9-12 films textured in (220) direction, but Ni15-18 were in (111) direction mostly.

For un-heated deposited films, 30 min annealing increased the polycrystalline quality in all directions (Figure 4.27 and Figure 4.28 (a)). So, increasing annealing time allowed obtaining mostly texturing in (111) direction which is more suitable to grow graphene on it.

#### 4.4.1. Calculation of Ni (111) Grain Sizes

Average grain sizes of the crystallites in (111) directions were calculated via X-Pert HighScore software and also Origin Data Analysis and Graphing software by Scherer's formula:

$$\tau = \frac{K\lambda}{B \cos \theta}$$

Figure 4.29 (a) shows the calculated profile of asgrown Ni1 film, which had not buffer layer, by Origin Data Analysis and Graphing software. The asgrown Ni1 film has fcc structure, it grows along the [111] direction and a well-defined (111) peak appears at  $2\theta=44.5^\circ$ . In Figure 4.29 (a) background was subtracted to fit correctly due to the noisy experimental profile. The characteristic peak of Ni (111) was at  $2\theta=44.52^\circ$  with FWHM of  $0.78^\circ$  and the calculated average grain size of Ni (111) was 22 nm which was also compatible with the calculated grain size by X-Pert HighScore Peak Search software. After annealing the sample at  $900^\circ\text{C}$  grain size increased to 59 nm.

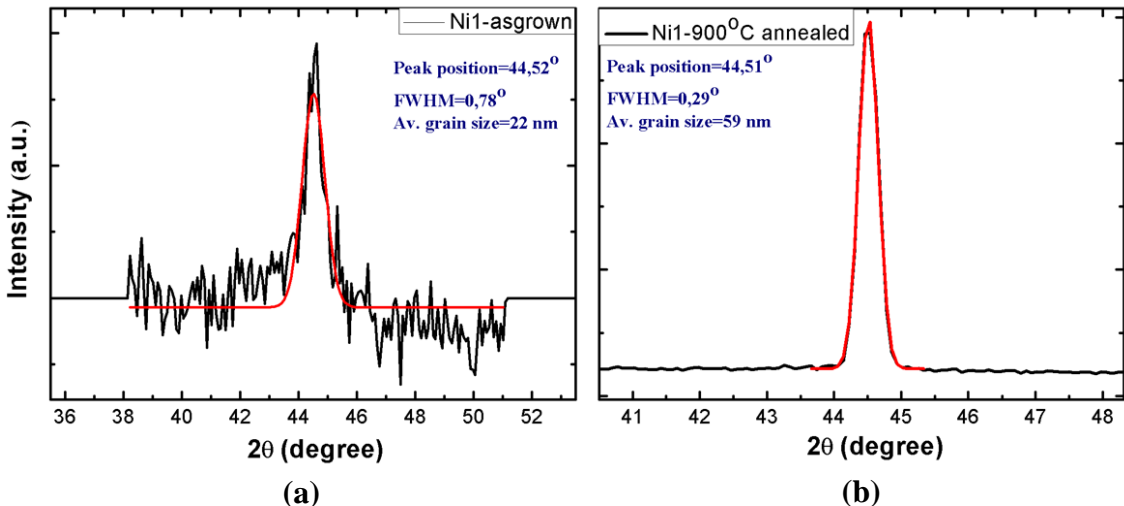


Figure 4.29. Fitted XRD peak of asgrown (a) and annealed at 900 °C (b) Ni1 films by Origin Data Analysis and Graphing software. Red lines refer to calculated profile and the background was subtracted

Figure 4.30 (a, b) show calculated profile of asgrown Ni7 film, which had Al<sub>2</sub>O<sub>3</sub> buffer layer, by X-Pert HighScore Peak Search software and Origin Data Analysis and Graphing software, respectively. Figure 4.30 (c, d) belong to annealed at 900 °C case. As seen from Figure 4.30 (c), there is distortion on the left side of the peak. The reason for this could be that oxidized of the film due to XRD measurement of this sample could not perform right after the annealing. Hence, the shapes of peaks which had distortions were explained considering all factors, such as oxidization, substrate and buffer layers. The incident angle was enough to get information from buffer layer and even substrate. All XRD  $\theta$ - $2\theta$  scans were analyzed by fitting of the peaks, to be sure about about grain sizes of Ni films.

In Figure 4.30 (b), vertical green line refers to cubic NiO (200). Ni7 film has Al<sub>2</sub>O<sub>3</sub> buffer layer which has  $2\theta$  peak around 43-44° as well, and congruent 43.9°. Also, dewetting of Ni particles by annealing caused X-ray more exposed to Al<sub>2</sub>O<sub>3</sub> buffer and SiO<sub>2</sub> substrate than asgrown case. The vertical purple lines refer to rhombohedral Al<sub>2</sub>O<sub>3</sub> (113). There are lots of calculated peaks of various types Al<sub>2</sub>O<sub>3</sub> crystal structure very close to purple line at  $2\theta=43.9^\circ$ . So, there were more than a few Al<sub>2</sub>O<sub>3</sub> crystal structures on the surface. Characteristic peak of Ni (111) at  $2\theta=44.5^\circ$  congruent cubic Ni (111) shown by coincident vertical red lines. NiO peak was at  $2\theta=44.3^\circ$ .

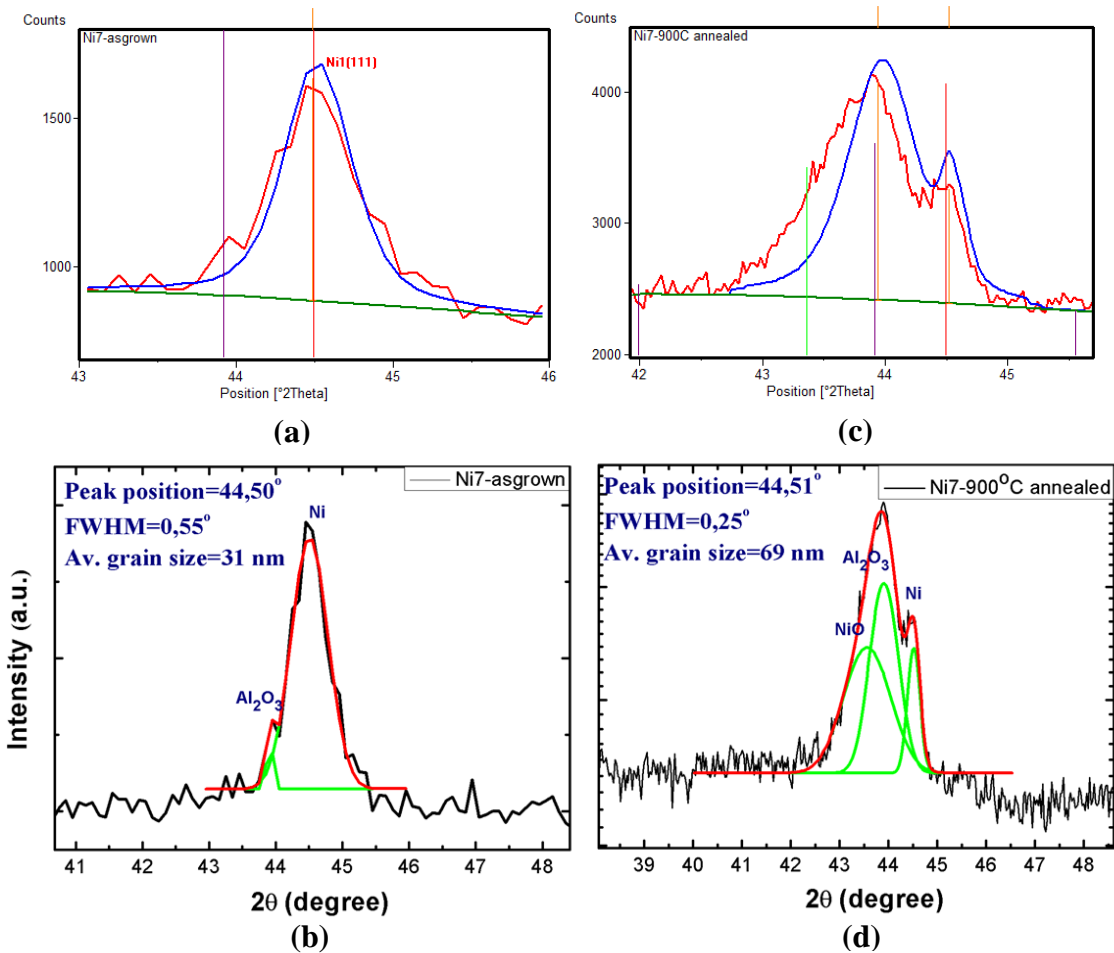


Figure 4.30. Fitted XRD  $\theta$  -  $2\theta$  measurement results of asgrown (a, b) and annealed Ni7 sample (c, d). Their potential NiO and  $\text{Al}_2\text{O}_3$  peaks calculated by X-Pert HighScore peak search software (a, c). Blue line refers to calculated profile and green line is background. Their potential NiO and  $\text{Al}_2\text{O}_3$  peaks calculated by origin data analysis and graphing software (a, c)

Figure 4.30 (c) and (d) show that experimental and Lorentzian fitted profile around  $2\theta=44^\circ$  and calculated peak positions, FWHM and average grain size of Ni (111) by Origin Data Analysis and Graphing software. Experimental profile of asgrown film was quite noisy unlike annealed film, so qualities of fits ( $R^2$ ) were 0.991 and 0.999, respectively. (111) direction  $2\theta$  position of asgrown Ni7 film was at  $2\theta=44.50^\circ$  with  $0.55^\circ$  FWHM and the calculated average grain size was 31 nm.  $2\theta$  position of annealed sample was at  $2\theta=44.51^\circ$  with 0.25 FWHM, and average grain size of Ni (111) was 69 nm by this method.

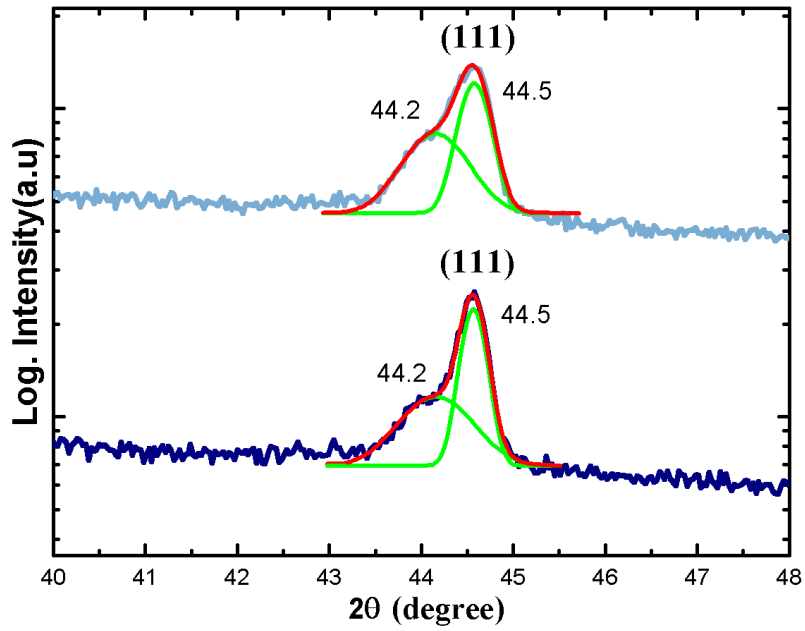


Figure 4.31. Fitted XRD  $\theta$  -  $2\theta$  measurements of Ni18 film. The dark blue line indicates asgrown Ni18 film, the light blue line indicates annealed at 900 °C during 60 minutes of Ni18 film.

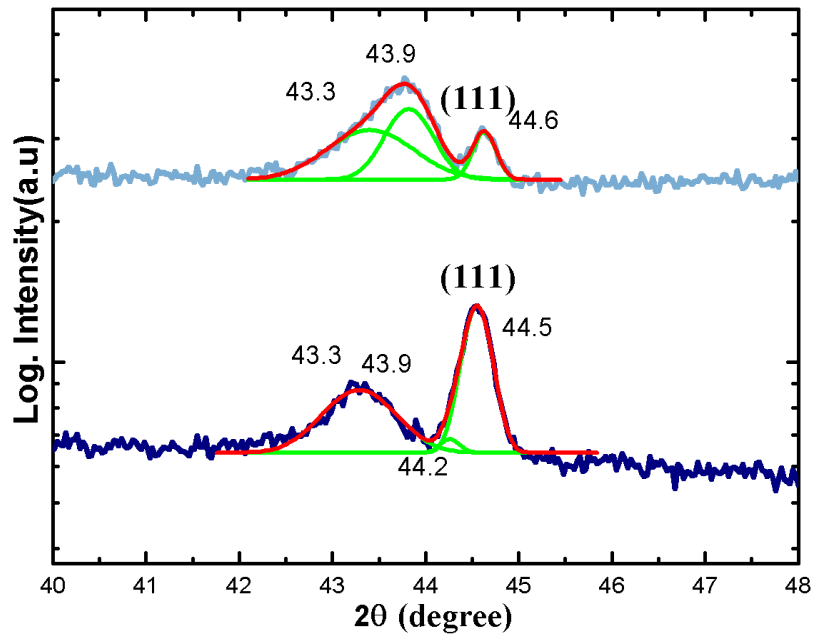


Figure 4.32. Fitted XRD  $\theta$  -  $2\theta$  measurements of Ni16 film. The dark blue line indicates asgrown Ni16 film, the light blue line indicates annealed at 900 °C during 60 minutes of Ni16 film.

XRD  $\theta$  -  $2\theta$  measurement results of Ni18 film, which has 10 nm thick Cr adhesive layer, were analyzed by fitting the two of Ni (111) peak at  $2\theta=44.5^\circ$  and Cr (110) peak at  $2\theta=44.2^\circ$  (Figure 4.31).

Figure 4.31, Cr (110) peak is at  $2\theta=44.2^\circ$ . However, for Ni15 and Ni16 films the intensity of  $\text{Al}_2\text{O}_3$  peaks are dominant than Cr peaks. Also, as mentioned before  $\text{SiO}_2$  substrate had a peak at  $2\theta=43.25^\circ$  besides NiO. All calculated grain sizes of Ni (111) are shown in Figure 4.33.

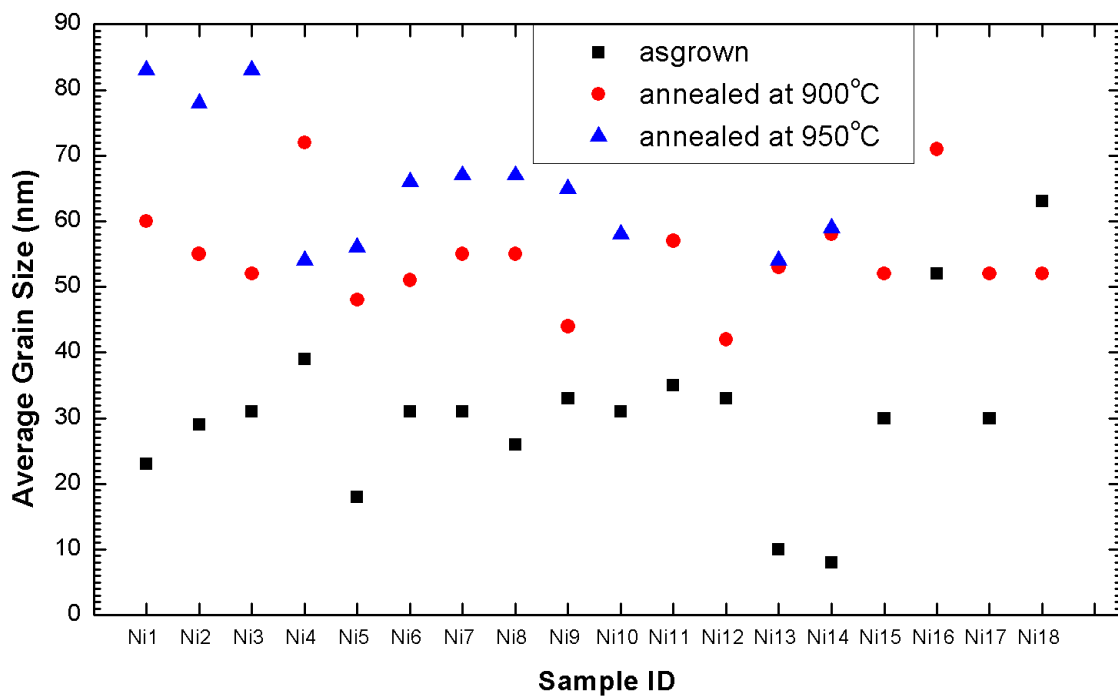


Figure 4.33. Calculated grain sizes of Ni (111) for all samples

Denser graphene grows on Ni thin film which has bigger Ni (111) grains. Graphene growth temperature, which is exactly same with annealing temperature, is important for grain size as deposition conditions of the film. Among Ni1-6 samples, asgrown and annealed at 900 °C Ni4 samples had bigger (111) grains, which was the thickest film deposited at 3.0 mTorr pressure (Table 4.2). On the other hand, annealed at 950 °C Ni4 sample had smaller (111) grains. This means that increasing temperature caused excess energy that led to change of the film structure. Between Ni7 and Ni8 samples, there was no such obvious difference, but again it can be concluded that from asgrown grain sizes the thinner buffer was better for crystallinity of the film. For Ni9 and Ni10 films, that had  $\text{Al}_2\text{O}_3$  buffer and 400 nm thick Ni films, increasing

temperature gave the better grain sizes unlike non-buffered films of Ni11 and Ni12. Ni13 and Ni14 films, were deposited by heating the substrate to 450 °C, had obviously (200) direction, but they had also (111) grains which can be limitedly growing by temperature.

#### 4.5. AFM and SEM Results

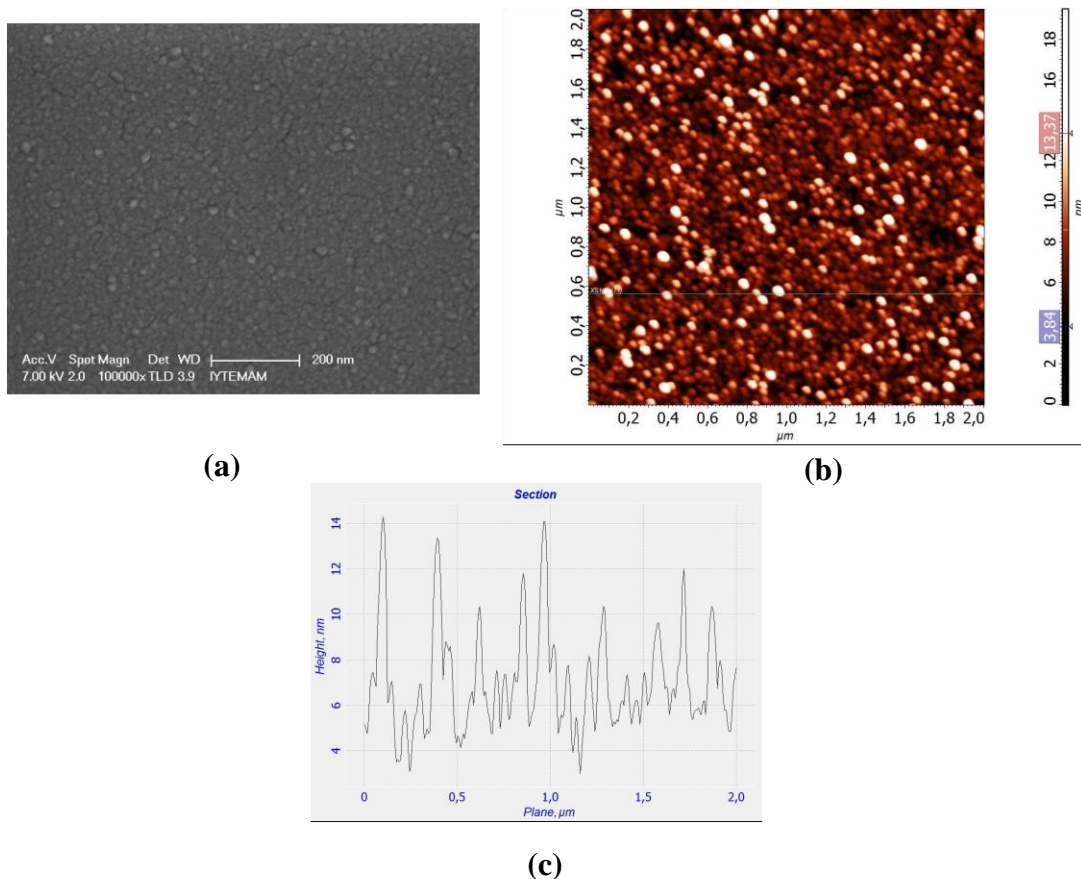


Figure 4.34. SEM micrograph (a), AFM topographic image (b), and 1 dimensional grain analysis of the line on topographic image (c) of asgrown Ni1 film

SEM micrographs of asgrown (Figure 4.34 (a)) and annealed at 900 °C Ni1 films (Figure 4.35 (a)) were in conformity with AFM topographic images (Figure 4.34 and Figure 4.35 (b)). The polycrystalline Ni surface acquired a multigrain-like appearance after thermal annealing. Grain sizes were grown by annealing and due to the effect of dewetting larger particles formed on the surface.

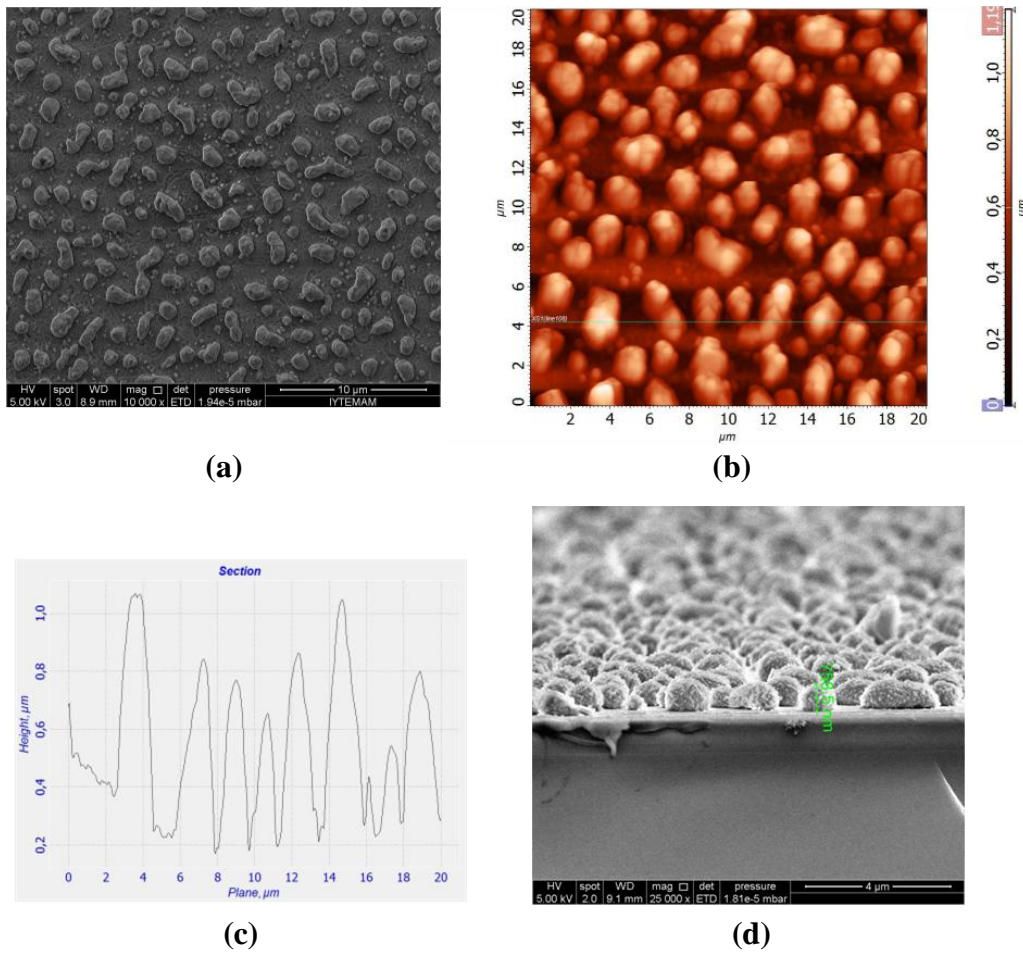
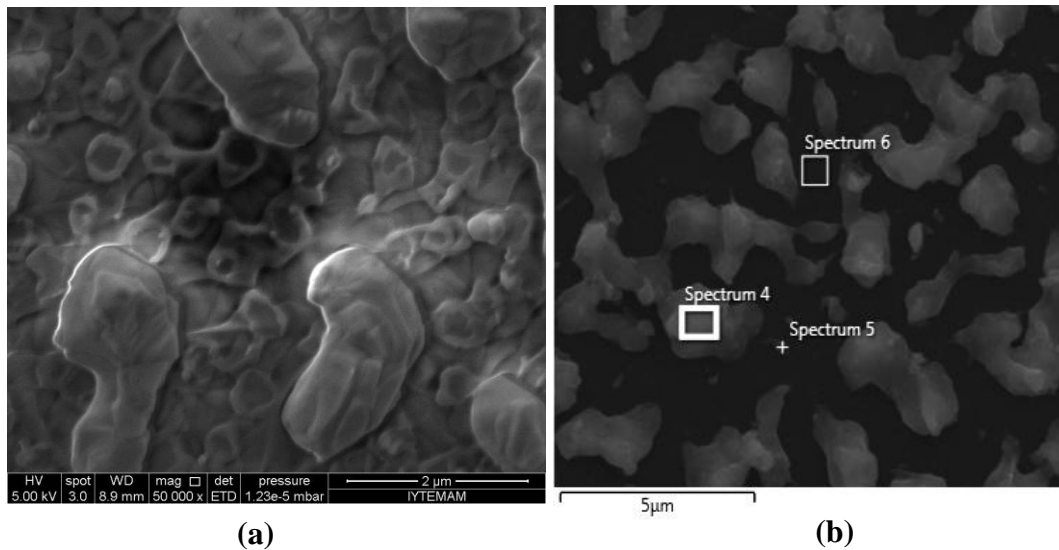


Figure 4.35. SEM micrograph (a), AFM topographic image (b), 1 dimensional grain analysis of the line on topographic image (c), and cross sectional SEM micrograph (d) of annealed Ni1 film at 900 °C

As understand from Figure 4.34 and Figure 4.35 (c), the height of the Ni particles raised by annealing about 67 times of asgrown case. However, this does not mean that grain sizes also increased in that way. The calculated average grain sizes, which had same direction, increased almost 2 times (Figure 4.33). To verify that also EDX measurement of the films were performed.



Element	Wt%	Atomic %	Oxide	Oxide %
<b>Spectrum 4</b>				
<b>O</b>	38.97	61.61		
<b>Si</b>	25.78	23.21	$\text{SiO}_2$	55.14
<b>Ni</b>	35.25	15.18	$\text{NiO}$	44.86
<b>Spectrum 5</b>				
<b>O</b>	52.96	66.58		
<b>Si</b>	46.31	33.17	$\text{SiO}_2$	99.08
<b>Ni</b>	0.73	0.25	$\text{NiO}$	0.92
<b>Spectrum 6</b>				
<b>O</b>	52.91	66.57		
<b>Si</b>	46.24	33.14	$\text{SiO}_2$	98.92
<b>Ni</b>	0.85	0.29	$\text{NiO}$	1.08
<b>Total:</b>	100.00	100.00		100.00

Figure 4.36. SEM micrographs of annealed Ni1 film at 900 °C (a-b). Spectrums show the regions that EDX performed and the table shows the percentage distributions of the elements.

As expected, larger grains are nickel particles (spectrum 4) and the ground is  $\text{SiO}_2$  with full of little Ni grains (spectrum 5 and 6). This was also explained why so sharp  $\text{SiO}_2$  peaks showed up in the XRD spectra (Figure 4.36). So, the first aim was deposition thicker and smoother Ni films to reduce the effect of dewetting and growth widely graphene on.

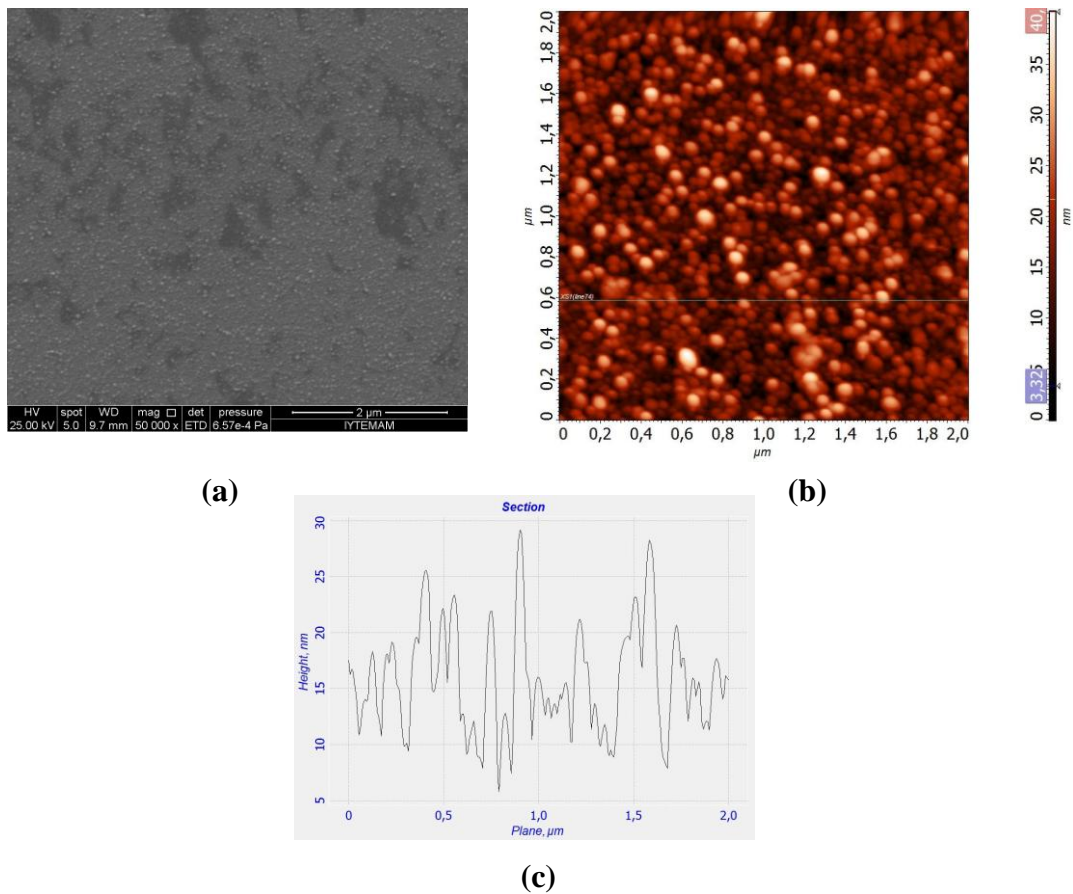


Figure 4.37. SEM micrograph (a), AFM topographic image (b), and 1 dimensional grain analysis of the line on topographic image (c) of asgrown Ni4 film

Among Ni1-6, Ni1 film was the thinnest and Ni4 film was the thickest ones. For both of asgrown and annealed cases, if film thickness increased the mean Z (mean height of the Ni particles) and surface roughness (RMS) increased (Figure 4.37 and 4.38).

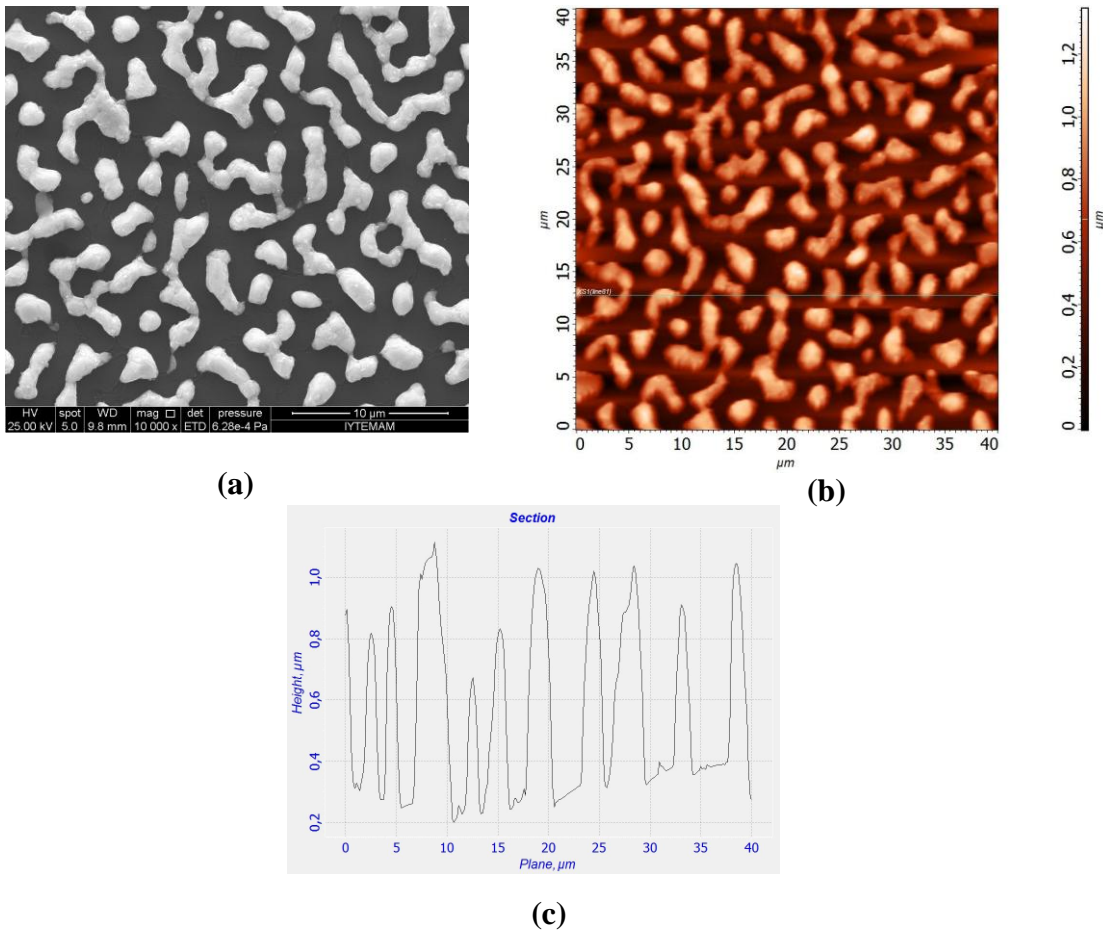


Figure 4.38. SEM micrograph (a), AFM topographic image (b), and 1 dimensional grain analysis of the line on topographic image (c) of annealed Ni4 film at 900 °C

As seen from Table 4.6, there was relation between the RMS, mean Z values and the thickness of films. However, the same relation non-existence for the films that annealed at 900 °C. All topographic images of asgrown samples performed 2μm scale, whereas for annealed samples 40 μm scale performed, that is the maximum scanning scale which we can use is it.

Table 4.6. Surface roughness (RMS), average height of particles (mean Z) and thickness of Ni films of asgrown and annealed at 900 °C Ni1-6 films.

Sample ID	Thickness (nm)	ASGROWN		ANNEALED	
		RMS (nm)	Mean Z (nm)	RMS (nm)	Mean Z (μm)
<b>Ni1</b>	~100	2.2	10.7	209.5	0.73
<b>Ni2</b>	~160	3.9	19.8	288.4	0.94
<b>Ni3</b>	~200	4.5	19.9	295.3	0.89
<b>Ni4</b>	~230	5.8	22.5	297.1	0.87
<b>Ni5</b>	~200	4.8	21.7	312.1	1.09
<b>Ni6</b>	~130	2.8	13.6	211.2	0.79

AFM and SEM images of Ni7 film are shown in Figure 4.39. There is no difference between Ni7 and Ni8 films. However, it can be seen from Table 4.7, Ni7 film, which had thinner Al<sub>2</sub>O<sub>3</sub> buffer layer, has lower surface roughness and mean Z height of the particles for both asgrown and annealed cases. This was conformity with XRD results. In previous section, it was concluded that thinner buffer was more effective to decrease dewetting, and also to texture in (111) direction more intensely.

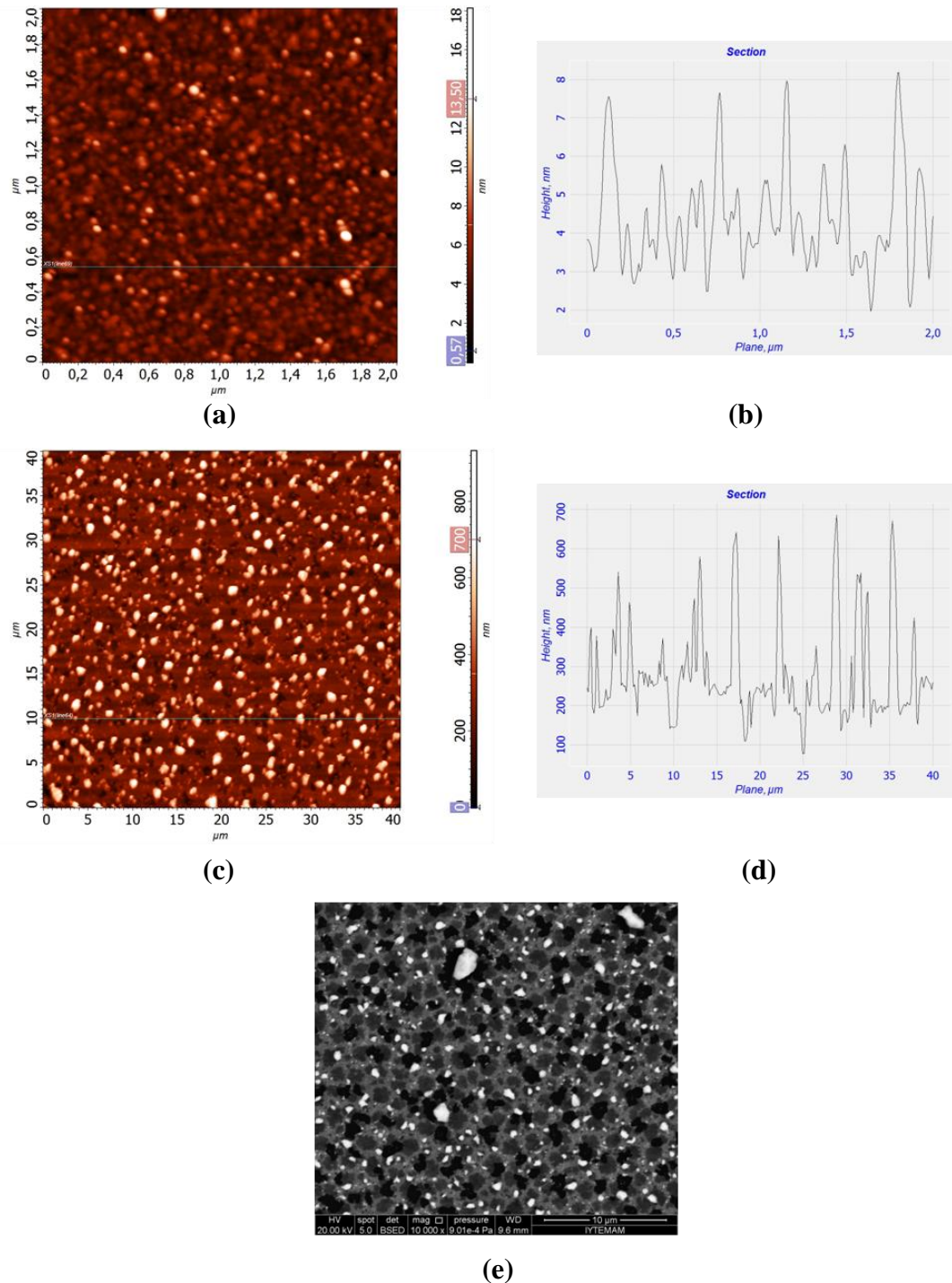


Figure 4.39. AFM topographic image (a), and 1 dimensional grain analysis of the line on topographic image (b) of asgrown Ni7 film. AFM topographic image (c), 1 dimensional grain analysis of the line on topographic image (d), and SEM micrograph (e) of annealed Ni7 film at 900 °C

As seen from Figure 4.38, Ni7 and Ni8 films have different phases. To figure out these phases EDX measurement was performed on these films after annealed at 900 °C.

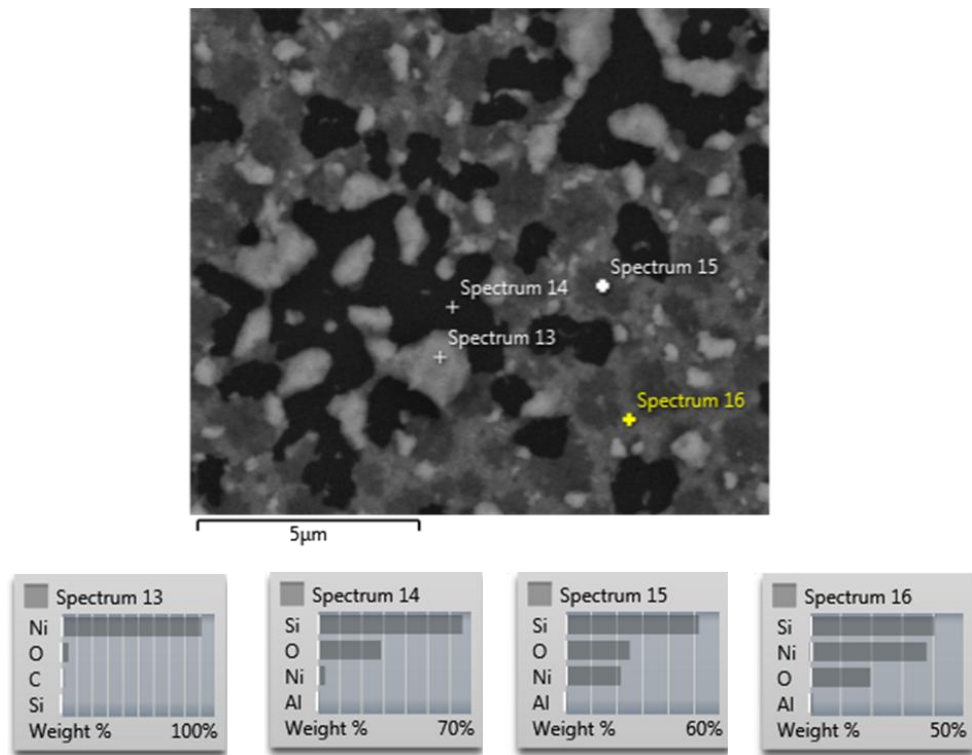


Figure 4.40. Electron image of annealed Ni7 film at 900 °C. The bottom line shows weight percentages of Ni, Si, O and Al elements according to EDX results

Considering EDX results, it can be understood the lightest parts of the film are Ni (spectrum 13) and light parts are thinner Ni film (spectrum 16) than the lightest parts. The darkest parts are  $\text{SiO}_2$  substrate (spectrum 14) which show up due dewetting of Ni film and dark parts are thinner Ni film (spectrum 15) than light parts (spectrum 16). Also, 30 nm  $\text{Al}_3\text{O}_2$  film under the Ni film, which shows up all parts except for the lightest Ni film part which is the top of the film, is seen. So, as expected the Ni element which has the largest atomic number is the brightest part in EDX image.

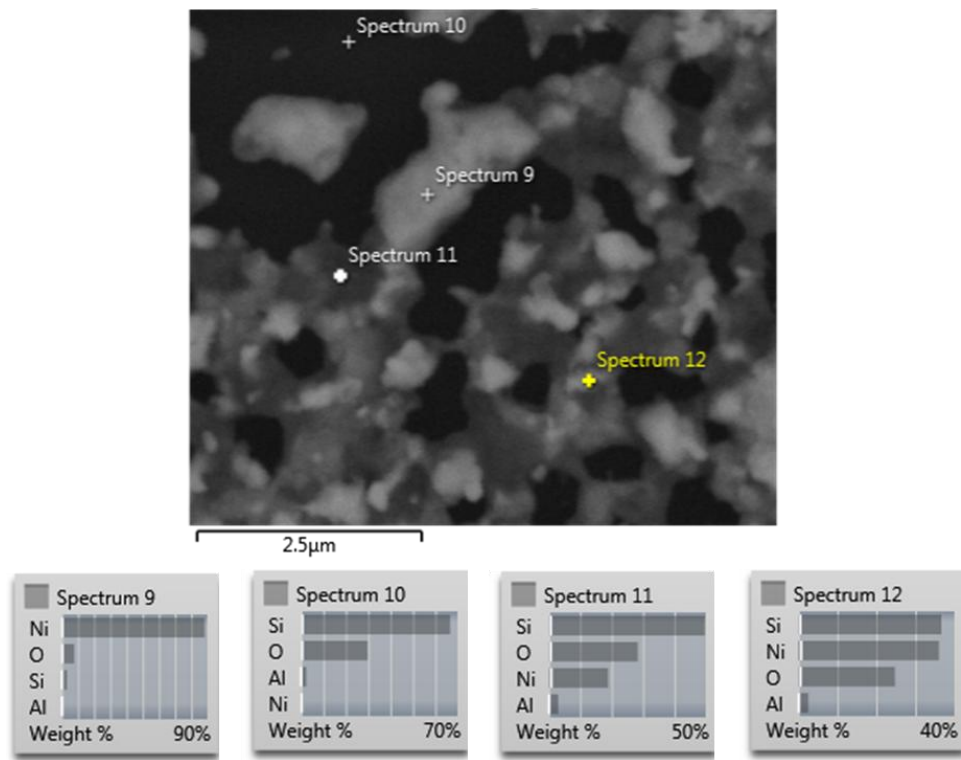


Figure 4.41. Electron image of annealed Ni7 film at 900 °C. The bottom line weight percentages of Ni, Si, O and Al elements according to EDX results

EDX results of Ni7 and Ni8 films were not different except Al weight percentages. Ni8 had 56 nm Al<sub>2</sub>O<sub>3</sub> film, whereas Ni7 had 30 nm Al<sub>2</sub>O<sub>3</sub> film. So, it was very convenient with getting high Al percentage from Ni8 film.

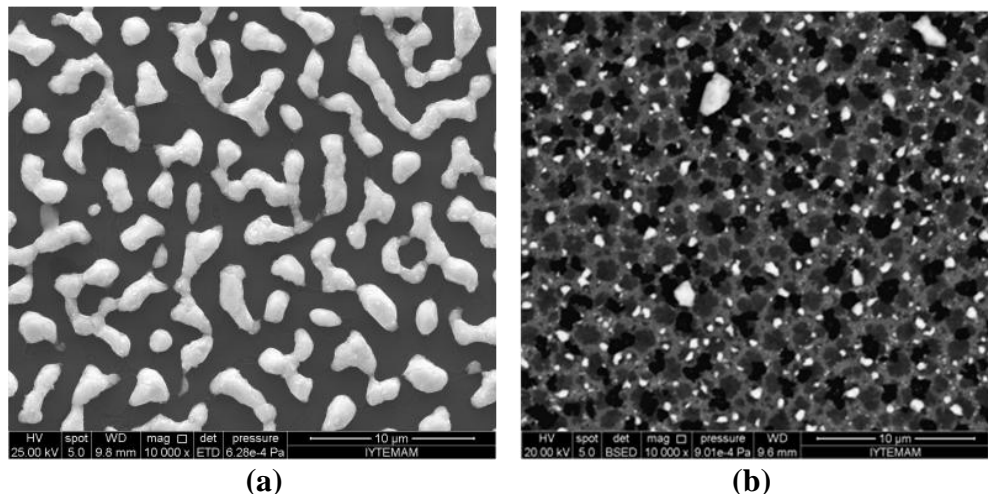


Figure 4.42. SEM micrographs of annealed at 900 °C Ni1 film (a), and Ni7 film (b)

When Ni1 film, which was deposited 100 nm Ni thick under 3 mTorr pressure, and Ni7 film, which was deposited also about 100 nm Ni and 30 nm thick Al<sub>2</sub>O<sub>3</sub> buffer layer, buffer prevented dewetting of the Ni film, considerably (Figure 4.42). Thus, roughness of the surface and mean height of the Ni particles were reduced by depositing buffer layer.

Nickel films of Ni9 and Ni10 samples were deposited thicker than Ni7 and Ni8 samples. They had 56 nm thick Al<sub>2</sub>O<sub>3</sub> buffer and 400 nm thick Ni (Table 4.3). Raising thickness of Ni film caused bigger particles on the surface, whereas average grain size did not change, significantly (Figure 3.43). However, surface roughness and mean height of particles on the surface of annealed Ni9 sample were reduced, dramatically (Table 4.7). Ni9 and Ni10 samples were pretty well similarly about AFM and SEM images.

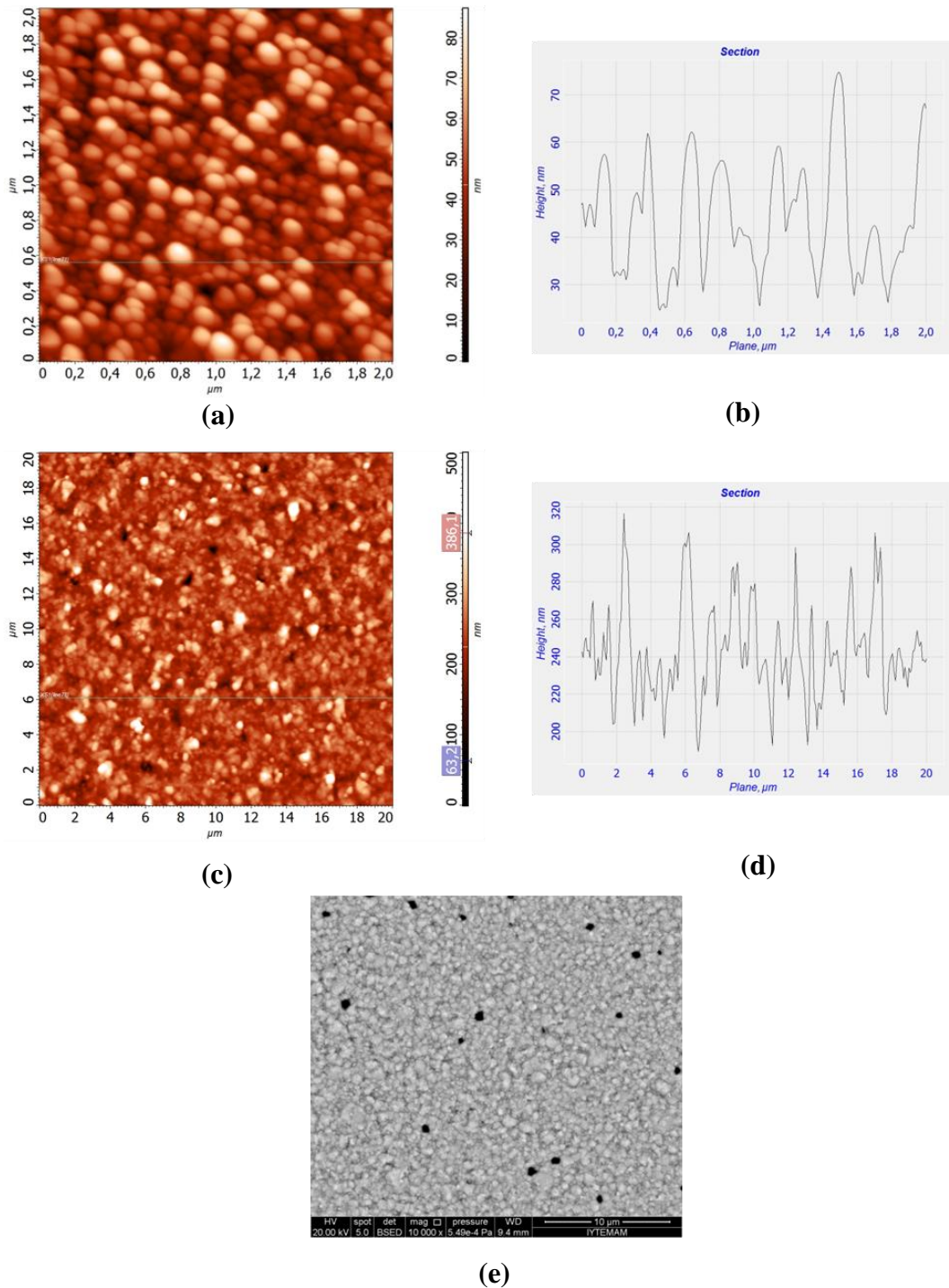


Figure 4.43. AFM topographic image (a), and 1 dimensional grain analysis of the line on topographic image (b) of asgrown Ni9 film. AFM topographic image (c), 1 dimensional grain analysis of the line on topographic image (d), and SEM micrograph (e) of annealed Ni9 film at 900°C

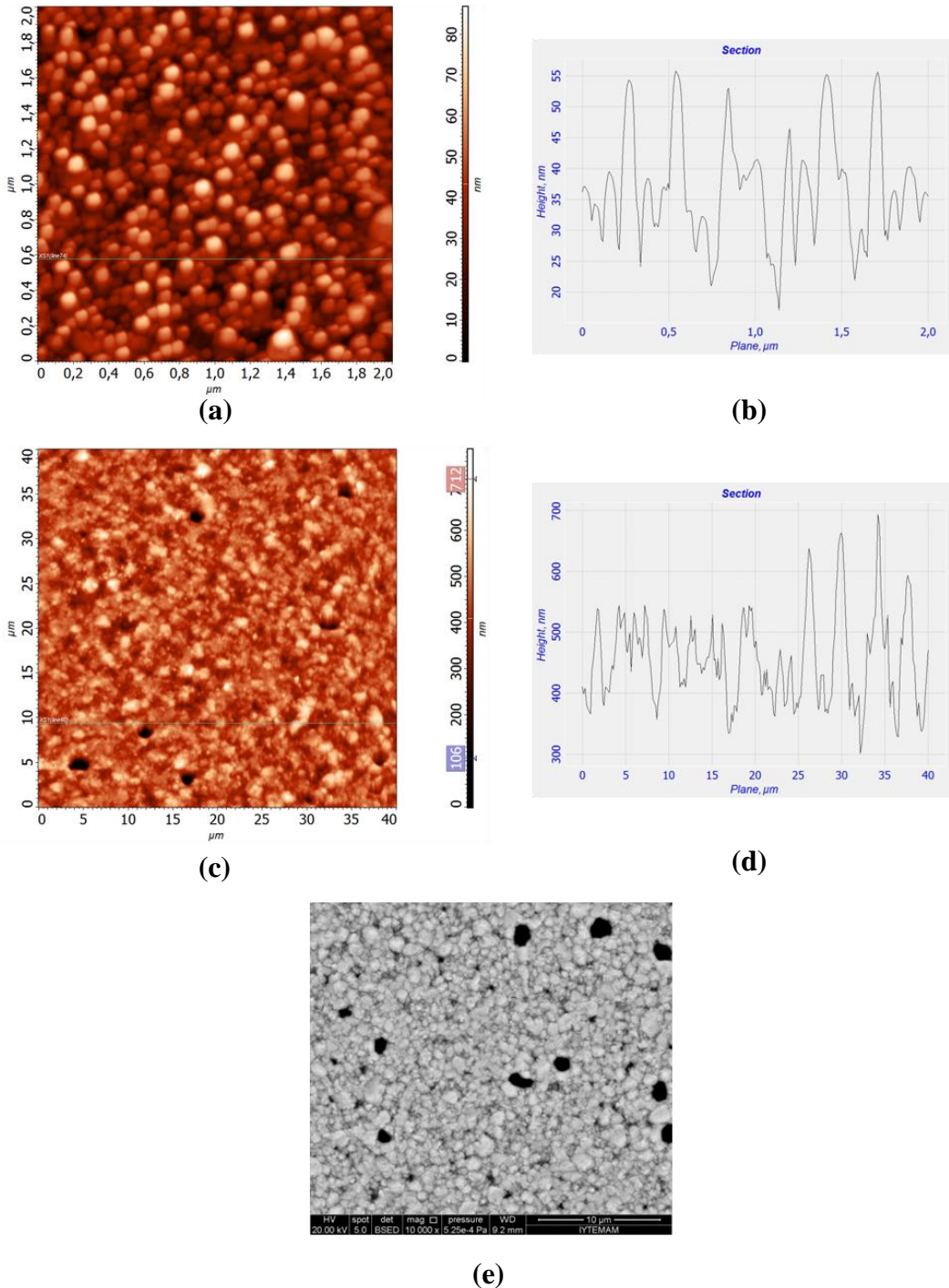


Figure 4.44. AFM topographic image (a), and 1 dimensional grain analysis of the line on topographic image (b) of asgrown Ni11 film. AFM topographic image (c), 1 dimensional grain analysis of the line on topographic image (d), and SEM micrograph (e) of annealed Ni11 film at 900°C

Ni films of Ni11 and Ni12 samples were deposited thicker than Ni7 and Ni8 samples. They were not buffered, directly deposited on the SiO<sub>2</sub> substrate and about 400 nm thick (Table 4.3), contrary to Ni9 and Ni10 films. Ni11 and Ni12 films had very

similar structures about AFM and SEM results. Raising thickness of Ni film caused bigger Ni particles on the surface, whereas average grain size did not change, significantly. However, surface roughness and mean height of particles on the surface of annealed Ni11 and Ni12 films were almost twice more than Ni9 and Ni10 films, which were buffered (Figure 4.44). So, Al<sub>2</sub>O<sub>3</sub> buffer was effective in reducing the RMS and mean height values of the film.

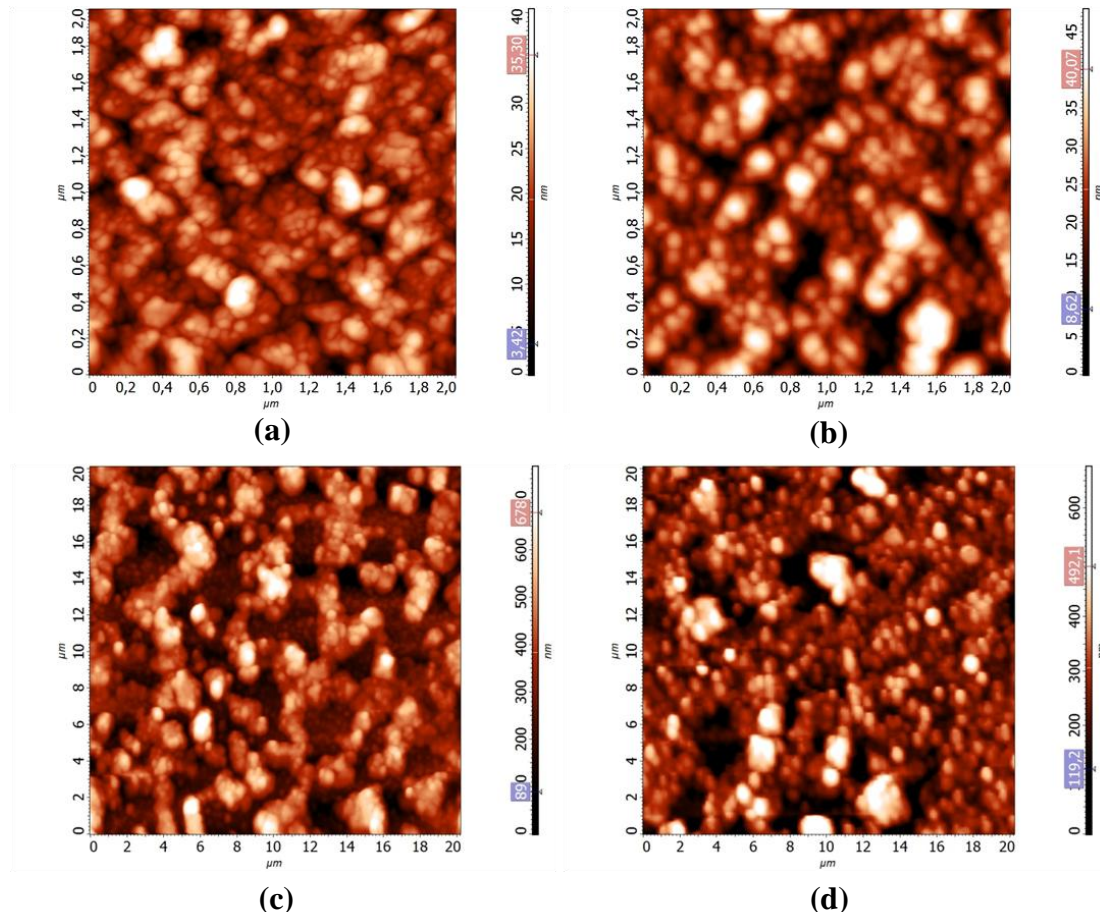


Figure 4.45. SEM micrographs of asgrown Ni13 (a), and Ni14 films (b). Ni13 (c), Ni14 (d) after annealed at 900 °C

Ni13 and Ni14 films were deposited by heating the substrate to 450 °C by magnetron sputter. Their RMS and mean height values of asgrown cases were obviously more than other 100 nm thick films such as Ni1, Ni7 and Ni8 (Table 4.7). However, in annealed cases, Ni13 and Ni14 seemed smoother than the buffered films, Ni7 and Ni8 (Figure 4.45).

Table 4.7. Surface roughness (RMS), mean height of particles (mean Z) and Ni film thickness of asgrown and annealed at 900°C Ni7-14 films

Sample ID	Thickness (nm)	ASGROWN		ANNEALED	
		RMS (nm)	Mean Z (nm)	RMS (nm)	Mean Z (μm)
<b>Ni7</b>	~100	1.3	9.7	119.5	508.1
<b>Ni8</b>	~100	2.0	10.0	126.6	531.4
<b>Ni9</b>	~400	12.5	49.9	38.8	285.2
<b>Ni10</b>	~400	12.0	43.3	44.4	298.8
<b>Ni11</b>	~400	12.4	49.4	72.9	439.3
<b>Ni12</b>	~400	12.6	49.4	76.6	440.3
<b>Ni13</b>	~100	5.6	21.8	128.5	423.7
<b>Ni14</b>	~100	7.3	26.8	102.5	442.2

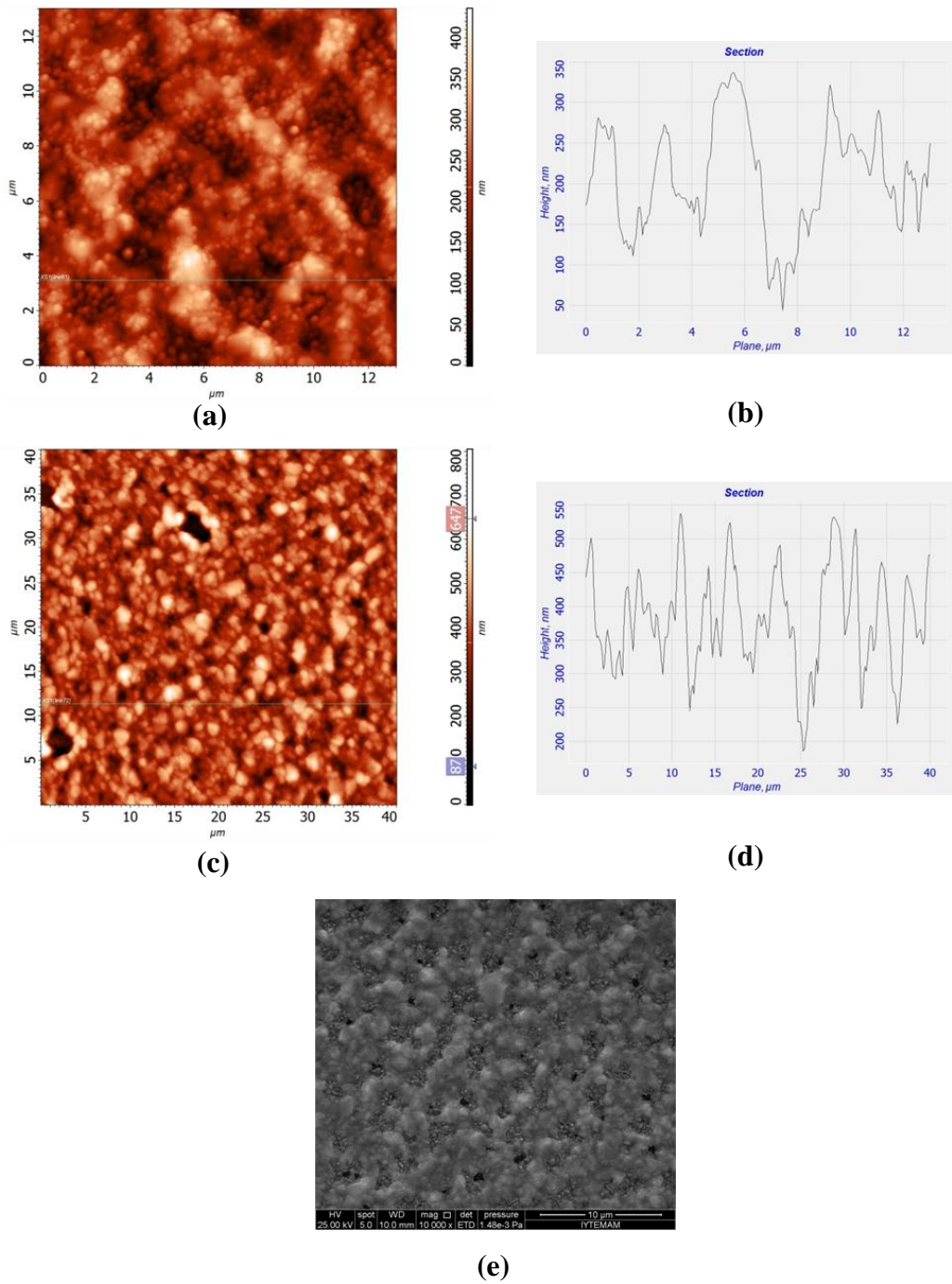


Figure 4.46. AFM topographic image (a), and 1 dimensional grain analysis of the line on topographic image (b) of asgrown Ni15 film. AFM topographic image (c), 1 dimensional grain analysis of the line on topographic image (d), and SEM micrograph (e) of annealed Ni15 film at 900 °C

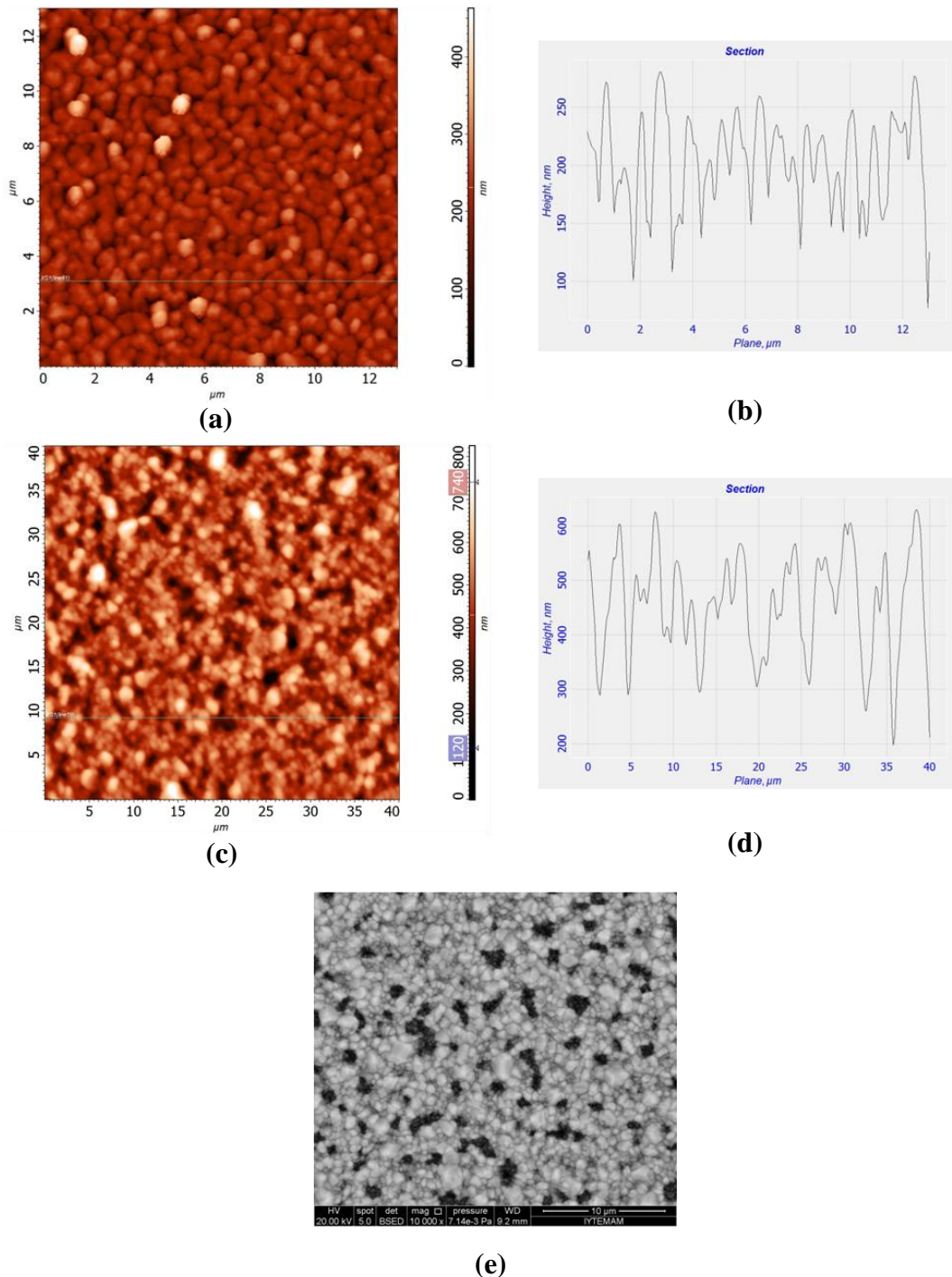


Figure 4.47. AFM topographic image (a), and 1 dimensional grain analysis of the line on topographic image (b) of asgrown Ni16 film. AFM topographic image (c), 1 dimensional grain analysis of the line on topographic image (d), and SEM micrograph (e) of annealed Ni16 film at 900 °C

In asgrown cases, RMS values of Ni16 and Ni18 films were lower than Ni15 and Ni17 films which were unheated deposited cases of Ni16 and Ni18 films, respectively, but any relation between mean height values of these films was not observed (Figure

4.46 and Figure 4.47). However, in annealed case, mean height values of Ni16 and Ni18 films were lower than Ni15 and Ni17 films, but there was no certain relation between RMS values of these films (Figure 4.46 and Figure 4.47).

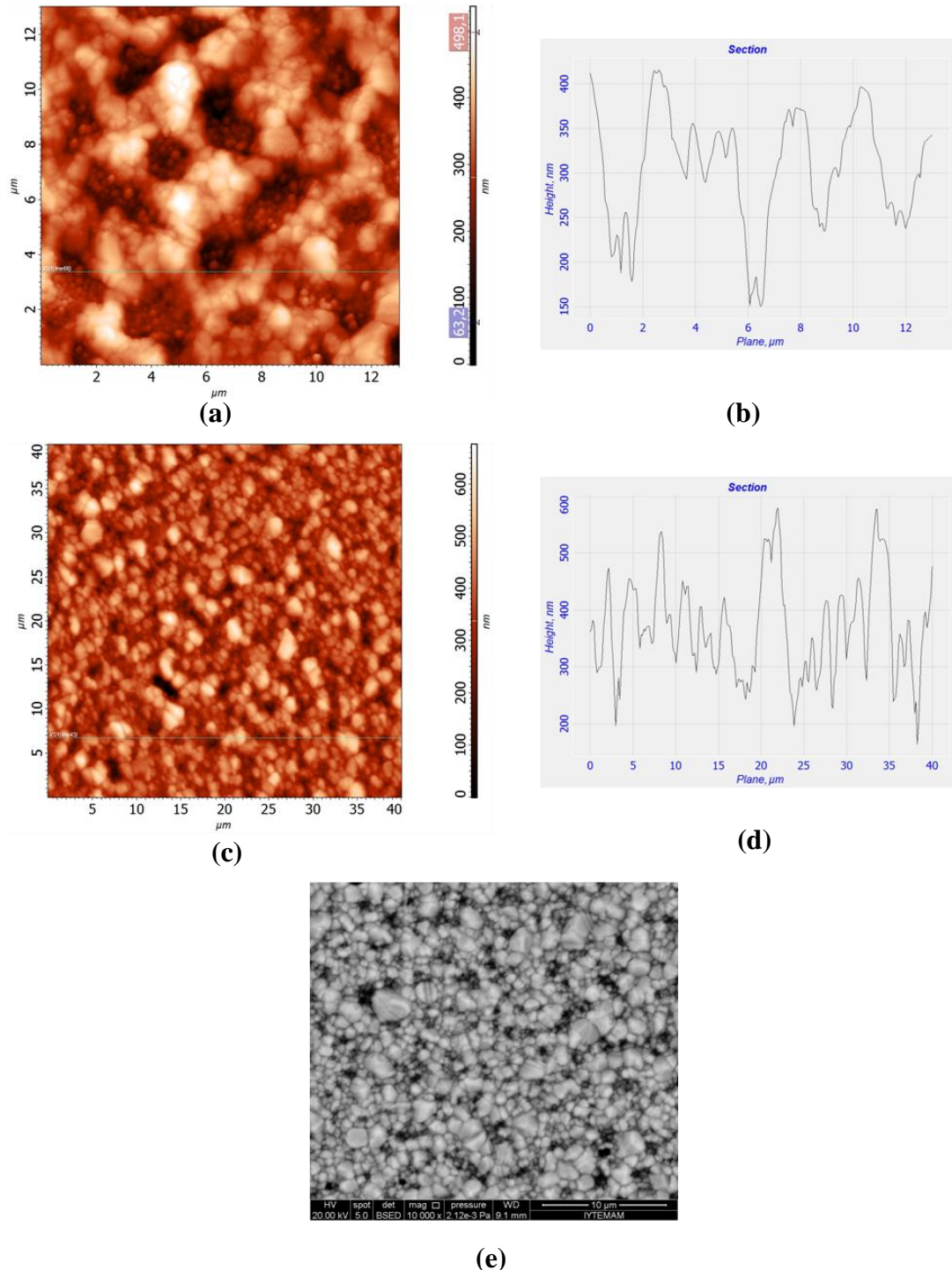


Figure 4.48. AFM topographic image (a), and 1 dimensional grain analysis of the line on topographic image (b) of asgrown Ni<sub>17</sub> film. AFM topographic image (c), 1 dimensional grain analysis of the line on topographic image (d), and SEM micrograph (e) of annealed Ni<sub>17</sub> film at 900 °C

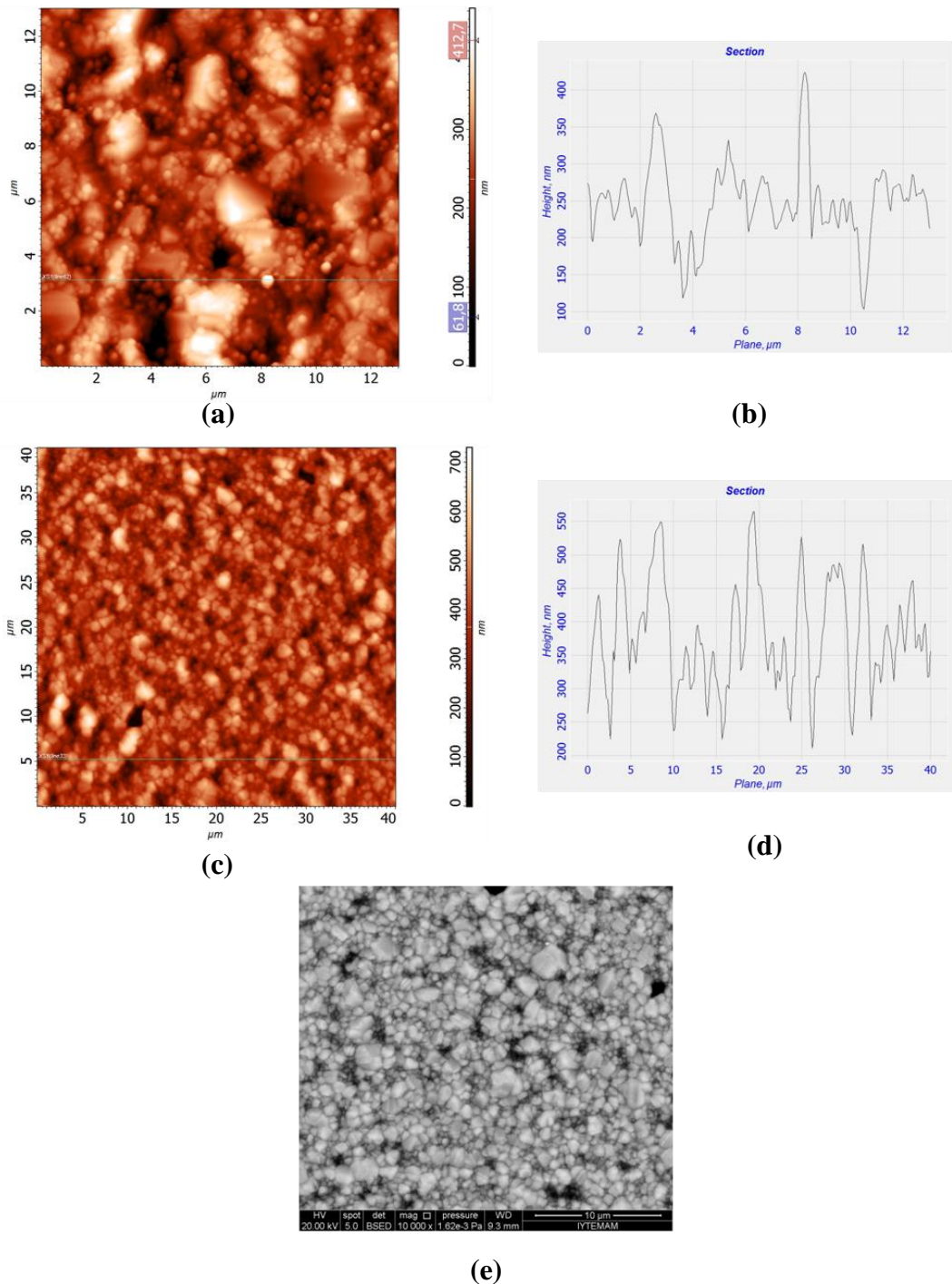


Figure 4.49. AFM topographic image (a), and 1 dimensional grain analysis of the line on topographic image (b) of asgrown Ni18 film. AFM topographic image (c), 1 dimensional grain analysis of the line on topographic image (d), and SEM micrograph (e) of annealed Ni18 film at 900 °C.

Table 4.8. Surface roughness (RMS), average height of particles (mean Z) and Ni film thickness of asgrown and annealed at 900°C Ni15-18 films.

Sample ID	Thickness (nm)	ASGROWN		ANNEALED	
		RMS (nm)	Mean Z (nm)	RMS (nm)	Mean Z (μm)
Ni15	~400	61.5	230.1	84.1	431.5
Ni16	~400	45.0	256.7	95.2	413.1
Ni17	~400	74.1	239.8	94.3	437.5
Ni18	~400	62.5	238.0	89.5	386.7

The difference between Ni15 and Ni16 was that Ni16 film was deposited by heating the substrate to 450 °C. Ni15 and Ni16 had Al<sub>2</sub>O<sub>3</sub> buffer and Cr adhesive layers, whereas Ni9 and Ni10 have only Al<sub>2</sub>O<sub>3</sub> buffer layer. Ni18 was deposited by heating the substrate to 450 °C, on the contrary Ni17 was not deposited by heating the substrate. Ni17 and Ni18 films had only 10 nm Cr adhesive layers. In asgrown and annealed cases, RMS and mean height values of Ni15, Ni16, Ni17 and Ni18 films were more than Ni9 and Ni10 films, remarkably. These values were close to the values of Ni11 and Ni12 which are non-buffered films. Ni9 and Ni10 films were the most smooth and thick films which had only Al<sub>2</sub>O<sub>3</sub> buffer layer.

In this chapter, also annealing was performed at 950 °C. XRD  $\theta$  -  $2\theta$  measurements of these films carried out and their average grain size calculated. The films were very rough, so performing of tapping mode AFM height measurements were very difficult. Thus, not to damage the tips their AFM height measurements were not carried out. In this study, only roughness and average grain size relations of the films which annealed at 900 °C were compared from AFM height measurement results. However, we sustained XRD  $\theta$  -  $2\theta$  measurements of the films that annealed at 950 °C, but they were not represented. All calculated average grain sizes of the annealed films both at 900 and 950 °C were given in Figure 4.33.

## CHAPTER 5

### SYNTHESIS OF GRAPHENE BY CVD ON POLYCRYSTALLINE NICKEL AND CHARACTERIZATION BY RAMAN SPECTROSCOPY

#### 5.1. Graphene Growth Process by CVD

To grow graphene, sample preparation was carried out after deposition of polycrystalline Ni films with various thickness and crystal structure onto  $\text{SiO}_2$  and buffered substrates by magnetron sputtering. Details of sample preparation and deposition was mentioned in chapter 3 and chapter 4. Then the films were loaded inside the quartz tube in CVD furnace.

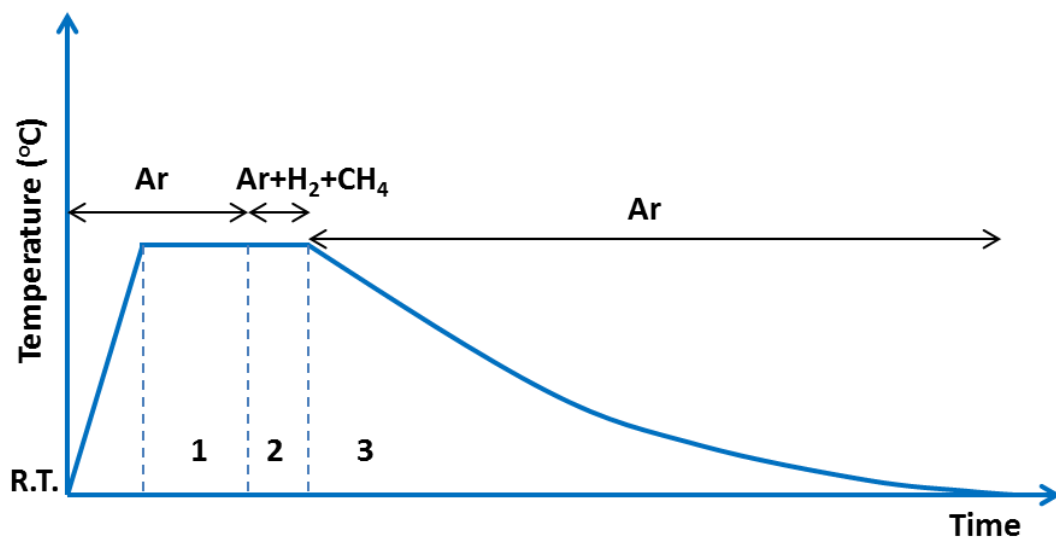


Figure 5.1. Heating, annealing, growth and cooling stages of graphene growth process by CVD

Figure 5.1 shows the process of graphene growth with three stages. First, Ar was flown into the furnace while the temperature increased from the room temperature to desired growth temperate. The heating rate was always  $28\text{ }^{\circ}\text{C}/\text{min}$  from room

temperature (RT) to desired growth temperature. During catalyst preparation, also known as pretreatment, just Ar or Ar and H<sub>2</sub> were flown through the tube to prevent the oxidation contamination of samples. When the furnace reached the desired temperature after waiting for a while growth was started by flow of CH<sub>4</sub>. At the beginning of the cooling hydrocarbon source was shut off and the furnace was then cooled done to room temperature under a certain cooling rate. The main stage of the process is cooling which dissolved carbon atoms precipitate on the Ni film surface and bond each other on the surface creating honeycomb lattices. Formation of graphene on Ni film was explained in detail in previous chapters. Various flow rates of gases and cooling rates were used for polycrystalline Ni films in order to favor the formation of thin graphene films on under ambient pressure by CVD. All the process parameters studied in this work were given in Table 5.1. After the CVD process all samples denominated as GRP and its number.

Table 5.1. Growth parameters of graphene grown by CVD. RT indicates room temperature (23-24°C).

METHOD	Stages	Temperature (°C)	Ar (sccm)	H <sub>2</sub> (sccm)	CH <sub>4</sub> (sccm)	Time (min)	Cooling rate (°C/min)
Method 1	1	900	150	-	-	20	
	2	900	200	100	10	40	
	3	900-RT	200	-	-	~290	3 °C/min
Method 2	1	800	150	-	-	20	
	2	800	200	100	10	40	
	3	800-RT	200	-	-	~290	3 °C/min
Method 3	1	900	150	-	-	20	
	2	900	200	100	20	40	
	3	900- RT	200	-	-	~290	3 °C/min
Method 4	1	900	150	-	-	20	
	2	900	200	100	8	40	
	3	900- RT	200	-	-	~290	3 °C/min
Method 5	1	950	150	-	-	20	
	2	950	200	100	10	40	
	3	950- RT	200	-	-	~290	3 °C/min
Method 6	1	950	150	-	-	20	
	2	950	200	100	20	40	
	3	950- RT	200	-	-	~290	3 °C/min

(cont. on next page)

**Table 5.1. (cont.)**

<b>Method 7</b>	<b>1</b>	950	150	-	-	50	
	<b>2</b>	950	200	100	8	10	
	<b>3</b>	950- RT	200	-	-	~290	3 °C/min
<b>Method 8</b>	<b>1</b>	900	150	-	-	20	
	<b>2</b>	900	150	100	10	40	
	<b>3</b>	900- RT	150	-	-	~438	2 °C/min
<b>Method 9</b>	<b>1</b>	900	150	-	-	20	
	<b>2</b>	900	150	100	15	40	
	<b>3</b>	900- RT	150	-	-	~290	3 °C/min
<b>Method 10</b>	<b>1</b>	900	150	-	-	20	
	<b>2</b>	900	150	100	10	40	
	<b>3</b>	900- RT	150	-	-	~219	4 °C/min
<b>Method 11</b>	<b>1</b>	900	150	100	-	20	
	<b>2</b>	900	200	150	20	40	
	<b>3</b>	900- RT	200	150	-	~87	10 °C/min
<b>Method 12</b>	<b>1</b>	900	150	100	-	20	
	<b>2</b>	900	200	150	20	40	
	<b>3</b>	900- RT	200	150	-	~58	15 °C/min
<b>Method 13</b>	<b>1</b>	900	150	100	-	20	
	<b>2</b>	900	200	150	20	40	
	<b>3</b>	900- RT	200	150	-	~175	5 °C/min
<b>Method 14</b>	<b>1</b>	900	100	200	-	20	
	<b>2</b>	900	100	200	30	10	
	<b>3</b>	900- RT	200	50	-	~175	5 °C/min
<b>Method 15</b>	<b>1</b>	900	100	200	-	20	
	<b>2</b>	900	100	200	30	10	
	<b>3</b>	900- RT	200	50	-	~438	2 °C/min
<b>Method 16</b>	<b>1</b>	900	100	200	-	20	
	<b>2</b>	900	100	200	30	10	
	<b>3</b>	900- RT	200	50	-	~876	1 °C/min
<b>Method 17</b>	<b>1</b>	900	100	200	-	50	
	<b>2</b>	900	100	200	30	10	
	<b>3</b>	900- RT	200	50	-	~876	1 °C/min
<b>Method 18</b>	<b>1</b>	900	100	200	-	50	
	<b>2</b>	900	100	200	30	10	
	<b>3</b>	900- RT	200	50	-	~438	2 °C/min

As seen from Table 5.1, cooling rates of 1, 2, 3, 4, 5, 10 and 15 °C/min were studied [131, 159, 184, 185]. The aim was to find medium cooling rate which gives mono layer graphene [159]. Raman spectra of the samples, which were performed with fast cooling rates, were yielded mostly multilayer graphene or graphite. An exception to this trend was observed for Method1-10 which did not include H<sub>2</sub> in growth stage. Then regarding a recent works on the effect of hydrogen to growing graphene residual methods includes H<sub>2</sub> flow in all stages [160, 186]. Hydrogen sites yield diffusion and segregation of carbon atoms. Graphene without a D peak in Raman spectra could be grown on polycrystalline Ni with optimized hydrogen content. Eighteen Ni films were used to grow graphene on by these methods. In next part when comparing Raman spectra of films all methods were named by numbers, and these method numbers were used instead of explain all process about mentioned sample in details.

## 5.2. Raman Spectroscopy Results

Due to large height difference in Ni films areal mapping of Raman spectra were very difficult. Instead mapping, Raman spectra were just carried out single measurements at visibly the densest areas on the Ni substrate. As mentioned before Raman spectroscopy only can distinguish multilayer from 1 or 2-LG, but cannot distinguish 1-LG from 2-LG [4]. In this study, layer number or stacking order of CVD grown graphene layers were identified only via Raman spectrum results. The measurements performed on the original Ni substrates they were grown with any further processing. The graphene layers were not transferred on to SiO<sub>2</sub> for Raman and/or optical measurements. Thus, Raman signals were observed from 1-LG if there is no coupling between Ni substrate and graphene layer. All Raman spectra results carried out by 514 nm (2.41eV) excitation with a 600 grooves/mm grating to see all three dominant peaks of graphene in a single spectrum.

In chapter 3, the difference between AB stacking and turbostratic graphene was explained (Figure 3.13). However, for CVD grown graphene G' band looks well-shaped Lorentzian, which causes confusion to differentiate turbostratic graphene and 1-L or 2-L graphene. Thus, G' band was fitted by a single sharp Lorentzian for 1 or 2-LG, or two and more sharp Lorentzian for more than 2-LG. The FWHMs of G' bands were broaden and up-shifted when the graphene layer number increases from 1-L to bulk graphite.

However, if G' band of Raman spectrum has distorted shape, it is 2- or more layered AB stacked graphene. In Figure 3.13 and Figure 5.2 (right), the evolution of the spectra of AB stacked graphene at 514 nm excitation with the number of layers is shown. As it was mentioned in Chapter 3, G' band of AB stacked 2-LG can be fitted by four peaks which are named as 2D<sub>1B</sub>, 2D<sub>1A</sub>, 2D<sub>2A</sub>, 2D<sub>2B</sub>. These peaks come from different electron-phonon scattering processes (discussed in Chapter 3 in detail). The two of them, named 2D<sub>1A</sub>, 2D<sub>2A</sub>, have higher intensity compared to the other two. Increasing number of layers causes decrease in the intensity of 2D<sub>1B</sub>, 2D<sub>1A</sub> peaks hence for bulk graphite the G' band have only two-components and up-shifts (Figure 5.2 (right)) [82, 172]. Thus, Raman spectra can only provide to identify single layer from few (less than 5) layers for AB stacking graphene. In this study, the intensity ratio of G band and G' band ( $I_G/I_G'$ ) in Raman spectra was used to distinguish graphene layers. This ratio increases with number of layers.

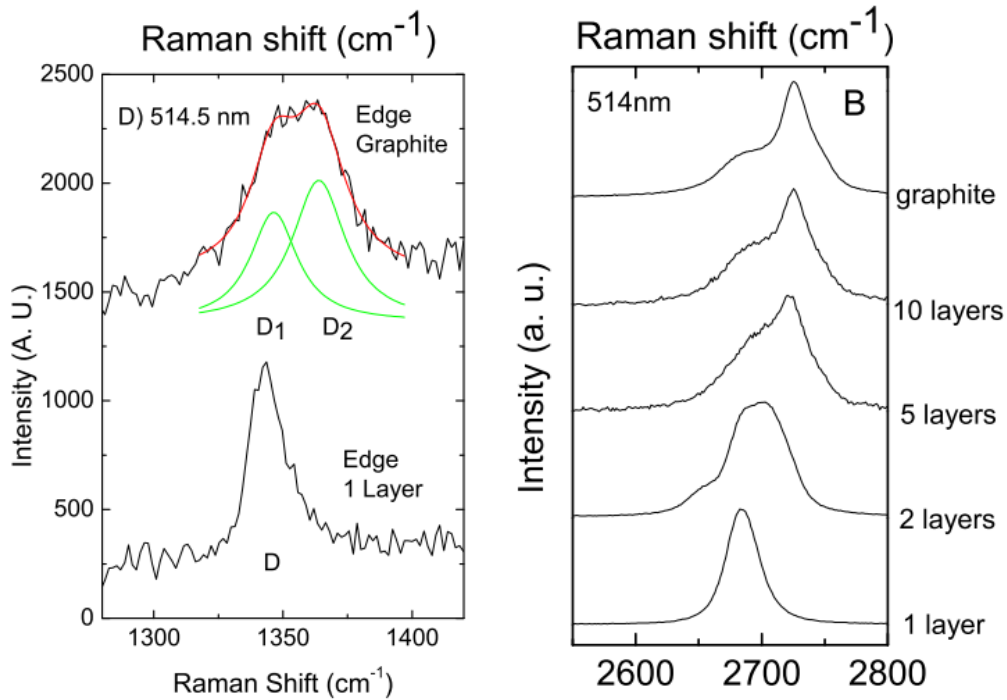


Figure 5.2. Comparison of the D band at 514.5 nm at the edge of bulk graphite and single layer graphene. The fit of the D<sub>1</sub> and D<sub>2</sub> components of the D band of bulk graphite is shown (left). Evolution of the spectra at 514 nm with the number of layers. They are scaled to have similar height of the 2D peaks (right) [82, 172]

Edges of graphene increases D and D' band intensities by breaking the symmetry of the graphene. D band intensity can give information of defects in the structure and

edges also. In Figure 5.2 (left), the difference of D band between 1-LG and bulk graphite is shown. Increasing numbers of layers also broadens FWHM of D band.

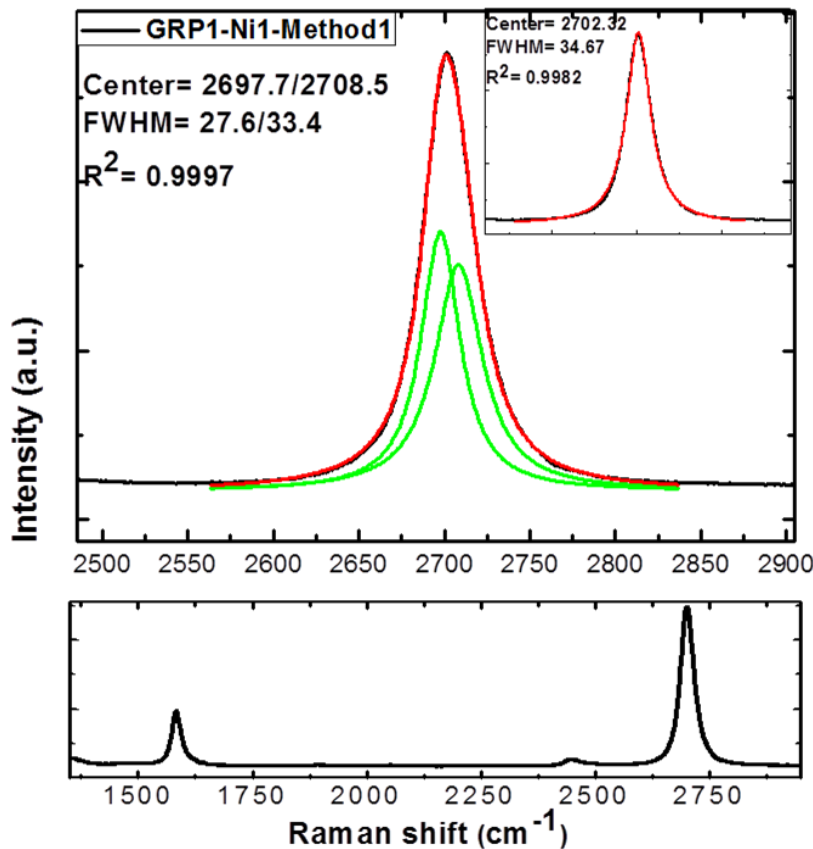


Figure 5.3. G' band Raman spectrum of GRP1 sample which was grown on Ni1 film by Method1. The inset shows the same result fitted with a single Lorentzian peak. The green lines are the components of red line which is the fitted profile. At the bottom, the whole range of the respective spectrum is shown.

The G' band Raman spectrum of GRP1 sample which was grown by Method1 on Ni1 substrate and at the bottom the whole range Raman spectrum are shown in the Figure 5.3 (a). As seen in the Figure 5.3, a fit can be made to the same G' band by two or just one Lorentzian peak with given FWHM of each peak in the graphs. In such cases the quality of fits ( $R^2$ ) and the intensity ratio of G band and G' band ( $I_G/I_{G'}$ ) were compared. Therefore, it can be said that the Raman spectrum of GRP1 sample, which had  $I_G/I_{G'}$  ratio of 0.30 and FWHM of G' band of  $34\text{ cm}^{-1}$ , belong to 1-LG [3].

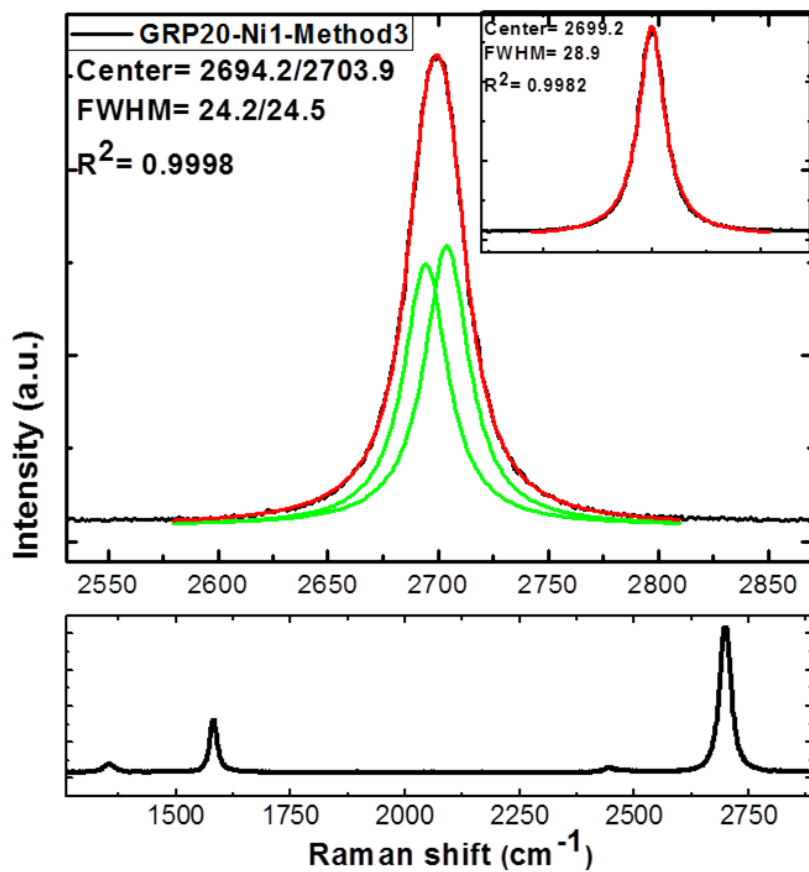


Figure 5.4. G' band Raman spectrum of GRP20 sample which was grown on Ni1 film by Method3. The inset shows the same result fitted with a single Lorentzian peak. The green lines are components of red line which is fitted profile. At the bottom, the whole range of the respective spectrum is shown.

The G' band Raman spectrum of GRP20 sample, which was grown by Method3 on Ni1 substrate, and at the bottom the whole range Raman spectrum are shown in the Figure 5.4. When Method3 was used to grow graphene on Ni1 substrate, the FWHMs of grown graphene layers decreased to a value  $\sim 28 \text{ cm}^{-1}$  with  $I_G/I_{G'}$  ratio of 0.34. As mentioned in Chapter 3, G' band of Raman spectrum of graphene grown on a Ni substrate the FWHM values ranged in  $25 - 55 \text{ cm}^{-1}$  and  $I_G/I_{G'}$  ratio is less than one [3]. A two-component fit with each component has FWHM of  $24-30 \text{ cm}^{-1}$ , it is signature of 2-L turbostratic graphene. It could be both 1 and 2-L turbostratic graphene, but considering reported Raman measurements performed on Ni films the possibility of being 1-LG more than that of turbostratic graphene. Raman measurements must be combined with other technique in order to decide the number of layers.

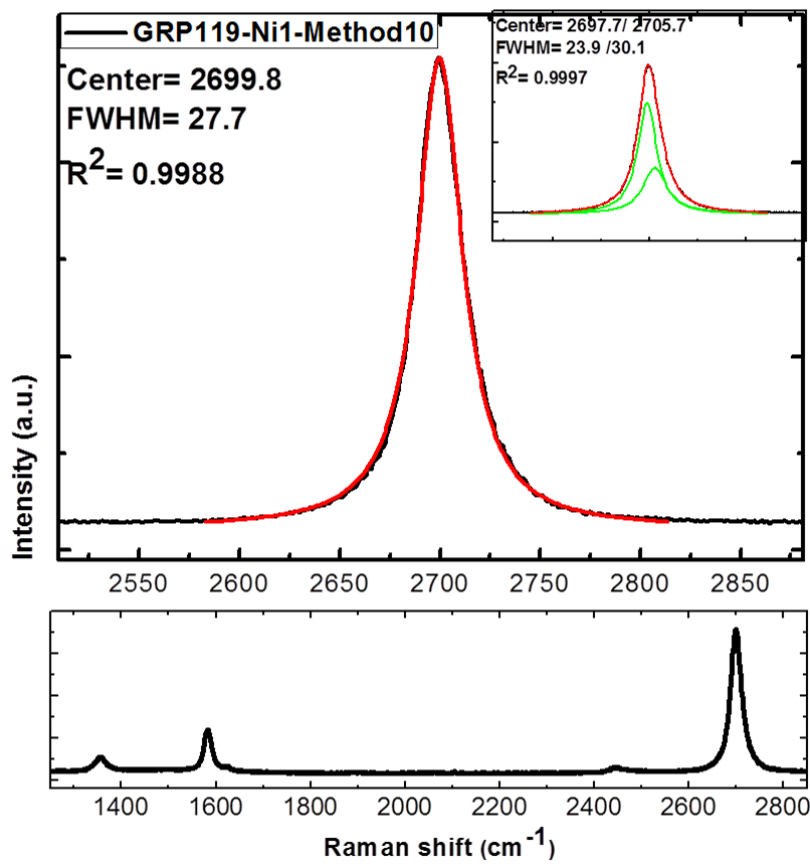


Figure 5. 5. G' band Raman spectrum of GRP119 sample which grown on Ni1 film by Method10. The inset shows the same result fitted with two Lorentzians. The green lines are components of red line which is calculated profile. At the bottom, the whole range of the spectrum is shown.

GRP60-Method5 was performed at  $950^\circ\text{C}$  on Ni1 substrate and the resulting average values of grown graphene layers were similar with GRP1-Method1, so increasing temperature did not have any pronounced effect on number of layers affect so much, but increasing  $\text{CH}_4$  flow during diffusion of carbon atoms in Ni substrate led to narrower FWHM values, one example was GRP20-Method3. When temperature increased while  $\text{CH}_4$  decreased (GRP88-Method7), it was difficult to locate 1 or 2-L graphene.

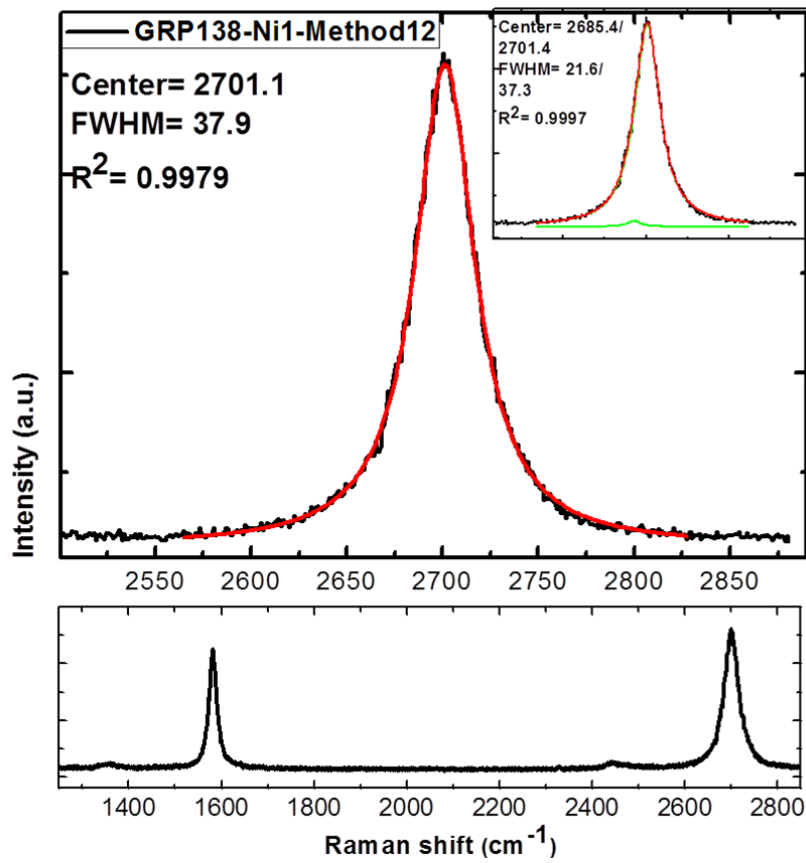


Figure 5.6. G' band Raman spectrum of GRP138 sample which grown on Ni1 film by Method12. The inset shows the same result fitted with two Lorentzians. The green lines are components of red line which is calculated profile. At the bottom, the whole range of the spectrum is shown

Instead of increasing the  $\text{CH}_4$  flow the cooling rate could be increased from 3  $^{\circ}\text{C}/\text{min}$  to 4  $^{\circ}\text{C}/\text{min}$ , in order to have narrower FWHM values. The lower intensity ratio  $I_G/I_{G'}$  was seen from GRP119-Method10. The FWHM values for this growth was about  $\sim 27 \text{ cm}^{-1}$  with  $I_G/I_{G'}$  of 0.27 (Figure 5.6 (a)). These values were enough to say the spectrum belongs to 1 or 2-L graphene. If the cooling rates were further increased to 15  $^{\circ}\text{C}/\text{min}$  and even with increase in the flow rate of  $\text{CH}_4$ , FWHM increased to  $\sim 37 \text{ cm}^{-1}$  and intensity ratio of  $I_G/I_{G'}$  increased to 0.87 (GRP138-Method12, Figure 5.6 (b)). A fit with two components one with very small intensity, one had a FWHM of  $\sim 37 \text{ cm}^{-1}$ .

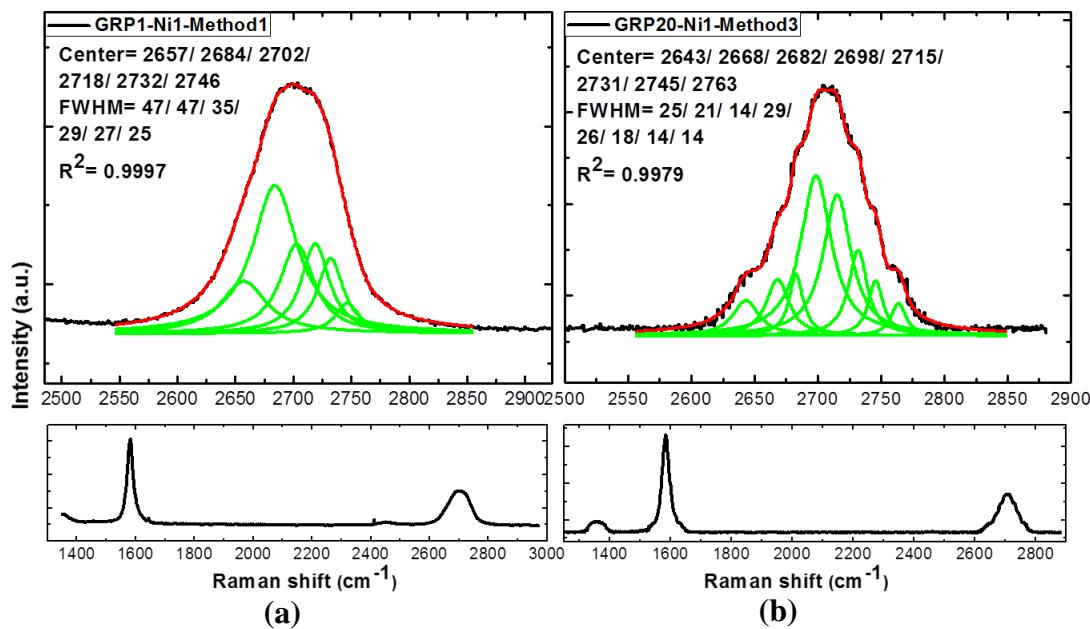


Figure 5.7. G' band Raman spectrum of GRP1 (a) and GRP20 (b) samples which grown on Ni1films by Method1 and Method3, respectively. The green lines refer to component of red line which is calculated profile. At the bottom, the whole ranges of the spectra are shown

Looking at Figure 3.13 and Figure 5.2 (right), if G' band shape is not distorted, looks like Lorentzian peak with broaden FWHM, the layers stacked turbostratic or just not AB. In Figure 3.13, Raman spectra from few or multilayered graphene are shown. As mentioned in Chapter 3, when the layer number of graphene is more than 2-L with  $\text{FWHM} > 50 \text{ cm}^{-1}$  and  $I_G/I_G' > 1$ , G' band is fitted by more than four Lorentzian peaks, for CVD grown graphene on Ni film [3]. Thus, as seen Figure 5.7, the line shapes of G' bands look like distorted, but it is hard to decide exactly the stacking order and layer number only from that spectrum. The peak shape also affects from detector converter of the system.

The G' band Raman spectrum of GRP1 (Figure 5.7 (a)) had the ratio of  $I_G/I_G$  2.53 and FWHM of  $89\text{ cm}^{-1}$ . Six-component fit, which was the best fit using the least number of components had the  $R^2$  of 0.9997, refers to 3-L AB stacked graphene, but the line shape did not look like in Figure 3.13 or Figure 5.2 (right). The line shape looks like more Lorentzian with very broaden FWHM. On the other hand, in Figure 5.7 (b) G' band Raman spectrum from GRP20 is shown, which has very attractive line shape of G' band, because it does not looks like AB stacking, whereas well symmetric shaped. The best fit using the least number of components was eight-component fit with  $R^2$  of

0.9979, the ratio of  $I_G/I_{G'}$  2.50 and FWHM of  $65\text{ cm}^{-1}$ . So, there was no relation between the ratio of  $I_G/I_{G'}$  and FWHM values for more than 2-LG which Raman measurements of the CVD-grown graphene were performed on Ni film. All observed G' band Raman spectra, which had FWHM  $>50$  and  $I_G/I_{G'}>1$  if layer number of graphene was more than 2-L, so G' band was fitted by more than three Lorentzian peaks.

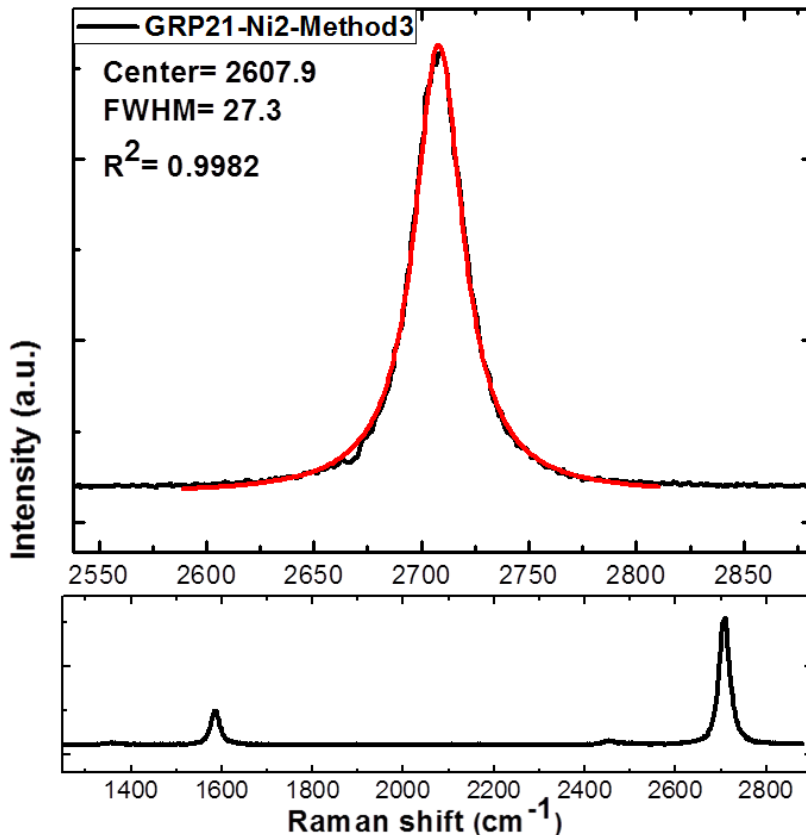


Figure 5.8. G' band Raman spectrum of GRP21 sample which grown on Ni2 film by Method3. The red line is calculated profile. At the bottom, the whole range of the spectrum is shown.

G' band of GRP21 which was grown on Ni2 film had FWHM of  $27\text{ cm}^{-1}$  and the ratio of  $I_G/I_{G'}$  0.25 (Figure 5.8). The conditions of Method3 gave the best results of 1-LG, like for Ni1 film. Also, Method1 caused a little broaden FWHM of G' band spactra.

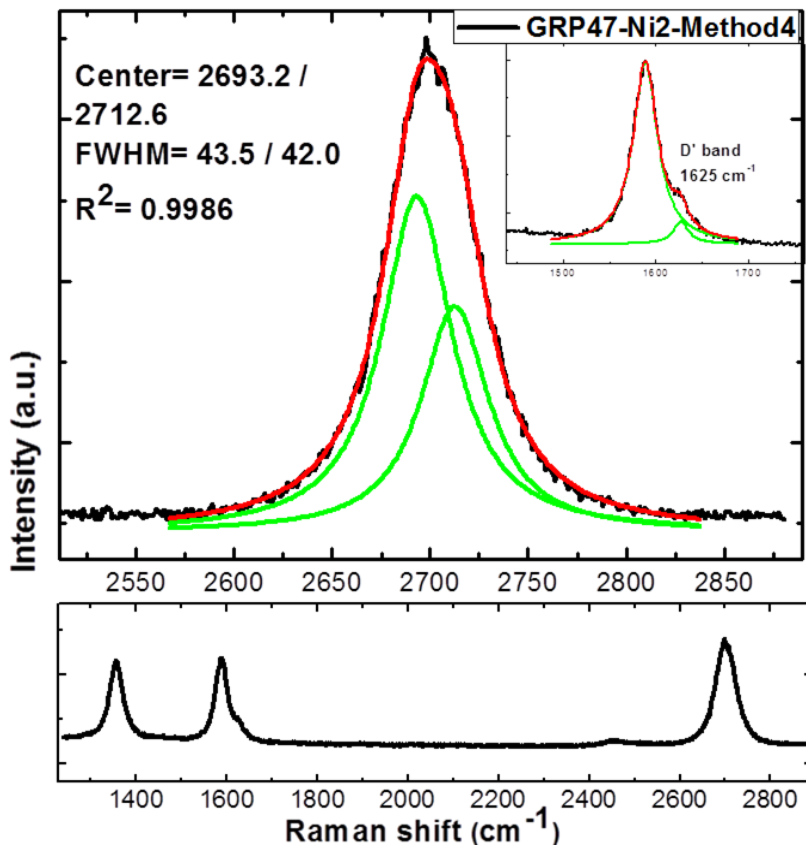


Figure 5.9. G' band Raman spectrum of GRP47 sample which grown on Ni2 film by Method4. The green lines are components of red line which is calculated profile. At the bottom, the whole range of the spectrum is shown. The inset shows the D' band of GRP47

When the CH<sub>4</sub> flow was decreased (Method4) on the contrary of Ni1, 1 or 2-LG grew on Ni2 film, but with broad FWHM values ( $38\text{-}56\text{ cm}^{-1}$ ) (Figure 5.9). However, D and D' bands, which indicate defects of the graphene layer, showed up, remarkably. For Ni1 film, Method7 did not lead to grow 1 or 2-LG, but on Ni2 film 1 or 2-LG was observed with average FWHM of  $39\text{ cm}^{-1}$ . However, when cooling rate increased (Method10), 1 or 2-LG was not observed by contrast with Ni1 film.

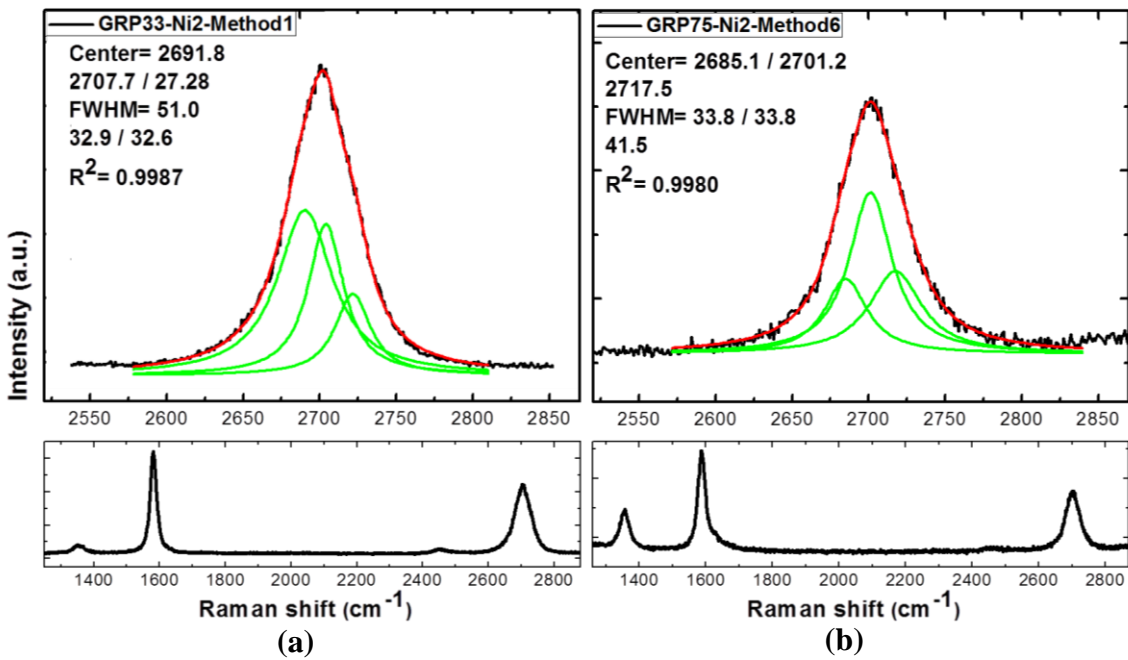


Figure 5.10. G' band Raman spectrum of GRP33 (a) and GRP75 (b) samples which grown on Ni2 sample by Method1 and Method6, respectively. The green lines refer to component of red line which is calculated profile. At the bottom, the whole ranges of the spectra are shown.

Gomez De Arco reported that when the layer number of graphene is more than 2-L with  $\text{FWHM} > 50 \text{ cm}^{-1}$  and  $I_G/I_{G'} > 1$ , G' band is fitted by more than four peaks, for CVD grown graphene on Ni film [3]. However, G' band FWHM of GRP33 was  $59 \text{ cm}^{-1}$  and  $I_G/I_{G'}$  was 1.5 and fitted by three components (Figure 5.10 (a) with FWHM and center positions of all components). Also, 1 or 2-LG was not observed on Ni1 film when graphene growth performed by Method6, but on Ni2 increasing temperature and  $\text{CH}_4$  flow caused to grow 1 or 2-LG grown. GRP75 sample was grown by using Method6 on Ni2 film and 1or 2-LG was observed with broad FWHM (average  $39 \text{ cm}^{-1}$ ). In Figure 5.10 (b), there is another G' band Raman spectrum of GRP75 which has FWHM of  $52 \text{ cm}^{-1}$  and the intensity ratio  $I_G/I_{G'}$  of 1.7, also fitted by three components.

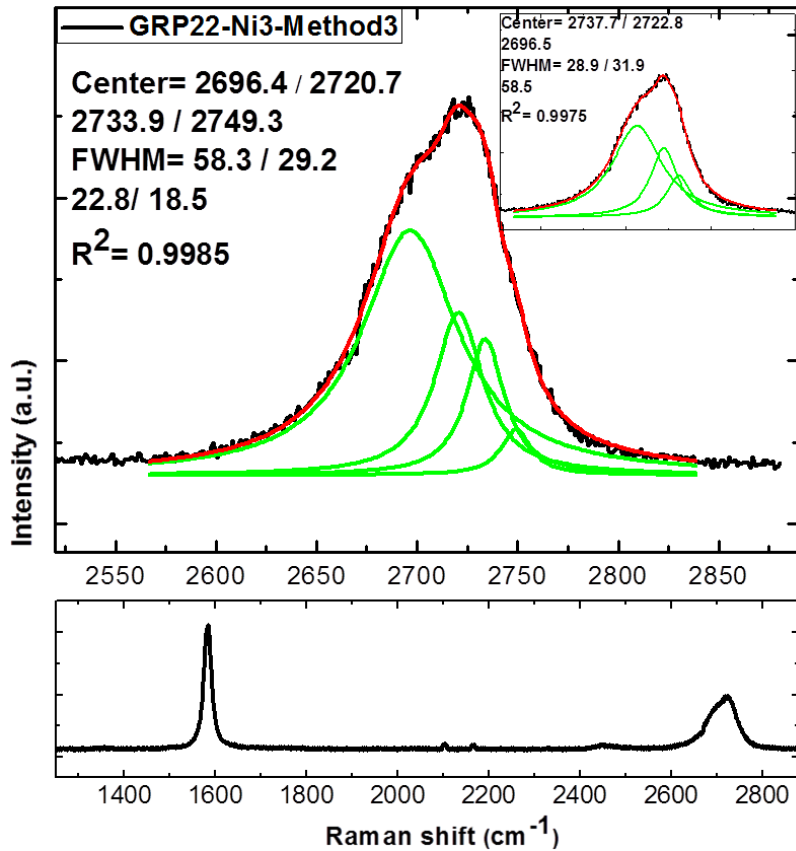


Figure 5.11. G' band Raman spectrum of GRP22 sample which grown on Ni3 sample by Method3. The green lines refer to component of red line which is calculated profile. At the bottom, the whole ranges of the spectra are shown.

For Ni3 film, Method1-3 and 6 gave the narrowest FWHM of G' band and the lowest  $I_G/I_{G'}$  ratio. However, on Ni3 film there were interesting G' band Raman Spectrums which had line shape like AB stacked 4-LG. The AB like G' band line shape was observed mostly from GRP22 and GRP34 samples which were grown by Method3 and 1, respectively. To being AB stacked 4-LG, G' band is fitted by three components. In Figure 5.11, three-component fit is shown in the inset, but the intensities of components decrease from left to right. However, in Figure 3.13, for 4-LG the intensities of the components decrease from right to left. For GRP22, four-component fit gave the best  $R^2$  of 0.9985. The Raman spectrum of GRP22 had FWHM of  $78\text{ cm}^{-1}$  and  $I_G/I_{G'}$  ratio of 2.4. These values refer to more than 2 or multi layer graphene. Also, in Figure 3.15 (b) which belongs to Raman spectra of multilayered graphene on Ni film, it is shown that increasing layer number caused the line shape of G' band distort, exactly as Figure 5.11.

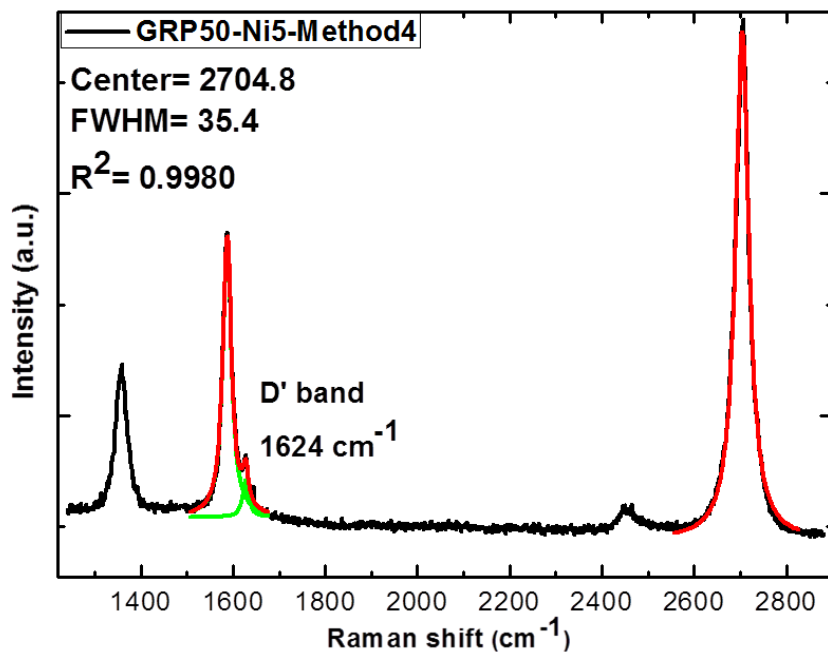


Figure 5.12. Raman spectrum of GRP50 sample which grown on Ni5 substrate by Method4. The green lines refer to component of red line which is calculated profile

For Ni4, Ni5 and Ni6 films, mostly Method1 and 3 provided 1or 2-LG with the intensity ratio  $I_G/I_G'$  of 0.2-0.6 and average FWHM of 32-37  $\text{cm}^{-1}$  when Raman spectra analysis were carried out. GRP63 and GRP77, which were grown by using Method5 and Method6 on Ni4 film, respectively, had remarkable D and D' band intensities. Raman spectrum of GRP50 sample, which was grown by Method4 on Ni5 film had also remarkable D and D' bands (Figure 5.12). Also, GRP91 and GRP122 samples, which were grown by Method7 and Method10 on Ni4 film, had more narrow FWHM and low  $I_G/I_G'$  ratio. GRP64 and GRP65 samples, which were grown by Method6 on Ni5 and Ni6 films, respectively, had denser multilayer graphene than 1or 2-LG.

To sum up for Ni1-6 films, Method1 and Method 3 were more successful than Method4, 5 and 7 to grow 1 or 2-LG on all six films. Thus, cooling rate of 3  $^{\circ}\text{C}/\text{min}$  was more appropriate than 2, 4 and 15  $^{\circ}\text{C}/\text{min}$  rates. Too short and too long cooling rates did not allow carbon atoms precipitate on the surface. The annealing and growth temperature of 800  $^{\circ}\text{C}$  was low, so 1 or 2-LG did not grow by Method2. Reducing  $\text{CH}_4$  flow rate or increasing the growth temperature to 950  $^{\circ}\text{C}$  D and D' band intensities increased, because diffused carbon atoms decreased and they could not well precipitate

on to the Ni film surface. However, increasing CH<sub>4</sub> flow rates with the same other conditions, 1 or 2-LG was much more observed on thicker films.

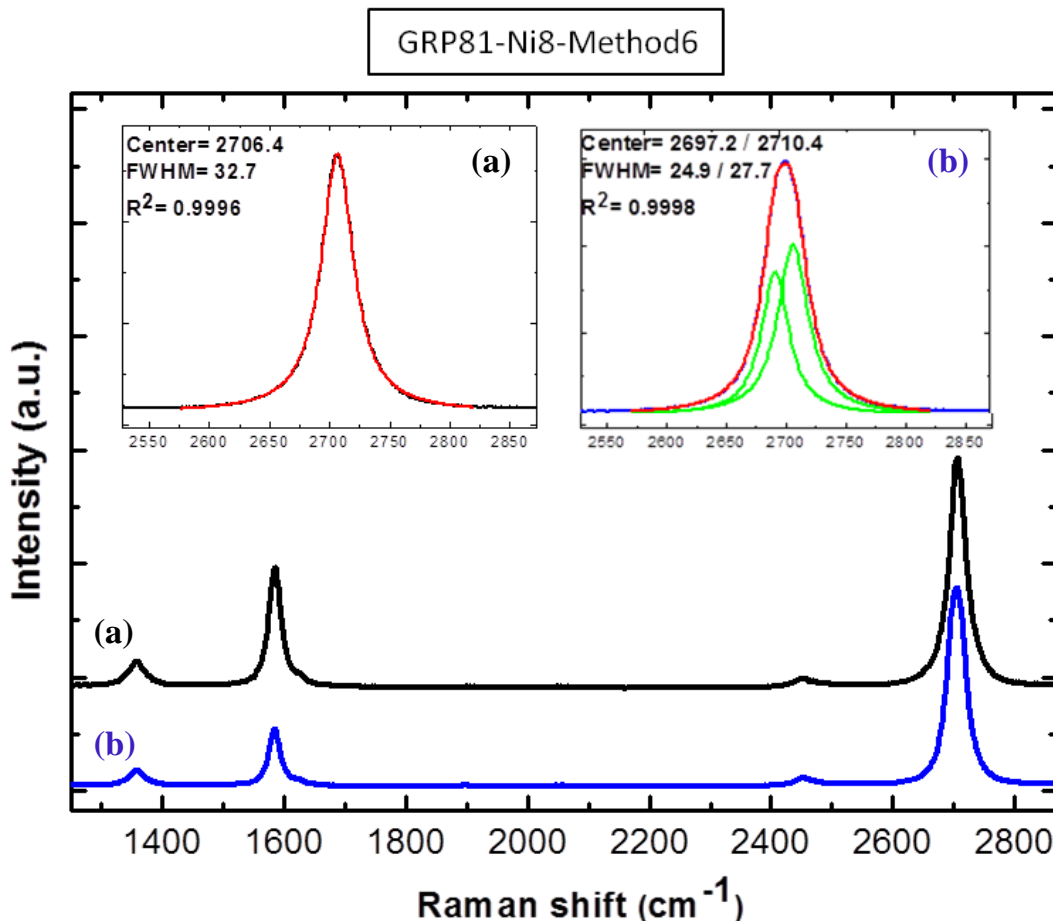


Figure 5.13. Two different Raman spectra of GRP81 sample which were grown on Ni8 film by Method6. The green lines refer to component of red line which is calculated profile in the insets. The inset (a) represent the G' band fit of black spectrum and (b) refer to the G' band fit of blue spectrum.

On Ni7 and Ni8 films using Method3, the narrowest FWHM ( $30\text{-}52\text{ cm}^{-1}$ ) (which had the intensity ratio  $I_G/I_G < 1$ ) values and the lowest  $I_G/I_G$  ratios were observed from Raman spectra of the samples. If just growth temperature increased to 950 °C (Method6), D and D' bands showed up intensely, and FWHM value of G' band increased to  $\sim 58\text{ cm}^{-1}$  for Ni7 film, whereas FWHM value of G' band was  $33\text{-}45\text{ cm}^{-1}$  for Ni8 film. When CH<sub>4</sub> flow rate reduced (Method4 and 5) or both CH<sub>4</sub> flow rate reduced and growth temperature increased (Method7) 1 or 2-LG did not observed on Ni7-8 films. Also, 1 or 2-LG did not grow on to Ni7-8 films when CH<sub>4</sub> flow rate and cooling rate reduced (Method8). If CH<sub>4</sub> flow rate reduced, to observe 1or 2-LG system

should be cooled down faster (Method10). Observed 1or 2-LG had the intensity ratio  $I_G/I_{G'}$ <1 with FWHM  $\sim$ 44 cm<sup>-1</sup> by that way. The intensity ratio  $I_G/I_{G'}$  of blue line is 0.25 and black line is 0.51. 1 or 2-component fit is signature of 1or 2-LG with the intensity ratio  $I_G/I_{G'}$ <1.

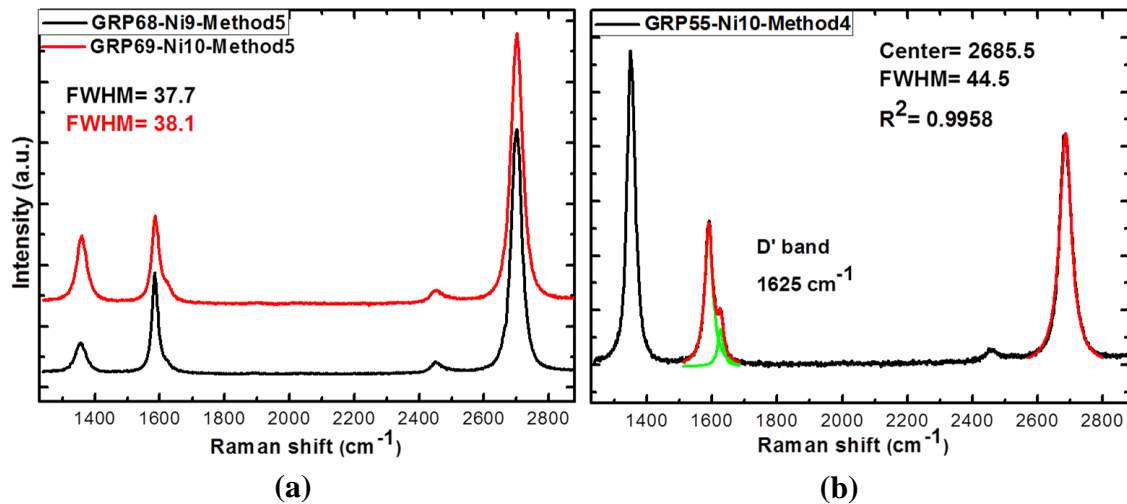


Figure 5.14. G' band Raman spectrum of GRP68 and GRP69 (a) and GRP55 (b) samples which grown on Ni9, Ni10 and Ni10 films; by Method5-5 and Method4, respectively. The green lines refer to component of red line which is calculated profile

Considering all observed Raman spectra, there were no remarkable differences between Methods which were performed on Ni9 and Ni10 films. In Figure 5.14 (a), observed G' band FWHM values are not so narrow. GRP55 and GRP54 samples had the most intense D and D' bands which were grown by Method4. Also, there were no remarkable differences between Methods which were performed on Ni11 and Ni12 films when their Raman spectra compared. However, on these films it was difficult that to find 1or 2-LG when compared with Ni9 and Ni10 films.

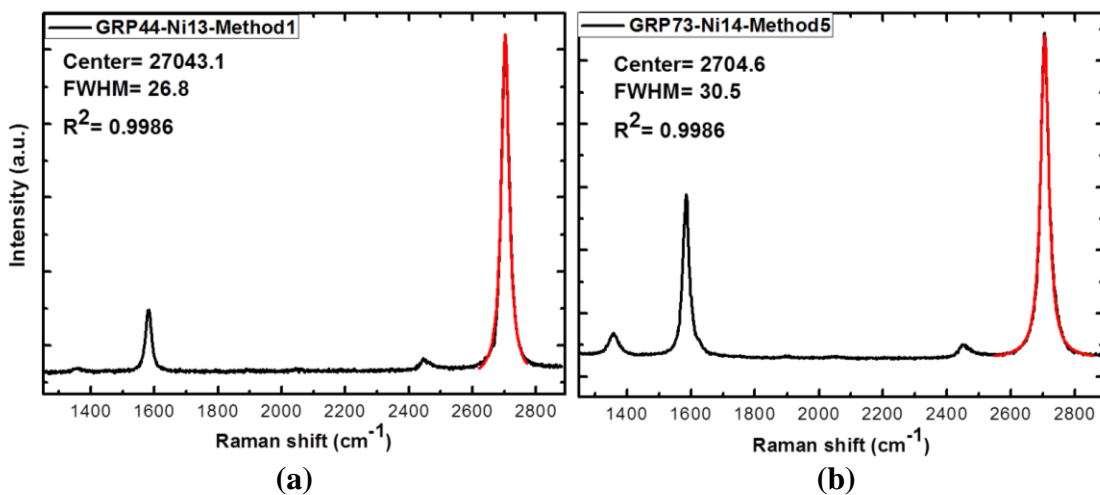


Figure 5.15.  $G'$  band Raman spectrum of GRP44 (a) and GRP73 (b) samples which grown on Ni13 and Ni14 films; by Method1 and Method5, respectively. The red lines refer to calculated profile

There were no remarkable differences between Methods which were performed on Ni9 and Ni10 substrates when all observations from Raman measurements were considered. Figure 5.15 shows Raman spectra from two different samples which were grown on Ni13 and Ni14 films. The FWHM values were so narrow ( $26\text{-}31\text{ cm}^{-1}$ ) when the intensity ratio is  $I_G/I_{G'} < 1$ .

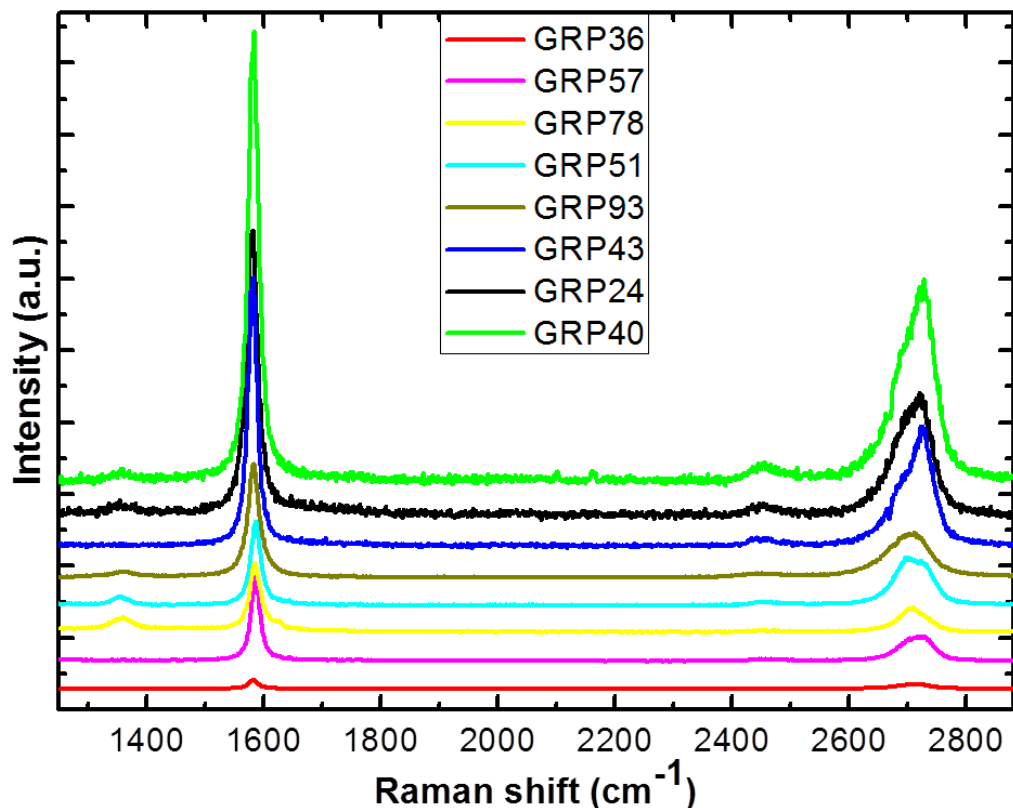


Figure 5.16. Raman spectra of GRP24, GRP36, GRP40, GRP43, GRP51, GRP57, GRP78 and GRP93 samples and G' band line shape distortion

As mentioned in Figure 5.11, more than 2-LG has distorted G' band line shape (Figure 5.16). When fitting G' band of these spectra, the intensity of components were not congruent with AB stacked multilayer graphene which is shown in Figure 3.13. These observations of this study were exactly match the observations of L. M. Gomez de Arco [3] when Raman measurement performed on Ni film (Figure 3.15 (b)).

For Ni15-18 films, different Methods were carried out which are Method11-18 given in Table 5.1. In these methods  $\text{H}_2$  flow was used all CVD process stages. Also,  $\text{CH}_4$  gas was flew into last 10 minutes of annealing instead of 40 minutes. Annealing performed during 1 hour and 30 minutes. Given Method11-18 were very effective on producing 1 or 2-LG.

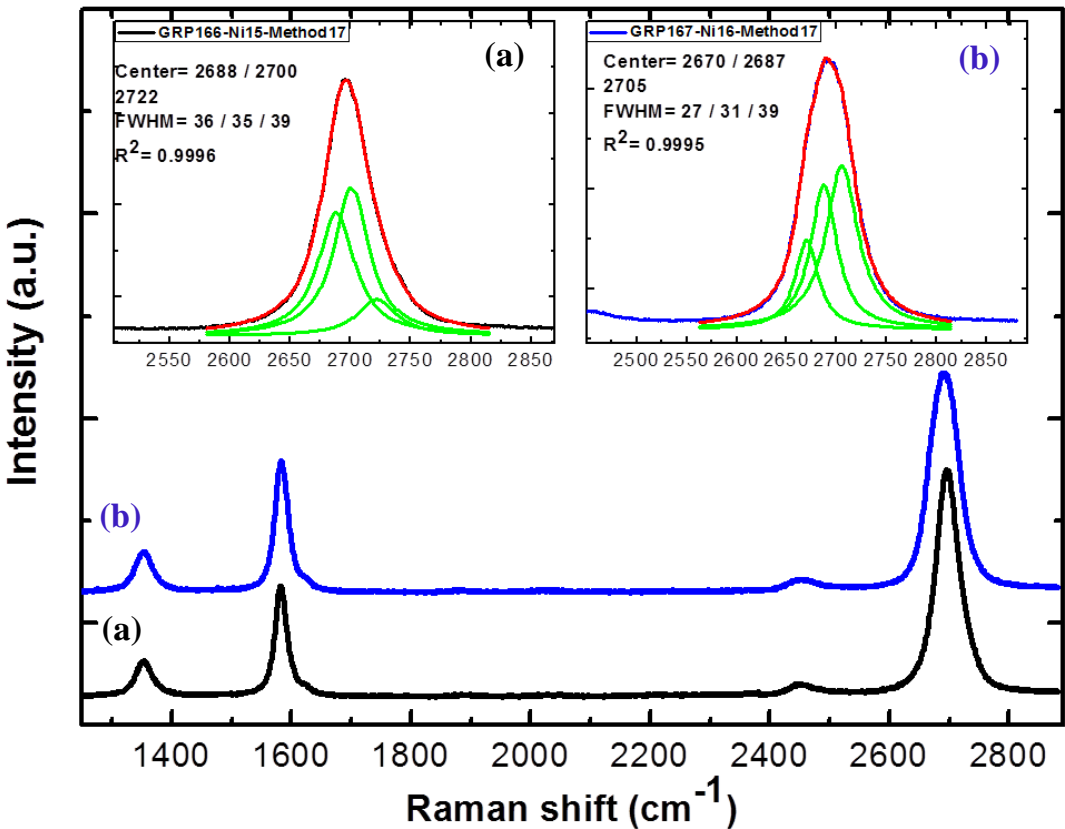


Figure 5.17. Two different Raman spectra of GRP166 and GRP167 samples which grown on Ni15 and Ni16 films by Method17. The green lines refer to component of red line which is calculated profile in the insets. The inset (a) represent the G' band fit of black spectrum and (b) refer to the G' band fit of blue spectrum

The Raman spectra of GRP166 and GRP167 samples, which were grown on Ni15 and Ni16 films by Method17, are shown in Figure 5.17. For these samples, one or two-component fit were not well matched, so at least three peaks were used to fit of G' band. The FWHM values were so broaden ( $45-60\text{ cm}^{-1}$ ) when the intensity ratio was  $I_G/I_G < 1$ . For GRP164 and GRP165 samples, which were grown on Ni17 and Ni18 films by Method17, FWHM values were maximum  $42\text{ cm}^{-1}$  when the intensity ratio was  $I_G/I_G < 1$ , and their G' bands were fitted at most by one or two component. When we used Method18 to growth graphene on Ni15-18 films, 1 or 2-LG was observed less than Method17. If annealing time was decreased to 30 minutes, so using Method15 and 16 to grow 1or 2-LG on Ni15-18 films, observed FWHM of G' band reduced ( $35\text{ cm}^{-1}$ ) when the intensity ratio  $I_G/I_G < 1$ . GRP148-151 samples were grown by speed up the cooling rate to  $5\text{ }^{\circ}\text{C/min}$ , but neither 1 or 2-LG or multilayer graphene could not observe from Raman measurements.

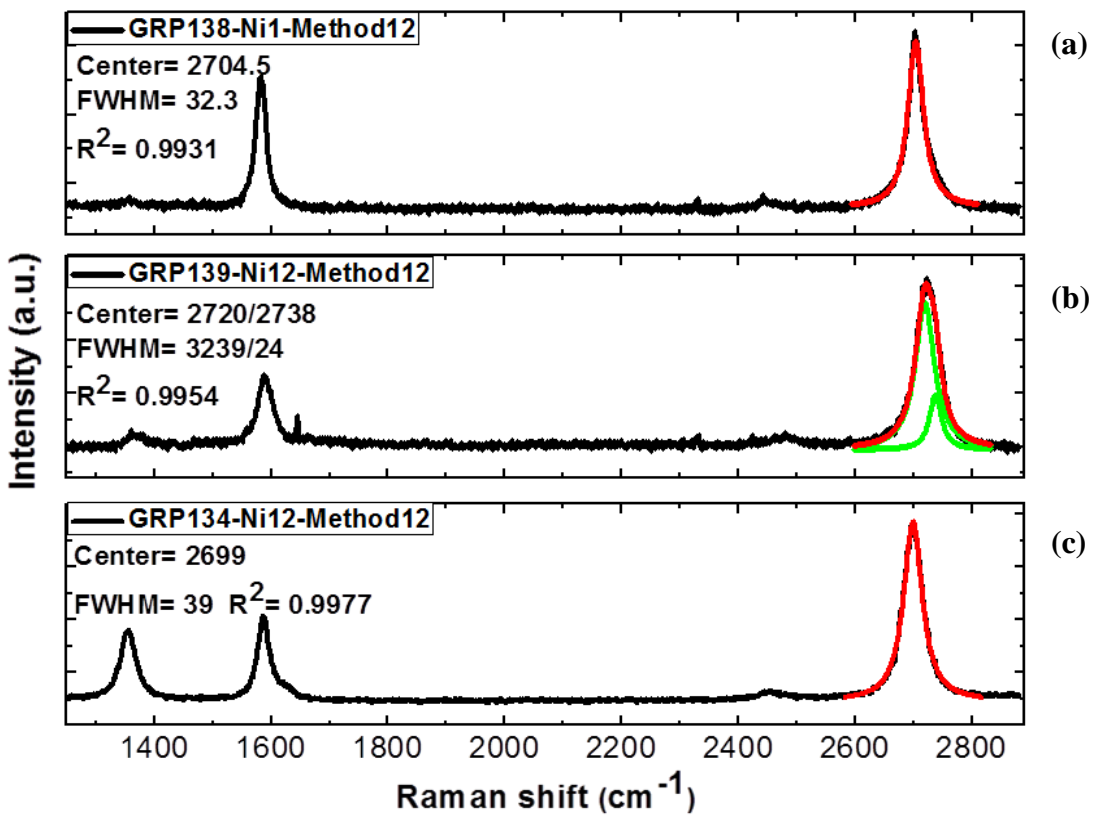


Figure 5.18. Raman spectra of GRP138, GRP139 and GRP134 samples which were grown on Ni1, Ni12 and Ni12 films by Method12, 12 and 11, respectively. The green lines refer to component of red lines which are calculated profiles

To decide the medium cooling rate to grow 1 or 2-LG different cooling rates were performed. Even using very fast cooling rates like 15 °C/min (Method12), 1 or 2-LG on Ni1 film, which was the thinnest nickel film, was observed (Figure 5.18 (a)). Also the FWHM values of G' bands were narrow ( $\sim 30 \text{ cm}^{-1}$ ). Using the same cooling rate (Method12), 1 or 2-LG was grown on Ni12 film; this was thicker than Ni1 film. However, on Ni15-18 films 1 or 2-LG were not observed when the growth carried out using this fast cooling rate. When cooling rate slows down graphene was observed on also Ni15-18 films.

### 5.3. SEM Results

To figure out the number of layers from contrast difference and Carbon element weight percentage SEM and EDX analysis performed, respectively, after graphene

growth by CVD on Ni films. However, EDX results did not provide reliable results due to penetration problem. The carbon percentages were not compatible with the contrast.

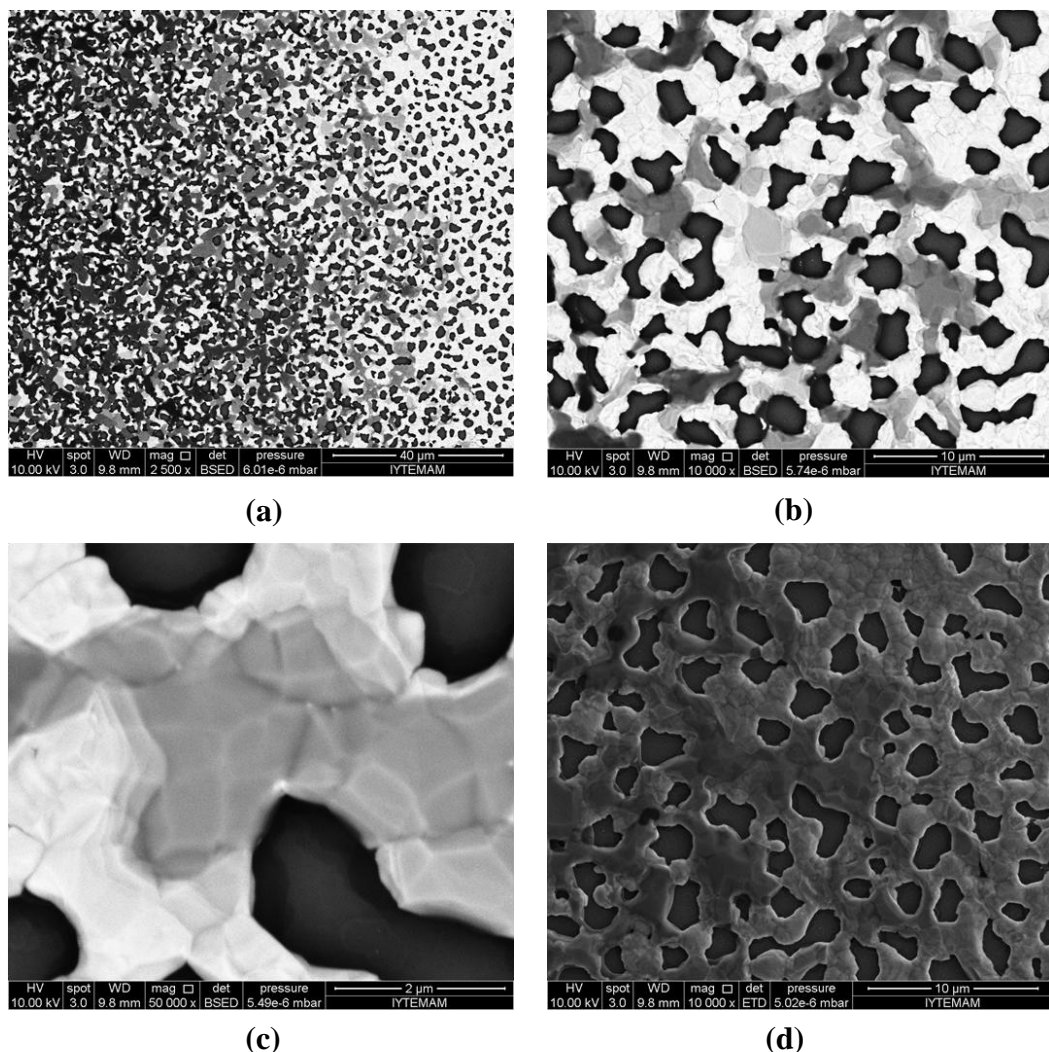


Figure 5.19. SEM images of GRP23 sample with 2500x (a), 10000x (b), 50000x (c) and 10000x (d) magnifications

SEM images of GRP23 sample which was grown on Ni4 film with Method3 are shown in Figure 5.19. Figure 5.19 (b) and (d) have same magnification but different contrasts. Especially from Figure 5.19 (c) the grain boundary regions are seen. As seen if the grain sizes larger so we can grow larger size graphene on Ni garains. Some parts of the film smoother, but some parts formed as islands away from each other. On and between these islands the carbon accumulated more than smoother parts due to the boundary grooves. This effect is seen from Figure 5.19 (a), darker parts like islands away from each other on the left.

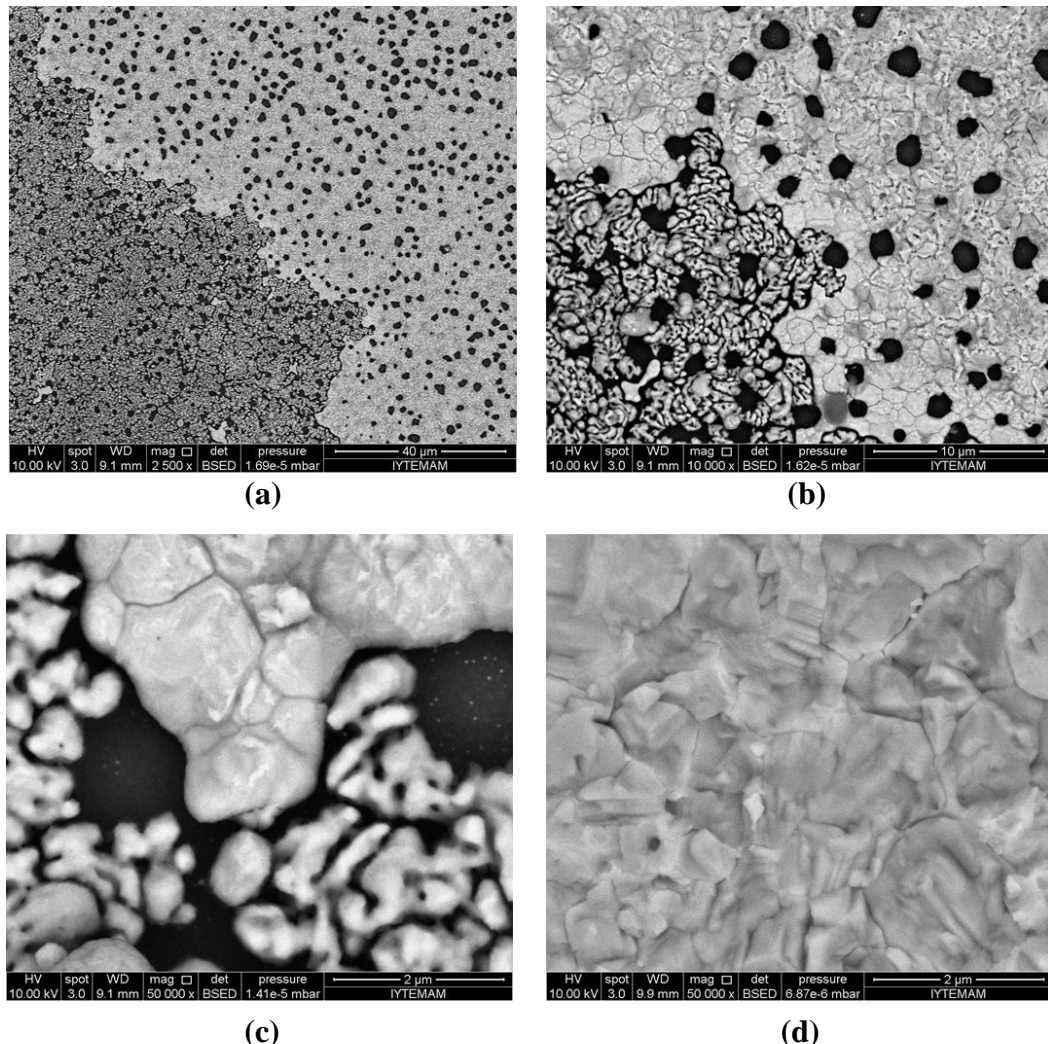


Figure 5.20. SEM image of GRP28 sample with 2500x (a), 10000x (b) and 10000x (c, d) magnifications

In Figure 5.20 SEM images of GRP28 sample, which was grown on Ni9 film with Method3, are shown. Grain boundary grooves, which were deep and away from each other caused accumulation of more carbon atoms and this effect is seen from left of Figure 5.20 (a, b). Grooves had much more carbon atoms and looked darker from smooth parts of the film. So, this is in accordance with the fact that, which was mentioned at the beginning of the Chapter 4, 1 or few-LG can be grown mostly on smooth parts of the film [3]. When grown graphene layers on Ni4 film (230 nm, Figure 5.19), and Ni9 film (400 nm, Figure 5.20) were compared, it can be concluded that the thicker film less affected from dewetting of Ni and had smoother parts (Figure 5.20 (d)).

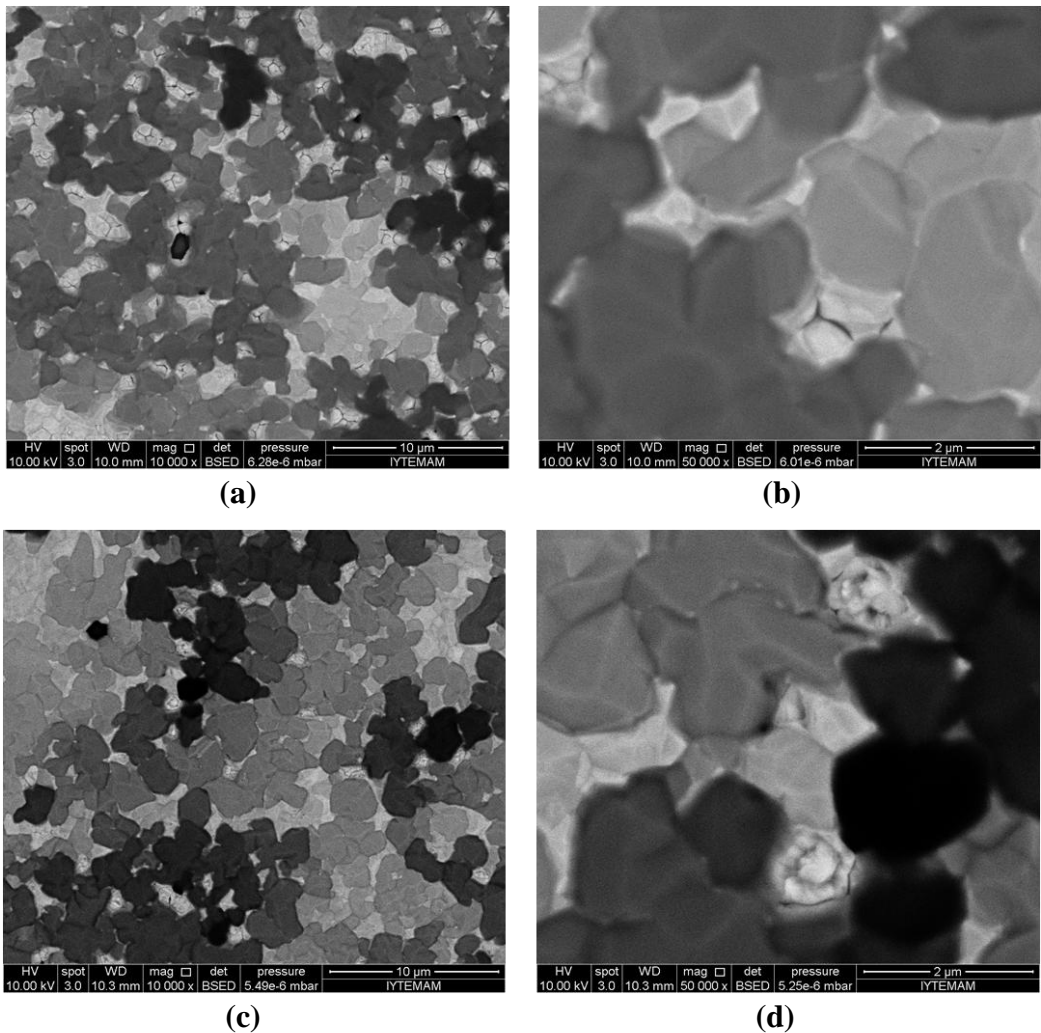


Figure 5.21. SEM image of SEM image of GRP30 sample (a, b) and GRP31 sample (c, d) with 10000x (a, c), 50000x (b, d) magnifications

GRP30 and GRP31 samples, which were grown on Ni11 and Ni12 films, respectively, with Method3, are shown in Figure 5.21. These films had no buffer layers and also their surface roughness and groove depths were greater than Ni9 and Ni10 films which had  $\text{Al}_2\text{O}_3$  buffer layers. As seen their SEM images (Figure 5.21), these films have much darker parts on the surface than Figure 5.20 because of the deeper grooves. When SEM images of GRP28 and GRP30-31 samples, which were grown by the same method, were compared, it can be concluded that the buffer effected the surface roughness and groove depth and resulting number of graphene layer (Figure 5.20 (d) and Figure 5.21 (b, d)).

## CHAPTER 6

### CONCLUSIONS

In this work, the aim was to identify the influence of Ni structural properties such as crystallinity, surface roughness and interface boundaries on the formation of graphene grown by CVD. To grow large area and single layer graphene on the Ni substrate should be mostly (111) direction and as smooth as possible without deep grain boundary regions. For that purpose, different deposition parameters were studied to growth Ni and buffered Ni thin films with various thicknesses by magnetron sputtering technique on Si/SiO<sub>2</sub> substrates. Both asgrown and annealed films examined by X-ray Diffraction (XRD) and Atomic Force Microscopy (AFM) techniques. After graphene growth by CVD, Raman spectroscopy was utilized in order to determine the number of the layers and quality of graphene growth over Ni catalyst film.

First, six Ni thin films deposited under 3 mTorr pressure using different deposition conditions by DCMS. Their thicknesses and columnar structure identified by cross sectional SEM images. According to the results of XRD increasing annealing temperature increased the textured (111) direction and grain sizes of polycrystalline Ni. When these samples were annealed at 900°C, intensity of (111) peak of Ni1-2-5 samples increased, significantly. The other films preserve their polycrystalline structures. To get mostly textured in (111) direction, power and thickness should be low as soon as possible at 3mTorr deposition pressure. According to the AFM results, increasing thickness of the Ni film increased the surface roughness and mean height which refer to groove boundary depth of grains of the film.

Then, in order to decrease the surface roughness and dewetting of the Ni film Al<sub>2</sub>O<sub>3</sub> buffer layer film deposited by RFMS and DCMS at 7 mTorr pressure. The thinnest (100 nm) buffered Ni films have the highest surface roughness and mean height values. The thinner buffer layer improved the crystallinity of the Ni film more than thicker buffer layer. Thicker Ni film (400 nm) on Al<sub>2</sub>O<sub>3</sub> film decreased the surface roughness and mean height, significantly. We compared the results with depositing non-buffered and same thick Ni films, so thin layer of Al<sub>2</sub>O<sub>3</sub> supports and help to decrease roughness of thick Ni films best. The why is that Al<sub>2</sub>O<sub>3</sub> has porous structure and causes

interface so many defects between itself and Ni. Increasing thickness causes to reduce these defects and resulting film surface become smoother.

We also deposited Ni films by heating at 450 °C. These polycrystalline films have (200) direction more than (111), and their roughness and mean height values higher than unheated films which have same thickness.

Last, four different non-heated and heated at 450 °C, Cr and Cr/Al<sub>2</sub>O<sub>3</sub> buffered samples deposited by MS at 6.9 mTorr pressure. Cr buffer led to more intense formation of crystalline Ni (111) grains. Also, Cr buffer prevented texture in (200) direction for heated deposited samples. But surface roughness and mean height values were high. Both 30 minutes and 60 minutes annealing time were carried out and we observed increased annealing improved crystallinity.

To sum up, a thin layer of Al<sub>2</sub>O<sub>3</sub> buffer reduce the roughness and depth of boundary regions for thicker Ni films. Cr buffer help texturing in (111) direction of Ni.

Graphene growths by CVD were carried out at 800 °C, 900 °C and 950 °C. We performed Raman spectroscopy technique to identify graphene, but we did not observe graphene on Ni films which grown at 800 °C by CVD. So, we just sustained XRD and AFM measurements for the samples which were annealed at 900 °C and 950 °C. CVD process performed for first 14 samples. During heating and pretreatment stages just Ar flew into the tube and Ar and Hydrogen was added to different flow rates of methane during growth at ambient pressure. The last stage, cooling, run under just Ar flow. Raman spectroscopy performed on growth films on Ni substrate by CVD for these methods, and grown graphene layers were not denser on the surface. For last four samples CVD process performed with Hydrogen flow in all stages and Raman spectrums showed us grown graphene layers on these films were denser.

Increasing groove boundary depth increased the formation of multilayer graphene on the surface, because gathering carbon impurities increase at deeper boundary regions. So, we got more Raman spectra which belong to multilayer graphene from the films have deeper boundary regions. Reducing methane flow rate and increasing growth temperature led to observe more intense defect peaks by Raman spectroscopy. Increasing thickness cause broaden FWHM values of 1or 2-LG G' band. Also, FWHM value of 1 or 2-LG G' band is more tight which obtained from graphene grown on thinner Ni films. G' band FWHM values of 1or 2-LG were found as ~24-60 cm<sup>-1</sup> which obtained from Raman spectra which belong to the intensity ratio I<sub>G</sub>/I<sub>G'</sub><1. We fit G' band by one or two components. The FWHM values of each component were

$\sim$ 24-40  $\text{cm}^{-1}$ . 1 or 2 component fit with the best fitting quality ( $R^2=0.99$ ) and the intensity ratio  $I_G/I_G < 1$  are signature of 1or 2-LG because Raman measurement sustained on Ni substrate. So, we could not decide exactly to the stacking order and layer number just using Raman spectroscopy, but we can say given parameters belong to 1 or 2 layer graphene. Also, G' bands, which belong to more than 2-LG and have the intensity ratio of  $I_G/I_G > 1$ , were fitted by at least three components.

As a conclusion, minimum surface roughness and groove depth of grains obtained by depositing a thin layer of  $\text{Al}_2\text{O}_3$  buffer. Ni (111) crystal direction which is necessary to growth graphene on was mostly textured by depositing Cr buffer and increasing annealing temperature. Raman spectroscopy results showed that multilayered graphene grown mostly rough samples. Using Hydrogen in growth process improved the density of grown graphene on Ni catalyst.

## REFERENCES

- [1] V. Adamyan, V. Zavalniuk, Phonons in graphene with point defects, *Journal of Physics: Condensed Matter*, 23 (2010) 015402.
- [2] A. Neto, K. Novoselov, New directions in science and technology: two-dimensional crystals, *Reports on Progress in Physics*, 74 (2011) 82501-82509.
- [3] L.M. Gomez de Arco, Graphene and carbon nanotubes: synthesis, characterization and applications for beyond silicon electronics, (2010).
- [4] A. Reina, S. Thiele, X. Jia, S. Bhaviripudi, M.S. Dresselhaus, J.A. Schaefer, J. Kong, Growth of large-area single-and bi-layer graphene by controlled carbon precipitation on polycrystalline Ni surfaces, *Nano Research*, 2 (2009) 509-516.
- [5] H.O. Pierson, *Handbook of Carbon, Graphite, Diamond and Fullerenes - Properties, Processing and Applications*, William Andrew Publishing/Noyes, 1993.
- [6] M.I. Katsnelson, Graphene: carbon in two dimensions, *Materials today*, 10 (2007) 20-27.
- [7] A. İnce, Growth and characterization of carbon nanotubes over Co-Mo/MgO catalysts, (2010).
- [8] A. Mostofizadeh, Y. Li, B. Song, Y. Huang, Synthesis, Properties, and Applications of Low-Dimensional Carbon-Related Nanomaterials, *Journal of Nanomaterials*, 2011 (2011) 21.
- [9] J.-M. Bonard, Carbon nanostructures by hot filament chemical vapor deposition: Growth, properties, applications, *Thin Solid Films*, 501 (2006) 8-14.
- [10] K. Novoselov, A. Geim, S. Morozov, D. Jiang, Y. Zhang, S. Dubonos, I. Grigorieva, A. Firsov, Electric field effect in atomically thin carbon films, *Science*, 306 (2004) 666-669.
- [11] Nanostructured Carbon for Advanced Applications, Kluwer Academic Publishers, Netherlands, 2001.
- [12] V.P. Verma, Enhanced zinc oxide and graphene nanostructures for electronics and sensing applications, (2010).
- [13] J. Hass, W. De Heer, E. Conrad, The growth and morphology of epitaxial multilayer graphene, *Journal of Physics: Condensed Matter*, 20 (2008) 323202.
- [14] M. Birowska, K. Milowska, J. Majewski, Van Der Waals Density Functionals for Graphene Layers and Graphite.

- [15] Y. Shibuta, J.A. Elliott, Interaction between two graphene sheets with a turbostratic orientational relationship, *Chemical Physics Letters*, 512 (2011) 146-150.
- [16] J.-S. Hwang, Y.-H. Lin, J.-Y. Hwang, R. Chang, S. Chattopadhyay, C.-J. Chen, P. Chen, H.-P. Chiang, T.-R. Tsai, L.-C. Chen, Imaging layer number and stacking order through formulating Raman fingerprints obtained from hexagonal single crystals of few layer graphene, *Nanotechnology*, 24 (2013) 015702.
- [17] C.E. Baddour, C. Briens, Carbon nanotube synthesis: a review, *International journal of chemical reactor engineering*, 3 (2005).
- [18] C. Frondel, U.B. Marvin, Lonsdaleite, a hexagonal polymorph of diamond, (1967).
- [19] M.H. Sluiter, Y. Kawazoe, Cluster expansion method for adsorption: Application to hydrogen chemisorption on graphene, *Physical Review B*, 68 (2003) 085410.
- [20] [www.rsc.org/chemistryworld/News/2009/January/29010902.asp](http://www.rsc.org/chemistryworld/News/2009/January/29010902.asp), Graphene to graphane by chemical conversion, in, 2009.
- [21] J.O. Sofo, A.S. Chaudhari, G.D. Barber, Graphane: A two-dimensional hydrocarbon, *Physical Review B*, 75 (2007) 153401.
- [22] X.-D. Wen, L. Hand, V. Labet, T. Yang, R. Hoffmann, N. Ashcroft, A.R. Oganov, A.O. Lyakhov, Graphane sheets and crystals under pressure, *Proceedings of the National Academy of Sciences*, 108 (2011) 6833-6837.
- [23] D. Elias, R. Nair, T. Mohiuddin, S. Morozov, P. Blake, M. Halsall, A. Ferrari, D. Boukhvalov, M. Katsnelson, A. Geim, Control of graphene's properties by reversible hydrogenation: evidence for graphane, *Science*, 323 (2009) 610-613.
- [24] D. Boukhvalov, M. Katsnelson, A. Lichtenstein, Hydrogen on graphene: Electronic structure, total energy, structural distortions and magnetism from first-principles calculations, *Physical Review B*, 77 (2008) 035427.
- [25] R. Baughman, H. Eckhardt, M. Kertesz, Structure-property predictions for new planar forms of carbon: Layered phases containing sp<sup>2</sup> and sp atoms, *The Journal of chemical physics*, 87 (1987) 6687.
- [26] Z. Liu, G. Yu, H. Yao, L. Liu, L. Jiang, Y. Zheng, A simple tight-binding model for typical graphyne structures, *New Journal of Physics*, 14 (2012) 113007.
- [27] D. Malko, C. Neiss, F. Viñes, A. Görling, Competition for Graphene: Graphynes with Direction-Dependent Dirac Cones, *Physical Review Letters*, 108 (2012) 86804.
- [28] J.A. Marsden, G.J. Palmer, M.M. Haley, Synthetic Strategies for Dehydrobenzo [n] annulenes, *European Journal of Organic Chemistry*, 2003 (2003) 2355-2369.

- [29] Y. Kehan, B. Zheng, L. Ganhua, M. Shun, C. Shumao, Z. Yanwu, C. Xinqi, R. Rodney, C. Junhong, Growth of carbon nanowalls at atmospheric pressure for one-step gas sensor fabrication, *Nanoscale Research Letters*, 6 (2011).
- [30] Y. Wu, P. Qiao, T. Chong, Z. Shen, Carbon nanowalls grown by microwave plasma enhanced chemical vapor deposition, *Advanced Materials*, 14 (2002) 64-67.
- [31] Y. Wu, B. Yang, B. Zong, H. Sun, Z. Shen, Y. Feng, Carbon nanowalls and related materials, *J. Mater. Chem.*, 14 (2004) 469-477.
- [32] A. Malesevic, R. Kemps, A. Vanhulsel, M.P. Chowdhury, A. Volodin, C. Van Haesendonck, Field emission from vertically aligned few-layer graphene, *Journal of applied physics*, 104 (2008) 084301-084301-084305.
- [33] O. Shenderova, V. Zhirnov, D. Brenner, Carbon nanostructures, *Critical Reviews in Solid State and Material Sciences*, 27 (2002) 227-356.
- [34] A. Vetushka, T. Itoh, Y. Nakanishi, A. Fejfar, S. Nonomura, M. Ledinský, J. Kočka, Conductive atomic force microscopy on carbon nanowalls, *Journal of Non-Crystalline Solids*, 358 (2012) 2545-2547.
- [35] K. Shiji, M. Hiramatsu, A. Enomoto, M. Nakamura, H. Amano, M. Hori, Vertical growth of carbon nanowalls using rf plasma-enhanced chemical vapor deposition, *Diamond and related materials*, 14 (2005) 831-834.
- [36] S. Vizireanu, L. Nistor, M. Haupt, V. Katzenmaier, C. Oehr, G. Dinescu, Carbon Nanowalls Growth by Radiofrequency Plasma-Beam-Enhanced Chemical Vapor Deposition, *Plasma Processes and Polymers*, 5 (2008) 263-268.
- [37] T. Itoh, S. Shimabukuro, S. Kawamura, S. Nonomura, Preparation and electron field emission of carbon nanowall by Cat-CVD, *Thin solid films*, 501 (2006) 314-317.
- [38] T. Mori, M. Hiramatsu, K. Yamakawa, K. Takeda, M. Hori, Fabrication of carbon nanowalls using electron beam excited plasma-enhanced chemical vapor deposition, *Diamond and Related Materials*, 17 (2008) 1513-1517.
- [39] S. Watcharotone, R. Ruoff, F. Read, Possibilities for graphene for field emission: modeling studies using the BEM, *Physics Procedia*, 1 (2008) 71-75.
- [40] G. Takyo, S. Kono, T. Goto, H. Sasaoka, K. Nishimura, Origin of field emission from a nano-diamond/carbon nanowall electron emitter, *Japanese Journal of Applied Physics*, 47 (2008) 2241.
- [41] O. Tanaike, N. Kitada, H. Yoshimura, H. Hatori, K. Kojima, M. Tachibana, Lithium insertion behavior of carbon nanowalls by dc plasma CVD and its heat-treatment effect, *Solid State Ionics*, 180 (2009) 381-385.

- [42] T.-C. Hung, C.-F. Chen, W.-T. Whang, Deposition of carbon nanowall flowers on two-dimensional sheet for electrochemical capacitor application, *Electrochemical and Solid-State Letters*, 12 (2009) K41-K44.
- [43] U. Meier, Carbon fiber-reinforced polymers: modern materials in bridge engineering, *Structural Engineering International*, 2 (1992) 7-12.
- [44] T.Y. Hughes, Charles Roland Chambers, in, Google Patents, 1889.
- [45] Y. Zhu, Z.J. Sui, T. Zhao, Y.C. Dai, Z.M. Cheng, W. Yuan, Modeling of fishbone-type carbon nanofibers: a theoretical study, *Carbon*, 43 (2005) 1694-1699.
- [46] J. Huang, Y. Liu, T. You, Carbon nanofiber based electrochemical biosensors: A review, *Analytical Methods*, 2 (2010) 202-211.
- [47] A. Carol, K. Laubernds, N.M. Rodriguez, R.T.K. Baker, Graphite nanofibers as an electrode for fuel cell applications, *The Journal of Physical Chemistry B*, 105 (2001) 1115-1118.
- [48] N.M. Rodriguez, A. Chambers, R.T.K. Baker, Catalytic engineering of carbon nanostructures, *Langmuir*, 11 (1995) 3862-3866.
- [49] P. Serp, M. Corrias, P. Kalck, Carbon nanotubes and nanofibers in catalysis, *Applied Catalysis A: General*, 253 (2003) 337-358.
- [50] V. Choudhary, A. Gupta, *Polymer/Carbon Nanotube Nanocomposites*, (2011).
- [51] S. Iijima, Helical microtubules of graphitic carbon, *nature*, 354 (1991) 56-58.
- [52] S. Iijima, T. Ichihashi, Single-shell carbon nanotubes of 1-nm diameter, (1993).
- [53] H.-S.P. Wong, D. Akinwande, *Carbon nanotube and graphene device physics*, Cambridge University Press, 2010.
- [54] K.H. An, Y.H. Lee, Electronic-structure engineering of carbon nanotubes, *Nano*, 1 (2006) 115-138.
- [55] H. Dai, Carbon nanotubes: opportunities and challenges, *Surface Science*, 500 (2002) 218-241.
- [56] C.T. White, T.N. Todorov, Carbon nanotubes as long ballistic conductors, *Nature*, 393 (1998) 240-242.
- [57] M. Paradise, T. Goswami, Carbon nanotubes—Production and industrial applications, *Materials & design*, 28 (2007) 1477-1489.
- [58] L.T. Scott, Fragments of fullerenes: novel syntheses, structures and reactions, *Pure and applied chemistry*, 68 (1996) 291-300.

- [59] H.W. Kroto, J.R. Heath, S.C. O'Brien, R.F. Curl, R.E. Smalley, C 60: buckminsterfullerene, *Nature*, 318 (1985) 162-163.
- [60] A. Sygula, G. Xu, Z. Marcinow, P.W. Rabideau, ‘Buckybowls’—introducing curvature by solution phase synthesis, *Tetrahedron*, 57 (2001) 3637-3644.
- [61] G. Mehta, G. Panda, A new synthesis of corannulene, *Tetrahedron letters*, 38 (1997) 2145-2148.
- [62] G. Sun, M. Kertesz, Theoretical  $^{13}\text{C}$  NMR spectra of IPR isomers of fullerene  $\text{C}_{80}$ : a density functional theory study, *Chemical Physics Letters*, 328 (2000) 387-395.
- [63] D. Wang, C. Zhao, G. Xin, D. Hou, Theoretical study on the derivatives of the nonclassical seven-membered ring fullerene  $\text{C}_{100}$ , *Journal of Molecular Structure: THEOCHEM*, 952 (2010) 120-123.
- [64] L. Xu, W. Cai, X. Shao, Systematic search for energetically favored isomers of large fullerenes  $\text{C}_{122}$ - $\text{C}_{130}$  and  $\text{C}_{162}$ - $\text{C}_{180}$ , *Computational Materials Science*, 41 (2008) 522-528.
- [65] R.S. Ruoff, D.C. Lorents, B. Chan, R. Malhotra, S. Subramoney, Single crystal metals encapsulated in carbon nanoparticles, *SCIENCE-NEW YORK THEN WASHINGTON-*, 259 (1993) 346-346.
- [66] R.S. Lewis, T. Ming, J.F. Wacker, E. Anders, E. Steel, Interstellar diamonds in meteorites, *Nature*, 326 (1987) 160-162.
- [67] D. Ugarte, Curling and closure of graphitic networks under electron-beam irradiation, *Nature*, 359 (1992) 707-709.
- [68] P. Wallace, The band theory of graphite, *Physical Review*, 71 (1947) 622.
- [69] B. Lang, A LEED study of the deposition of carbon on platinum crystal surfaces, *Surface Science*, 53 (1975) 317-329.
- [70] E. Rokuta, Y. Hasegawa, A. Itoh, K. Yamashita, T. Tanaka, S. Otani, C. Oshima, Vibrational spectra of the monolayer films of hexagonal boron nitride and graphite on faceted Ni (755), *Surface science*, 427 (1999) 97-101.
- [71] L.D. Landau, E.M. Lifshitz, L.P. Pitaevskii, *Statistical physics*, Pergamon Press, , Oxford ; New York,, 1980.
- [72] N.D. Mermin, H. Wagner, Absence of ferromagnetism or antiferromagnetism in one-or two-dimensional isotropic Heisenberg models, *Physical Review Letters*, 17 (1966) 1133-1136.
- [73] A. Fasolino, J. Los, M. Katsnelson, Intrinsic ripples in graphene, *Nature Materials*, 6 (2007) 858-861.

- [74] R. Nair, P. Blake, A. Grigorenko, K. Novoselov, T. Booth, T. Stauber, N. Peres, A. Geim, Fine structure constant defines visual transparency of graphene, *Science*, 320 (2008) 1308-1308.
- [75] K. Novoselov, A.K. Geim, S. Morozov, D. Jiang, M.K.I. Grigorieva, S. Dubonos, A. Firsov, Two-dimensional gas of massless Dirac fermions in graphene, *Nature*, 438 (2005) 197-200.
- [76] K. Novoselov, D. Jiang, F. Schedin, T. Booth, V. Khotkevich, S. Morozov, A. Geim, Two-dimensional atomic crystals, *Proceedings of the National Academy of Sciences of the United States of America*, 102 (2005) 10451-10453.
- [77] F. Schedin, A. Geim, S. Morozov, E. Hill, P. Blake, M. Katsnelson, K. Novoselov, Detection of individual gas molecules adsorbed on graphene, *Nature materials*, 6 (2007) 652-655.
- [78] A.K. Geim, Nobel lecture: Random walk to graphene, *Reviews of Modern Physics*, 83 (2011) 851.
- [79] L. Falkovsky, Phonon dispersion in graphene, *Journal of Experimental and Theoretical Physics*, 105 (2007) 397-403.
- [80] D.R. Cooper, B. D'Anjou, N. Ghattamaneni, B. Harack, M. Hilke, A. Horth, N. Majlis, M. Massicotte, L. Vandsburger, E. Whiteway, Experimental review of graphene, (2011).
- [81] Z. Ni, H. Wang, J. Kasim, H. Fan, T. Yu, Y. Wu, Y. Feng, Z. Shen, Graphene thickness determination using reflection and contrast spectroscopy, *Nano letters*, 7 (2007) 2758-2763.
- [82] A. Ferrari, J. Meyer, V. Scardaci, C. Casiraghi, M. Lazzeri, F. Mauri, S. Piscanec, D. Jiang, K. Novoselov, S. Roth, Raman spectrum of graphene and graphene layers, *Physical Review Letters*, 97 (2006) 187401.
- [83] M.H. Huntley, Transport studies on CVD-grown graphene, in, Massachusetts Institute of Technology, 2009.
- [84] Y. Zhu, S. Murali, W. Cai, X. Li, J.W. Suk, J.R. Potts, R.S. Ruoff, Graphene and graphene oxide: synthesis, properties, and applications, *Advanced materials*, 22 (2010) 3906-3924.
- [85] S. Morozov, K. Novoselov, M. Katsnelson, F. Schedin, D. Elias, J. Jasdzczak, A. Geim, Giant intrinsic carrier mobilities in graphene and its bilayer, *Physical Review Letters*, 100 (2008) 16602.
- [86] X. Du, I. Skachko, A. Barker, E.Y. Andrei, Approaching ballistic transport in suspended graphene, *Nature Nanotechnology*, 3 (2008) 491-495.

- [87] J.-H. Chen, C. Jang, S. Xiao, M. Ishigami, M.S. Fuhrer, Intrinsic and extrinsic performance limits of graphene devices on SiO<sub>2</sub>, *Nature nanotechnology*, 3 (2008) 206-209.
- [88] K.I. Bolotin, K. Sikes, Z. Jiang, M. Klima, G. Fudenberg, J. Hone, P. Kim, H. Stormer, Ultra-high electron mobility in suspended graphene, *Solid State Communications*, 146 (2008) 351-355.
- [89] W. Liu, Z. Wang, Q. Shi, J. Yang, F. Liu, Band-gap scaling of graphene nanohole superlattices, *Physical Review B*, 80 (2009) 233405.
- [90] Y. Zhang, T.-T. Tang, C. Girit, Z. Hao, M.C. Martin, A. Zettl, M.F. Crommie, Y.R. Shen, F. Wang, Direct observation of a widely tunable bandgap in bilayer graphene, *Nature*, 459 (2009) 820-823.
- [91] M.Y. Han, B. Özyilmaz, Y. Zhang, P. Kim, Energy band-gap engineering of graphene nanoribbons, *Physical Review Letters*, 98 (2007) 206805.
- [92] L. Jiao, L. Zhang, X. Wang, G. Diankov, H. Dai, Narrow graphene nanoribbons from carbon nanotubes, *Nature*, 458 (2009) 877-880.
- [93] J. Liu, A. Wright, C. Zhang, Z. Ma, Strong terahertz conductance of graphene nanoribbons under a magnetic field, *Applied Physics Letters*, 93 (2008) 041106-041106-041103.
- [94] L. Gomez De Arco, Y. Zhang, C.W. Schlenker, K. Ryu, M.E. Thompson, C. Zhou, Continuous, highly flexible, and transparent graphene films by chemical vapor deposition for organic photovoltaics, *Acs Nano*, 4 (2010) 2865-2873.
- [95] J.C. Meyer, A. Geim, M. Katsnelson, K. Novoselov, T. Booth, S. Roth, The structure of suspended graphene sheets, *Nature*, 446 (2007) 60-63.
- [96] C. Lee, X. Wei, J.W. Kysar, J. Hone, Measurement of the elastic properties and intrinsic strength of monolayer graphene, *Science*, 321 (2008) 385-388.
- [97] H.K. Chae, D.Y. Siberio-Pérez, J. Kim, Y. Go, M. Eddaoudi, A.J. Matzger, M. O'Keeffe, O.M. Yaghi, A route to high surface area, porosity and inclusion of large molecules in crystals, *Nature*, 427 (2004) 523-527.
- [98] N. Stander, B. Huard, D. Goldhaber-Gordon, Evidence for Klein tunneling in graphene pn junctions, *Physical review letters*, 102 (2009) 26807.
- [99] M. Katsnelson, K. Novoselov, A. Geim, Chiral tunnelling and the Klein paradox in graphene, *Nature Physics*, 2 (2006) 620-625.
- [100] A.A. Balandin, S. Ghosh, W. Bao, I. Calizo, D. Teweldebrhan, F. Miao, C.N. Lau, Superior thermal conductivity of single-layer graphene, *Nano letters*, 8 (2008) 902-907.

- [101] M.S. Fuhrer, C.N. Lau, A.H. MacDonald, Graphene: materially better carbon, *MRS bulletin*, 35 (2010) 289-295.
- [102] C. Kane, E. Mele, Quantum spin Hall effect in graphene, *Physical review letters*, 95 (2005) 226801.
- [103] S.L. Yung Ho Kahng, Minhyeok Choe, Gunho Jo, Woojin Park, Jongwon Yoon, Woong-Ki Hong, Chun Hum Cho, Byoung Hun Lee and Takhee Lee, A study of graphene films synthesized on nickel substrates: existence and origin of small-base-area peaks, *nanotechnology*, 22 (2011) 9.
- [104] H. Zhu, J. Wei, K. Wang, D. Wu, Applications of carbon materials in photovoltaic solar cells, *Solar Energy Materials and Solar Cells*, 93 (2009) 1461-1470.
- [105] K. Jasuja, Designing Nanoscale Constructs from Atomic Thin Sheets of Graphene, Boron Nitride and Gold Nanoparticles for Advanced Material Applications, in, Kansas State University, 2011.
- [106] M. Abe, T. Mimura, K. Nishiuchi, A. Shibatomi, M. Kobayashi, Recent advances in ultra-high-speed HEMT technology, *Quantum Electronics, IEEE Journal of*, 22 (1986) 1870-1879.
- [107] J. Faist, F. Capasso, D.L. Sivco, C. Sirtori, A.L. Hutchinson, A.Y. Cho, Quantum Cascade Laser, *Science*, 264 (1994) 553-556.
- [108] M.N. Baibich, J. Broto, A. Fert, F.N. Van Dau, F. Petroff, P. Etienne, G. Creuzet, A. Friederich, J. Chazelas, Giant magnetoresistance of (001) Fe/(001) Cr magnetic superlattices, *Physical Review Letters*, 61 (1988) 2472-2475.
- [109] T. Sun, Z. Wang, Z. Shi, G. Ran, W. Xu, Z. Wang, Y. Li, L. Dai, G. Qin, Multilayered graphene used as anode of organic light emitting devices, *Applied physics letters*, 96 (2010) 133301-133301-133303.
- [110] B. Dieny, V.S. Speriosu, S.S. Parkin, B.A. Gurney, D.R. Wilhoit, D. Mauri, Giant magnetoresistive in soft ferromagnetic multilayers, *Physical Review B*, 43 (1991) 1297.
- [111] W. Choi, I. Lahiri, R. Seelaboyina, Y.S. Kang, Synthesis of Graphene and Its Applications: A Review, *Critical Reviews in Solid State and Materials Sciences*, 35 (2010) 52-71.
- [112] Y. Dan, Nanowire and graphene-based vapor sensors for electronic nose applications, in, University of Pennsylvania, 2009.
- [113] Y. Si, E.T. Samulski, Synthesis of water soluble graphene, *Nano letters*, 8 (2008) 1679-1682.

- [114] E.D. Grayfer, V.G. Makotchenko, A.S. Nazarov, S.-J. Kim, V.E. Fedorov, Graphene: chemical approaches to the synthesis and modification, *Russian Chemical Reviews*, 80 (2011) 751-770.
- [115] V.C. Tung, M.J. Allen, Y. Yang, R.B. Kaner, High-throughput solution processing of large-scale graphene, *Nature nanotechnology*, 4 (2008) 25-29.
- [116] V.C. Tung, L.-M. Chen, M.J. Allen, J.K. Wassei, K. Nelson, R.B. Kaner, Y. Yang, Low-temperature solution processing of graphene– carbon nanotube hybrid materials for high-performance transparent conductors, *Nano letters*, 9 (2009) 1949-1955.
- [117] J. Lin, Graphene and its Hybrid Nanostructures for Nanoelectronics and Energy Applications in: *Mechanical Engineering*, UNIVERSITY OF CALIFORNIA RIVERSIDE 2011, pp. 161.
- [118] S. Stankovich, R.D. Piner, S.T. Nguyen, R.S. Ruoff, Synthesis and exfoliation of isocyanate-treated graphene oxide nanoplatelets, *Carbon*, 44 (2006) 3342-3347.
- [119] S. Stankovich, R.D. Piner, X. Chen, N. Wu, S.T. Nguyen, R.S. Ruoff, Stable aqueous dispersions of graphitic nanoplatelets via the reduction of exfoliated graphite oxide in the presence of poly (sodium 4-styrenesulfonate), *Journal of Materials Chemistry*, 16 (2006) 155-158.
- [120] Y. Hernandez, V. Nicolosi, M. Lotya, F.M. Blighe, Z. Sun, S. De, I. McGovern, B. Holland, M. Byrne, Y.K. Gun'Ko, High-yield production of graphene by liquid-phase exfoliation of graphite, *Nature Nanotechnology*, 3 (2008) 563-568.
- [121] M. Lotya, Y. Hernandez, P.J. King, R.J. Smith, V. Nicolosi, L.S. Karlsson, F.M. Blighe, S. De, Z. Wang, I. McGovern, Liquid phase production of graphene by exfoliation of graphite in surfactant/water solutions, *Journal of the American Chemical Society*, 131 (2009) 3611-3620.
- [122] X. Wu, X. Li, Z. Song, C. Berger, W.A. De Heer, Weak antilocalization in epitaxial graphene: evidence for chiral electrons, *Physical review letters*, 98 (2007) 136801.
- [123] Z.G. Cambaz, G. Yushin, S. Osswald, V. Mochalin, Y. Gogotsi, Noncatalytic synthesis of carbon nanotubes, graphene and graphite on SiC, *Carbon*, 46 (2008) 841-849.
- [124] Z.-Y. Juang, C.-Y. Wu, C.-W. Lo, W.-Y. Chen, C.-F. Huang, J.-C. Hwang, F.-R. Chen, K.-C. Leou, C.-H. Tsai, Synthesis of graphene on silicon carbide substrates at low temperature, *Carbon*, 47 (2009) 2026-2031.
- [125] K.V. Emtsev, A. Bostwick, K. Horn, J. Jobst, G.L. Kellogg, L. Ley, J.L. McChesney, T. Ohta, S.A. Reshanov, J. Röhrl, Towards wafer-size graphene layers by atmospheric pressure graphitization of silicon carbide, *Nature materials*, 8 (2009) 203-207.

- [126] T. Ohta, F. El Gabaly, A. Bostwick, J.L. McChesney, K.V. Emtsev, A.K. Schmid, T. Seyller, K. Horn, E. Rotenberg, Morphology of graphene thin film growth on SiC (0001), *New Journal of Physics*, 10 (2008) 023034.
- [127] A. Vazquez de Parga, F. Calleja, B. Borca, M. Passeggi Jr, J. Hinarejos, F. Guinea, R. Miranda, Periodically rippled graphene: growth and spatially resolved electronic structure, *Physical review letters*, 100 (2008) 56807.
- [128] P.W. Sutter, J.-I. Flege, E.A. Sutter, Epitaxial graphene on ruthenium, *Nature materials*, 7 (2008) 406-411.
- [129] J. Wintterlin, M.-L. Bocquet, Graphene on metal surfaces, *Surface Science*, 603 (2009) 1841-1852.
- [130] J. Shelton, H. Patil, J. Blakely, Equilibrium segregation of carbon to a nickel (111) surface: A surface phase transition, *Surface Science*, 43 (1974) 493-520.
- [131] A. Reina, X. Jia, J. Ho, D. Nezich, H. Son, V. Bulovic, M.S. Dresselhaus, J. Kong, Large area, few-layer graphene films on arbitrary substrates by chemical vapor deposition, *Nano letters*, 9 (2008) 30-35.
- [132] Y. Gamo, A. Nagashima, M. Wakabayashi, M. Terai, C. Oshima, Atomic structure of monolayer graphite formed on Ni (111), *Surface Science*, 374 (1997) 61-64.
- [133] E. Rut'kov, A.Y. Tontegode, Interaction of silver atoms with iridium and with a two-dimensional graphite film on iridium: Adsorption, desorption, and dissolution, *Physics of the Solid State*, 46 (2004) 371-377.
- [134] H. Ueta, M. Saida, C. Nakai, Y. Yamada, M. Sasaki, S. Yamamoto, Highly oriented monolayer graphite formation on Pt (111) by a supersonic methane beam, *Surface science*, 560 (2004) 183-190.
- [135] D. Starr, E. Pazhetnov, A. Stadnichenko, A. Boronin, S. Shaikhutdinov, Carbon films grown on Pt (111) as supports for model gold catalysts, *Surface science*, 600 (2006) 2688-2695.
- [136] S. Marchini, S. Günther, J. Wintterlin, Scanning tunneling microscopy of graphene on Ru (0001), *Physical Review B*, 76 (2007) 075429.
- [137] J. Vaari, J. Lahtinen, P. Hautojärvi, The adsorption and decomposition of acetylene on clean and K-covered Co (0001), *Catalysis letters*, 44 (1997) 43-49.
- [138] J. Wang, M. Zhu, R. Outlaw, X. Zhao, D. Manos, B. Holloway, V. Mammana, Free-standing subnanometer graphite sheets, *Applied physics letters*, 85 (2004) 1265-1267.
- [139] J. Wang, M. Zhu, R.A. Outlaw, X. Zhao, D.M. Manos, B.C. Holloway, Synthesis of carbon nanosheets by inductively coupled radio-frequency plasma enhanced chemical vapor deposition, *Carbon*, 42 (2004) 2867-2872.

- [140] M. Zhu, J. Wang, B.C. Holloway, R. Outlaw, X. Zhao, K. Hou, V. Shuthanandan, D.M. Manos, A mechanism for carbon nanosheet formation, *Carbon*, 45 (2007) 2229-2234.
- [141] N. Zhan, M. Olmedo, G. Wang, J. Liu, Layer-by-layer synthesis of large-area graphene films by thermal cracker enhanced gas source molecular beam epitaxy, *Carbon*, 49 (2011) 2046-2052.
- [142] M.J. McAllister, J.-L. Li, D.H. Adamson, H.C. Schniepp, A.A. Abdala, J. Liu, M. Herrera-Alonso, D.L. Milius, R. Car, R.K. Prud'homme, Single sheet functionalized graphene by oxidation and thermal expansion of graphite, *Chemistry of Materials*, 19 (2007) 4396-4404.
- [143] D.V. Kosynkin, A.L. Higginbotham, A. Sinitskii, J.R. Lomeda, A. Dimiev, B.K. Price, J.M. Tour, Longitudinal unzipping of carbon nanotubes to form graphene nanoribbons, *Nature*, 458 (2009) 872-876.
- [144] M. Terrones, Materials science: Nanotubes unzipped, *Nature*, 458 (2009) 845-846.
- [145] A.G. Cano-Márquez, F.J. Rodríguez-Macías, J. Campos-Delgado, C.G. Espinosa-González, F. Tristán-López, D. Ramírez-González, D.A. Cullen, D.J. Smith, M. Terrones, Y.I. Vega-Cantú, Ex-MWNTs: Graphene sheets and ribbons produced by lithium intercalation and exfoliation of carbon nanotubes, *Nano letters*, 9 (2009) 1527-1533.
- [146] A.L. Elías, A.R. Botello-Méndez, D. Meneses-Rodríguez, V. Jehová González, D. Ramírez-González, L. Ci, E. Muñoz-Sandoval, P.M. Ajayan, H. Terrones, M. Terrones, Longitudinal cutting of pure and doped carbon nanotubes to form graphitic nanoribbons using metal clusters as nanoscalpels, *Nano letters*, 10 (2009) 366-372.
- [147] K. Seshan, *Handbook of thin film deposition*, William Andrew, 2012.
- [148] M. Ohring, *Materials science of thin films*, Academic press, 2001.
- [149] G. Binnig, C.F. Quate, C. Gerber, Atomic force microscope, *Physical review letters*, 56 (1986) 930-933.
- [150] C. Kittel, P. McEuen, *Introduction to solid state physics*, Wiley New York, 1996.
- [151] Accessories Catalogue in: NT-MDT (Ed.), 2012.
- [152] F. Haguenau, P. Hawkes, J. Hutchison, B. Satiat-Jeunemaître, G. Simon, D. Williams, Key events in the history of electron microscopy, *Microscopy and Microanalysis*, 9 (2003) 96-138.

- [153] X. Li, W. Cai, J. An, S. Kim, J. Nah, D. Yang, R. Piner, A. Velamakanni, I. Jung, E. Tutuc, Large-area synthesis of high-quality and uniform graphene films on copper foils, *Science*, 324 (2009) 1312-1314.
- [154] X. Li, W. Cai, L. Colombo, R.S. Ruoff, Evolution of graphene growth on Ni and Cu by carbon isotope labeling, *Nano letters*, 9 (2009) 4268-4272.
- [155] J. Kong, A. Reina Ceeco, Single-and few-layer graphene by ambient pressure chemical vapor deposition on nickel, in, Massachusetts Institute of Technology, 2010.
- [156] Y. Lee, S. Bae, H. Jang, S. Jang, S.E. Zhu, S.H. Sim, Y.I. Song, B.H. Hong, J.H. Ahn, Wafer-scale synthesis and transfer of graphene films, *Nano letters*, 10 (2010) 490-493.
- [157] B. Banerjee, T. Hirt, P. Walker, Pyrolytic carbon formation from carbon suboxide, (1961).
- [158] A. Presland, P. Walker, Growth of single-crystal graphite by pyrolysis of acetylene over metals, *Carbon*, 7 (1969) 1-8.
- [159] Q. Yu, J. Lian, S. Siriponglert, H. Li, Y.P. Chen, S.-S. Pei, Graphene segregated on Ni surfaces and transferred to insulators, *Applied Physics Letters*, 93 (2008) 113103-113103-113103.
- [160] M. Losurdo, M.M. Giangregorio, P. Capezzuto, G. Bruno, Graphene CVD growth on copper and nickel: role of hydrogen in kinetics and structure, *Physical Chemistry Chemical Physics*, 13 (2011) 20836-20843.
- [161] R. Abbaschian, L. Abbaschian, R.E. Reed-Hill, *Physical metallurgy principles*, Thomson Engineering, 2008.
- [162] E. Loginova, N.C. Bartelt, P.J. Feibelman, K.F. McCarty, Evidence for graphene growth by C cluster attachment, *New Journal of Physics*, 10 (2008) 093026.
- [163] L.G. De Arco, Z. Yi, A. Kumar, Z. Chongwu, Synthesis, Transfer, and Devices of Single- and Few-Layer Graphene by Chemical Vapor Deposition, *Nanotechnology, IEEE Transactions on*, 8 (2009) 135-138.
- [164] L. Malard, M. Pimenta, G. Dresselhaus, M. Dresselhaus, Raman spectroscopy in graphene, *Physics Reports*, 473 (2009) 51-87.
- [165] I. Milošević, N. Kepčija, E. Dobardžić, M. Damnjanović, M. Mohr, J. Maultzsch, C. Thomsen, Kohn anomaly in graphene, *Materials Science and Engineering: B*, 176 (2011) 510-511.
- [166] M. Lazzeri, Double resonant Raman in graphene.

- [167] L. Wirtz, A. Allard, C. Attaccalite, M. Lazzeri, F. Mauri, A. Rubio, Tuning the Kohn Anomaly in the Phonon Dispersion of Graphene by Interaction with the Substrate and by Doping, *Bulletin of the American Physical Society*, 56 (2011).
- [168] D. Graf, F. Molitor, K. Ensslin, C. Stampfer, A. Jungen, C. Hierold, L. Wirtz, Spatially resolved Raman spectroscopy of single-and few-layer graphene, *Nano letters*, 7 (2007) 238-242.
- [169] J. Park, A. Reina, R. Saito, J. Kong, G. Dresselhaus, M. Dresselhaus, G' band Raman spectra of single, double and triple layer graphene, *Carbon*, 47 (2009) 1303-1310.
- [170] M.S. Dresselhaus, A. Jorio, M. Hofmann, G. Dresselhaus, R. Saito, Perspectives on carbon nanotubes and graphene Raman spectroscopy, *Nano letters*, 10 (2010) 751-758.
- [171] L. Cancado, M. Pimenta, B. Neves, M. Dantas, A. Jorio, Influence of the atomic structure on the Raman spectra of graphite edges, *Physical review letters*, 93 (2004) 247401.
- [172] A. Ferrari, J. Meyer, V. Scardaci, C. Casiraghi, M. Lazzeri, F. Mauri, S. Piscanec, D. Jiang, K. Novoselov, S. Roth, The raman fingerprint of graphene, arXiv preprint cond-mat/0606284, (2006).
- [173] C.V. Thompson, R. Carel, Stress and grain growth in thin films, *Journal of the Mechanics and Physics of Solids*, 44 (1996) 657-673.
- [174] G. Bertoni, L. Calmels, A. Altibelli, V. Serin, First-principles calculation of the electronic structure and EELS spectra at the graphene/Ni (111) interface, *Physical Review B*, 71 (2005) 075402.
- [175] Y.S. Dedkov, M. Fonin, Electronic and magnetic properties of the graphene–ferromagnet interface, *New Journal of Physics*, 12 (2010) 125004.
- [176] R. Rosei, M. De Crescenzi, F. Sette, C. Quaresima, A. Savoia, P. Perfetti, Structure of graphitic carbon on Ni (111): A surface extended-energy-loss fine-structure study, *Physical Review B*, 28 (1983) 1161.
- [177] V. Rothová, M. Svoboda, J. Buršík, The Effect of Annealing Conditions on Grain Growth and Microstructure in Nickel, in, Institute of Physics of Materials AS CR, 2009.
- [178] A.M. Thron, P. Greene, K. Liu, K.v. Benthem, Wetting -Dewetting Transitions of Ultrathin Nickel Films Deposited on Silicon (100) Substrates, *Microsc. Microanal.*, 17 (Suppl 2) (2011).
- [179] J.A. Thornton, D.W. Hoffman, Stress-related effects in thin films, *Thin Solid Films*, 171 (1989) 5-31.

- [180] Y. Selamet, S. Kir, Growth and electrical characterization of high purity carbon nanotubes, (2009).
- [181] A.M. Cassell, J.A. Raymakers, J. Kong, H. Dai, Large scale CVD synthesis of single-walled carbon nanotubes, *The Journal of Physical Chemistry B*, 103 (1999) 6484-6492.
- [182] K. Teo, M. Chhowalla, G. Amaratunga, W. Milne, D. Hasko, G. Piro, P. Legagneux, F. Wyczisk, D. Pribat, Uniform patterned growth of carbon nanotubes without surface carbon, *Applied Physics Letters*, 79 (2001) 1534-1536.
- [183] H.T. Li, L.F. Chen, X. Yuan, W.Q. Zhang, J.R. Smith, A.G. Evans, Interfacial Stoichiometry and Adhesion at Metal/ $\alpha$ -Al<sub>2</sub>O<sub>3</sub> Interfaces, *Journal of the American Ceramic Society*, 94 (2011) s154-s159.
- [184] K.S. Kim, Y. Zhao, H. Jang, S.Y. Lee, J.M. Kim, K.S. Kim, J.-H. Ahn, P. Kim, J.-Y. Choi, B.H. Hong, Large-scale pattern growth of graphene films for stretchable transparent electrodes, *Nature*, 457 (2009) 706-710.
- [185] D.R. Lenski, M.S. Fuhrer, Raman and optical characterization of multilayer turbostratic graphene grown via chemical vapor deposition, *Journal of Applied Physics*, 110 (2011) 013720-013720-013724.
- [186] G. Henkelman, A. Arnaldsson, H. Jónsson, Theoretical calculations of CH<sub>4</sub> and H<sub>2</sub> associative desorption from Ni (111): Could subsurface hydrogen play an important role?, *The Journal of chemical physics*, 124 (2006) 044706-044706-044709.